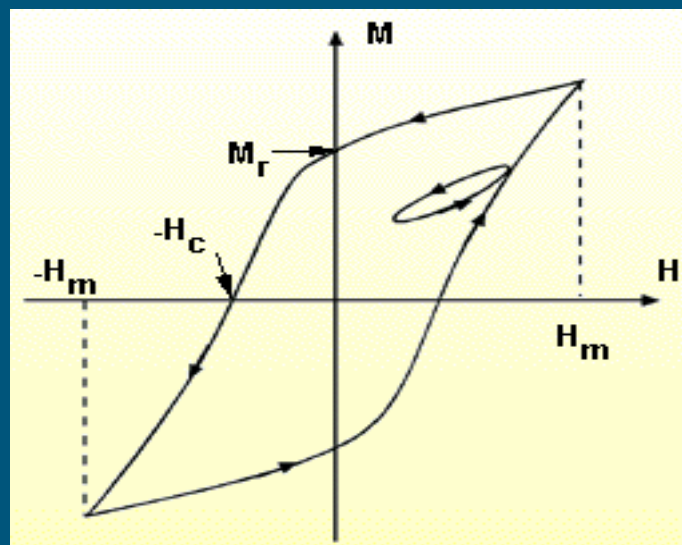


Numerical Simulation of Hysteresis Effects in Ferromagnetic Material with the Finite Integration Technique



Numerical Simulation of Hysteresis Effects in Ferromagnetic Material with the Finite Integration Technique

Vom Fachbereich Elektrotechnik und Informationstechnik
der Technischen Universität Darmstadt

zur Erlangung
der Würde einer Doktor-Ingenieurin (Dr.-Ing.)
genehmigte

DISSERTATION

von
MSc.-Eng. Jing Yuan
geboren am 06. April 1975 in Wuhan

Referent: Prof. Dr.-Ing. Thomas Weiland
Korreferent: Prof. Dr.-Ing. habil. Andreas Binder

Tag der Einreichung: 22.02.2005
Tag der mündlichen Prüfung: 26.04.2005

D17
Darmstädter Dissertation

Bibliografische Information Der Deutschen Bibliothek

Die Deutsche Bibliothek verzeichnet diese Publikation in der Deutschen Nationalbibliografie; detaillierte bibliografische Daten sind im Internet über <http://dnb.ddb.de> abrufbar.

1. Aufl. - Göttingen : Cuvillier, 2005
Zugl.: Darmstadt, Univ., Diss., 2005
ISBN 3-86537-503-0

© CUVILLIER VERLAG, Göttingen 2005
Nonnenstieg 8, 37075 Göttingen
Telefon: 0551-54724-0
Telefax: 0551-54724-21
www.cuvillier.de

Alle Rechte vorbehalten. Ohne ausdrückliche Genehmigung des Verlages ist es nicht gestattet, das Buch oder Teile daraus auf fotomechanischem Weg (Fotokopie, Mikrokopie) zu vervielfältigen.

1. Auflage, 2005
Gedruckt auf säurefreiem Papier

ISBN 3-86537-503-0

Numerische Simulation von Hysterese-Effekten in ferromagnetischen Materialien mit der Methode der Finiten Integration

Kurzfassung der Arbeit

Die vorliegende Arbeit befasst sich mit der Anwendung von Hysterese-Modellen und der Methode der Finiten Integration zur Lösung von Hysterese-Effekten in ferromagnetischen Materialien. Der Schwerpunkt liegt in der Entwicklung und Implementierung geeigneter numerischer Verfahren, mit denen Hysterese-Effekte in ferromagnetischen Materialien bei der Berechnung zeitlich langsam veränderlicher Magnetfelder nachgebildet werden können.

Bei dem Phänomen der Hysterese ist der tatsächliche funktionale Zusammenhang zwischen der magnetischen Flussdichte und der magnetischen Feldstärke von der Geschichte der vorangegangenen Materialbeeinflussung, der vorangegangenen Magnetisierung, bestimmt. Das Preisach Modell und das Jiles-Atherton Modell werden als mathematische Hysterese-Modelle ausgewählt. Die Beziehung zwischen der magnetischen Flussdichte und der magnetischen Feldstärke kann nicht mehr als eine Funktion im mathematischen Sinne beschrieben werden. Der Zusammenhang zwischen diesen Größen wird für das Preisach-Modell von den gemessenen Übergangskurven erster Ordnung bestimmt. Bei der Interpolation der gemessenen Kurven wird eine zweischrittige polynomiale Interpolation, abhängig vom Preisach-Modell oder dem invertierten Preisach-Modell, angewandt. Das Jiles-Atherton Modell ist abhängig von fünf Materialparametern, die aus den gemessenen Kurven gewonnen werden.

Die Algorithmen zur Berücksichtigung eines solchen nichtlinearen Materialverhaltens bei der transienten Magnetfeldberechnung werden mit zwei verschiedenen Modellierungen nichtlinearer Materialien realisiert: dem Schema zur Aktualisierung der magnetischen Polarisation und dem nichtlinearen Aktualisierungsschema. Das Verfahren von Newton-Raphson und das Verfahren der Sukzessiven Approximation mit geeignetem Relaxationsansatz werden als Linearisierungsverfahren für das nichtlineare Aktualisierungsschema vorgestellt.

Das nichtlineare Aktualisierungsschema ist im Vergleich mit dem Schema zur Aktualisierung der magnetischen Polarisation ein schnell konvergierendes Verfahren, dessen Konvergenz aber nur in der Nähe der Lösung garantiert ist. Dagegen ist das Schema zur Aktualisierung der magnetischen Polarisation sehr robust. Um die Vorteile beider Schemen zu kombinieren, wird ein neues iteratives hybrides Newton-Polarisations-Verfahren zur Berechnung von Hysterese-Effekten vorgestellt. Ein vereinfachtes Vektor-Preisach-Modell wird als eine Erweiterung der Hysterese-Modelle in diese Algorithmen der Methode der Finiten Integration eingebunden, um die wirklichen physikalischen Eigenschaften von Hysterese nachbilden zu können.

Die zuvor erwähnten Algorithmen werden anhand des TEAM Benchmark Problems 32 getestet. Die Ergebnisse zeigen gute Übereinstimmung mit den Messungen.

Numerical Simulation of Hysteresis Effects in ferromagnetic Material with the Finite Integration Technique

Abstract

In this dissertation, transient magnetoquasistatic field simulations are carried out considering hysteresis effects in ferromagnetic material. Numerical hysteresis models are combined with the Finite Integration Technique applied for the discretization of the model geometry.

Ferromagnetic hysteresis is a phenomenon where the magnetic flux density is not only determined by the instantaneous excitation, but also from the hysteresis history. Hence, the relationship between the magnetic flux density and the magnetic field strength can not be reduced to a time-independent material characteristic. As mathematical models for representing hysteresis, the Preisach model and the Jiles-Atherton model are used. The Preisach model is based on the assumption that any hysteresis can be expressed as a sum of elementary hysteresis loops. The distribution function of the elementary hysteresis is determined from a set of measured first-order transition curves. A two-step interpolation on the measurement data is applied. The Jiles-Atherton model is described by a first-order ordinary differential equation which depends on five parameters of the Jiles-Atherton model. These parameters are determined from the experimental data. Both models can be evaluated for arbitrary input values.

The hysteresis model are combined with the Finite Integration Technique yielding two possible nonlinear magnetoquasistatic formulations: the magnetic polarization update scheme and the magnetic reluctivity nonlinear update scheme. Using the magnetic polarization update scheme, only a magnetization term at the right hand side of the algebraic system of equations has to be updated between two successive nonlinear steps. In the magnetic reluctivity nonlinear update scheme, the reluctivity at the left hand side of the algebraic system of equations has to be updated. For the latter case, the system has to be linearized, which is here based on the Newton-Raphson method or the successive approximation technique, equipped with a relaxation strategy.

Compared with the magnetic polarization update scheme, the magnetic reluctivity nonlinear update scheme linearized by the Newton-Raphson method converges substantively faster. Its convergence is, however, only guaranteed in the vicinity of the solution. On the other hand, the magnetic polarization update scheme is very robust. In order to combine the advantages of the both update scheme, a new hybrid Newton-Polarization method is introduced within the magnetoquasistatic models. A vector hysteresis model as an extension of the hysteresis models is also with the Finite Integration Technique, in order to numerically simulate hysteresis phenomena in models parts submitted to rotational flux.

The above mentioned algorithms are tested using the TEAM Benchmark Problem 32. The results show a good agreement with the measurements.

Contents

1	Introduction	1
1.1	Motivation and History	1
1.2	Overview	2
2	Ferromagnetic Hysteresis	5
2.1	Maxwell's Equations	5
2.2	Physics of Magnetism	7
2.2.1	Magnetic Materials	7
2.2.2	Magnetic Domain Structure	11
2.2.3	Magnetization Process	15
2.2.4	Hysteresis Loops	17
2.3	Preisach Model	21
2.3.1	Classical Preisach Model	22
2.3.2	Main Properties of the Preisach Model	33
2.3.3	Generalized Preisach Models	35
2.3.4	Preisach Model and Hysteresis Losses	37
2.3.5	Vector Preisach Model	39
2.4	Jiles-Atherton Model	44
2.4.1	Physical Principles	44
2.4.2	Jiles-Atherton Model and Determination of Parameters	45
2.4.3	Comparison of the Jiles-Atherton Model and the Preisach Model	47
2.5	Conclusions	48

3	Electromagnetic Field Simulation	49
3.1	Finite Integration Technique	49
3.1.1	Maxwell-Grid-Equations	50
3.1.2	Discrete Material Properties	53
3.1.3	Boundary Conditions	56
3.2	Magnetoquasistatic Problems	57
3.2.1	Magnetostatic Problems	57
3.2.2	Magnetoquasistatic Problems	57
3.2.3	Time Integration Schemes for Differential Algebraic Equations . . .	59
3.2.4	Numerical Solution of Linear Equation Systems	63
4	Modelling and Implementation of Hysteresis	67
4.1	Magnetic Polarization Update Scheme	68
4.1.1	Implementation of the Scalar Preisach Model	68
4.1.2	Hysteresis Losses	72
4.1.3	Magnetic Polarization Iterative Scheme	75
4.1.4	Test Example A and Discussion	79
4.2	Nonlinear Update Scheme	82
4.2.1	Implementation of the Inverse Scalar Preisach Model	82
4.2.2	Implementation of the Inverse Scalar Jiles-Atherton Model	87
4.2.3	Linearization Techniques for Nonlinear Problems	89
4.2.4	Relaxation Methods	92
4.2.5	Nonlinear Iterative Scheme	94
4.2.6	Test Example A and Discussion	96
4.3	Hybrid Newton-Polarization Method	104
4.3.1	Newton Method and Polarization Method	104
4.3.2	Hybrid Newton-Polarization Method	105
4.3.3	Test Example A and Discussion	106
4.4	Vector Hysteresis Model	109
4.4.1	Simplified Vector Preisach Model	110
4.4.2	Test Example B and Discussion	112

<i>CONTENTS</i>	iii
5 Technical Application	115
5.1 TEAM Benchmark Problem 32	115
5.1.1 Simplified Model for the TEAM Benchmark Problem 32	118
5.1.2 Simulated Results and Discussion for Case I	118
5.1.3 Simulated Results and Discussion for Case II	120
6 Summary	125
A Magnetic Curves of Various Ferromagnetic Materials	129
B Applied Notations and Symbols	133
Acknowledgements	147

Chapter 1

Introduction

1.1 Motivation and History

The numerical simulation of hysteresis effects in ferromagnetic material plays an important role in many technological applications, which have been studied in the last decades. The quality of hysteresis models, measured as the correspondence of the simulated and experimental results, has been substantially improved in the last years. Careful implementation and increasing computer resources nowadays enable the application of hysteresis models within electromagnetic field simulations. Up to now, hysteresis models and their introduction in electromagnetic field simulation are still subject of ongoing research. Two basic ingredients are required here: an accurate hysteresis model, combined with an efficient numerical method for electromagnetic field simulation.

Models for the hysteresis of ferromagnetic materials based on the mutual interaction of the magnetic particles, were first developed by J.A. Ewing in 1890, who assumed that the magnetic dipoles can be freely turned according to the interactions between the magnetic moments and the interaction between the neighboring magnetic dipoles as well. On the basis of the experiment by Ewing, the hysteresis of ferromagnetic materials was expected to have qualitative and quantitative characteristics. The theory of quantum mechanics introduced by N. Bohr opens the way for simulating magnetic materials and moments on the basis of quantum theory. The analysis of the microstructure of materials and the physical interpretation of crystal structures from the point of magnetic field led to the theory of spin dynamics and the discovery of the optical properties of magnetic materials. The investigation of the microstructure of magnetic materials motivates the realization of weak magnetic materials and magnetic alloys with special properties. The next period of research is characterized by the development of different models based either on a mathematical or on a physical approach. First realization of dynamical hysteresis models for magnetic materials was presented by Y. Saito between 1982 and 1990 and M.L. Hodgdon in 1988. The Langevin model of paramagnetic materials based on Boltzmann statistics and the Weiss theory resulted in the Jiles-Atherton hysteresis model [23] [24] [25] in 1983 for the representation of the energy loss during the domain wall motion. The studies of Ewing were extended by several researchers and accumulated in the Preisach model [29]. Based on the studies of Preisach and Everett, a mathematical model for hysteresis based on a statistical characterization of material properties was developed by M.A.

Krasnoselskii and A.V. Pokrovskii in 1983. From this time on, a powerful development in the Preisach model started and resulted e.g. the books and papers of E. Della Torre [5], I.D. Mayergoyz [16], A. Visintin [28], O. Benadda, A. Ivanyi [17] and G. Bertotti [4] which are now considered standard reference. The first hysteresis model which also represents the vectorial property of the particle magnetization was the Stoner-Wohlfarth model [22] developed in 1947. A new generation of vector models was introduced by E. Della Torre [18] in 1998 to simplify the mathematical model considering the physical characteristics of ferromagnetic material.

Currently, research on hysteretic material and on hysteresis model is widely spread. Hysteretic materials are applied in many electrotechnical devices. New materials, e.g. compound materials, powder materials, rare-earth permanent magnet materials are applied which require increasingly accurate and efficient hysteresis models. On the basis of microscopic investigations of magnetic materials, the simulation of the nonlinear hysteresis characteristics can be realized by numerical techniques. With the development of the numerical computation in the twentieth century, discretization techniques for field simulation are classified as Finite Element Method (FEM), Boundary Element Method (BEM), Finite Difference in Time Domain (FDTD), and Finite Integration Technique (FIT) etc.. Hysteresis models can be introduced in electromagnetic field simulation based on a discretization of the geometry by arising a hysteresis model for each volumetric entity representing a piece of hysteretic material.

The FIT, presented by Weiland [51], [52], [53] in 1977, was first developed for frequency domain problems starting about three decades ago and later completed to a generalized scheme for the entire application range of Maxwell's equations. The FIT transfers the continuous Maxwell's Equations into a set of matrix equations, each of which is the discrete analogue of one of the original integral equations. The algebraic equations representing Maxwell's equations in the computational grid are called Maxwell-Grid-Equations. Important topological properties such as the curl-freeness of gradient fields and the divergence-freeness of curl fields carry over from the continuous level to the discrete level. The method allows different formulations for the discrete problem not only in frequency domain but also in time domain, which provides more flexibility to the numerical simulation scheme. These attractive features of the FIT motivated the numerical simulation of hysteresis effects in ferromagnetic materials by introducing hysteresis models into the FIT.

1.2 Overview

After introducing the motivation and the development history of hysteresis models and numerical computation for electromagnetic fields, the ferromagnetic hysteresis is introduced in Chapter 2. Starting from Maxwell's equations, the physics of magnetism including the domain structure in magnetic materials and the description of hysteresis loops during the magnetization process is introduced firstly. Then the Preisach models, classified as classical Preisach model, generalized Preisach model and vector model are shortly recalled. Then the Jiles-Atherton model is briefly introduced as a Langevin type hysteresis model.

In order to project Maxwell's equations from continuous space onto a finite grid space and to implement hysteresis models in electromagnetic field simulation based on the discretization of the finite grid space, the FIT is introduced in Chapter 3. The introduction of the

Finite Integration Implicit Time Domain formulation (FI^2TD) for magnetoquasistatic field problems prepares for hysteretic simulation.

The modelling and implementation of the hysteresis is introduced in Chapter 4. Two different models of hysteretic ferromagnetic material behavior are given: the Preisach model and the Jiles-Atherton model. The magnetic polarization update scheme and the hysteretic nonlinear update scheme are introduced combining the two hysteretic ferromagnetic material modelling and the Finite Integration Implicit Time Domain formulation, respectively. The polynomial interpolation from the measured first-order transition curves is described in order to numerically implement the Preisach model and the inverse Preisach model. The computation of hysteretic losses is discussed and given by the integration of the hysteresis loops. The Jiles-Atherton model is implemented by its inverse form in the hysteretic nonlinear update scheme. Although scalar Preisach models have been increasingly accurate and efficient in describing material behavior, in many cases the magnetizing processes is vectorial in nature. The simplified vector model as one of the most computationally efficient models is implemented and compared with the corresponding scalar model. A hybrid method combining the solutions from the overrelaxed polarization method and the underrelaxed Newton method at each iterative cycle is implemented and discussed. The purpose of the hybrid Newton-polarization method is to increase the robustness of the nonlinear iteration, without losing the quadratic speed of convergence in the vicinity of the solution. A 3D transient hysteretic test problem is used for assessing the properties of all of the modelling and implementation methods.

The selected example of Benchmark problem TEAM 32 as an application of the numerical simulation of hysteresis effects in ferromagnetic material is demonstrated in Chapter 5. Two different supply cases are used for assessing the properties of the modelling and implementation of the hysteresis for magnetoquasistatic field problems.

The thesis is concluded with a summary in Chapter 6.

Chapter 2

Ferromagnetic Hysteresis

Ferromagnetic hysteresis is an important behavior of magnetic materials. Its phenomena can affect all applications of magnetic cores from electrical machines to transformers. The physics of magnetism responsible for hysteresis and the adequate mathematical tools to its description are the basis for the theoretical and the numerical study of hysteretic effects in ferromagnetic material. The physics of magnetism has been introduced with various approaches in different works by Bozorth [1], Chikazumi [2], Jiles [3], Bertotti [4] etc.. The Preisach model and the Jiles-Atherton model are the most popular mathematical models for the description of hysteretic phenomena. They have been developed and implemented in many numerical simulations for years.

In this chapter, on the bases of Maxwell's equations, the physics of magnetism, ranging from pure theory of the domain structure in magnetic substances to a plain description of hysteresis loops during the magnetization process, is introduced. As the applied hysteretic model in this thesis work, the Preisach model is recalled in a short summary. The classical Preisach model is described concerning its geometric interpretation, the determination of the distribution function and the numerical implementation. After the discussion of the main properties of the Preisach model, some modified Preisach models, generalized from classical one are shortly mentioned, which overcome the certain limitation of the classical Preisach model. The hysteretic losses are also discussed here. The vector Preisach model is shortly introduced, which will be further discussed in Chapter 4 as well. The Jiles-Atherton model is a Langevin type hysteresis model. It incorporates physical principles in the determination of five material parameters according to the experimental data. The Jiles-Atherton model will be further studied in Chapter 4.

2.1 Maxwell's Equations

Maxwell's equations are the fundamental equations to describe macroscopic electromagnetic phenomena in continuous space. They reflect the relation between the electric field values (field strength \vec{E} and flux density \vec{D}) and magnetic field values (field strength \vec{H} and flux density \vec{B}). They can be written in integral form for arbitrary faces A and volumina V and their respective boundaries ∂A and ∂V for non-moving geometries as:

$$\int_{\partial A} \vec{E}(\vec{r}, t) \cdot d\vec{s} = - \iint_A \frac{\partial}{\partial t} \vec{B}(\vec{r}, t) \cdot d\vec{A}, \quad (2.1)$$

$$\int_{\partial A} \vec{H}(\vec{r}, t) \cdot d\vec{s} = \iint_A \left(\frac{\partial}{\partial t} \vec{D}(\vec{r}, t) + \vec{J}(\vec{r}, t) \right) \cdot d\vec{A}, \quad (2.2)$$

$$\iint_{\partial V} \vec{B}(\vec{r}, t) \cdot d\vec{A} = 0, \quad (2.3)$$

$$\iint_{\partial V} \vec{D}(\vec{r}, t) \cdot d\vec{A} = \iiint_V q(\vec{r}, t) \cdot dV. \quad (2.4)$$

Here, equation (2.1) takes into account Faraday's law and equation (2.2) is called Ampère's law. The third equation (2.3) states that the total magnetic flux crossing any closed, regular surface has zero balance and the fourth equation is called Gauss's law. Maxwell's equations can be written in differential form as well, the differential form is derived by applying the theorems of Gauss and Stokes to the integral forms [49].

The current density $J(\vec{r}, t)$ in the equation (2.2) is composed of

$$\vec{J}(\vec{r}, t) = \vec{J}_k(\vec{r}, t) + \vec{J}_q(\vec{r}, t) + \vec{J}_i(\vec{r}, t), \quad (2.5)$$

where the conduction current density $\vec{J}_k(\vec{r}, t) = \kappa \vec{E}$ arises in materials with electric conductivity κ from the existing electric field strength; the imposed current density $\vec{J}_i(\vec{r}, t)$ expresses the excitation of the problem and is independent of all field forces; the current density $\vec{J}_q(\vec{r}, t)$ is the current contribution of free charges with the charge density q moving at the speed \vec{v} .

The physical characteristics of materials are described by constitutive relations, which relate the electric and magnetic flux densities (\vec{D} and \vec{B}) to the electric and magnetic field strengths (\vec{E} and \vec{H}). In the general case, the constitutive equations are

$$\vec{D} = \varepsilon_0 \vec{E} + \vec{P}, \quad (2.6)$$

$$\vec{B} = \mu_0 (\vec{H} + \vec{M}), \quad (2.7)$$

where the electric polarization \vec{P} and the magnetization \vec{M} of the material can be used in dispersive, anisotropic, nonlinear and hysteretic cases. For linear materials, the electric polarization is $\vec{P} = \varepsilon_0 \chi_e \vec{E}$, where χ_e is the electric susceptibility, and the magnetization is $\vec{M} = \chi_m \vec{H}$, with the magnetic susceptibility χ_m . In the more general case, we have

$$\vec{P} = \varepsilon_0 \chi_e \vec{E} + \vec{P}_r, \quad (2.8)$$

$$\vec{M} = \chi_m \vec{H} + \vec{M}_r. \quad (2.9)$$

The description of the material characteristics in the electromagnetic field calculation is extended by the independent permanent polarization \vec{P}_r and independent permanent magnetization \vec{M}_r . The physical characterization of magnetic materials is the general subject of this thesis and will be discussed in the following sections.

2.2 Physics of Magnetism

2.2.1 Magnetic Materials

There are various types of magnetism. Each of them is characterized by its own magnetic properties. The various magnetism will be classified in this subsection and their magnetic structures and magnetic properties will be described.

The magnetic flux density \vec{B} and the magnetization vector \vec{M} are commonly used in engineering application to describe the magnetization. The relationship between \vec{B} and \vec{M} is

$$\vec{B} = \mu_0(\vec{H} + \vec{M}), \quad (2.10)$$

where μ_0 is the permeability in vacuum and \vec{H} is the magnetic field intensity. The relation between the magnetic field intensity \vec{H} and the magnetization vector \vec{M} can be represented by a linear operator, a nonlinear operator, or a hysteresis operator. However, for linear materials, the relation between the magnetization \vec{M} and the magnetic field intensity \vec{H} can be expressed by

$$\vec{M} = \chi_m \vec{H}, \quad (2.11)$$

where χ_m is the magnetic susceptibility. The observed value of the magnetic susceptibility ranges from 10^{-5} for soft magnetic materials to 10^6 for hard magnetic magnets. The susceptibility is not necessarily constant. It can vary as the function of the applied field. Moreover, the susceptibility does not need to be scalar, it can be also a tensor, to represent anisotropic material, and in some cases it takes negative values as well, e.g. in superconductors. Substituting (2.11) into (2.10), we have

$$\vec{B} = \mu_0(1 + \chi_m)\vec{H} = \mu_0\mu_r\vec{H}. \quad (2.12)$$

The relation between the magnetic induction \vec{B} and the applied field \vec{H} can be expressed by the relative permeability μ_r .

On the basis of the magnetic susceptibility, the magnetic behavior of materials can be classified as diamagnetism, paramagnetism, antiferromagnetism, ferrimagnetism and ferromagnetism [2].

1. Diamagnetism is a weak magnetism in which a magnetization is exhibited opposite to the direction of the applied field. The magnetic susceptibility χ_m is negative and order of magnitude is in general about 10^{-5} . Examples of diamagnetic materials are some rare gases and nonmetallic elements, but some metals, e.g. copper (Cu), silver (Ag), zinc (Zn) and gold (Au) also belong to the diamagnet materials.

2. Paramagnetism is a weak magnetism as well. In paramagnetism, the magnetization \vec{M} is proportional to the magnetic field \vec{H} . Paramagnetic materials contain magnetic atoms or ions whose spins are not compensated. At finite temperatures, the spins are thermally agitated and take random orientations. According to the Curie law, the susceptibility of paramagnetic materials is inversely proportional to the temperature. In the paramagnetic case, the magnetization \vec{M} is increasing with the applied field \vec{H} . The magnetic susceptibility χ_m is positive and its order of magnitude is 10^{-5} to 10^{-3} . Examples of paramagnetic materials are oxygen (O_2), aluminum (Al), manganese (Mn) and the alloys

of the rare earth elements from lanthanum (La) to ytterbium (Yb), and iron (Fe), cobalt (Co) and nickel (Ni).

3. Antiferromagnetism is similar to paramagnetism in the sense of exhibiting a small positive susceptibility. The susceptibility depends on the temperature, as characterized by the occurrence of a kink in the $\chi_m - T$ curve at the Néel temperature T_N (Fig. 2.1 B). According to the interaction between the magnetic moments, an antiparallel spin arrangement is established, in which the plus and minus spins completely cancel each other (Fig. 2.1 A). In such an antiferromagnetic arrangement of spins, the tendency to be magnetized by the external field is opposed by a strong negative interaction acting between plus and minus spins. If there is no external field, the opposite directed moments completely compensate each other. When applying an external field, the antiferromagnetic material proves weak magnetic properties with small positive susceptibilities. The compounds of manganese (MnO, MnS), vanadium (VO₂) and iron (FeS₂) belong to the antiferromagnetic materials.

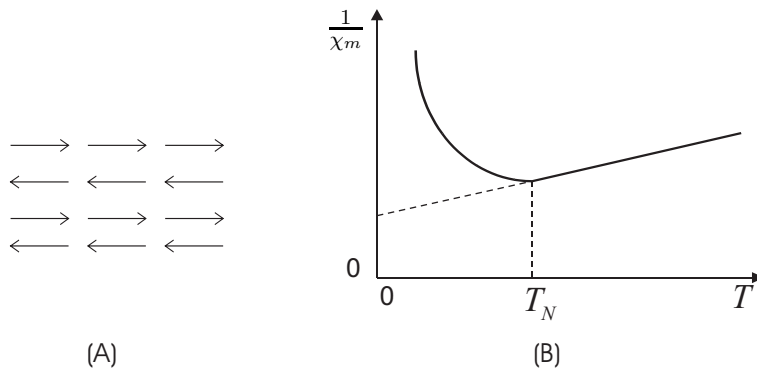


Figure 2.1: Antiferromagnetic material, (A) Configuration of magnetic spins, (B) Temperature dependence of the susceptibility.

4. Ferrimagnetism is the term proposed by Néel² to describe the magnetism of ferrites. In these substances, magnetic ions occupy two kinds of lattice sites, the spins on one site point in the plus direction, whereas those on the other site point in the minus direction. Since the number of magnetic ions and also the magnitude of spins of individual ions are different on the both sites, such an ordered arrangement of spins gives rise to a resultant magnetization, i.e. spontaneous magnetization. As the temperature increases, the arrangement of the spins is disturbed by thermal agitation. Above the Curie point T_C , the substance exhibits paramagnetism, and the susceptibility decreases with increase of temperature (Fig. 2.2). Ferrimagnetism is observed in various kinds of magnetic compounds. In these materials the divalent metal ions can be found as manganese (Mn), cobalt (Co), nickel (Ni), zinc (Zn). The ferrimagnetic garnets are the group of minerals, where the divalent elements are the rare earth materials, such as cadmium (Cd), terbium (Tb), yttrium (Y).

5. In the case of ferromagnetism, the spins are aligned parallel to one another as a result of a strong positive interaction acting between the neighboring spins (Fig. 2.3(A)). As the temperature increases, the arrangement of the spins is disturbed by thermal agitation, thus resulting in a temperature dependence of spontaneous magnetization (Fig. 2.3(B)). Above the Curie point, the susceptibility obeys the Curie-Weiss law, which states that

$1/\chi_m$ rises from zero at the Curie point T_C and increases linearly with temperature as shown in Fig. 2.3(C).

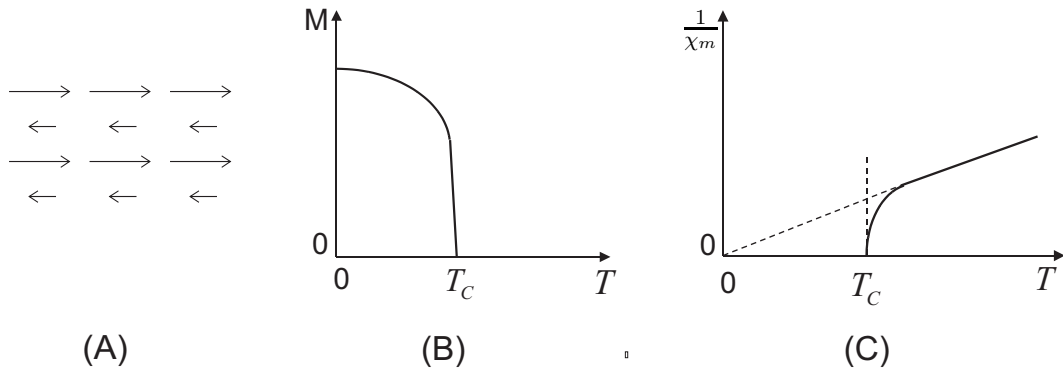


Figure 2.2: Ferrimagnetic material, (A) Configuration of magnetic spins; (B) Spontaneous magnetization; (C) Temperature dependence of the susceptibility.

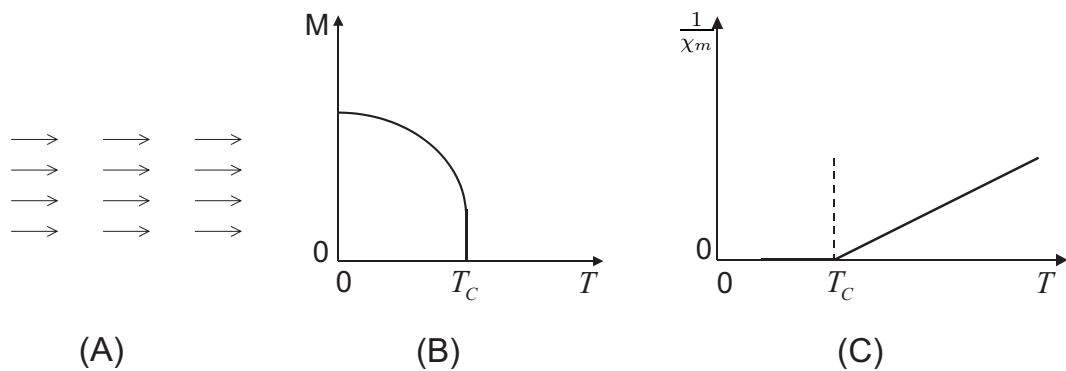


Figure 2.3: Ferromagnetic material, (A) Configuration of magnetic spins; (B) Spontaneous magnetization; (C) Temperature dependence of the susceptibility.

The interior of the ferromagnetic material is divided into many magnetic domains, each of which is spontaneously magnetized. The domain sizes change from a few microns to perhaps millimeters for many ferromagnetic materials. In the domains, a large number of atomic moments, i.e. 10^{12} to 10^{18} , are aligned parallel, so that the magnetization within the domain is almost saturated. Since only the direction of the domain magnetization is varying from domain to domain, the resultant magnetization can be changed from zero to the value of saturation magnetization.

The magnetic properties of a ferromagnetic material are represented by the plot of the magnetization \vec{M} or magnetic flux density \vec{B} at various field intensity \vec{H} , which is shown in Fig. 2.4. In the ferromagnetic materials, the orientation of the domains is randomly distributed. In demagnetized state at absence of the applied field the magnetization is zero

(point O). If an external field is applied the domain walls first move to favor the growth of those domains having magnetic moments aligned with the applied field (region A). Reversible condition is valid on removing the field. With the application of stronger fields an irreversible domain wall motion occurs (region B). For a sufficiently large alignment with the applied field the saturation magnetization \vec{M}_s is reached (region C).

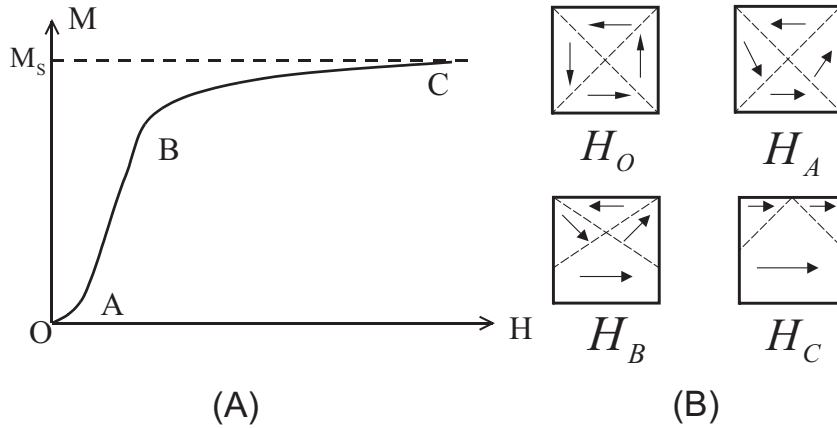


Figure 2.4: (A) The first magnetization curve (virgin curve or initial curve); (B) Variation of the domain structures with the applied field.

If the field is reduced, the magnetization is also decreased, but does not return to its original value. It can be seen that decreasing the applied field to zero the characteristic arrives at a working point with remanence, with the remanent magnetization \vec{M}_r , $\vec{H} = 0$, and remanent induction $\vec{B}_r = \mu_0 \vec{M}_r$, respectively. Further decreasing the applied field to the coercive field $-\vec{H}_c$, the field induction reaches to zero $\vec{B}_c = 0$, with $\mu_0(\vec{H}_c + \vec{M}_c) = 0$ (Fig. 2.5). Such an irreversible process of magnetization is called hysteresis.

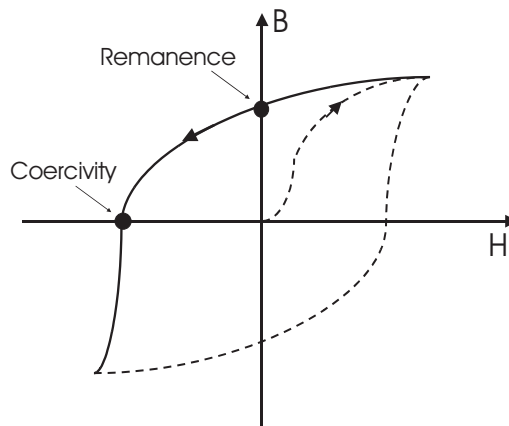


Figure 2.5: Irreversible process of magnetization.

The saturation phenomenon and the hysteresis characteristics are important properties of ferromagnetic materials, which will be recalled in the following sections of the magnetic domain structure and the magnetization process.

2.2.2 Magnetic Domain Structure

The magnetic behavior and the hysteresis loop can be described in terms of the domain theory. The ferromagnetic material is composed of many *domains*, each magnetized up to saturation in some direction. In this section, we discuss the fundamental properties of domain structures and the various factors which influence their distribution in ferromagnetic materials. The concept of the ferromagnetic domain structure was first proposed by P. Weiss in 1907 in his famous paper on the hypothesis of the molecular field [1]. The first experiment of the ferromagnetic domains was made by Barkhausen in 1919 [4]. The theoretical treatment of the ferromagnetic domain structure was first carried out by Landau and Lifshitz in 1935. The existence of domains is a consequence of the principle of energy minimization. The decomposition of the substance into localized domains associated with closed path of the flux lines reduces the magnetic energy. The domain structures with closed path of the flux lines prove demagnetized state of the substance even under saturated condition within the domains.

The domain structure

The domain structure is first discussed in a uniform ferromagnetic crystal [2] [17]. In the spherical single crystal specimen case (Fig. 2.6(A)), the magnetic poles appearing on the surface would give rise to the strong demagnetizing field, such a system has a large magnetostatic energy. To avoid this is to make the inner magnetization rotate inside the sphere as shown in Fig. 2.6(B). Then there would be no magnetic poles and no magnetostatic energy being stored. However, the neighboring spins instead make some angle with one another, so that some amount of exchange energy must be stored. The variation in the exchange energy with spin orientation is called the magnetocrystalline anisotropy energy.

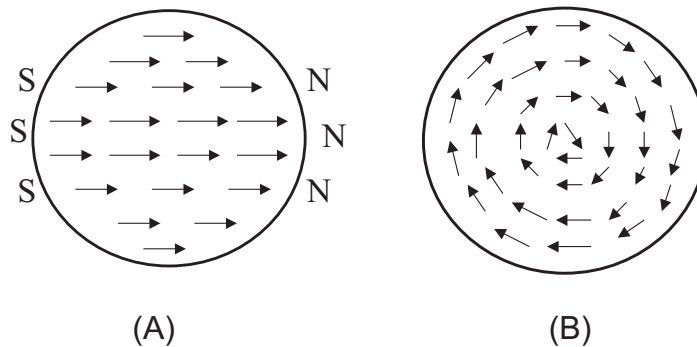


Figure 2.6: (A) *Single domain structure*, (B) *Domain structure of a material with small crystal anisotropy*.

If the crystal has a large magnetocrystalline anisotropy, the inner magnetization is forced to point parallel to a direction of easy magnetization. The direction of the magnetization within the domain is affected by the crystal structure of the specimen. In a single cubic crystal in the three principal crystallographic directions the magnetization can be distinguished, so they are referred as the axes $(1,0,0)$, $(1,1,0)$ and $(1,1,1)$, which are the easy, the medium and the hard magnetic axes for iron in Fig. 2.7. The direction of magnetization in a domain is determined by the crystal structure, provided strain and magnetic field are

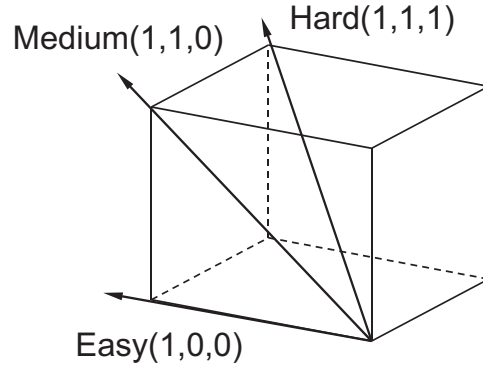


Figure 2.7: Magnetization directions in the cubic iron crystal: $(1,0,0)$ is the easy axis, $(1,1,0)$ is the medium axis, $(1,1,1)$ is the hard axis.

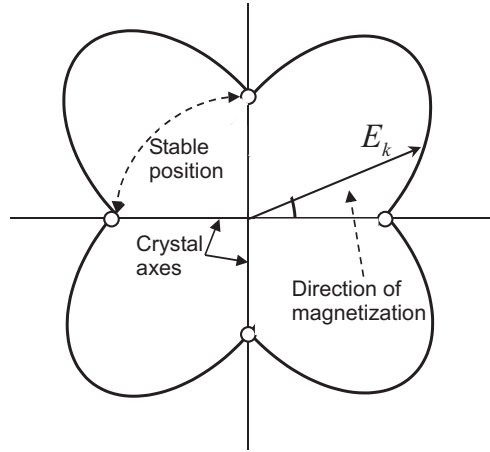


Figure 2.8: Variation of the energy with respect to the stable minimum energy directions of the magnetization.

absent. The crystal structure, stress, and field can be derived from the expressions for the following potential energy:

$$E_k = K(\alpha_1^2\alpha_2^2 + \alpha_2^2\alpha_3^2 + \alpha_3^2\alpha_1^2), \quad (2.13)$$

where E_k is the magnetocrystalline anisotropy energy density of the direction of its magnetization, and α_1 , α_2 , α_3 are the direction-cosines with respect to the three axes of the cubic crystal. K is the crystal anisotropy constant. The energy changes with the orientation of the domain is represented in Fig. 2.8, which indicates the stable positions corresponding to minimum energy [1]. This equilibrium is stable, reversible, if the total energy has a minimum, while the equilibrium is unstable, irreversible for maximum total energy. With an increase of the field \vec{H} the domain magnetization \vec{M}_s rotates gradually and then suddenly rotates toward the direction of the field when the equilibrium state becomes unstable.

Domain walls

The domain walls are interfaces between the domains. As the domains have different directed magnetizations, in this transition region the magnetic moments have to make

a reorientation. The structure of transition layers between the adjacent ferromagnetic domains was first investigated by F. Bloch in 1932. This transition layer is called the magnetic domain wall and is also referred to as the Bloch wall. The domain walls are commonly classified according to the direction of magnetization in the contiguous domains separated by the wall as in Fig. 2.9. One is the 180° domain wall, which separates domains

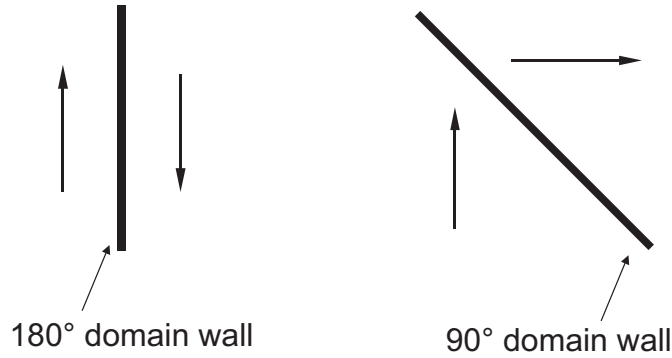


Figure 2.9: *Magnetization configuration in a 180° and a 90° domain wall.*

of opposite magnetization. In all other cases, one generically speaks of 90° domain walls, even if the magnetization does not necessarily rotate by 90° when passing from one domain to the other [4]. An amount of energy is necessary to create a domain wall of a given type, which plays a key role in domain theory.

The coupling between the atomic dipoles results in an exchange interaction, which can be represented by an exchange energy. Within the domain walls the atomic dipoles of different directions can be simulated by a set of very thin layers, considering a 180° wall through N atomic layers as it is plotted in Fig. 2.10 [2].

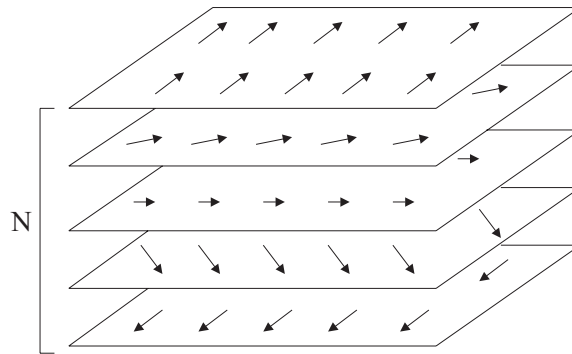


Figure 2.10: *Rotation of spins in the domain wall.*

In the domain walls the interaction energy between the neighboring moments can be expressed with the relation of the exchange energy

$$W_{\text{ex}} = -2JS^2 \cos\phi, \quad (2.14)$$

where J is the exchange integral and S is the total spin quantum number of each atom, while ϕ is the angle between the two moments. When $J > 0$, the lowest energy is attained when $\phi = 0$ or the two spins are parallel to each other. For iron, assuming $S = 1$, $J = 2.16 \times 10^{-21} \text{J}$. When $\phi \ll 1$, with the substitution $\cos\phi \approx 1 - \phi^2/2$, equation (2.14) is simplified as $W_{\text{ex}} = JS^2\phi^2 + \text{const}$.

Considering a 180° domain wall arrangement, assuming that the rotation of the moments is uniform through the N transition layers, so that $\phi = \pi/N$, for a simple cubic lattice with lattice constant a the number of atoms per unit area of a surface is $1/a^2$, the exchange energy per unit area of the transition layers is given by

$$w_{\text{ex}} = \frac{N}{a^2} W_{\text{ex}} = \frac{JS^2\pi^2}{a^2N}. \quad (2.15)$$

From the above expression it can be seen that the total exchange energy in the transition layers decreases with an increase of the number of transition layers N . Thus the exchange energy tends to increase the wall thickness.

On the other hand, the rotation of the moments in the wall out of the direction of easy magnetization causes an increase in magnetocrystalline anisotropy energy. Approximating the anisotropy of a cubic crystal with a constant, the deviation of the magnetic moments in the domain wall from the easy direction increases the magnetocrystalline anisotropy energy by K , where K is the anisotropy energy per unit volume. Since the volume of the transition region is given by Na per unit area of the wall surface, the anisotropy energy in this volume is given by

$$w_{\text{a}} = KNa. \quad (2.16)$$

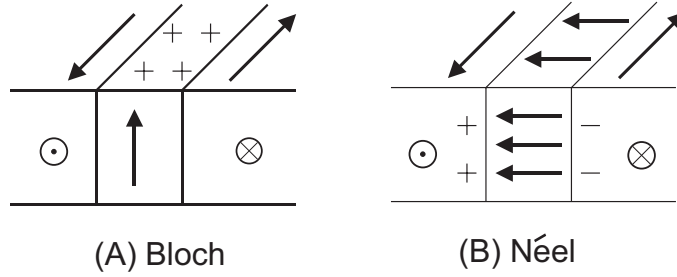
The exchange energy tends to make the walls thicker by increasing the number of the lattices in the wall, since the exchange energy is minimized if the neighboring moments are aligned parallel, the anisotropy energy tends to make the domain walls thinner, in order to reduce the number of moments pointing in no easy direction. The actual thickness of the domain wall is determined by the counterbalance of these two opposite trends. The total energy is $w = w_{\text{ex}} + w_{\text{a}}$, which is a minimum with respect to N the numbers of lattices when

$$\frac{\partial(w_{\text{ex}} + w_{\text{a}})}{\partial N} = 0. \quad (2.17)$$

Domain walls of many types are possible. For brevity, we limit this description to the particular case of 180° domain walls. In this section we discuss only the two simplest types: the Bloch wall and the Néel wall. Fig. 2.11 shows how magnetostatic energy may affect the wall structure in a thin film. If the magnetization rotations remain in the plane of the wall (Fig. 2.11(A)), the domain wall is a Bloch wall. On the other hand, if the magnetization rotations are outside or inside the film at ninety degrees to the surface (Fig. 2.11(B)), the domain wall is a Néel wall.

The difference between the Néel wall and the Bloch wall is that the magnetization rotations of the Néel wall turn from one domain to the other. From [5], the Néel wall will have larger energy than a Bloch wall, whereas the Bloch wall is energetically preferable to Néel wall. The Néel wall is thinner than a Bloch wall.

During the magnetization process, which will be introduced in the next section, the domain walls exhibit two different effects, the displacement of the domain walls and the bending of

Figure 2.11: *Schematic wall structures in thin films.*

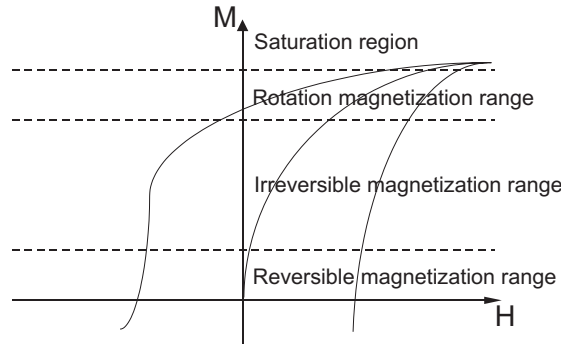
the domain walls. The behavior of the domain walls depends on several factors, including the applied field, the domain wall energy and the stress arising in the walls during the process. The strength of the domain wall pinning and the energy per unit area in the wall determine either the displacement or the bending of the domain walls occurring in the particular case.

2.2.3 Magnetization Process

The magnetic state is generally described through its average magnetization \vec{M} and magnetic field \vec{H} , but the information of \vec{M} and \vec{H} is not sufficient to give a complete description of the system. The state of the system is identified by its magnetic domain structure, and, for given values of \vec{M} and \vec{H} , it is the past history of the material that determines which domain structure will be actually realized and will now evolve when the field is further changed.

The magnetization process corresponds to the change in the domain structures in the ferromagnetic materials when a magnetic field \vec{H} is applied. During the magnetization process both the reversible and the irreversible changes occur together. Four different ranges in the magnetization characteristic can be distinguished according to the essentially achieved changes in the direction of the domain magnetization and in the intensity of spontaneous magnetization [17]. The processes may be classified as initial permeability range or reversible magnetization range, irreversible magnetization range, rotational magnetization range and saturation region (Fig. 2.12).

1. Starting from the demagnetized state, the first section on the magnetization characteristic is the reversible or the initial range. There, the magnetization changes reversibly. At low field amplitudes the magnetization can be characterized by the reversible rotation of the domains from a stable state toward the applied field direction. In this range the reversible magnetization is accomplished by the reversible displacement of domain walls. This reversible response $\Delta\vec{M} = \chi_{\text{rev}}\Delta\vec{H}$ gives rise to a change of magnetization $\Delta\vec{M}$, which is proportional to the small field variation $\Delta\vec{H}$, and the proportionality constant χ_{rev} is called reversible susceptibility. Because the demagnetized state is generated by an oscillating field slowly decreasing to zero amplitude, around the demagnetized state there is no difference between reversible and total susceptibility, and the magnetization

Figure 2.12: *Magnetization process.*

curve is in the limit of vanishing field amplitude, so we have $\vec{M} = \chi_{\text{in}}\vec{H}$, where χ_{in} is the initial susceptibility. The initial susceptibility has small value for crystalline substance as $\chi_{\text{in}} \approx 29$, while for soft magnetic materials this susceptibility exhibits $\chi_{\text{in}} \approx 100 \sim 200$ (e.g. pure iron shown in Table A.1). The contribution of the displacement of domain walls to the initial permeability is entirely dependent on the sort of material.

2. If the magnetic field is increased above the initial part of the characteristic, this intensity of magnetization increases more drastically. The range of the magnetization process is called the irreversible magnetization range. This range is mainly achieved by irreversible displacement of the domain walls from one position to another one. Irreversible rotation of domains can also be expected in materials composed of fine particles. In this range, a magnetothermal effect, which corresponds to the generation of heat accompanying the irreversible magnetization, is observable. A part of the work done by the magnetic field is dissipated as heat during the process of discontinuous magnetization.

Because many small discontinuous changes in magnetization are induced by irreversible displacement of domain walls and by irreversible rotation of local domain magnetization, the so called Barkhausen noise can be heard in this range. The Barkhausen effect (Fig. 2.13 (A)) was discovered by H. Barkhausen as the first experimental evidence of these magnetic instabilities. The noise persists only during a change in magnetization on the steep part of the magnetization curve or hysteresis loop. The intermittent character of the Barkhausen effect results in the staircase structure shown in Fig. 2.13 (B). The horizontal portions of the curve correspond to field intervals where the domain structure undergoes smooth distortions under the pressure of the applied field. On the contrary, the vertical parts represent the points where the domain configuration becomes unstable and suddenly jumps to a new state. The additional separation pictures (Fig. 2.13 (B)) give an intuitive idea of the process. The random features in the Barkhausen effect reflect the general need for statistical methods for treating magnetization processes and domain structures.

3. If the magnetic field is increased further, the magnetization curve becomes less steep and the magnetization changes become reversible once more. In this range the displacements of the domain walls have already been completed and the magnetization takes place by rotational magnetization. For this reason, this range is called the rotational magnetization range. A further process, irreversible rotation, may occur in the rotational magnetization range.

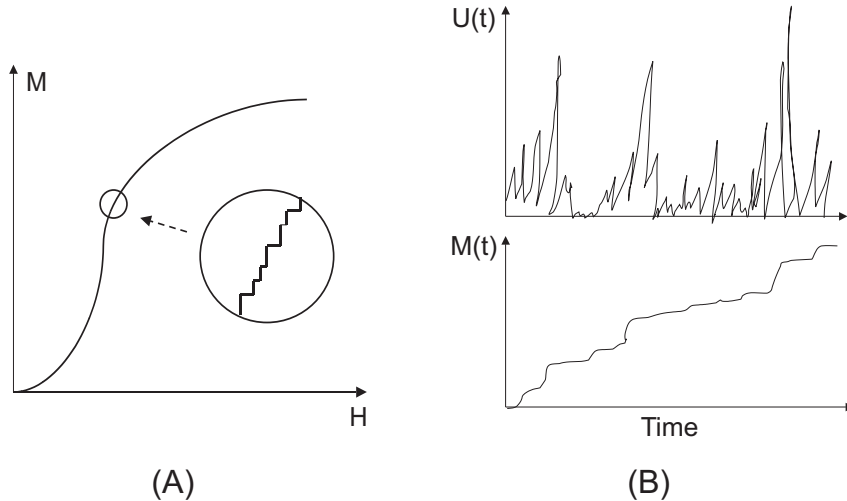


Figure 2.13: (A) Barkhausen effect, (B) Barkhausen effect Top: measured voltage signal. Bottom: magnetization curve associated with the signal.

4. The fourth part of the magnetization process is the saturation region. In this range the saturation magnetization inside the domains is achieved. If the magnetization arrives to the saturation there is no further increase with the intensity of the applied magnetic field. The magnetic field and magnetization vectors are almost parallel.

Mechanisms of magnetization along the hysteresis loop are similar to those discussed above. From saturation to remanence the magnetization can mainly be regarded as rotational magnetization. From remanence to midway of the ascending hysteresis curve is a irreversible magnetization, and that to the opposite saturation is again a rotational magnetization. The total heat generated during one cycle of hysteresis, which is measured by the area surrounded by a hysteresis loop, is equal to the total energy dissipated by the discontinuous magnetization process.

2.2.4 Hysteresis Loops

The observed hysteresis loops are the direct consequence of the variety of possible magnetic domain structures. Magnetic domains result from the balance of several competing energy terms: the exchange energy, which favors uniform magnetization configurations; the magnetocrystalline anisotropy energy, which favors the orientation of the magnetization vector along certain preferred directions; and the magnetostatic energy, which on the contrary favors configurations giving a zero average magnetic moment. A domain structure represents the compromise by which the system tries to satisfy all these competing requirements. The magnetization is coupled to the external field by the energy $-\mu_0 \vec{M} \cdot \vec{H}$, which favors domains magnetized in the direction of the applied field. When the magnetic field strength \vec{H} varies in time, the energy balance is altered and the domain structure is rearranged through the motion of the domain walls. At high fields, the material is magnetized along the applied field direction and the average magnetization of the specimen becomes close to the spontaneous magnetization. When the field is reversed, domains of reversed magnetization are formed, which progressively increase in size through domain wall motion, until a single domain of reversed magnetization is formed. This description

gives a interpretation of the mechanisms behind the hysteretic behavior of many magnetic materials.

The variety of hysteresis loops can be described with a few parameters for prime characterization of loop properties. Two quantities of particular importance in this respect are the remanent magnetization or remanence \vec{M}_r and the coercive field \vec{H}_c . Remanence is the natural quantity expressing the fact that a ferromagnetic material can keep spontaneously magnetized even in the absence of external sources. The order of magnitude of \vec{M}_r is that of the saturation magnetization \vec{M}_s , but various geometrical or structural features may contribute to decreasing \vec{M}_r well below \vec{M}_s . The coercive field \vec{H}_c is the field needed to bring the magnetization from the remanent value to zero. Unlike as the remanent field, the coercive field has a wide interval, from less than 1 Am^{-1} to more than 10^6 Am^{-1} , depending on the magnetic material.

According to the parameters \vec{M}_r and \vec{H}_c , the material can be classified into soft and hard magnetic materials. The term soft material is used to refer to materials that are easy to magnetize, destined to applications where a low coercive field is a prime requirement. The coercive field is of the order of $50 - 100 \text{ Am}^{-1}$ in non-oriented Si-Fe alloys and low-carbon steels used in electric motors, and decreases down to 10 Am^{-1} in grain-oriented Si-Fe alloys employed in transformer cores. On the contrary to soft materials, hard magnetic materials can be taken as a stable and permanent source of material field, insensitive to external actions. The coercive field is of the order of $50 - 100 \text{ kAm}^{-1}$ in AlNiCo alloys, but in rare-earth magnets of the Sm-Co or Nd-Fe-B type it can exceed 1000 kAm^{-1} [2].

A hysteresis loop can be represented in term of $\vec{B}(\vec{H})$ or of $\vec{M}(\vec{H})$. The relation between magnetization and induction is $\vec{B} = \mu_0(\vec{H} + \vec{M})$. In a soft material, the magnetic field strengths are much smaller than the corresponding magnetization values (Fig. 2.14(A)), so that, to a very good approximation, $\vec{B} \cong \mu_0\vec{M}$ and plotting $\vec{B}(\vec{H})$ or $\vec{M}(\vec{H})$ makes a tiny difference that can be safely neglected. On the contrary, in hard materials \vec{H} and \vec{M} have comparable order of magnitude, and the $\vec{B}(\vec{H})$ loop is significantly different from the $\vec{M}(\vec{H})$ one (Fig. 2.14 (B) and (C)). For example, there are two possible definitions for the coercive field, $H_{c,M}$ and $H_{c,B}$, depending on whether one considers the point where the induction or the magnetization is reduced to zero. The $\vec{M}(\vec{H})$ loop better reflects the intrinsic properties of the magnet, but the $\vec{B}(\vec{H})$ loop gives a more useful description of the system behavior for technical evaluation.

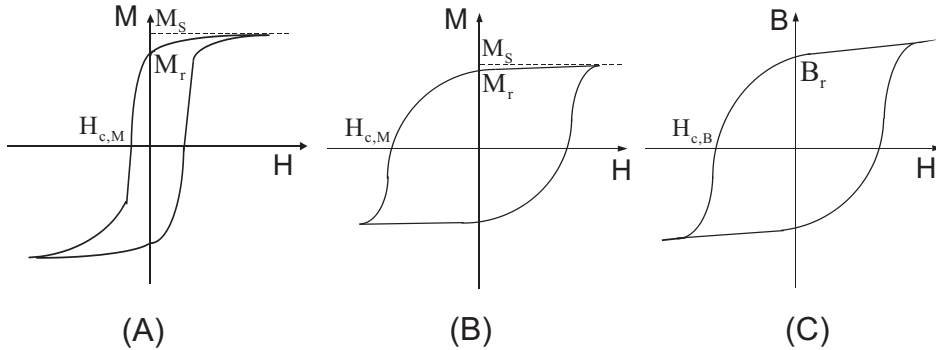


Figure 2.14: (A) soft material ($M - H$ curve), (B) hard material ($M - H$ curve) and (C) hard material ($B - H$ curve).

Each point on the hysteresis loop can be reached in an infinite number of increasing and decreasing field excitations depending on the material history. Two histories are of particular relevance, return branches and minor loops.

The simplest return branches are first-order return branches, which are obtained by starting from saturation and then reversing the field at a certain point of the saturation loop (Fig. 2.15). Return branches show that one can have an infinite number of different magnetization curves associated with the same interval for the magnetic field strength. It is evident from Fig. 2.15 that there will exist a return branch, starting from a particular reversal field, known as remanence coercivity H_{rc} , which passes through the origin. As a matter of fact, the origin can be reached not only from this first-order return branch, but also from second-order branches or third-order branches, and so on. A spiral magnetization history consisting of a large number of increasing and decreasing branches ending at the origin, transforms the materials into the demagnetized state. In practice, the demagnetized state is achieved by applying an oscillating field with an amplitude which slowly decreases from a large initial value to zero. The same procedure can be generalized by applying the superposition of a given constant field \vec{H} and an oscillating field of slowly decreasing amplitude. The resulting state is an anhysteretic state. The curve connecting all possible anhysteretic states obtained for different fields \vec{H} is known as the anhysteretic curve. The anhysteretic curve does not depend on the history of the material. An oscillating field with a sufficient initial amplitude erases any memory of previous states possibly accumulated by the system before demagnetization. The essence of hysteretic phenomena is just that they prevent the system from reaching equilibrium, and give rise to deviations from the stable working points represented by the minimum energy curve.

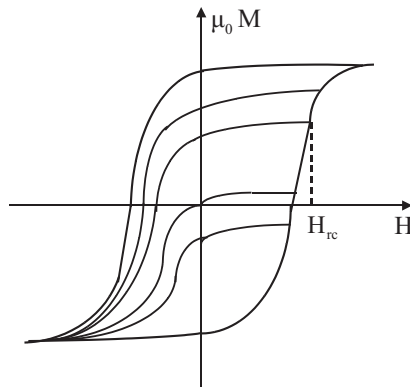


Figure 2.15: *First-order return branches.*

The minor loops (Fig. 2.16) are a set of curves obtained by applying a cyclic field of variable amplitude starting from the demagnetized state. The line connecting the loop tops is known as the normal magnetization curve, which is similar to the virgin curve. Its slope at the origin gives the initial susceptibility χ_{in} . One also defines the maximum susceptibility χ_{max} , given by the maximum ratio $\|\vec{M}\|/\|\vec{H}\|$ achieved along the curve, which can be obtained graphically by drawing the slope from the origin to the curve itself. The differential susceptibility also can be given by the slope $d\|\vec{M}\|/d\|\vec{H}\|$ at the point considered.

Four broad classes of mechanisms are involved in hysteresis loops: magnetization rotation, domain wall motion, nucleation, and topological hysteresis. The first two have been discussed in section 2.2.2.

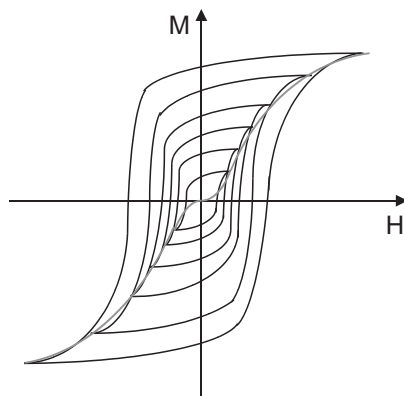


Figure 2.16: Set of minor loops.

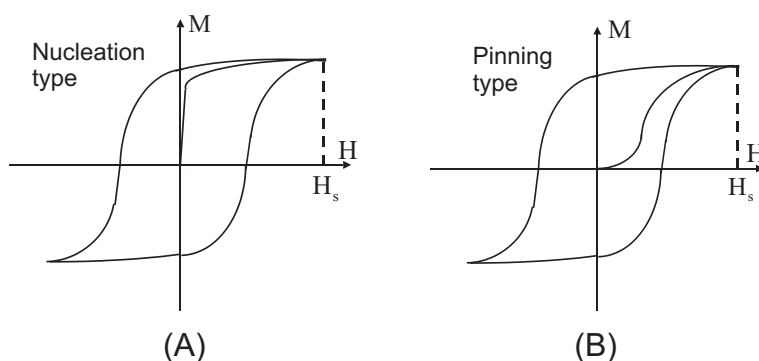


Figure 2.17: Schematic representation of magnetization curves in nucleation-type and pinning-type magnets.

1. *Nucleation* includes all phenomena where domains of reversed magnetization are formed inside a saturated region [4]. There is a qualitative aspect, important in particular in hard magnets, that may be associated with the concepts of nucleation and domain wall motion. By comparing the virgin magnetization curve after thermal demagnetization with the saturation hysteresis loop, one recognizes two qualitatively different kinds of behavior, and one accordingly speaks of nucleation-type and pinning-type magnets (Fig. 2.17). In a nucleation-type magnet, the virgin curve is steep and saturation is reached under fields much lower than the saturation loop coercive field H_s . Domain walls are present in the virgin state and the fact that the material can be easily saturated shows that walls are free to move and do not experience important pinning effects. Once the virgin domain structure has been swept away, the formation of reversed domains becomes a difficult process, and the demagnetization curve is characterized by a substantial coercivity. In a pinning-type magnet, on the contrary, fields of the order of the saturation loop coercive field H_s are required to saturate the material also when one starts from the virgin state. This indicates that domain wall pinning is the main mechanism responsible for coercivity. In soft materials, nucleation-type effects can be put in evidence by traversing the loop under a controlled rate of change for the magnetization. Under appropriate circumstances, one observes reentrant loops, in which a clear distinction appears between the field necessary to nucleate the relevant domain structure and the field necessary to move already existing domain walls.

2. *Topological hysteresis* reflects the topology of the domain structure [4]. It is important whenever the amount of structural disorder is relatively small and the minimization of magnetostatic energy dominates the problem.

In ordinary materials, the various mechanisms are active at the same time, in proportions different from case to case, and are not independent from each other.

The hysteresis loop can hardly be interpreted as a property of the material considered. It is the outcome of a number of steps, where the measurement method, the specimen geometry, and several other nontrivial assumptions have a role. For example, field and magnetization are vector quantities. Therefore, in principle, any representation of hysteresis loops should be given in vector terms. On the contrary, many experiments and theoretical interpretation are based on a scalar representation, where the magnetization component along the field is given as a function of the field intensity. This scalar description is of tempting clarity and simplicity, and it is quite convenient in all cases where the magnetic field has a privileged direction. It is however always to some extent incomplete, because it says nothing about the behavior of the magnetization component perpendicular to the field.

The emergence of the macroscopic hysteresis behavior is related to the existence of magnetic domains. It is only over scales larger than the domain size that macroscopic hysteresis properties of a material become manifest. The scale of domains is not necessarily closer to the atomic scale than to the geometric scale of the specimen. In certain magnetic materials, domain sizes can be in the range of millimeters, rather than nanometers.

2.3 Preisach Model

The Preisach model was established by F. Preisach [29], [6] in 1935 and is based on the results of the previous studies of J.A. Ewing [7] and other researchers from that period. The classical Preisach model is based on some hypotheses concerning the physical mechanisms of magnetization, which was the first regarded as a physical model of hysteresis. The model was primarily introduced in the area of magnetics where this model has been the focus of considerable research for many years. In parallel with the mentioned developments in magnetics, the Preisach model was independently invented and then extensively studied for magnetic hysteresis by D.H. Everett [8], [9], [10], [11]. Although the classical Preisach model is capable of describing minor loops as well as major hysteresis loop, it is limited in its ability to describe magnetic materials featuring the congruency property and the wiping-out property. For this reason, many modifications of the Preisach model have been suggested. In the 1970s, the mathematician M. Krasnoselskii recognized the mathematical generality of the Preisach model after separating it from its physical meaning and represented it in a pure mathematical form. As a result, a new mathematical tool has been developed for the mathematical description of hysteresis of arbitrary physical natures. The phenomenological treatment of the Preisach model opens a new period in the study and simulation of hysteresis by Mayergoyz (e.g. [12], [14], [15], [16]), Ivanyi (e.g. [17], [108]), Della Torre (e.g. [5], [18], [20]), and Bertotti (e.g. [4]).

2.3.1 Classical Preisach Model

The purely mathematical description of the classical Preisach model consists of an infinite set of simple hysteresis operators $\gamma_{\alpha\beta}$. Each of these operators can be represented by a rectangular loop (Fig. 2.18). Numbers α and β correspond to "up" and "down" switching

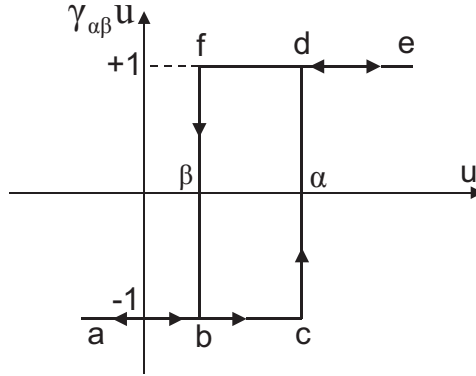


Figure 2.18: *Rectangular loop of hysteresis operator.*

values of input, respectively. It is assumed that $\alpha \geq \beta$. These operators can be interpreted as two-position relays with "up" and "down" positions corresponding to $\gamma_{\alpha\beta}u(t) = +1$ and $\gamma_{\alpha\beta}u(t) = -1$, respectively. When the input is monotonically increased, the ascending branch $abcde$ is followed. When the input is monotonically decreased, the descending branch $edfba$ is traced. The set of operators $\gamma_{\alpha\beta}$ is weighted by a weight function $\mu(\alpha, \beta)$ which is referred to as the Preisach function. Then the Preisach model can be written as

$$f(t) = \iint_{\alpha \geq \beta} \mu(\alpha, \beta) \gamma_{\alpha\beta} u(t) d\alpha d\beta. \tag{2.18}$$

It is apparent that the model can be interpreted as a continuous analog of a system. This interpretation is illustrated by the block diagram shown in Fig. 2.19. According to this

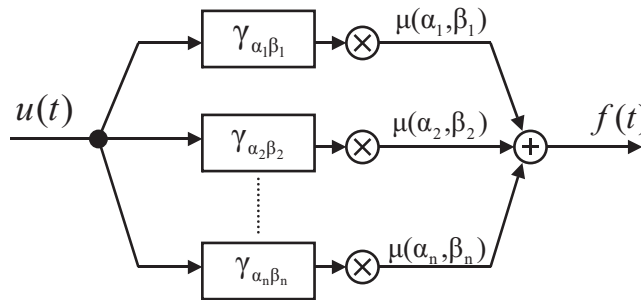


Figure 2.19: *Block diagram representing the Preisach model.*

diagram, the same input $u(t)$ is applied to each of the two-position relays. Their individual

output signals are multiplied by $\mu(\alpha, \beta)$ and then integrated over all appropriate value of α and β . As a result, the output $f(t)$ is obtained. A discrete approximation as in this block diagram can be used as an implementation of the Preisach model (2.18).

In magnetics, separate magnetic domains are introduced. These domains have rectangular hysteresis loops and they play the same role as elementary hysteresis operators $\gamma_{\alpha\beta}$. A loop typical for such domains is shown in Fig. 2.20. Here h_α and h_β are the "up" and "down" switching magnetic fields, respectively, and m_s is the magnetization which is identical for all particles. The notation $m(h_\alpha, h_\beta)$ is used for the domain having the hysteresis loops shown in Fig. 2.20. The magnetic material is considered to be composed of many such

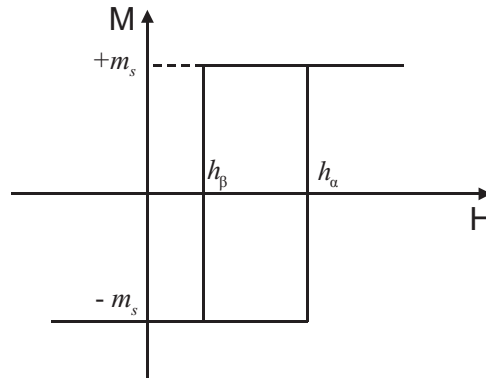


Figure 2.20: *Rectangular loop of hysteresis operator.*

domains. It is also assumed that the different particles have some distribution of reversal field h_α and h_β which can be characterized by the distribution function $\phi(h_\alpha, h_\beta)$, which plays the same role as $\mu(\alpha, \beta)$ in (2.18). It is typical to speak about the statistical nature of the distribution function $\phi(h_\alpha, h_\beta)$. By using the magnetic particles and their distribution function, the Preisach model is usually defined in magnetics as

$$M(t) = \iint_{h_\alpha \geq h_\beta} \phi(h_\alpha, h_\beta) m(h_\alpha, h_\beta) H(t) dh_\alpha dh_\beta, \quad (2.19)$$

where M is the magnetization, if the domain is switched up, $m(h_\alpha, h_\beta)H(t) = +m_s$, and if the domain is switched down, $m(h_\alpha, h_\beta)H(t) = -m_s$. It is obvious that the magnetic definition of the Preisach model is mathematically similar to the definition (2.18).

Geometric interpretation

The mathematical investigation of the Preisach model is facilitated by its geometric interpretation. In Fig. 2.21, each point of the half-plane $\alpha \geq \beta$ can be identified with a particular γ -operator whose "up" and "down" switching values are respectively equal to the α and β coordinates of the point. Consider a right triangle, its hypotenuse is a part of the line $\alpha = \beta$, while the vertex of its right angle has the coordinates α_0 and β_0 with $\beta_0 = -\alpha_0$. α_0 and β_0 represent the point of full saturation. We first assume that the input $u(t)$ at time t_0 has the value which is less than β_0 . Then the outputs of all γ -operators which correspond to the points of the triangle are in the "down" position. This corresponds to the state of negative saturation of the hysteresis nonlinearity represented by the model (2.18).

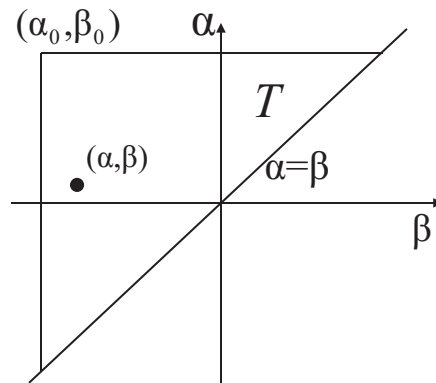


Figure 2.21: *Geometric interpretation in $\alpha - \beta$ diagram.*

If the input is monotonically increased, all γ -operators with "up" switching values α less than the current input value $u(t)$ are being turned into the "up" position. Geometrically, this leads to the subdivision of the triangle T into two sets: $S^+(t)$ consisting of points (α, β) for which the corresponding γ -operators are in the "up" position, and $S^-(t)$ consisting of points (α, β) for which the corresponding γ -operators are still in the "down" position. The interface between $S^+(t)$ and $S^-(t)$ is denoted by $L(t)$. This subdivision is made by the line $\alpha = u(t)$ (Fig. 2.22 (A)). After the input reaches a maximum value u_1 , it starts to monotonically decrease, all γ -operators with "down" switching values β above the current input value $u(t)$ are being turned back into the "down" position. This changes the previous subdivision of the triangle into positive and negative sets. The interface $L(t)$ additionally contains a vertical link which moves from right to left and is determined by $\beta = u(t)$ (Fig. 2.22 (B)).

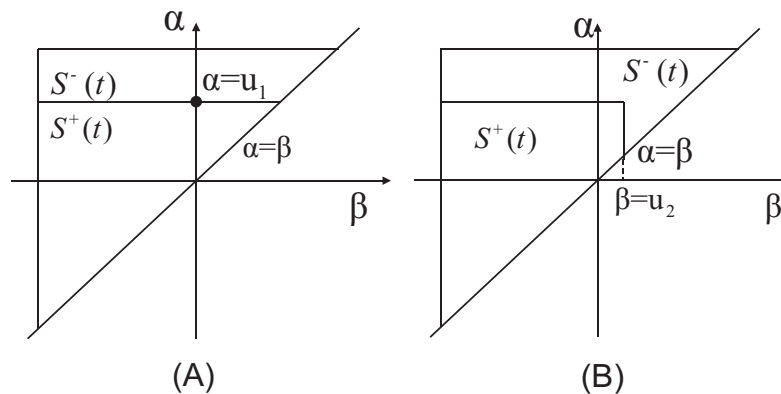


Figure 2.22: (A) *Geometric interpretation of the Preisach model at increasing input values $\alpha = u_1$ in the $\alpha - \beta$ diagram,* (B) *Geometric interpretation of the Preisach model at decreasing input values $\beta = u_2$ in the $\alpha - \beta$ diagram.*

After the input reaches the minimum value u_2 , the input is increased again until it reaches some maximum value u_3 . Geometrically, this increase results in the formation of a new horizontal link of $L(t)$ which moves up (Fig. 2.23 (A)). This upward motion is terminated when the maximum u_3 is reached. Next, the input is decreased again until it reaches some minimum value u_4 . Geometrically, this input variation results in the formation of a

new vertical link which moves from right to left. This motion is terminated as the input reaches the minimum value u_4 . As a result, a new vertex of $L(t)$ is formed which has the coordinates $\alpha = u_3$ and $\beta = u_4$ (Fig.2.23 (B)).

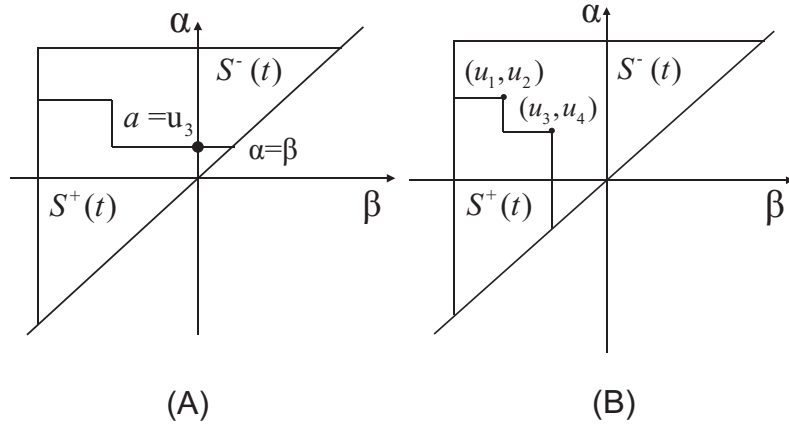


Figure 2.23: (A) Geometric interpretation of the Preisach model at increasing input values $\alpha = u_3$ in the $\alpha - \beta$ diagram, (B) Geometric interpretation of the Preisach model at decreasing input values $\beta = u_4$ in the $\alpha - \beta$ diagram.

At any instant of time, the triangle is subdivided into two sets: $S^+(t)$ consisting of points (α, β) for which the corresponding γ -operators are in the "up" position, and $S^-(t)$ consisting of points (α, β) for which the corresponding γ -operators are in the "down" position. The interface $L(t)$ between $S^+(t)$ and $S^-(t)$ is a staircase line. The final link of $L(t)$ is attached to the line $\alpha = \beta$ and it moves when the input is changed. This link is a horizontal one and it moves up as the input is increased (Fig. 2.24 (A)). The final link is a vertical one and it moves from right to left as the input is decreased (Fig. 2.24 (B)).

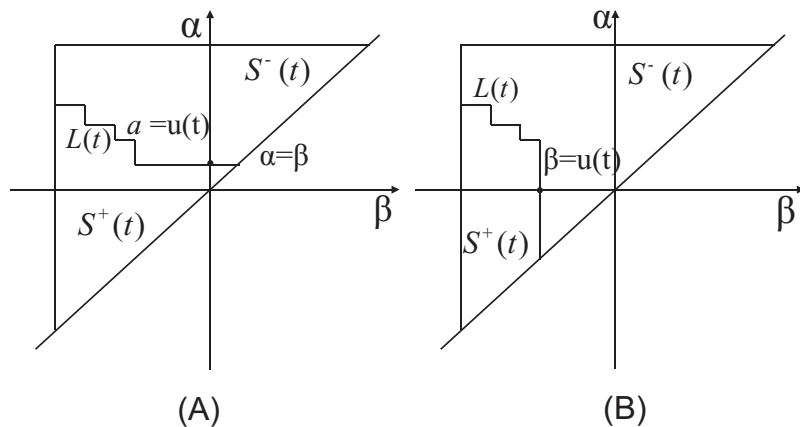


Figure 2.24: (A) $\alpha - \beta$ diagram corresponding γ -operators in "up" position, (B) $\alpha - \beta$ diagram corresponding γ -operators in "down" position.

At any instant of time the integral in (2.18) can be subdivided into two integrals, over

$S^+(t)$ and $S^-(t)$, respectively:

$$f(t) = \iint_{S^+(t)} \mu(\alpha, \beta) \gamma_{\alpha\beta} u(t) d\alpha d\beta + \iint_{S^-(t)} \mu(\alpha, \beta) \gamma_{\alpha\beta} u(t) d\alpha d\beta. \quad (2.20)$$

Since for $(\alpha, \beta) \in S^+(t)$, $\gamma_{\alpha\beta} u(t) = +1$, and if $(\alpha, \beta) \in S^-(t)$, $\gamma_{\alpha\beta} u(t) = -1$, we have

$$f(t) = \iint_{S^+(t)} \mu(\alpha, \beta) d\alpha d\beta - \iint_{S^-(t)} \mu(\alpha, \beta) d\alpha d\beta. \quad (2.21)$$

Experimental determination of the distribution function

Before applying the Preisach model in an electromagnetic simulation scheme, the distribution function according to the hysteretic material under consideration has to be determined. The determination of the distribution function is based on experimental results. A set of first-order transition (reversal) curves is needed to determine $\mu(\alpha, \beta)$. These curves can be experimentally found as follows. First, the input $u(t)$ is decreased to a value smaller than β_0 . It brings a hysteresis transducer to the state of negative saturation. Then, the input is monotonically increased until it reaches some value α_1 . As the input is increased, an ascending branch of a major loop is followed. The notation f_{α_1} will be used for the output value on this branch which corresponds to the input value $u = \alpha_1$. The first-order transition curves are attached to the ascending branch. Each of these curves is formed as the above monotonic increase of the input is followed by a subsequent monotonic decrease. The term "first-order" is used to emphasize the fact that each of these curves is formed after the first reversal of input. The notation $f_{\alpha_1\beta_1}$ will be used for the output value on the transition curve attached to the ascending branch at the point f_{α_1} . This output value corresponds to the input value $u = \beta_1$ (Fig. 2.25 (A)). The corresponding $\alpha_1 - \beta_1$ diagram is shown in Fig. 2.25 (B).

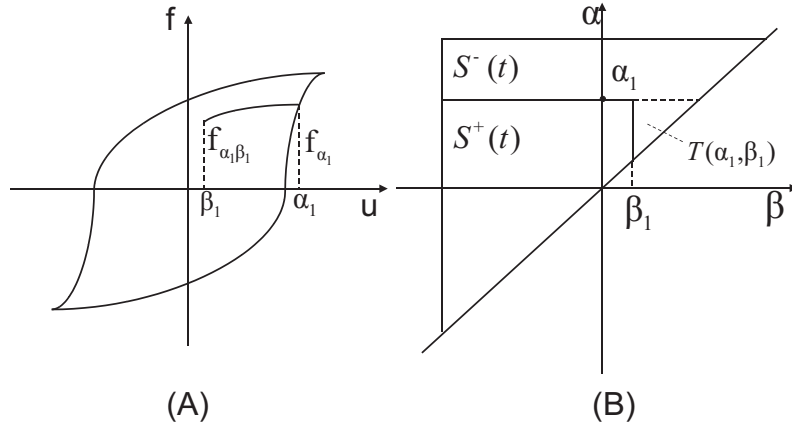


Figure 2.25: (A) A first order transition curve at point $u = \beta_1$ with $\alpha = \alpha_1$, (B) corresponding $\alpha_1 - \beta_1$ diagram.

According to Fig. 2.25 (B), the triangle $T(\alpha_1, \beta_1)$ is added to the negative set S^- and subtracted from the positive set S^+ as a result of the monotonic input decrease from the value $u = \alpha_1$ to the value $u = \beta_1$. Using the above fact and formula (2.21), the Preisach

model matches the output increments along the first-order transition curves if the function $\mu(\alpha, \beta)$ satisfies the equation

$$f_{\alpha_1, \beta_1} - f_{\alpha_1} = -2 \iint_{T(\alpha_1, \beta_1)} \mu(\alpha, \beta) d\alpha d\beta. \quad (2.22)$$

To define the function

$$F(\alpha_1, \beta_1) = \frac{1}{2}(f_{\alpha_1} - f_{\alpha_1, \beta_1}). \quad (2.23)$$

The integral over the triangle $T(\alpha_1, \beta_1)$ can be written as the following double integral:

$$F(\alpha_1, \beta_1) = \int_{\beta_1}^{\alpha_1} \left(\int_{\beta_1}^{\alpha_1} \mu(\alpha, \beta) d\alpha \right) d\beta. \quad (2.24)$$

By differentiating the last expression twice, the density function can be obtained as

$$\mu(\alpha_1, \beta_1) = -\frac{\partial^2 F(\alpha_1, \beta_1)}{\partial \alpha_1 \partial \beta_1}. \quad (2.25)$$

The Preisach function $\mu(\alpha, \beta)$ has been found by using the first-order transition curves. These curves are attached to the ascending branch and each of them is formed when a monotonic increase along this branch is followed by a subsequent input decrease. For this reason, these curves are named first-order decreasing transition curves. However, a similar expression for $\mu(\alpha, \beta)$ can be found by using the first-order increasing transition curves. These curves are attached to the descending branch of the major loop. Each of these first-order increasing transition curves is formed as a monotonic decrease along the descending branch is followed by a subsequent input increase. The notation f_{β_2} will be used for the output value on the descending branch. This value is achieved when the input is monotonically decreased from some value above α_0 to the value $u = \beta_2$. The notation $f_{\beta_2 \alpha_2}$ will be used for the output value on the first order increasing transition curve which is attached to the descending branch at the point f_{β_2} . This output value corresponds to $u = \alpha_2$ (Fig. 2.26 (A)). The corresponding $\alpha - \beta$ diagram is shown in Fig. 2.26 (B).

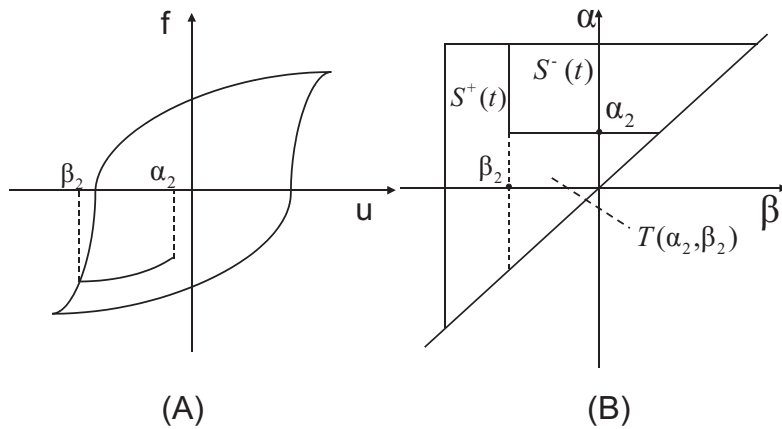


Figure 2.26: (A) A first order transition curve at point $u = \alpha_2$ with $\beta = \beta_2$, (B) corresponding $\alpha_2 - \beta_2$ diagram.

Using the function

$$f_{\alpha_2, \beta_2} - f_{\alpha_2} = -2 \iint_{T(\alpha_2, \beta_2)} \mu(\alpha, \beta) d\alpha d\beta, \quad (2.26)$$

and

$$F(\alpha_2, \beta_2) = \frac{1}{2}(f_{\alpha_2, \beta_2} - f_{\alpha_2}), \quad (2.27)$$

the Preisach density function is

$$\mu(\alpha_2, \beta_2) = -\frac{\partial^2 F(\alpha_2, \beta_2)}{\partial \alpha_2 \partial \beta_2}. \quad (2.28)$$

On the symmetry considerations, the first-order decreasing and increasing transition curves are congruent. In mathematical terms, $f_{\beta_2} = f_{\alpha_1}$ and $f_{\beta_2, \alpha_2} = -f_{\alpha_1, \beta_1}$ if $\beta_2 = -\alpha_1$ and $\alpha_2 = -\beta_1$. From the above we obtain:

$$F(-\beta_1, -\alpha_1) = F(\alpha_1, \beta_1), \quad (2.29)$$

and

$$\mu(-\beta_1, -\alpha_1) = \mu(\alpha_1, \beta_1). \quad (2.30)$$

The formulas (2.29) and (2.30) express the mirror symmetry of functions $F(\alpha, \beta)$ and $\mu(\alpha, \beta)$ with respect to the line $\alpha = -\beta$ (Fig. 2.27). This symmetry is a consequence of the congruency of the first-order decreasing and increasing transition curves.

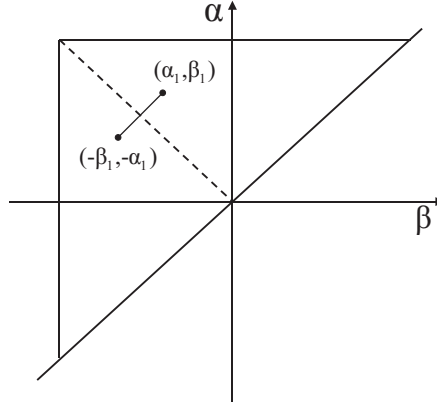


Figure 2.27: *Symmetry property of the distribution function.*

Analytical approximation of the distribution function

For the determination of the distribution function the other popular ways are the analytical approximation methods. Taking into account the interaction on the magnetization of the single domain particles [19] [30], a useful approximation for hard materials is to assume that the Preisach function is Gaussian, in both the interaction-free critical field H_k of the hysteron, and the interaction field H_i . Then this integral can be evaluated in closed form. The interaction field dependence can be justified on the basis of the central limit theorem of statistical theory, since the interaction field is the sum of the fields due to all the other hysterons, which are independent and identically distributed. The critical field dependence is an approximation to a log-normal dependence for the case when the mean

critical field \bar{h}_k is more than twice its standard deviation. The relationship between the Gaussian function and the log-normal function is discussed in [5]. For hard materials the Preisach function is given by

$$p(H_k, H_i) = \frac{1}{2\pi\sigma_i\sigma_k} \exp \left\{ -\frac{1}{2} \left[\frac{(H_k - \bar{h}_k)^2}{\sigma_k^2} + \frac{H_i^2}{\sigma_i^2} \right] \right\}, \quad (2.31)$$

where σ_k and σ_i are the standard deviations in the critical field and interaction field, respectively.

The classical Preisach model assumes that the ferromagnetic material consists of many elementary interacting domains, and each of them can be represented by a rectangular elementary hysteresis loop of two statistically distributed parameters, the critical or the coercive field of the free particles H_k , and the interaction field H_i , due to the interaction of the neighboring domains (Fig. 2.28). The elementary hysteresis operator can be char-

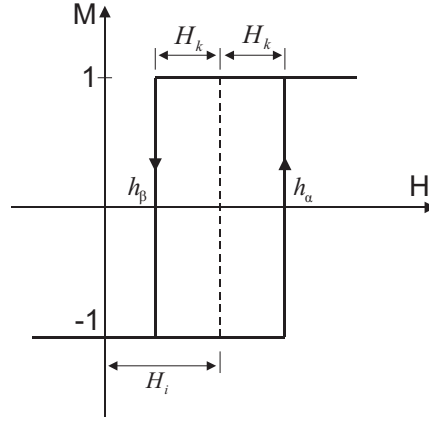


Figure 2.28: *Magnetization curve for an elementary hysteresis loop.*

acterized by the switching fields as well as at which the magnetization is setting up or down h_α and h_β , corresponding to the direction of the applied magnetic field. Replacing the Preisach variable H_k and H_i with the switching field h_α and h_β

$$\begin{aligned} H_i &= \frac{h_\alpha + h_\beta}{2}; \\ H_k &= \frac{h_\alpha - h_\beta}{2}, \end{aligned} \quad (2.32)$$

indicate that in case of $h_\alpha = h_\beta$ the critical field has zero value $H_k = 0$ in the elementary hysteresis loop and it results in an anhysteretic characteristic. The product distribution function can be obtained, respectively, by

$$p(h_\alpha, h_\beta) = \frac{k}{2\pi\sigma_i\sigma_k} \exp \left[-\frac{(h_\alpha - h_\beta - 2H_k)^2}{4\sigma_k^2} \right] \exp \left[-\frac{(h_\alpha + h_\beta)^2}{4\sigma_i^2} \right]. \quad (2.33)$$

To overcome the problems resulting from the discretization of the continuous variation of the magnetic field according to the available, discrete volumes of the distribution function in the Preisach triangle, a variable variance Preisach model is introduced in the paper of Pardavi-Horvath, Della Torre et al. [21].

Another analytical approximation method is the power series approximation of the Everett integral. On the basis of measured values getting for the integrals of the distribution function in [16], a newly created square mesh covers the limiting triangle (Fig. 2.29). A

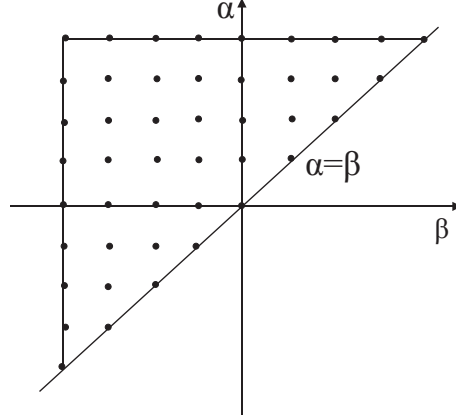


Figure 2.29: *Approximation of the Everett integral.*

discretized set of first-order transition curves is available here. A power series expansion of the Everett integral over the discrete cells of the Preisach triangles is developed:

$$E(h_\alpha, h_\beta) = C_0 + C_1 h_\alpha + C_2 h_\beta + C_3 h_\alpha^2 + C_4 h_\alpha h_\beta + C_5 h_\beta^2. \quad (2.34)$$

This expression takes into account the odd symmetry of the magnetization characteristics in (2.34) the even powers of the switching fields can be disregarding with selection of the coefficients to be zero $C_3 = 0$ and $C_5 = 0$.

Numerical implementation

The Preisach model can be numerically implemented by using formula (2.21) for the computation of the output $f(t)$ and the formula (2.25) for the determination of the weight function $\mu(\alpha, \beta)$. Although the above approach is straightforward, it encounters two main difficulties. First, it requires the numerical evaluation of the double integral in (2.21). This is a time-consuming procedure which may impede the use of the Preisach model in practical applications. Second, the determination of the weight function $\mu(\alpha, \beta)$ by employing formula (2.25) requires differentiations of experimentally obtained data. It turns out that another approach can be developed for the numerical implementation of the Preisach model. This approach completely circumvents the above difficulties. It is based on the explicit formula for the integrals in (2.21). This formula directly involves the experimental data used for the identification of $\mu(\alpha, \beta)$.

The expression (2.21) is the starting point for the derivation of the explicit formula for $f(t)$. The positive $S^+(t)$ and negative $S^-(t)$ sets in (2.21) are separated by the staircase interface $L(t)$. This interface has vertices whose α and β coordinates are equal to M_k and m_k , respectively (Fig. 2.30). By adding and subtracting the integral of $\mu(\alpha, \beta)$ over $S^+(t)$, the expression (2.21) can be represented in the form

$$f(t) = - \iint_T \mu(\alpha, \beta) d\alpha d\beta + 2 \iint_{S^+(t)} \mu(\alpha, \beta) d\alpha d\beta, \quad (2.35)$$

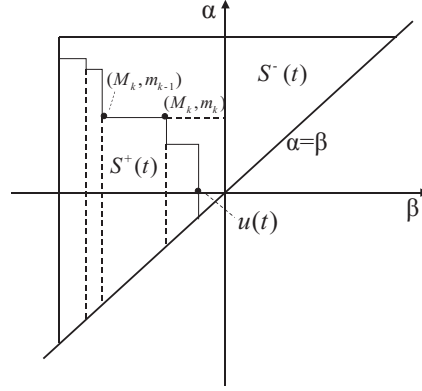


Figure 2.30: n trapezoids Q_k in $\alpha - \beta$ diagram with the monotonically decreasing input.

where T is the limiting triangle, and $\iint_T \mu(\alpha, \beta) d\alpha d\beta = F(\alpha_0, \beta_0)$. The positive set $S^+(t)$ can be subdivided into n trapezoids Q_k (see Fig. 2.30). As a result, we have

$$\iint_{S^+(t)} \mu(\alpha, \beta) d\alpha d\beta = \sum_{k=1}^{n(t)} \iint_{Q_k} \mu(\alpha, \beta) d\alpha d\beta. \quad (2.36)$$

The number n of these trapezoids and their shapes may change with time. For this reason, n and Q_k are functions of time.

Each trapezoid Q_k can be represented as a difference of two triangles, $T(M_k, m_{k-1})$ and $T(M_k, m_k)$. Thus,

$$\iint_{Q_k} \mu(\alpha, \beta) d\alpha d\beta = \iint_{T(M_k, m_{k-1})} \mu(\alpha, \beta) d\alpha d\beta - \iint_{T(M_k, m_k)} \mu(\alpha, \beta) d\alpha d\beta, \quad (2.37)$$

where for the case of $k = 1$, m_0 in (2.37) is equal to β_0 .

According to (2.24),

$$\iint_{T(M_k, m_{k-1})} \mu(\alpha, \beta) d\alpha d\beta = F(M_k, m_{k-1}), \quad (2.38)$$

and

$$\iint_{T(M_k, m_k)} \mu(\alpha, \beta) d\alpha d\beta = F(M_k, m_k). \quad (2.39)$$

From the above expression (2.37), (2.38), and (2.39),

$$\iint_{Q_k} \mu(\alpha, \beta) d\alpha d\beta = F(M_k, m_{k-1}) - F(M_k, m_k). \quad (2.40)$$

From the formulae (2.35) and (2.40),

$$f(t) = -F(\alpha_0, \beta_0) + 2 \sum_{k=1}^{n(t)} [F(M_k, m_{k-1}) - F(M_k, m_k)]. \quad (2.41)$$

From Fig. 2.30, it is clear that m_n is equal to the current value of input $m_n = u(t)$ for the case of monotonically decreasing input, when the final link of interface $L(t)$ is a vertical one. Expression (2.41) can be written as

$$f(t) = -F(\alpha_0, \beta_0) + 2 \sum_{k=1}^{n(t)-1} [F(M_k, m_{k-1}) - F(M_k, m_k)] + 2[F(M_n, m_{n-1}) - F(M_n, u(t))]. \quad (2.42)$$

For the case of monotonically increasing input, the final link of $L(t)$ is a horizontal one and the $\alpha - \beta$ diagram shown in Fig. 2.31. This case can be considered as a particular

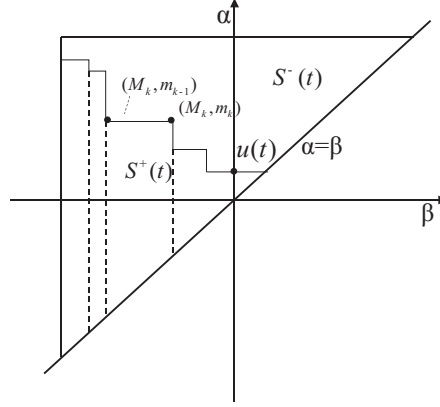


Figure 2.31: n trapezoids Q_k in $\alpha - \beta$ diagram with the monotonically increasing input.

case of the previous one. The expression (2.41) can be written as

$$f(t) = -F(\alpha_0, \beta_0) + 2 \sum_{k=1}^{n(t)-1} [F(M_k, m_{k-1}) - F(M_k, m_k)] + 2F(u(t), m_{n-1}). \quad (2.43)$$

The function $F(\alpha, \beta)$ is related to experimentally measured first-order transition curves by the formula (2.23). Using this formula, the expressions (2.42) and (2.43) can be written in terms of the experimental data as follows:

$$f(t) = -f^+ + \sum_{k=1}^{n-1} (f_{M_k, m_k} - f_{M_k, m_{k-1}}) + f_{M_n, u(t)} - f_{M_n, m_{n-1}}, \quad (2.44)$$

$$f(t) = -f^+ + \sum_{k=1}^{n-1} (f_{M_k, m_k} - f_{M_k, m_{k-1}}) + f_{-m_{n-1}} - f_{-m_{n-1}, -u(t)}. \quad (2.45)$$

Here, f^+ is the positive saturation value of output, and the last term in (2.45) has been transformed by using the formulas (2.23) and (2.30). Thus, we have derived the explicit expressions (2.44) and (2.45) for evaluating $f(t)$ in terms of experimentally measured data. These expressions constitute the basis for the numerical implementation of the Preisach model [16].

2.3.2 Main Properties of the Preisach Model

Nonlocal memory

The Preisach hysteresis nonlinearity (2.18) is constructed as a superposition of elementary hysteresis nonlinearities $\gamma_{\alpha\beta}$ with local memories, where only one curve of each set passes through each point in the $B - H$ or $M - H$ diagram. It is clear with local memories that every reachable point in the $B - H$ or $M - H$ diagram corresponds to a uniquely defined state. At any point in the $B - H$ or $M - H$ diagram there are only one or two curves that may represent the future behavior of hysteresis with local memories. But the entire model usually behaves as if it has a nonlocal memory, at any reachable point in the $B - H$ or $M - H$ diagram there is an infinity of curves that may represent the future behavior of the hysteresis. It is remarkable that a new qualitative property of nonlocal memory emerges as a collective property of a system having an infinite number of simple and qualitatively similar components.

Consider two inputs $u_1(t)$ and $u_2(t)$ with two different past histories for $t < t_1$ (Fig. 2.32). This means that they had different local memory for $t < t_1$, i.e. $f_1(t) \neq f_2(t)$ for $t < t_1$. If we assume that $f_1(t_1) = f_2(t_1)$ for $t = t_1$, then for the same input values for $t > t_1$, we have $f_1(t_1 + \Delta t) \neq f_2(t_1 + \Delta t)$, since $\Delta S_1^+ \neq \Delta S_2^+$. In Fig. 2.32, $S_1^+(t)$, $S_1^-(t)$ and ΔS_1^+ , and $S_2^+(t)$, $S_2^-(t)$ and ΔS_2^+ , are positive and negative sets of two different subdivisions of the limiting triangle associated with $u_1(t)$ and $u_2(t)$, respectively. The above two subdivisions for $t = t_1 + \Delta t$ are different because they correspond to two different input histories. Thus, the Preisach model (2.18) describes hysteresis nonlinearities with nonlocal memories, which reveals the mechanism of memory formation in the Preisach model.

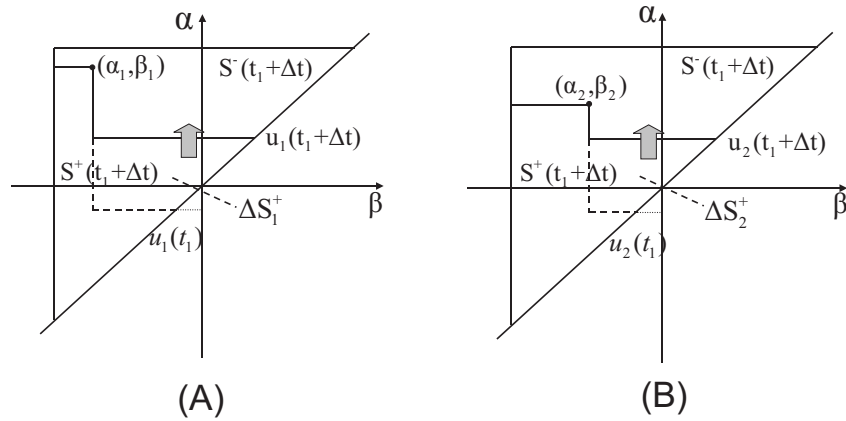


Figure 2.32: *Nonlocal memory property: Although featuring the same output value $f_1(t_1) = f_2(t_1)$ at a time instant $t = t_1$, the following output values can be different, i.e. $f_1(t_1 + \Delta t) \neq f_2(t_1 + \Delta t)$ even if the same input is applied. This follows from the fact that $\Delta S_1^+ \neq \Delta S_2^+$ because they depend on a different history. (A) $\alpha - \beta$ diagram with input $u_1(t)$, (B) $\alpha - \beta$ diagram with input $u_2(t)$.*

Wiping out property

The wiping out property of the Preisach model is related to the memory of the material. The notation of "wiping out property" was introduced by Mayergoyz [16], which further

elucidates the mechanism of memory formulation in the Preisach model. It turns out that this model does not accumulate all past extremum values of input. Some of them are wiped out by subsequent input variations.

Assume a particular past history which is characterized by a finite sequence $\{u_1, u_3, u_5, u_7\}$ of local input maxima and an increasing sequence $\{u_2, u_4, u_6, u_8\}$ of local input minima. An $\alpha - \beta$ diagram for this kind of history is shown in Fig. 2.33 (A). Now, assume that the input $u(t)$ is monotonically increased until it reaches some maximum value u_9 which is larger than u_3 . This monotonic increase of input $u(t)$ results in the formulation of a horizontal final link of $L(t)$ which moves upwards until the maximum value u_9 is reached. This results in a modified $\alpha - \beta$ diagram shown in Fig. 2.33 (B). It is evident that all vertices whose α -coordinates were below u_9 have been wiped out. The wiping out of vertices is equivalent to erasing the history associated with these vertices. It is obvious that the wiping out of vertices occurs in a similar manner for monotonically decreasing inputs as well.

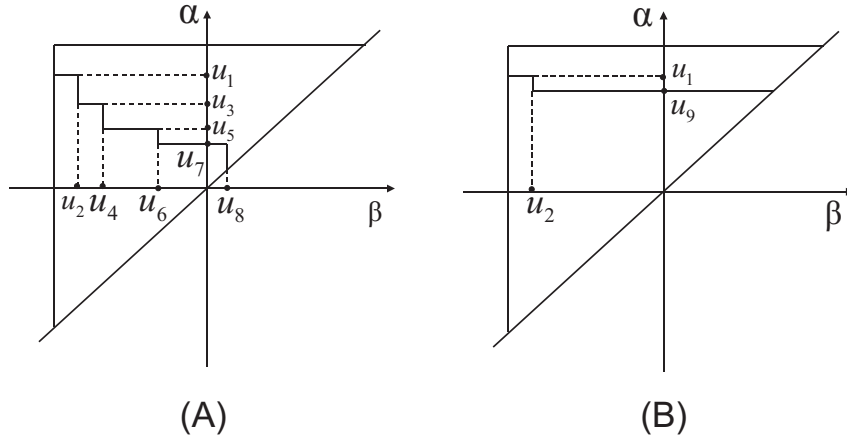


Figure 2.33: *Wiping out property.* (A) $\alpha - \beta$ diagram with input u_1, u_2, \dots, u_8 , (B) $\alpha - \beta$ diagram with input u_1, u_2, \dots, u_9 .

Congruency property

The congruency property reads: all minor hysteresis loops corresponding to back-and-forth variations of inputs between the same two consecutive extremum values are congruent.

The congruency property of the Preisach model is valid for periodic input variations. Let $u_1(t)$ and $u_2(t)$ be two inputs which may have different histories. Starting from some instant of time t_0 , these inputs vary back and forth between the same two consecutive extremum values, u_+ and u_- . The periodic input variations result in minor hysteresis loops. The $\alpha - \beta$ diagrams for the inputs $u_1(t)$ and $u_2(t)$ are shown in Fig. 2.34 (A) and (B), respectively. As the inputs vary back and forth between u_+ and u_- , the final links of the staircase interfaces $L_1(t)$ and $L_2(t)$ move within identical triangles T_1 and T_2 . This results in periodic shape variations for $L_1(t)$ and $L_2(t)$ which in turn produce periodic variations of the outputs $f_1(t)$ and $f_2(t)$. This means that some minor hysteresis loops are traced in the $f - u$ diagram for both inputs (Fig. 2.35). The positions of these two loops with respect to the f -axis are different. This is because the two inputs have different histories which lead to different shapes for the staircase interfaces $L_1(t)$ and $L_2(t)$. As a

result, the values of inputs are different, but the values of the outputs are the same. It is proven by Mayergoz [16] that the two hysteresis loops are congruent.

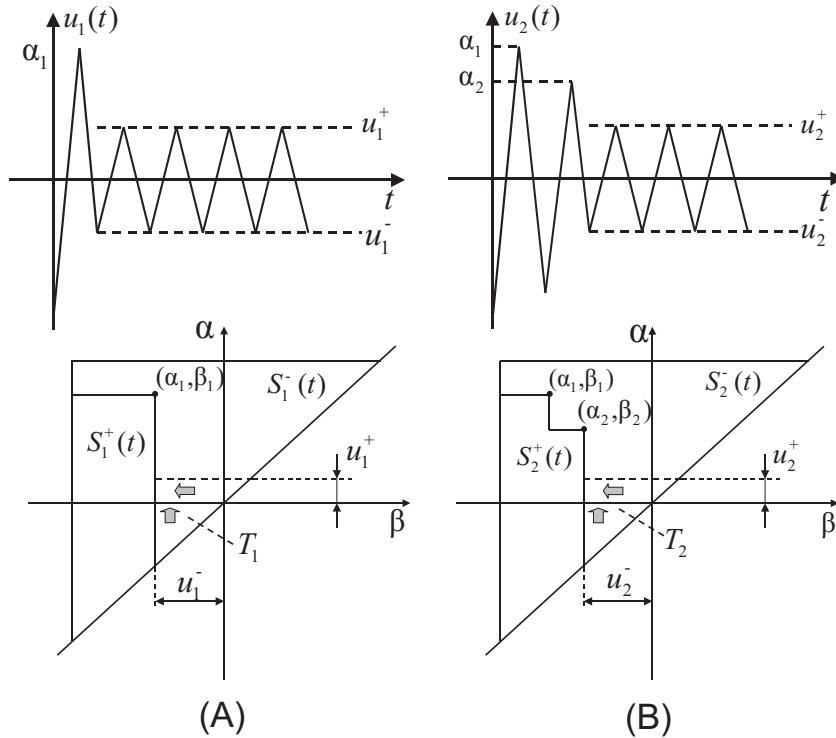


Figure 2.34: *Congruency property.* Input values are periodic, the extremal values are $u_1^+ = u_2^+$ and $u_1^- = u_2^-$. (A) Top: Waveform of the applied input values $u_1(t)$. Bottom: $\alpha - \beta$ diagram for input $u_1(t)$. (B) Top: Waveform of the applied input values $u_2(t)$. Bottom: $\alpha - \beta$ diagram for input $u_2(t)$.

It is clear from the above discussion of the main properties that the Preisach model has the ability to detect and store alternating series of dominant extreme input. For this reason, the Preisach model is feasible as a mathematical model for memory formulation with some properties. Its device realization might be utilized as an unusual storage device.

2.3.3 Generalized Preisach Models

The classical Preisach model describes hysteresis nonlinearities which exhibit congruency of minor loops formed for the same reversal values of input. However, many experiments show that actual hysteresis nonlinearities may substantially deviate from this property. The classical Preisach model also describes hysteresis nonlinearities with the wiping-out property. This property is similar to the immediate formation of the hysteresis loop after only one cycle of back-and-forth variation of the input between any two extreme values. However, experiments show that hysteresis loop formation is often preceded by some stabilization process which may require a large number of cycles to achieve a stable minor loop. This process is called "accommodation". To avoid such intrinsic limitations of the classical Preisach model, generalizations of the classical Preisach model are needed. The following generalized scalar Preisach models have been described by Mayergoz [16]:

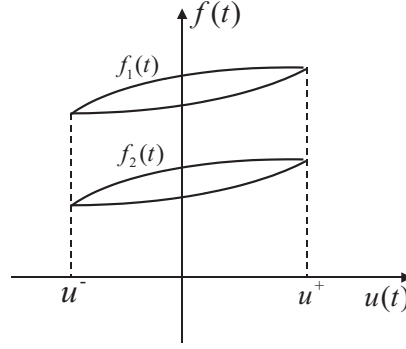


Figure 2.35: $f - u$ diagram illustrating the congruency property $u^+ = u_1^+ = u_2^+$ and $u^- = u_1^- = u_2^-$.

Moving Preisach model

$$f(t) = \iint_{R_{u(t)}} \mu(\alpha, \beta) \gamma_{\alpha\beta} u(t) d\alpha d\beta + \frac{1}{2}(f_{u(t)}^+ + f_{u(t)}^-). \quad (2.46)$$

The expression is formally equivalent to the classical one (2.18). However, in this expression, the integration is performed not over the fixed limiting triangle but over the rectangle $R_{u(t)}$ which changes with input variations (Fig. 2.36 (A)).

Nonlinear Preisach model

$$f(t) = \iint_{R_{u(t)}} \mu(\alpha, \beta, u(t)) \gamma_{\alpha\beta} u(t) d\alpha d\beta + \frac{1}{2}(f_{u(t)}^+ + f_{u(t)}^-). \quad (2.47)$$

The difference in comparison with the moving model (2.46) is the dependence of the distribution function μ on the current value of input $u(t)$.

Dynamic Preisach model

$$f(t) = \iint_{R_{u(t)}} \mu(\alpha, \beta, u(t), \frac{df}{dt}) \gamma_{\alpha\beta} u(t) d\alpha d\beta + \frac{1}{2}(f_{u(t)}^+ + f_{u(t)}^-). \quad (2.48)$$

In dynamic Preisach models, the distribution function depends on the speed of output variations, df/dt . The above model is a dynamic generalization of the nonlinear Preisach model.

The term $\frac{1}{2}(f_{u(t)}^+ + f_{u(t)}^-)$ in (2.46), (2.47) and (2.48) represents the fully reversible component of the hysteresis nonlinearity described by the classical Preisach model. In this respect, the term $\iint_{R_{u(t)}} \mu(\alpha, \beta) \gamma_{\alpha\beta} u(t) d\alpha d\beta$ for the moving Preisach model, the

term $\iint_{R_{u(t)}} \mu(\alpha, \beta, u(t)) \gamma_{\alpha\beta} u(t) d\alpha d\beta$ for the nonlinear Preisach model, and the term

$\iint_{R_{u(t)}} \mu(\alpha, \beta, u(t), \frac{df}{dt}) \gamma_{\alpha\beta} u(t) d\alpha d\beta$ for the dynamic Preisach model could represent an ir-

reversible component of the classical Preisach model. Therefore, the expressions (2.46),

(2.47) and (2.48) reflect the decomposition of the hysteresis nonlinearity described by the classical Preisach model into irreversible and reversible components. The irreversible component is responsible for the energy losses associated with the irreversible magnetization process in the domains and the domain walls. The reversible component can be associated with the stored and the returned energy. For the case of the reversible component, the medium stores the supplied energy, and the material returns this energy when the applied field is reduced to zero. The reversible component means that the magnetization characteristic is a single valued function of the applied field.

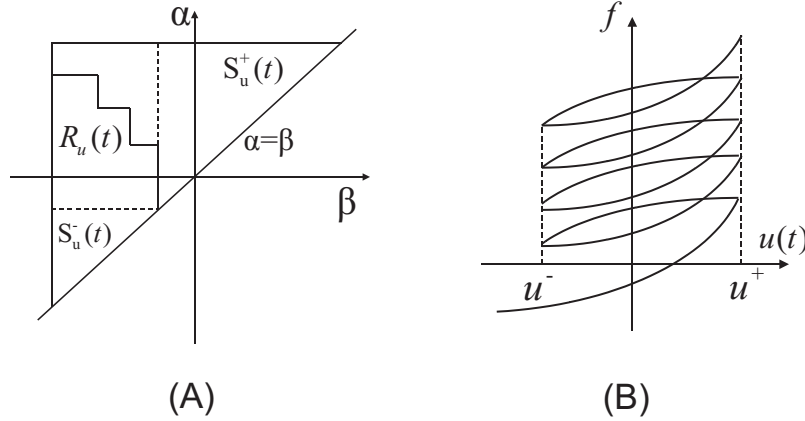


Figure 2.36: (A) $\alpha - \beta$ diagram of the generalized Preisach model, (B) the accommodation process.

Preisach model with accommodation

The accommodation process (Fig. 2.36 (B)) is relevant in particular applications. In that case, it is indispensable to model it. The modified Preisach model is described by Mayergoyz [16], and allows one to account for the accommodation process,

$$f(t) = \iint_{R_{u(t)}} \mu(\alpha, \beta, f^{(m)}) \gamma_{\alpha, \beta} u(t) d\alpha d\beta + r(u(t)). \quad (2.49)$$

In this formula, $r(u(t))$ stands for a fully reversible component which is represented by a single valued function of $u(t)$, and $f^{(m)} = M_k^f$ if $(\alpha, \beta) \in R_k(t)$, where M_k^f are local extremum values of the output f and $R_k(t)$ are rectangular regions formed after the extremum M_k^f had been achieved.

2.3.4 Preisach Model and Hysteresis Losses

The hysteresis losses are an important component of the core losses occurring in almost all electromagnetic power devices as well as in many high frequency microwave devices. For this reason, an accurate prediction of hysteresis losses and their reduction are important for the optimal design of various equipment. The hysteresis losses for the particular case of periodic input variations is equal to the area enclosed by the hysteresis loop. However, energy dissipation is a continuous process, and it occurs for arbitrary variations of input

which corresponds to non-closed paths in the $B - H$ characteristics. The problem of computing hysteresis losses for the general case has been investigated by Mayergoyz [16]. The Preisach model will be used for the derivation of general expression for hysteresis. These expressions will be given in terms of the weight function $\mu(\alpha, \beta)$ as well as in terms of experimentally measured first-order transition curves. Furthermore, a formula which relates the hysteretic losses occurring for arbitrary input variations to the losses occurring for certain periodic input variations, will be introduced. The formula may result in simple techniques for the measurement of hysteretic losses occurring for arbitrary input variations.

If the input $u(t)$ and the output $f(t)$ are defined as work variables, the infinitesimal energy supplied to the transducer in the form of work is given by $\partial W = udf$. In magnetics, u is the magnetic field H , f is the magnetic flux density B , and the function $B = B(H)$ at any point in the ferromagnetic material follows a curve of the form indicated by Fig. 2.37. The work done while magnetizing a unit volume of the material is represented by

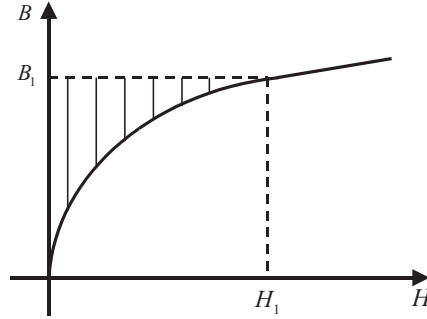


Figure 2.37: *Magnetic energy in shaded area.*

the shaded area in Fig. 2.37. The function $B(H)$ is single-valued. A decrease of the field from H_1, B_1 to zero would follow the same curve and the entire energy would be available for useful work. However, in case of the hysteresis with periodic input variations as shown in Fig. 2.38 (A), starting at H_1 , the field is decreased until $H = 0$. The associated value of $B = B_2$, however, is still positive. To reduce B to zero, negative values must be imparted to H , meaning physically that H must be increased in the opposite direction. At $H = -H_3$ the flux density B is zero, and as H continues to increase in negative value a point is eventually reached where simultaneously $H = H_1, B = B_1$. The return to the positive values H_1, B_1 follows the symmetrical path through $B = B_2, H = 0$ and $B = 0, H = H_3$. Assume w is the work done per unit volume of magnetic material in changing the field from the value B_1 to B .

$$w = \int_{B_1}^B H dB = H \cdot B \Big|_{B_1}^B - \int_{H_1}^H B \cdot dH. \quad (2.50)$$

If the variation of the field is carried through a complete cycle following the hysteresis loop from B_1 through $B_2, -B_1, -B_2$ and returning to B_1 , the net work done per unit volume is

$$w = - \oint B \cdot dH, \quad (2.51)$$

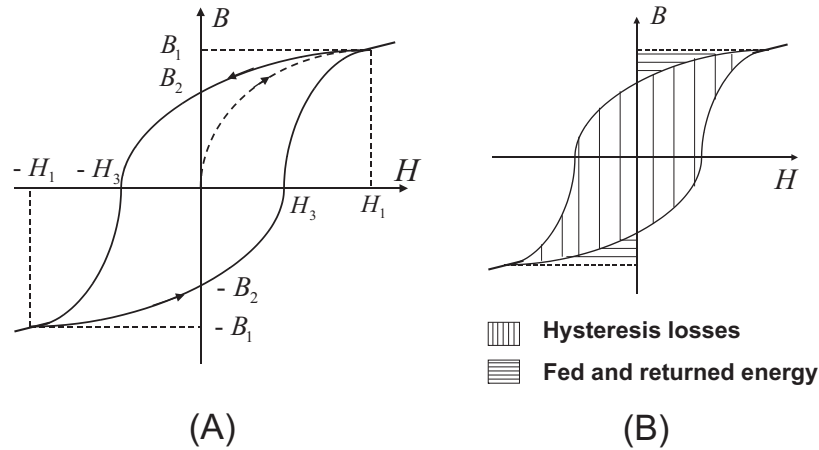


Figure 2.38: (A) Hysteresis loop, (B) Stored magnetic and hysteresis losses of the hysteresis loop.

a quantity evidently represented by the enclosed area of the hysteresis loop illustrated in Fig. 2.38 (B). The net work done per cycle throughout the entire field is

$$Q = - \int dv \oint B \cdot dH, \quad (2.52)$$

where Q is the hysteresis loss, which is an irretrievable fraction of the field energy dissipated in heat. The function $B = B(H)$ is determined by the weight function $\mu(\alpha, \beta)$ and the measured first-order transition curves. This is the fundamental formula for hysteretic losses, and all subsequent results will follow from expression (2.52).

2.3.5 Vector Preisach Model

The research on the scalar and vector hysteresis model has quite distinct lines. The phenomenological modelling of vector hysteresis has long been centered around the classical Stoner-Wohlfarth (S-W) model [22]. The S-W model is designed as a representation of an ensemble of single-domain, uniaxial magnetic particles. Since these particles have some features of physical relevance, the S-W model is commonly regarded as a physical model. Due to its popularity in magnetics, the S-W model is a natural benchmark for comparison with other vector hysteresis model. For this reason, the S-W model will be introduced at first.

Stoner-Wohlfarth model of vector hysteresis

The S-W model describes the magnetization process as the assemble of the rotation of the magnetic moments in single domain particles with uniaxial anisotropy, resulted either by the particle shape, the magnetocrystalline anisotropy or by the strain. The reversible and irreversible magnetization are represented by these rotations. Since single-domain, uniaxial magnetic particles are the main building block of the S-W model, the discussion of hysteresis begins with these S-W particles. As a symmetry consideration it is assumed that the vector magnetization \vec{M} of this particle lies in the plane formed by the easy axis

x and the applied magnetic field \vec{H} (Fig. 2.39). The orientation-dependent part of the free energy w of the S-W particle is given by

$$w = K \sin^2 \theta - \vec{M} \cdot \vec{H}, \quad (2.53)$$

where K is the anisotropy constant and θ is the angle between the easy axis and \vec{M} . The first term $K \sin^2 \theta$ represents the anisotropy energy, while the second term $\vec{M} \cdot \vec{H}$ is the energy of the interaction of magnetic moment \vec{M} with the applied magnetic field. Using the cartesian coordinates shown in Fig. 2.39, expression (2.53) can be represented as

$$w = K \sin^2 \theta - M H_x \cos \theta - M H_y \sin \theta. \quad (2.54)$$

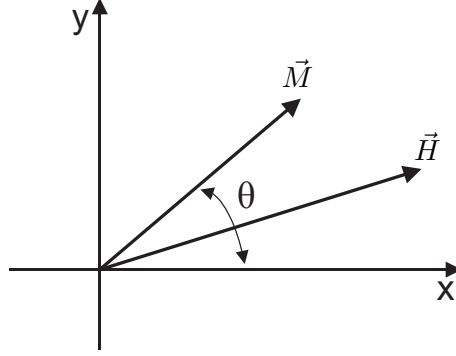


Figure 2.39: Vector magnetization \vec{M} and vector magnetic field \vec{H} .

Equilibrium orientations of \vec{M} correspond to minima of w , and they can be found from

$$\frac{\partial w}{\partial \theta} = 0; \quad \text{and} \quad \frac{\partial^2 w}{\partial \theta^2} \geq 0. \quad (2.55)$$

From expressions (2.54) and (2.55), we have

$$\frac{\partial w}{\partial \theta} = 2K \sin \theta \cos \theta + M H_x \sin \theta - M H_y \cos \theta = 0, \quad (2.56)$$

which can be rewritten as

$$\frac{H_y}{\sin \theta} - \frac{H_x}{\cos \theta} = \alpha_{\text{stoner}}, \quad (2.57)$$

where $\alpha_{\text{stoner}} = 2K/M$. The equation (2.57) is a quartic equation with respect to $\cos \theta$. For this reason, this equation may have two or four real solutions. In the case of two solutions, there is only one equilibrium orientation of \vec{M} and one minimum. In the case of four solutions, there are two minima which correspond to two equilibrium orientations of \vec{M} . Thus, on the \vec{H} -plane there are two different regions where \vec{M} has one and two equilibrium orientations, respectively. On the boundary between the two regions of one minimum and one maximum, we have $\frac{\partial w}{\partial \theta} = 0$ and $\frac{\partial^2 w}{\partial \theta^2} = 0$. Using the above expressions and equation (2.54), we have

$$\frac{H_x}{\cos^3 \theta} + \frac{H_y}{\sin^3 \theta} = 0. \quad (2.58)$$

By solving the two equations (2.57) and (2.58) with respect to H_x and H_y , we have $H_x = -\alpha_{\text{stoner}} \cos^3 \theta$, and $H_y = \alpha_{\text{stoner}} \sin^3 \theta$, i.e. $H_x^{2/3} + H_y^{2/3} = \alpha_{\text{stoner}}^{2/3}$, this equation represents the astroid curve shown in Fig. 2.40.

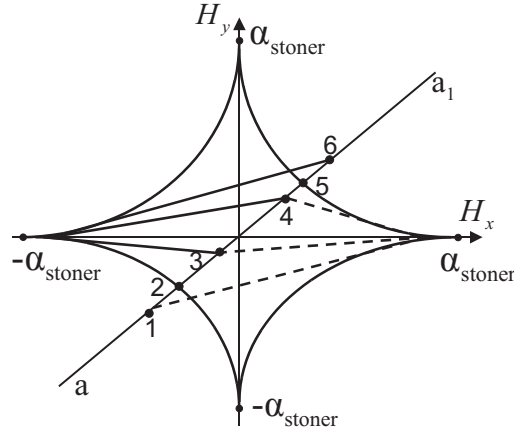


Figure 2.40: *The astroid curve of Stoner-Wohlfarth method.*

The described geometric rules allow one to compute hysteresis loops of a S-W particle for the case when the applied magnetic field is restricted to vary along one arbitrarily chosen direction. Suppose that this direction is specified by the line $a - a_1$ and that the magnetic field is varying between the value $-h$ corresponding to the point 1 to $+h$ corresponding to the point 6.

Starting the magnetization from the value $-h$, represented by the point 1, and monotonously increasing its value along the points 2-5 to the value $+h$, signed by point 6 and then monotonously decreasing its value back to $-h$ represents a total hysteresis loop in the S-W particle. As the value of the applied field is moving along the line $a - a_1$, the equilibrium orientation of \vec{M} is changing with the direction of the tangent lines to the right side of the asteroïd until point 5. At this point the magnetic moment flips, the tangent lines switch from right side to left side of the asteroïd. The stable direction of the magnetization is determined by the tangent line to the last point 6. Turning back with the applied field along the line $a - a_1$, the stable equilibrium belong to the tangent lines of left side of the asteroïd. At point 2, the stable position becomes unstable and the magnetic moment flips over again, the tangent line turns from left side to right side of the asteroïd. So, the equilibrium direction of the moment magnetization is changing continuously if the applied field is moving from outside to the inside region of the asteroïd, and there is an abrupt change in the orientation of magnetization if the magnetic field crosses the asteroïd from the inside to the outside region. This means that the points of the line $a - a_1$ being inside the asteroïd prove two stable orientations for the magnetic moment, resulting in two different branches of the hysteresis loop plotted in Fig. 2.41(B). It is clear that if the applied field varies along the easy axis x then a S-W particle exhibits a rectangular hysteresis loop as shown in Fig. 2.41 (A). If the applied field varies along the perpendicular to the easy axis, then due to the symmetry there is no hysteresis effect and a S-W particle exhibits a single value magnetization curve shown in Fig. 2.41 (B). Thus the shape of the hysteresis loops depends on the direction along which the applied field is being varied.

Having described the basic properties of a S-W particle, the S-W hysteresis model is designed as an ensemble of S-W particles. Consider an infinite set of S-W particles with different orientations of their easy axes and different values of the switching field α_{stoner} . The notation $S_{\theta, \alpha_{\text{stoner}}}$ will be used for a S-W particle whose switching field is equal to α_{stoner} and whose easy axis forms the angle θ with the x -axis. The S-W model can be

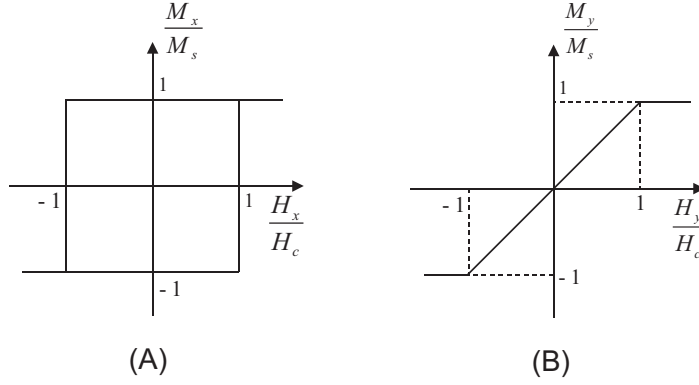


Figure 2.41: *The magnetization curve (A) The applied field is parallel to the easy axis, (B) The applied field is perpendicular to the easy axis.*

represented mathematically as

$$\vec{f}(t) = \iint \xi(\theta, \alpha_{\text{stoner}}) S_{\theta, \alpha_{\text{stoner}}} \vec{u}(t) d\theta d\alpha_{\text{stoner}}, \quad (2.59)$$

where $\xi(\theta, \alpha_{\text{stoner}})$ is a distribution function which should be determined by fitting the model to experimental data.

Identification of the vector Preisach model

The starting point of the identification for the vector Preisach model is the fact that scalar hysteresis is a particular case of vector hysteresis. The scalar hysteresis corresponds to vector hysteresis where some specific properties which have been observed for input variations along some fixed directions. Thus, it can be concluded that vector hysteresis is reduced to scalar hysteresis when the vector input is restricted to vary along any arbitrarily fixed direction. Vector hysteresis is a vector nonlinearity with the property that past extremum values of input values along all possible directions may affect future values of the output. Thus, the mathematical model of vector hysteresis should be able to detect and store past extreme of input values along all possible directions and choose the appropriate value of the vector output according to the accumulated history. To detect and accumulate the past extremum values of input values along all possible directions, the scalar models are continuously distributed along all possible directions (Fig. 2.42). Therefore, scalar Preisach models are main building blocks for the vector model, which is constructed as a superposition of scalar models. The expression mathematically in two dimensions is

$$\vec{f}(t) = \oint_{|\vec{r}|=1} \vec{r} \Gamma_{\vec{r}}(\vec{r} \cdot \vec{u}(t)) dl_r. \quad (2.60)$$

Similarly, a three dimensions vector Preisach model is written in the form

$$\vec{f}(t) = \oint_{|\vec{r}|=1} \vec{r} \Gamma_{\vec{r}}(\vec{r} \cdot \vec{u}(t)) ds_r. \quad (2.61)$$

The scalar Preisach models $\Gamma_{\vec{r}}$ for isotropic vector models are defined by

$$\Gamma_{\vec{r}}(\vec{r} \cdot \vec{u}(t)) = \iint_{\alpha \geq \beta} \nu(\alpha, \beta) \gamma_{\alpha\beta}(\vec{r} \cdot \vec{u}(t)) d\alpha d\beta. \quad (2.62)$$

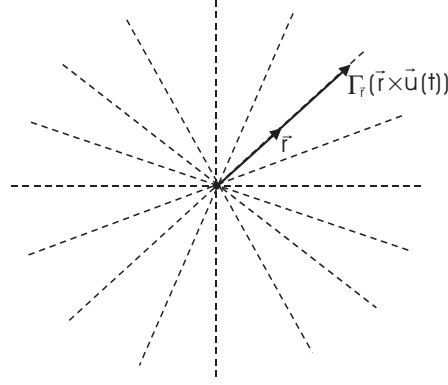


Figure 2.42: Possible directions for vector Preisach model.

The further definition of the vector Preisach model was explained by Mayergoyz [16], the 2-D and 3-D isotropic vector Preisach models are formulated as following

$$\vec{f}(t) = \int_{-\pi/2}^{\pi/2} \vec{e}_{\varphi} \left(\iint_{\alpha \geq \beta} \nu(\alpha, \beta) \gamma_{\alpha\beta} u_{\varphi}(t) d\alpha d\beta \right) d\varphi, \quad (2.63)$$

$$\vec{f}(t) = \int_0^{2\pi} \int_0^{\pi/2} \vec{e}_{\theta, \varphi} \left(\iint_{\alpha \geq \beta} \nu(\alpha, \beta) \gamma_{\alpha\beta} u_{\theta, \varphi}(t) d\alpha d\beta \right) \sin\theta d\theta d\varphi, \quad (2.64)$$

where $\vec{e}_{\theta, \varphi}$ (or in 2-D \vec{e}_{φ}) is a unit vector along the direction specified by angles φ and θ (in 2-D only φ), and $u_{\theta, \varphi}(t)$ (in 2-D $u_{\varphi}(t)$) is the projection of $\vec{u}(t)$ along the direction of $\vec{e}_{\theta, \varphi}$ (or in 2-D \vec{e}_{φ}). The definition of the $P(\alpha, \beta, \theta, \varphi)$ (or in 2-D $P(\alpha, \beta, \varphi)$) along some fixed θ and φ is

$$P(\alpha, \beta, \theta, \varphi) = \iint_{T(\alpha, \beta)} \nu_1(\alpha, \beta, \theta, \varphi) d\alpha d\beta, \quad (2.65)$$

which can be easier determined by experimental data than the function $\nu(\alpha, \beta, \varphi)$ ($\nu(\alpha, \beta)$ in 2-D).

Mayergoyz solved the identification problem of the Preisach model in one, two, and three dimensions [31]. The essence of the identification problem is in determining the function $P(\alpha, \beta)$ from some experimental data. It turns out that this problem can be reduced to the solution of a special integral equation which relates the function $P(\alpha, \beta)$ to some scalar hysteresis data. In one dimension, the Everett function can be determined by measuring the first-order return branches. In two and three dimensions, it is necessary to solve some integral equations for which closed expression is available. In the two-dimensional case, it is

$$P(\alpha, \lambda\alpha) = \frac{1}{\pi} \int_0^{\alpha} \frac{F(s, \lambda s) + s \frac{d}{ds} F(s, \lambda s)}{\sqrt{\alpha^2 - s^2}} ds. \quad (2.66)$$

To circumvent the problem of the singularity in the numerical analysis, the integral can be evaluated by subdividing the interval or integration into small intervals (s_i, s_{i+1}) [13]:

$$\int_0^{\alpha} \frac{V(s) ds}{\sqrt{\alpha^2 - s^2}} \approx \sum_{i=1}^n V(\bar{s}_i) \left[\arcsin \frac{s_{i+1}}{\alpha} - \arcsin \frac{s_i}{\alpha} \right], \quad (2.67)$$

where

$$V(s) = F(s, \lambda s) + s \frac{d}{ds} F(s, \lambda s), \quad (2.68)$$

and \bar{s}_i are the middle points of the above intervals.

In the three-dimensional case, it is

$$P(\alpha, \lambda\alpha) = \frac{1}{2\pi\alpha} \frac{d}{d\alpha} [F(\alpha, \lambda\alpha)]. \quad (2.69)$$

The function $F(\alpha, \lambda\alpha)$ is related to the experimental measured first-order return branches while $P(\alpha, \lambda\alpha)$ is related to the integral of the Preisach function.

2.4 Jiles-Atherton Model

Jiles and Atherton introduced the Jiles-Atherton model for the simulation of the hysteresis characteristic of ferromagnetic materials in 1983 [23], [24], [25], on the basis of the physical principles, rather than mathematical arguments or experimental curves. The mathematical model is based on the assumption of an anhysteretic magnetization which follows the Langevin function. The magnetization M is decomposed into the irreversible component M_{irr} , whose variations are due to the pinning encountered by the domain walls, and the reversible component M_{rev} , which has its origin in reversible processes like domain wall bending.

2.4.1 Physical Principles

In ferromagnetic materials, the neighboring dipoles have interaction with each other. This interaction between the magnetic dipoles results in an exchange field H_{ex} introduced by Weiss [1]. The exchange field for all dipoles in the domain is

$$H_{\text{ex}} = \sum_j \alpha_{\text{ja},ij} m_j, \quad (2.70)$$

where m_i and m_j are neighboring dipoles and $\alpha_{\text{ja},ij}$ are constants. If the interaction between all dipoles are supposed to be identical and hence independent of the displacement between the dipoles, then all $\alpha_{\text{ja},ij}$ are equal to α_{ja} , and the interaction field can be written as

$$H_{\text{ex}} = \alpha_{\text{ja}} \sum_j m_j = \alpha_{\text{ja}} M, \quad (2.71)$$

while the effective field can be defined as $H_e = H + \alpha_{\text{ja}} M$. Substituting this relation into the Curie law for ferromagnetic material $M = \frac{C}{T} (H + \alpha_{\text{ja}} M)$, a representation for the ferromagnetic susceptibility in the paramagnetic region $\chi = \frac{C}{T - T_c}$, where $T_c = \alpha_{\text{ja}} C$ is the Curie temperature. The magnetization in the paramagnetic region, with respect of the magnetic moments aligned parallel to the applied field, can be formulated as

$$M = Nm \left(\coth \lambda - \frac{1}{\lambda} \right); \quad \lambda = \frac{\mu_0 m H}{kT}. \quad (2.72)$$

The Langevin function $\mathcal{L}(\lambda) = \coth\lambda - 1/\lambda$, lies in the range of $-1 < \mathcal{L}(\lambda) < 1$. For high values of the parameter λ , the Langevin function approaches 1. When H reaches $+\infty$, the magnetization approaches $M_s = Nm$, where the dipole tends to be perfectly aligned. However, to reach saturation, an extremely high external field is needed at very low temperature. In the practice, the magnitude of $\lambda = \mu_0 m H / kT$ at room temperature is small and the Langevin function can be expanded in series

$$\mathcal{L}(\lambda) = \frac{\lambda}{3} - \frac{\lambda^3}{45} \dots \quad (2.73)$$

For small values of λ , the series expansion results in the magnetization M and a field independent susceptibility χ

$$\mathcal{L}(\lambda) \approx \frac{\lambda}{3}, \quad (2.74)$$

$$M = M_s \frac{\mu_0 m H}{3kT} = \chi H; \quad \chi = \frac{\mu_0 N m^2}{3kT}. \quad (2.75)$$

A hysteresis free magnetization characteristic is determined by the relation

$$M = M_s \left(\coth \frac{H}{a} - \frac{a}{H} \right); \quad a = \frac{kT}{\mu_0 m}. \quad (2.76)$$

As a consequence of the Weiss law, the magnetization characteristic resulted by the Langevin theory has been modified for ferromagnetic materials as

$$M = M_s \left(\coth \frac{\mu_0 m (H + \alpha_{ja} M)}{kT} - \frac{kT}{\mu_0 m (H + \alpha_{ja} M)} \right). \quad (2.77)$$

Therefore, for an isotropic material the magnetization characteristic due to the interaction describes the magnetization determined by the relation of

$$M = M_s \left(\coth \frac{H + \alpha_{ja} M}{a} - \frac{a}{H + \alpha_{ja} M} \right); \quad a = \frac{kT}{\mu_0 m}. \quad (2.78)$$

2.4.2 Jiles-Atherton Model and Determination of Parameters

In the Jiles-Atherton model, the magnetization is composed of the reversible component M_{rev} and the irreversible component M_{irr}

$$M = M_{irr} + M_{rev}. \quad (2.79)$$

The reversible component represents the reversible domain wall bending. The irreversible component corresponds to the irreversible domain and domain wall processes representing the energy losses in the hysteretic material. The irreversible component can be determined from the energy balance of the magnetization process.

If there are no hysteresis losses during the magnetization process, the magnetization characteristic follows the anhysteretic curve $M_{an}(H)$ generated on the basis of the Langevin

and Weiss theory as introduced above. So, the energy balance in the change of the supplied energy, the magnetic energy and the hysteresis losses generated by the domain wall motion can be expressed as

$$\mu_0 \int M_{\text{an}}(H)dH = \mu_0 \int M dH + \mu_0 \int k\delta \frac{dM}{dH} dH, \quad (2.80)$$

which results in the relation between the magnetic field intensity and the magnetization $M_{\text{an}}(H) = M + k\delta \frac{dM}{dH}$. Considering the interaction between the domains according to Weiss's law, with the effective field, $H_e = H + \alpha_{\text{ja}}M$, the irreversible component of the magnetization process can be determined by the solution of the differential equation

$$M_{\text{an}}(H) = M_{\text{irr}} + k\delta \frac{dM_{\text{irr}}}{dH_e}. \quad (2.81)$$

Evaluating the derivative of the above equation with respect to the applied field intensity yields the form for the irreversible susceptibility

$$\frac{dM_{\text{irr}}}{dH} = \frac{dM_{\text{irr}}}{dH_e} \cdot \frac{dH_e}{dH}, \quad (2.82)$$

$$\frac{dM_{\text{irr}}}{dH} = \frac{M_{\text{an}}(H_e) - M_{\text{irr}}}{k\delta - \alpha_{\text{ja}}(M_{\text{an}}(H_e) - M_{\text{irr}})}. \quad (2.83)$$

The reversible component of the magnetization can be represented as the difference between the anhysteretic and the irreversible magnetization

$$M_{\text{rev}} = c(M_{\text{an}}(H_e) - M_{\text{irr}}), \quad (2.84)$$

where c is the reversible coefficient. So, the total magnetization characteristic has the form

$$M = M_{\text{irr}} + M_{\text{rev}} = (1 - c)M_{\text{irr}} + cM_{\text{an}}(H_e). \quad (2.85)$$

The differential susceptibility of the characteristic represented by (2.85) is formulated as

$$\frac{dM}{dH} = \frac{dM_{\text{irr}}}{dH} + c \left(\frac{dM_{\text{an}}(H_e)}{dH} - \frac{dM_{\text{irr}}}{dH} \right). \quad (2.86)$$

From the expressions (2.83) and (2.86), the differential susceptibility of the characteristic follows by

$$\frac{dM}{dH} = (1 - c) \frac{M_{\text{an}}(H_e) - M_{\text{irr}}}{k\delta - \alpha_{\text{ja}}(M_{\text{an}}(H_e) - M_{\text{irr}})} + c \frac{dM_{\text{an}}(H_e)}{dH}. \quad (2.87)$$

In the Jiles-Atherton model, the five parameters $a, \alpha_{\text{ja}}, c, k$ and M_s are determined from experimental data following the procedure proposed in [26], [27]. Matching experimental values for the field quantities to the Jiles-Atherton model, the parameter values for the anhysteretic susceptibility, initial susceptibility, coercivity and remanence, the five parameters of the model can be determined.

The Jiles-Atherton model is based on two equations, dM_{irr}/dH , which has been introduced in formula (2.83), and dM_{rev}/dH

$$\frac{dM_{\text{rev}}}{dH} = c \left(\frac{dM_{\text{an}}}{dH} - \frac{dM_{\text{irr}}}{dH} \right). \quad (2.88)$$

These equations contain five independent parameters, a , α_{ja} , c , k and M_s , which are defined above. The anhysteretic susceptibility at the origin $\chi_{an}(O)$ can be used to define a relationship between M_s , a and α_{ja} :

$$a = \frac{M_s}{3} \left(\frac{1}{\chi_{an}(O)} + \alpha_{ja} \right). \quad (2.89)$$

In the solution of the model equations currently in use the initial susceptibility $\chi_{in}(O)$ at the origin can be used to determine c :

$$c = \frac{3a}{M_s} \chi_{in}(O). \quad (2.90)$$

The hysteresis losses parameter k can be determined from the coercivity H_c and the differential susceptibility at the coercive point $\chi_c(H_c)$:

$$k = \frac{M_{an}(H_c)}{1-c} \left\{ a + \frac{1}{\chi_c(H_c) - \left(\frac{c}{1-c}\right) \frac{dM}{dH}} \right\}. \quad (2.91)$$

The coupling parameter α_{ja} can be determined independently if a is known by using the remanent magnetization M_r and the differential susceptibility at remanence $\chi_r(M_r)$:

$$M_r = M_{an}(M_r) + \frac{k}{\left(\frac{\alpha_{ja}}{1-c}\right) + \left(\frac{1}{\chi_r(M_r) - c \frac{dM}{dH}}\right)}. \quad (2.92)$$

On the basis of the above formulae (2.83), (2.88), (2.89), (2.90), (2.91) and (2.92), a set of equations is constructed. From the measured values at the characteristic points of the hysteresis loops the parameters a , α_{ja} , c , k and M_s of the Jiles-Atherton model can be determined by iteratively solving this nonlinear system of equations [26], [27].

2.4.3 Comparison of the Jiles-Atherton Model and the Preisach Model

The Jiles-Atherton model and the Preisach model are two main streams in the hysteresis models.

The Preisach model is based on the assumption that any hysteresis can be expressed as a sum of elementary hysteresis loops. The distribution function of the elementary hysteresis is determined fully from the measured first-order transition curves, or is assumed to be expressed as one of special functions such as the Gaussian function with unknown parameters that must be determined by curve fitting technique.

On the other hand, in the Jiles-Atherton model, magnetic hysteresis is described by a first-order ordinary differential equation which is derived from physical insight into the magnetization process. The differential equation depends on the five parameters a , α_{ja} , c , k and M_s . These parameters are determined from the experimental data following a procedure proposed in the above.

2.5 Conclusions

In this chapter, the physical phenomenon of the ferromagnetic hysteresis and several models describing hysteresis are summarized. As scalar hysteresis models, the classical Preisach model, several generalized Preisach models and the Jiles-Atherton model are introduced. As examples of vector hysteresis models, the Stoner-Wohlfarth model and the vector Preisach model are shortly discussed.

This thesis deals with the construction of efficient algorithms combining hysteresis models with the finite integration technique. In all further simulations, the classical Preisach model, the Jiles-Atherton model and the vector Preisach model serves as examples.

Chapter 3

Electromagnetic Field Simulation

The Finite Integration Technique (FIT) is used as a spatial discretization method for hysteretic materials. Some fundamental properties of FIT are presented in this chapter. In addition, magnetoquasistatic field simulation taking into account hysteretic effects is developed in this chapter. Implicit time stepping methods are used to discretize the model in time domain. The differential algebraic equations allow to consider the solution of the first order equation for the magnetoquasistatic field problems numerically. Different time integration methods for the differential algebraic equation are discussed. The numerical problems in magnetoquasistatic field discretized by the FIT lead to large space linear system of equations, which requires a solution method for the linear systems. For this reason, different methods for solving the linear system are discussed in order to improve the numerical process. The magnetoquasistatic field simulation with FIT is modified to include hysteresis material modelling for the transient hysteretic numerical computation in Chapter 4.

3.1 Finite Integration Technique

The FIT presents a reformulation of Maxwell's equations in integral form, resulting in a set of matrix equations, each of which is the discrete analogue to one of the original Maxwell's equations. The FIT was originally developed for frequency domain problems starting almost three decades ago [51], [52], [53], and later completed to a generalized scheme for the entire application range of Maxwell's equations. The central idea of FIT is the introduction of discrete topological operators (curl operator, divergence operator and gradient operator), and the discrete material operators.

The starting point of FIT is to define a finite three dimensional volume $\Omega \in \mathbf{R}^3$, the calculation domain, comprising the part of space where the relevant electromagnetic fields are existing. A spatial discretization is given by decomposition of Ω into a finite number of volumes. A grid cell complex G is created at Ω . In this thesis, only a three dimensional Cartesian coordinate grid is used. Grids G can be applied in conjunction with FIT which are more general as e.g. non-coordinate grids and non-orthogonal grids. The Cartesian grid cell complex (see Fig. 3.1) is composed of elementary volumes $V(i, j, k)$. The nodes on the volumes $V(i, j, k)$ are enumerated along the grid coordinates u, v, w with $P(i, j, k)$,

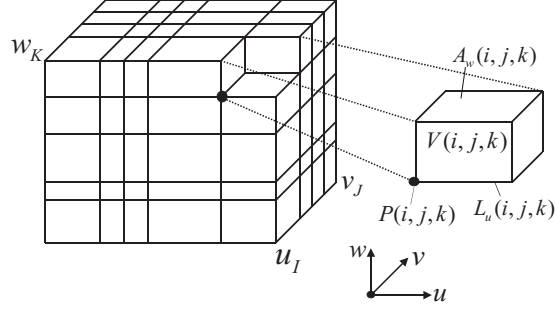


Figure 3.1: Example of a grid cell G in Cartesian coordinates.

where $1 \leq i \leq I, 1 \leq j \leq J, 1 \leq k \leq K$ with total number of nodes $N = I \cdot J \cdot K$. The intersection of two grid volumes is called a grid facet. The grid facets associated with the three different coordinates u, v, w are denoted by $A_u(i, j, k)$, $A_v(i, j, k)$, or $A_w(i, j, k)$. The intersection of two facets is called a grid edge and denoted by $L_u(i, j, k)$, $L_v(i, j, k)$, or $L_w(i, j, k)$ depending on whether its orientation is in the u, v , or w direction, respectively. Edges and facets have an initial orientation, pointing into the direction of the respective grid coordinates towards higher indices.

3.1.1 Maxwell-Grid-Equations

In FIT, the Maxwell equations are transformed into a set of matrix equations, each of which is the discrete analogue to one of the original Maxwell equations. The collection of the discretized Maxwell equations is referred to as Maxwell-Grid-Equations (MGE).

When expressing the MGE, edge voltages and facet fluxes should be introduced first. For example, the electric edge voltage along the edge $L_u(i, j, k)$ is defined by

$$\widehat{\mathbf{e}}_u(i, j, k) = \int_{L_u(i, j, k)} \vec{E} \cdot d\vec{s}, \quad (3.1)$$

the magnetic flux through the facet $A_w(i, j, k)$ can be written as

$$\widehat{\mathbf{b}}_w(i, j, k) = \int_{A_w(i, j, k)} \vec{B} \cdot d\vec{A}. \quad (3.2)$$

Using the integrals (3.1) and (3.2), the first Maxwell equation (2.1) is derived for the grid facet $A_w(i, j, k)$ is shown in Fig. 3.2 (A):

$$\widehat{\mathbf{e}}_u(i, j, k) + \widehat{\mathbf{e}}_v(i + 1, j, k) - \widehat{\mathbf{e}}_u(i, j + 1, k) - \widehat{\mathbf{e}}_v(i, j, k) = -\frac{d}{dt} \widehat{\mathbf{b}}_w(i, j, k), \quad (3.3)$$

where each edge voltage (e.g. $\widehat{\mathbf{e}}_u(i, j, k)$) is allocated at one edge of the considered facet and represents the exact value of the integrated electric field strength along that path. The $\widehat{\mathbf{b}}_w(i, j, k)$ represents the exact value of the magnetic flux through the grid facet.

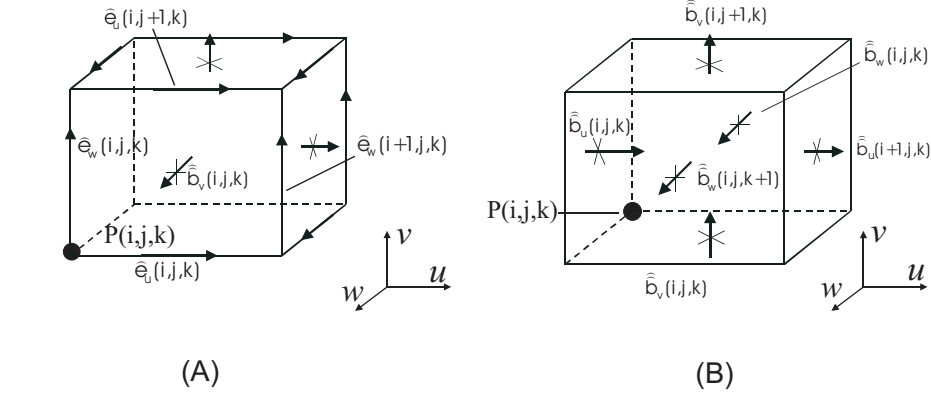


Figure 3.2: A grid cell G in Cartesian coordinates, (A) Allocation of the edge voltages on the edges of $A_w(i, j, k)$ and the facet fluxes through the facets $A_w(i, j, k)$ used in (3.3), (B) Allocation of the facet fluxes on the facets of $V(i, j, k)$ used in (3.5).

All the edge voltages $\hat{\mathbf{e}}$ and facet fluxes $\hat{\mathbf{b}}$ defined on grid G can be arranged in vectors $\hat{\mathbf{e}} = (\hat{\mathbf{e}}_1, \dots, \hat{\mathbf{e}}_{N_l})^T$ and $\hat{\mathbf{b}} = (\hat{\mathbf{b}}_1, \dots, \hat{\mathbf{b}}_{N_a})^T$, respectively, so that the first Maxwell equation (2.1) in its discrete form reads:

$$\mathbf{C}\hat{\mathbf{e}} = -\frac{d}{dt}\hat{\mathbf{b}}. \quad (3.4)$$

The topological matrix \mathbf{C} is the discrete curl operator defined at grid G . It contains all signs appearing in (3.3), thus it is composed of two-banded matrices:

$$\mathbf{C} = \begin{bmatrix} 0 & -P_w & P_v \\ P_w & 0 & -P_u \\ -P_v & P_u & 0 \end{bmatrix},$$

and

$$[P_u]_{i,j} := \begin{cases} -1 & : j = i \\ +1 & : j = i + 1 \\ 0 & : \text{else} \end{cases}$$

$$[P_v]_{i,j} := \begin{cases} -1 & : j = i \\ +1 & : j = i + I \\ 0 & : \text{else} \end{cases}$$

$$[P_w]_{i,j} := \begin{cases} -1 & : j = i \\ +1 & : j = i + I \cdot J \\ 0 & : \text{else} \end{cases}$$

The P_u , P_v and P_w are discrete partial differential operators. Zeros are inserted in the rows and columns corresponding to components outside the grid.

The second important operator in Maxwell's equations is the divergence operator. The Maxwell equation (2.2) can be derived on the grid G for the volume $V(i, j, k)$ (Fig. 3.2 (B)).

The closed surface integral yields the following exact relation between the six employed flux quantities:

$$\begin{aligned} \widehat{\mathbf{b}}_u(i+1, j, k) + \widehat{\mathbf{b}}_v(i, j+1, k) + \widehat{\mathbf{b}}_w(i, j, k+1) \\ - \widehat{\mathbf{b}}_u(i, j, k) - \widehat{\mathbf{b}}_v(i, j, k) - \widehat{\mathbf{b}}_w(i, j, k) = 0. \end{aligned} \quad (3.5)$$

When applied at grid G , the Maxwell equation (2.2) in its discrete form is written as:

$$\mathbf{S}\widehat{\mathbf{b}} = 0, \quad (3.6)$$

where the discrete divergence operator \mathbf{S} of the dimension $N \times 3N$ is the topological operator, which picks up the right components of the column vector $\widehat{\mathbf{b}} = (\widehat{\mathbf{b}}_1, \dots, \widehat{\mathbf{b}}_{N_a})^T$ related to the zero flux balance of each cell of G . It is also sub-structured and made of the same basic discrete partial differential operators as the discrete curl operator \mathbf{C} :

$$\mathbf{S} = [\mathbf{P}_u \ \mathbf{P}_v \ \mathbf{P}_w]. \quad (3.7)$$

In order to resolve the two remaining Maxwell equations, the grid G is accomplished by a grid cell complex pair $\{G, \widetilde{G}\}$ (Fig. 3.3) by introducing the dual grid \widetilde{G} . The grid nodes

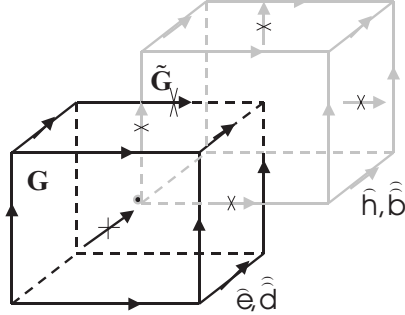


Figure 3.3: *Spatial allocation of electric and magnetic field values on the prime grid G and dual grid \widetilde{G} in Cartesian coordinates.*

of the dual grid $\widetilde{P}(i, j, k)$ are defined as the focal points of the grid G . In the dual grid \widetilde{G} , the components of the magnetic voltage and the electric flux are allocated at the edges of the dual grid and the dual grid facets, for example, the magnetic voltage along the edge \widetilde{L}_u is given by

$$\widehat{\mathbf{h}}_u(i, j, k) = \int_{\widetilde{L}_u(i, j, k)} \vec{H} \cdot d\vec{s}, \quad (3.8)$$

and electric flux through the facet \widetilde{A}_w can be defined as

$$\widehat{\mathbf{d}}_w(i, j, k) = \int_{\widetilde{A}_w(i, j, k)} \vec{D} \cdot d\vec{A}. \quad (3.9)$$

With this, an exact representation of Maxwell's equations on the grid cell complex pair $\{G, \tilde{G}\}$, the so called Maxwell-Grid-Equations (MGE), are derived:

$$\mathbf{C}\hat{\mathbf{e}} = -\frac{d}{dt}\hat{\mathbf{b}}; \quad (3.10)$$

$$\tilde{\mathbf{C}}\hat{\mathbf{h}} = \frac{d}{dt}\hat{\mathbf{d}} + \hat{\mathbf{j}}; \quad (3.11)$$

$$\mathbf{S}\hat{\mathbf{b}} = 0; \quad (3.12)$$

$$\tilde{\mathbf{S}}\hat{\mathbf{d}} = \mathbf{q}. \quad (3.13)$$

Here, $\tilde{\mathbf{C}}$ and $\tilde{\mathbf{S}}$ are the dual discrete curl operator and the dual discrete divergence operator, respectively. The additional electromagnetic quantities are the vector of the integrated current densities $\hat{\mathbf{j}}$ through a dual grid facet, and the vector of charges \mathbf{q} inside a dual grid cell. Similar to the continuous case (2.5), the current is composed of three contributions here, the imposed current, the current due to the finite conductivity and the current due to moving charges.

A gradient operator can be introduced on the primal grid by $\mathbf{G} = -\tilde{\mathbf{S}}^T$ as well as on the dual grid by $\tilde{\mathbf{G}} = -\mathbf{S}^T$ [60]. Another important property relates the primary grid curl operator \mathbf{C} and the dual grid curl operator $\tilde{\mathbf{C}}$ by [54]:

$$\mathbf{C} = \tilde{\mathbf{C}}^T. \quad (3.14)$$

The vector analytical identities $\nabla \cdot \nabla \times \vec{A} \equiv 0$ and $\nabla \times \nabla \Phi \equiv 0$ hold in the grid cell complex pair $\{G, \tilde{G}\}$. As it was proved in [53] [54] and [55], from the algebraic properties of the topological matrices,

$$\begin{aligned} \mathbf{S}\mathbf{C} = 0 & \quad ; \quad \tilde{\mathbf{S}}\tilde{\mathbf{C}} = 0; \quad \text{and} \\ \mathbf{C}\tilde{\mathbf{S}}^T = 0 & \quad ; \quad \tilde{\mathbf{C}}\mathbf{S}^T = 0, \quad \text{holds.} \end{aligned} \quad (3.15)$$

3.1.2 Discrete Material Properties

Up to now, no approximations have been introduced at all. These, however, will be necessary to transfer the material equations from the continuous space to the grid space. The discrete formulation of the constitutive equations is derived from the edge voltages and facet fluxes on the prime and dual grid cell complex pair $\{G, \tilde{G}\}$. Approximations for the integration are carried out here in order to transfer material equations from continuous space to discrete grid. Substantial research deals with enhanced approaches for the discretization of the material relation, such as triangular filling [61], sub-grid [62], [59], partially filled cells (PFC) [63] and non-orthogonal FIT [64], which were introduced to improve the numerical accuracy during the material approximation process.

Construction of the material matrices

The discrete permittivity matrices or conductivity matrices can be derived from the integration approximation of the ratio of the electric flux density \vec{D} and the electric field

strength \vec{E} , or the ratio of the current source \vec{J} and the electric field strength \vec{E} on the doublet grid $\{G, \tilde{G}\}$:

$$\begin{aligned} \frac{\int \int_{\tilde{A}_j} \vec{D} \cdot d\vec{A}}{\int_{L_j} \vec{E} \cdot d\vec{s}} &= \frac{\int \int_{\tilde{A}_j} \epsilon |\vec{E}_{m,j}| d\vec{A} + \mathcal{O}(h^{k+2})}{\int_{L_j} |\vec{E}_{m,j}| d\vec{s} + \mathcal{O}(h^{k+1})} = \frac{\bar{\epsilon} \int \int_{\tilde{A}_j} d\vec{A}}{\int_{L_j} d\vec{s}} + \mathcal{O}(h^{k+1}) \\ &\approx \frac{\bar{\epsilon} |\tilde{A}_j|}{|L_j|} =: [M_\epsilon]_{j,j} = \frac{\hat{\mathbf{d}}_j}{\mathbf{e}_j}, \end{aligned} \quad (3.16)$$

$$\begin{aligned} \frac{\int \int_{\tilde{A}_j} \vec{J} \cdot d\vec{A}}{\int_{L_j} \vec{E} \cdot d\vec{s}} &= \frac{\int \int_{\tilde{A}_j} \kappa |\vec{E}_{m,j}| d\vec{A} + \mathcal{O}(h^{k+2})}{\int_{L_j} |\vec{E}_{m,j}| d\vec{s} + \mathcal{O}(h^{k+1})} = \frac{\bar{\kappa} \int \int_{\tilde{A}_j} d\vec{A}}{\int_{L_j} d\vec{s}} + \mathcal{O}(h^{k+1}) \\ &\approx \frac{\bar{\kappa} |\tilde{A}_j|}{|L_j|} =: [M_\kappa]_{j,j} = \frac{\hat{\mathbf{j}}_j}{\mathbf{e}_j}. \end{aligned} \quad (3.17)$$

The $\bar{\epsilon}$ is the average of permittivity, the $\bar{\kappa}$ is the average of conductivity, the quantity h is defined as the maximum length of grid edges of the primary grid G , i.e. $h := \max_{L_k \in G} \left\{ \int_{L_k} d\vec{s} \right\}$.

The \tilde{A}_j is the facet at the dual grid and L_j is the edge at the primary grid (Fig. 3.4 (A)). The $|\vec{E}_{m,j}|$ is the average value of the electric field strength \vec{E} along the grid edge

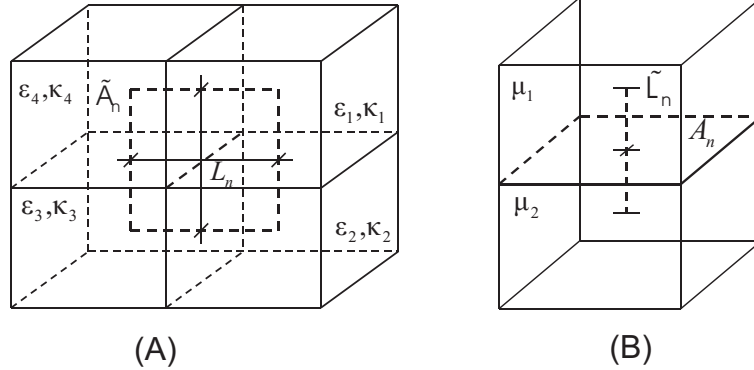


Figure 3.4: *Material averaging for the construction of the material matrices. (A) Averaging over a dual facet \tilde{A}_n for the derivation of \mathbf{M}_ϵ and \mathbf{M}_κ , (B) averaging over a dual edge \tilde{L}_n for the derivation of the inverse permeability matrix \mathbf{M}_μ^{-1} .*

L_j . \mathbf{M}_ϵ and \mathbf{M}_κ are material matrices including the information of the permittivity and conductivity. For isotropic materials, \mathbf{M}_ϵ and \mathbf{M}_κ are diagonal matrices. The parameter k is the convergence order of the error of the approximation of the integration. For staircase discretization the convergence order k is between 1 and 2 [65]. In case of an equidistant grid and a homogeneous material distribution, the convergence order k attains 2, which results in an error of order $\mathcal{O}(h^3)$ for the grid voltages and $\mathcal{O}(h^4)$ for the grid fluxes.

Similarly, the discrete permeability matrices can be derived from the approximation of the integration through the ratio of the magnetic field strength \vec{H} and the magnetic flux

density \vec{B} . The component of the inverse permeability matrix along the edge length \tilde{L}_j on the dual grid (fig. 3.4 (B)) is given with the integration approximation

$$\begin{aligned} \frac{\int_{\tilde{L}_j} \vec{H} \cdot d\vec{s}}{\int \int_{A_j} \vec{B} \cdot d\vec{A}} &= \frac{\int_{\tilde{L}_j} |\vec{H}_{m,j}| d\vec{S} + \mathcal{O}(h^{k+1})}{\int \int_{A_j} \mu |\vec{H}_{m,j}| d\vec{A} + \mathcal{O}(h^{k+2})} = \frac{\int_{\tilde{L}_j} d\vec{s}}{\bar{\mu} \int_{A_j} d\vec{A}} + \mathcal{O}(h^{k+2}) \\ &\approx \frac{\bar{\mu}^{-1} |\tilde{L}_j|}{|A_j|} =: [M_{\mu^{-1}}]_{j,j} = \frac{\widehat{\mathbf{h}}_j}{\widehat{\mathbf{b}}_j}. \end{aligned} \quad (3.18)$$

where the value $\vec{H}_{m,j}$ is the average of the magnetic field strength along the dual edge \tilde{L}_j .

Using the above formula (3.16), (3.17) and (3.18), the material parameters are averaged over the dual grid facets for the permittivity and the conductivity, and over the dual edges for the permeability. The material averaging for the permittivity and the conductivity reads

$$\bar{\epsilon} = \frac{\epsilon_1 A_1 + \epsilon_2 A_2 + \epsilon_3 A_3 + \epsilon_4 A_4}{A_1 + A_2 + A_3 + A_4}, \quad (3.19)$$

$$\bar{\kappa} = \frac{\kappa_1 A_1 + \kappa_2 A_2 + \kappa_3 A_3 + \kappa_4 A_4}{A_1 + A_2 + A_3 + A_4}, \quad (3.20)$$

and for the permeability

$$\bar{\mu}^{-1} = \frac{\mu_1^{-1} L_1 + \mu_2^{-1} L_2}{L_1 + L_2}, \quad (3.21)$$

where the A_1, A_2, A_3, A_4 are the area of the four dual facet parts inside each primary cell, and the L_1, L_2 are the lengths of the two dual edge parts in each primary cell. The averaged material parameters at the crossing points of edges through facet in all directions (u, v, w) are collected into the matrices $\mathbf{D}_\epsilon, \mathbf{D}_\kappa$ and \mathbf{D}_μ , respectively. The material matrices are composed:

$$\mathbf{M}_\epsilon = \tilde{\mathbf{D}}_A \mathbf{D}_\epsilon \mathbf{D}_S^{-1}; \quad (3.22)$$

$$\mathbf{M}_\kappa = \tilde{\mathbf{D}}_A \mathbf{D}_\kappa \mathbf{D}_S^{-1}; \quad (3.23)$$

$$\mathbf{M}_\mu = \mathbf{D}_A \mathbf{D}_\mu \tilde{\mathbf{D}}_S^{-1}, \quad (3.24)$$

where the matrices $\mathbf{D}_A, \tilde{\mathbf{D}}_A$ are diagonal matrices with the cross-sections of the primary and dual facets, respectively. The $\mathbf{D}_S, \tilde{\mathbf{D}}_S$ are diagonal matrices with the lengths of the primary and dual edges, respectively.

At the grid cell complex pair $\{G, \tilde{G}\}$, the discrete constitutive equations including the material matrices are written as

$$\widehat{\mathbf{d}} = \mathbf{M}_\epsilon \widehat{\mathbf{e}}, \quad (3.25)$$

$$\widehat{\mathbf{j}} = \mathbf{M}_\kappa \widehat{\mathbf{e}} + \widehat{\mathbf{j}}_e, \quad (3.26)$$

$$\widehat{\mathbf{b}} = \mathbf{M}_\mu \widehat{\mathbf{h}}. \quad (3.27)$$

Improvement of the material approximation

In order to reduce the numerical inaccuracy which is introduced by the discretization of the constitutive equations, a more refined approach is necessary to improve the material modelling inside the grid, or to modify the computational grid in order to conform to the

material boundaries. A lot of different techniques have been introduced in previous FIT research for this problem. The most important of them are the introduction of trigonal prism fillings, sub-grids, partially filled cells (PFC) and the extension towards the non-orthogonal FIT.

Since the trigonal prism filling technique is used to improve material approximation in this thesis, it will be introduced first. The technique was developed within the classical FIT in the 70's [61]. Further research is reported for the isotropic and anisotropic cases in [66]. The simplest way is to divide the cell volume into two trigonal prisms with different materials for the isotropic case (Fig. 3.5). As a further development of this technique

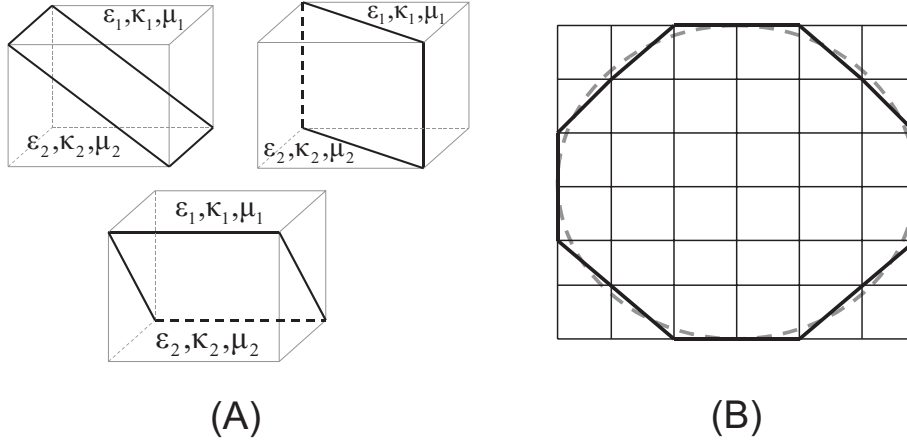


Figure 3.5: *Improved material approximation using trigonal prism filling. (A) Trigonal prism filling in 3D grid (B) Trigonal prism filling in 2D grid.*

especially for anisotropic materials, each grid cell can be split into 24 tetrahedra [63]. This approach, however, leads to a significant increase of the computational cost in the matrix generation process.

In contrast to a modified material modelling inside the grid, a better approximation of complicated material distributions can be achieved by the appropriate modification of the grid itself. For example, the sub-grid technique [62], [59] inserts sub-grids to refine the grid locally. Non-orthogonal grids [64] allow the description of complex structures using regular grids for the conformal discretization of curved shape boundaries. The Partially Filled Cells (PFC) technique is also very efficient, the considered integration region on the doublet grid is selected only over the exact portion of the grid edges and facets, which is outside perfectly electric conducting. All of these enhanced material modelling techniques results in an improvement in the numerical accuracy of the FIT method.

3.1.3 Boundary Conditions

Because the computational domain is commonly limited in space, boundary conditions are necessary at the boundaries of the model. The boundary conditions can be classified as electric boundary condition, magnetic boundary condition, mixed boundary condition, periodic boundary condition and open boundary condition. Open and mixed boundary

conditions are dissipative whereas electric and magnetic boundary condition are energy conserving. In this work, only the so-called electric and magnetic boundary conditions are discussed.

Electric boundary conditions force the tangential components of the electric field strength on the boundary to disappear, i.e. $\vec{E} \times \vec{n} = 0$, which corresponds to the assumption that the electric conductivity is infinite at the boundary. In case of magnetoquasistatics, the electric boundary conditions corresponds to the elimination of the normal component of the magnetic flux density at the boundary: $\vec{B} \cdot \vec{n} = 0$.

Magnetic boundary conditions force the tangential components of the magnetic field strength on the boundary to disappear, i.e. $\vec{H} \times \vec{n} = 0$, which corresponds to perfectly permeability material wall, i.e. $\mu \rightarrow \infty$.

3.2 Magnetoquasistatic Problems

3.2.1 Magnetostatic Problems

A magnetostatics formulation can be applied when all time derivatives in the Maxwell equations are negligible with respect to the other terms. Accordingly, the MGE are rewritten as:

$$\tilde{\mathbf{C}}\hat{\mathbf{h}} = \hat{\mathbf{j}}, \quad (3.28)$$

$$\mathbf{S}\hat{\mathbf{b}} = 0. \quad (3.29)$$

Magnetic vector potential formulation

Expression (3.29) can be satisfied by the choice of the magnetic vector potential $\hat{\mathbf{a}}$ [56], such that $\hat{\mathbf{b}} = \mathbf{C}\hat{\mathbf{a}}$. Inserting the material relation $\hat{\mathbf{h}} = \mathbf{M}_\nu \hat{\mathbf{b}}$ into (3.28) leads to the magnetostatic formulation

$$\tilde{\mathbf{C}}\mathbf{M}_\nu \mathbf{C}\hat{\mathbf{a}} = \hat{\mathbf{j}}. \quad (3.30)$$

In the three dimensional case, the formulation is based on a vector potential leading to $3N_p$ degrees of freedom, where N_p is the number of nodes of the primary and dual grid. Magnetostatic field problems can be also solved with a reduced scalar potential formulation in order to reduce the number of degrees of N_p .

3.2.2 Magnetoquasistatic Problems

For slowly-varying electromagnetic field problems the following inequality for the displacement currents commonly holds

$$\left\| \frac{d}{dt} \hat{\mathbf{d}}(t) \right\|_\infty \ll \|\mathbf{M}_\kappa \hat{\mathbf{e}}(t) + \hat{\mathbf{j}}_e(t)\|_\infty, \quad (3.31)$$

which allows to rewrite the continuous Maxwell equations into the discrete magnetoquasistatic Maxwell-Grid-Equations

$$\mathbf{C}\widehat{\mathbf{e}}(t) = -\frac{d}{dt}\widehat{\mathbf{b}}(t); \quad (3.32)$$

$$\widetilde{\mathbf{C}}\widehat{\mathbf{h}}(t) = \mathbf{M}_\kappa\widehat{\mathbf{e}}(t) + \widehat{\mathbf{j}}_e(t); \quad (3.33)$$

$$\mathbf{S}\widehat{\mathbf{b}}(t) = 0; \quad (3.34)$$

$$\widetilde{\mathbf{S}}\widehat{\mathbf{d}}(t) = 0. \quad (3.35)$$

If expression (3.33) is left multiplied by the divergence operator $\widetilde{\mathbf{S}}$, and because of the property of discrete topological operators $\widetilde{\mathbf{S}}\widetilde{\mathbf{C}} = 0$, the following relation holds at the discrete level:

$$\widetilde{\mathbf{S}}\mathbf{M}_\kappa\widehat{\mathbf{e}}(t) = -\widetilde{\mathbf{S}}\widehat{\mathbf{j}}_e(t). \quad (3.36)$$

Since the current excitation of the problem is commonly defined in model regions Ω_{cond} without conductivity [68], the left part of the equation (3.36) equates to zero

$$\widetilde{\mathbf{S}}\mathbf{M}_\kappa\widehat{\mathbf{e}}(t) = 0 \quad \text{in } \Omega_{\text{cond}}, \quad (3.37)$$

From (3.36) and (3.37), it can be concluded that the current excitation has to obey

$$\widetilde{\mathbf{S}}\widehat{\mathbf{j}}_e(t) = 0 \quad \text{in } \Omega_{\text{cond}}, \quad (3.38)$$

i.e. the current excitation must be divergence-free.

Such consistent current excitation vectors $\widehat{\mathbf{j}}_e(t)$ are typically obtained from the modelling of closed coils. Configurations where the coils touch the boundary require special care with the choice of the boundary condition and are therefore not closed, are not considered in this thesis.

The discrete Maxwell-Grid-Equations can be reduced to a first order differential equation for the magnetoquasistatic field problem

$$\widetilde{\mathbf{C}}\mathbf{M}_\nu\mathbf{C}\widehat{\mathbf{a}}(t) + \mathbf{M}_\kappa\frac{d}{dt}\widehat{\mathbf{a}}(t) = \widehat{\mathbf{j}}_e(t), \quad (3.39)$$

with the start solution at time t_0 ,

$$\widehat{\mathbf{a}}(t_0) = \widehat{\mathbf{a}}_0, \quad (3.40)$$

where the vector $\widehat{\mathbf{a}}(t)$ is the modified magnetic vector potential defined by $\widehat{\mathbf{e}}(t) = -\frac{d}{dt}\widehat{\mathbf{a}}(t)$ [68].

With the relation $\widehat{\mathbf{b}} = \mathbf{C}\widehat{\mathbf{a}}$, it is easy to directly obtain the magnetic flux density vectors $\widehat{\mathbf{b}}$ through the primary facets of grid G from the calculated magnetic vector potentials $\widehat{\mathbf{a}}$.

Expression (3.37) can be rewritten in terms of the magnetic vector potential

$$\widetilde{\mathbf{S}}\mathbf{M}_\kappa\frac{d}{dt}\widehat{\mathbf{a}} = 0. \quad (3.41)$$

It is an auxiliary equation in the numerical calculation using the modified magnetic vector potential formulation, and the information of the conductivity can be utilized here.

The conductivity matrix \mathbf{M}_κ is zero in the non-conductive region of the model. The diffusion term $\tilde{\mathbf{C}}\mathbf{M}_\nu\mathbf{C}\hat{\mathbf{a}}$ is zero for curl-free contributions of $\hat{\mathbf{a}}$. As a consequence, formulation (3.39) is singular as the irrotational components of $\hat{\mathbf{a}}$ are not determined in the non-conductive regions of the model. The singularity of the formulation can be alleviated by an appropriate regularization.

Another possibility is to add a locally defined gradient-divergence-term $\mathbf{M}\tilde{\mathbf{S}}^T\mathbf{M}_N\tilde{\mathbf{S}}\mathbf{M}$ to enforce the zero charge condition $\tilde{\mathbf{S}}\hat{\mathbf{a}}|_{\kappa=0} = 0$ in the non-conductive regions of the model

$$[\tilde{\mathbf{C}}\mathbf{M}_\nu\mathbf{C} + \mathbf{M}\tilde{\mathbf{S}}^T\mathbf{M}_N\tilde{\mathbf{S}}\mathbf{M}]\hat{\mathbf{a}}(t) + \mathbf{M}_\kappa\frac{d}{dt}\hat{\mathbf{a}}(t) = \hat{\mathbf{j}}_e(t), \quad (3.42)$$

where the matrix \mathbf{M}_N is defined by $\mathbf{M}_{N,i}|_{i:\kappa\neq 0} = 0$ and $\mathbf{M}_{N,i}|_{i:\kappa=0} \neq 0$ [69], respectively. Using the Coulomb gauging $\tilde{\mathbf{S}}\hat{\mathbf{a}} = 0$, it is easy to rewrite expression (3.42) in the same form as (3.39).

The idea was first introduced in 1983 [73] in the Finite Element Method (FEM) and further development was introduced in [68] in magnetoquasistatic formulations based on FIT.

3.2.3 Time Integration Schemes for Differential Algebraic Equations

The Courant-Friedrichs-Levy-criterium (CFL-Criterium) of the explicit Leapfrog FDTD scheme in [50] severely restricts the length of possible stable time steps and thus this scheme is not applicable to slowly-varying electromagnetic fields for typical applications including computational regions with metallic conductivity. The most flexible approach to overcome the problem of a maximum possible time step is to use implicit time integration schemes. Their usage is utilized in case of nonlinear material behavior occurring with ferromagnetic materials described within the discrete differential algebraic system of equation resulting from the FIT. A suitable choice of implicit time integration methods is required. The magnetic vector potential formulation (3.39) constitutes a degenerate and parabolical equation of first order

$$\mathbf{M}_\kappa\frac{d}{dt}\hat{\mathbf{a}}(t) + \tilde{\mathbf{C}}\mathbf{M}_\nu\mathbf{C}\hat{\mathbf{a}}(t) + \hat{\mathbf{j}}_e(t) = 0, \quad (3.43)$$

with a given start value

$$\hat{\mathbf{a}}_0 = \hat{\mathbf{a}}(t_0). \quad (3.44)$$

The conductivity matrix \mathbf{M}_κ in (3.43) is singular, since model configurations for typical magnetoquasistatic field problems contain non-conductive parts. Hence, (3.43) is not a regular ordinary differential equations (ODE), but a system of differential algebraic equations (DAE). Depending on the conductivity matrix \mathbf{M}_κ and the reluctivity matrix \mathbf{M}_ν , the differential algebraic equations can be classified as linear differential algebraic equation with constant coefficient matrix, quasi-linear differential algebraic equation with nonlinear magnetic reluctivities \mathbf{M}_ν for the ferromagnetic material, and nonlinear differential algebraic equation with nonlinear electric conductivities \mathbf{M}_κ .

First to consider the linear differential algebraic equation with a constant coefficient matrix, the numerical solution of (3.43) requires a time discretization. The vector at the new time step is written as $\hat{\mathbf{a}}_{n+1} = \hat{\mathbf{a}}(t_n + \Delta t)$. A simple scheme of linear one step θ -methods [74] is given as

$$\mathbf{M}_\kappa\frac{\hat{\mathbf{a}}_{n+1} - \hat{\mathbf{a}}_n}{\Delta t} + \tilde{\mathbf{C}}\mathbf{M}_\nu\mathbf{C}(\theta\hat{\mathbf{a}}_{n+1} + (1 - \theta)\hat{\mathbf{a}}_n) = \theta\hat{\mathbf{j}}_{e,n+1} + (1 - \theta)\hat{\mathbf{j}}_{e,n}. \quad (3.45)$$

The stability region for implicit θ -methods is cited in [68] as

$$R(z) = \frac{1 + (1 - \theta)z}{(1 - \theta)z}. \quad (3.46)$$

The methods are A-stable for the choice parameter $\theta \geq 0.5$ and L-stable for the choice parameter $\theta = 1$. A-stability is absolute stability. L-stability includes A-stability and moreover guarantees that phenomena with small time constants will be rapidly damped, even when large time steps are used [74] [76].

The class of θ -methods covers well-known methods as the implicit backward Euler method ($\theta = 1$), the Galerkin method ($\theta = 2/3$), the Crank-Nicolson method ($\theta = 1/2$), and the one-step singly diagonally implicit Runge-Kutta method (SDIRK1) ($\theta = 1/2$).

The second order Crank-Nicolson time integration scheme is unconditionally A-stable. The behavior of pure magnetoquasistatic systems is a simple damping even for nonlinear problems for which the Crank-Nicolson method is often stable and accurate enough. However, if the nonlinear magnetoquasistatic model is coupled to another model, for example, a mechanical model for moving parts or circuit equations for the feeding of conductors, it exhibits a much more complicated behavior. In this case, the Crank-Nicolson method becomes unstable.

The Galerkin time integration scheme is stable, but it only features first order convergence. This method provides less numerical dampening than the implicit Euler backward differentiation time integration scheme in one step (BDF1) method.

The implicit Euler backward differentiation time integration scheme (BDF) is L-stable. If the differential algebraic equation is solved in one time step, it is called BDF1, similarly, BDF2 is selected as two time steps. Because the L-stable implicit Euler backward differentiation formulation (BDF) has special stability properties, BDF is often selected as the implicit time integration scheme for transient magnetoquasistatic field simulations.

A detailed presentation of the backward differentiation formulation (BDF) can be found in [75], [76]. For the Cauchy problem, a general ordinary differential equation (ODE) of first order is given by

$$\begin{aligned} y'(t) &= f(t, y(t)), \\ y(t_0) &= y_0, \end{aligned} \quad (3.47)$$

where the function $f(t, y(t))$ only depends on $y(t)$.

The procedure of time integration for the implicit k-step BDF method with the constant time step Δt is written in terms of the discrete time approximation $y_{n+1-i}, i = 0, \dots, k$

$$\frac{1}{\Delta t} \sum_{i=0}^k \alpha_i y_{n+1-i} = f(t_{n+1}, y_{n+1}). \quad (3.48)$$

For each time step the equation is expressed as

$$y_{n+1} = \sum_{i=0}^k \alpha'_i y_{n+1-i} + \Delta t b_{-1} f(t_{n+1}, y_{n+1}), \quad (3.49)$$

with $b_{-1} \neq 0$. The coefficient values α'_i and b_{-1} of the BDF method vary with the number of k -steps, as derived in [77]. As an example, the coefficient values are presented for the 3-steps BDF method ($k \leq 3$):

k	α'_0	α'_1	α'_2	α'_3	b_{-1}
0	1	0	0	0	1
1	4/3	-1/3	0	0	2/3
2	18/11	-9/11	2/11	0	6/11
3	48/25	-36/25	16/25	-3/25	12/25

The BDF1 is the most robust time integration method of all of the mentioned methods, and requires only one system solution per time step. It, however, only attains first order convergence and is stiffly accurate [77]. From the expression (3.45), the equation for the new time step $\widehat{\mathbf{a}}_{n+1}$ is

$$\left[\frac{1}{\Delta t} \mathbf{M}_\kappa + \widetilde{\mathbf{C}} \mathbf{M}_\nu \mathbf{C} \right] \widehat{\mathbf{a}}_{n+1} = \frac{1}{\Delta t} \mathbf{M}_\kappa \widehat{\mathbf{a}}_n + \widehat{\mathbf{j}}_{e,n+1}. \quad (3.50)$$

The 2-steps BDF method (BDF2) applied to (3.45) can be written as

$$\left[\frac{3}{2\Delta t} \mathbf{M}_\kappa + \widetilde{\mathbf{C}} \mathbf{M}_\nu \mathbf{C} \right] \widehat{\mathbf{a}}_{n+1} = \frac{2}{\Delta t} \mathbf{M}_\kappa \widehat{\mathbf{a}}_n - \frac{1}{2\Delta t} \mathbf{M}_\kappa \widehat{\mathbf{a}}_{n-1} + \widehat{\mathbf{j}}_{e,n+1}. \quad (3.51)$$

The multi-step BDF2 scheme requires only one system solution per time step as well, but needs the solutions of the last two time steps. In order to obtain the start up value in the first time step performed, a one-stage singly diagonally implicit Runge-Kutta (SDIRK2) time integration scheme [78] is used here.

The singly diagonally implicit Runge-Kutta time integration scheme (SDIRK) is more stable. The SDIRK scheme can be divided into more stage SDIRK methods, such as the one-stage singly diagonally implicit Runge-Kutta, two-stage singly diagonally implicit Runge-Kutta. Similar to the BDF method, the general differential system $y'(t) = f(t, y(t))$ is considered here. An approximation of the solution y_{n+1} at time t_{n+1} from the values y_n of the solution at the previous time step can be obtained by computing the following expressions [76]:

$$k_i = \Delta t f \left(y_n + \sum_{j=1}^s a_{ij} k_j, t_n + c_i \Delta t \right), \quad i = 1, \dots, s, \quad (3.52)$$

$$y_{n+1} = y_n + \sum_{i=1}^s b_i k_i. \quad (3.53)$$

An s -step method is characterized by the coefficients a_{ij} , c_i and b_i with the relation $c_i = \sum_{j=1}^s a_{ij}$. The method is summarized by a Butcher-scheme:

$$\frac{c}{b^T} \Big| \begin{array}{c} A \\ \hline \end{array} = \begin{array}{c|cccc} c_1 & a_{11} & a_{12} & \dots & a_{1s} \\ c_2 & a_{21} & a_{22} & \dots & a_{2s} \\ \vdots & \vdots & \vdots & \ddots & \vdots \\ c_s & a_{s1} & a_{s2} & \dots & a_{ss} \\ \hline & b_1 & b_2 & \dots & b_s \end{array} \quad (3.54)$$

Runge-Kutta methods are cataloged according to their coefficient structure. The classical explicit methods are the methods for which $a_{ij} = 0$, if $j \geq i$. If this condition is not fulfilled ($a_{ij} \neq 0$ for $j \geq i$), the methods are called implicit Runge-Kutta methods (IRK). Special cases of IRK methods are the diagonally implicit Runge-Kutta (DIRK) methods ($a_{ij} = 0$ for $j > i$), a subcategory of which are the singly diagonally implicit Runge-Kutta (SDIRK) methods ($a_{ij} = 0$ for $j > i$ and $a_{ij} = a$ for all i).

Similar to the classical SDIRK method with s stages ($s \leq 2$) introduced in [74] for two-dimensional magnetoquasistatic finite element simulation with nonlinear materials in time domain, the SDIRK scheme can be used in FIT for the magnetoquasistatic numerical time integration as well. The following scheme can be applied:

$$\mathbf{M}_\kappa k_i = \Delta t \left[-\tilde{\mathbf{C}}\mathbf{M}_\nu \mathbf{C}(y_n + \Delta t \sum_{j=1}^s a_{ij} k_j)(y_n + \Delta t \sum_{j=1}^s a_{ij} k_j) - \widehat{\mathbf{j}}_e(t_n + c_i \Delta t) \right],$$

$$i = 1, \dots, s, \quad (3.55)$$

$$y_{n+1} := y_n + \sum_{i=1}^s b_i k_i. \quad (3.56)$$

The one-stage singly diagonally implicit Runge-Kutta method (SDIRK1) has following Butcher-scheme:

$$\frac{\alpha_{\text{rk}}}{1 - \alpha_{\text{rk}}} \left| \begin{array}{c} \alpha_{\text{rk}} \\ 1 \end{array} \right.$$

In the case of linear problems, this method reduces to (3.45) except for the independent term $\widehat{\mathbf{j}}_e(t)$ which is discretized as $\widehat{\mathbf{j}}_e(t + \alpha_{\text{rk}} \Delta t)$ instead of $(1 - \theta)\widehat{\mathbf{j}}_e(t_n) + \theta\widehat{\mathbf{j}}_e(t_{n+1})$. Therefore in the particular cases $\alpha_{\text{rk}} = 0$ and $\alpha_{\text{rk}} = 1$, SDIRK1 reduces to forward and backward Euler respectively. In the case $\alpha_{\text{rk}} = 0.5$, SDIRK1 is the trapezoidal rule time integrator, which slightly differs from the Crank-Nicolson scheme in the way the currents are evaluated. The parameter α_{rk} to be chosen between 0.5 and 1 allows to shift between the second order accurate scheme ($\alpha_{\text{rk}} = 0.5$) and first order accurate schemes with numerical damping ($\alpha_{\text{rk}} > 0.5$).

The two-stage singly diagonally implicit Runge-Kutta method has following Butcher-scheme:

$$\frac{\alpha_{\text{rk}}}{1 - \alpha_{\text{rk}}} \left| \begin{array}{cc} \alpha_{\text{rk}} & \alpha_{\text{rk}} \\ 1 - \alpha_{\text{rk}} & 1 - 2\alpha_{\text{rk}} \quad \alpha_{\text{rk}} \\ & 1/2 \quad 1/2 \end{array} \right.$$

This 2-stage scheme leads to more interesting methods than the previous 1-stage SDIRK method. The scheme is A-stable for $\alpha_{\text{rk}} \geq 1/4$ [79]. L-stable and second order accuracy are achieved in the SDIRK22 scheme by the choice $\alpha_{\text{rk}} = 1 - \sqrt{2}/2$ [80]. A-stable and third order convergence is provided by the SDIRK23 scheme for which $\alpha_{\text{rk}} = (3 - \sqrt{3})/6$.

Another 2-stage SDIRK was described by Alexander in [78], and is here adapted for the calculation of the transient magnetoquasistatic field problems with FIT. Its Butcher-scheme is given by

$$\begin{array}{c|cc} \alpha_{rk} & & \alpha_{rk} \\ 1 & 1 - \alpha_{rk} & \alpha_{rk} \\ \hline & 1 - \alpha_{rk} & \alpha_{rk} \end{array},$$

with $\alpha_{rk} = 1 - \sqrt{2}/2$. The scheme is L-stable and has a second order convergence of the time discretization error. The method is called SDIRK2, and it is used in order to obtain the start up value in the first time step needed for BDF2. These 2-stage SDIRK methods require two interior system solutions per time step.

Compared the s-stage SDIRK methods with the s-step BDF methods, the s-step BDF methods solve only one equation system per time step, but they have the problem to require suitable start-up values in the first time step. On the other hand, the s-stage SDIRK methods only need one previous solution, but require more interior system solutions per time step.

3.2.4 Numerical Solution of Linear Equation Systems

In the previous subsections, the electromagnetic field problems discretized by the FIT leads to a large sparse linear system of equations

$$Ax = b. \quad (3.57)$$

The system matrix A is defined as $A \in \mathcal{K}^{n \times n}$. The solution vector x is $x \in \mathcal{K}^n$. The right hand side vector b is $b \in \mathcal{K}^n$. The system matrix A varies from real, symmetric and positive definite to complex, non-hermitian and singular. For the model discretized by the FIT as discussed in this work, the matrices are sparse.

Although direct solution methods can be used to solve the linear systems of equations, they are not well suited for large sparse systems which are typical for magnetoquasistatic field problems discretized by the FIT. A LU decomposition would produce a substantial fill-in at places where the original matrix is empty. For this reason, iterative methods are required to solve the linear systems. The Krylov subspace methods [96] will be introduced in this subsection as iterative methods for the solution of linear systems in magnetoquasistatic field problems. The convergence behavior of the Krylov subspace methods strongly depends on the spectrum of the system matrix A . Therefore, appropriate precondition methods are also important to improve the spectrum and thus improve the convergence of the solutions for linear systems.

Precondition conjugate gradient method

In this thesis, the precondition conjugate gradient method, a Krylov subspace method, is applied for solving the linear system of equations. In the iterative solution of equation system (3.57) for $x = A^{-1}b$, the approximation of the solution at the k -th iteration reads

$$x_k = x_0 + V_k y_k, \quad V_k \in \mathcal{K}^{n \times k}, \quad y_k \in \mathcal{K}^k, \quad (3.58)$$

with the starting solution x_0 , and the Krylov subspace \mathcal{K}_k defined by

$$\mathcal{K}_k = \mathcal{K}_k(A, r_0) := \text{span}\{r_0, Ar_0, A^2r_0, \dots, A^{k-1}r_0\}. \quad (3.59)$$

Here, $r_0 = b - Ax_0$ is the residual corresponding to the initial solution x_0 . The columns of the matrix $V_k = [v_1 | \dots | v_k]$ form the basis of the Krylov subspace and can be created successively.

The discrete formulation based on the FIT to calculate the transient magnetoquasistatic field problems is a positive-semi-definite, real-valued, symmetric equation system. For the quasi-static field simulation, the curl-curl equation system belongs also to the above mentioned class of systems. The conjugate gradient method, a typical Krylov subspace method, is used to solve the linear systems for the magnetoquasistatic field problems in this thesis.

The Conjugate Gradient algorithm was published by Hestenes and Stiefel in 1952 [81]. The idea of the algorithm is to solve the linear system $Ax = b$ by searching for the minimum of the quadratic function

$$f(x) = \frac{1}{2}x^T Ax - x^T b. \quad (3.60)$$

By setting the derivative of f to 0, a stationary point of f occurs at x for which $Ax = b$. The minimum can be approached iteratively by starting at a point x_0 , moving to a point x_1 that yields a smaller value of the function, and continuing to move to points yielding smaller values of the function. The k -th point is $x_{k-1} + \alpha_k d_k$, where α_k is a scalar and d_k is a vector giving the direction of the increment. Hence, for the k -th point we have the linear combination,

$$x_k = x_0 + \alpha_1 d_1 + \dots + \alpha_k d_k, \quad (3.61)$$

the convergence criterion is based on $\|x_k - x_{k-1}\|$ or on $\|r_k\|$, where $r_k = b - Ax_k$.

At a point x_k , the function f decreases most rapidly in the direction of the negative gradient, $-\Delta f(x_k)$. The negative gradient coincides with the residual,

$$r_k = b - Ax_k, \quad (3.62)$$

if this residual is zero, the exact solution is obtained.

A good choice for the sequence of directions d_1, d_2, \dots is such that

$$d_k^T A d_i = 0, \quad \text{for } i = 1, \dots, k-1. \quad (3.63)$$

The vector d_k is said to be A conjugate to d_1, d_2, \dots, d_{k-1} . The algorithm is called "conjugate gradient" because two successive search directions are conjugate with respect to each other. The conjugate gradient method for solving the linear system is shown in Algorithm 1.

Algorithm 1: The precondition conjugate gradient (PCG) method for solving $Ax = b$, starting with x_0 :

- 1) Set $k = 0$; $r_k = b - Ax_k$; $M s_k = r_k$; $p_k = s_k$;
- 2) If $\gamma_k \leq \epsilon$, set $x = x_k$ and terminate.
- 3) Set $\alpha_k = \frac{\langle r_k, s_k \rangle}{\langle A g_k, g_k \rangle}$.
- 4) Set $x_{k+1} = x_k + \alpha_k p_k$.
- 5) Set $r_{k+1} = r_k - \alpha_k A p_k$.

6) Set s_{k+1} by solving $Ms_{k+1} = r_{k+1}$.

7) Set $\beta_k = \frac{\langle s_{k+1}, r_{k+1} \rangle}{\langle s_k, r_k \rangle}$.

8) Set $p_{k+1} = s_{k+1} + \beta_k p_k$.

9) Set $k = k + 1$ and goto 2).

The conjugate gradient method and related procedures iterate towards the exact solution. The conjugate gradient method, in conjunction with preconditioning, is used as the main iterative method to solve the real-valued, symmetrical, linear equation systems arising after implicit time discretization in this thesis.

Preconditioning

A suitable preconditioning is important to improve the performance of Krylov subspace methods in terms of computational time required for the solution. The purpose of preconditioning is to improve the eigenvalue distribution of the system matrix in the complex plane. One possibility of the preconditioning is the multiplication by a suitable polynomial in A . Another possibility is to apply a non-singular matrix M which represents a good approximation to the original matrix A and which can be easily inverted. The second possibility is used here. Multiplying A by the inverse of the preconditioning matrix, one obtains a better conditioned system if the spectrum of M approximates the one of A well enough. According to the relative order of both matrices, three different types of preconditioning are introduced:

1) Left-handed preconditioning, $M^{-1}Ax = M^{-1}b$, where the preconditioned system has the same solution as the original system. This type is usually preferred.

2) Right-handed preconditioning, $AM^{-1}(Mx) = b$, where the right hand side remains unchanged.

3) Split preconditioning, $M_1^{-1}AM_2^{-1}(M_2x) = M_1^{-1}b$, which, for suitable choices of M_1 and M_2 , keeps a given symmetry.

The transformed system $A'x' = b'$ is then solved by a Krylov subspace method.

SSOR (Symmetric Successive Over-Relaxation)-preconditioning improves the spectrum of the linear system and in many cases leads to a remarkable reduction of the required number of iterations. In this thesis SSOR-preconditioning is used. The SSOR-preconditioning approach decomposes the system matrix A into $A = D - L - U$, where the matrix D is the main diagonal matrix from A and matrices $-L$ and $-U$ are the triangular matrices to represent the lower left triangular matrix of A and the upper right triangular matrix of A , respectively. For the symmetric system matrices encountered in this work, the matrices U and L are related by $U = L^T$.

The preconditioning matrix is then given by

$$M := \left(\frac{1}{\omega_1}D - \frac{1}{\omega_2}L\right)\left(\frac{1}{\omega_1}D\right)^{-1}\left(\frac{1}{\omega_1}D - \frac{1}{\omega_2}U\right), \quad (3.64)$$

where $A = D - L - U$, D is the diagonal matrix and U holds the $U = L^T$ for a symmetric system matrix A . The advantage of this decomposition lies in the fact that it is not necessary to compute M explicitly neither to store it. For an acceleration of the method,

the parameters ω_1 and ω_2 have to be chosen appropriately. A typical choice is $\omega_1 = \omega_2 = 1$, since the sensitivity of the preconditioning process to these parameters is usually small. For this choice of the parameters, the method is called Symmetric Gauss-Seidel preconditioning (SGS). The SSOR or SGS method is often used as a split preconditioning. Then the forward SOR algorithm is applied from the left and the backward SOR algorithm from the right. For a nearly symmetric matrix, it is often possible to use the storage efficient SSOR preconditioning by merely applying it to the symmetric part of the system matrix.

Chapter 4

Modelling and Implementation of Hysteresis

In the present chapter, the hysteresis models discussed in chapter 3 are embedded in transient magnetoquasistatic formulation based on the finite integration technique. The Preisach model and the Jiles-Atherton model were already applied and studied in the numerical simulation of electromagnetic field problems in combination with the finite-element method (FEM). One dimensional problems in laminated structures are described in detail in e.g. [98], [99], [100], [101]. In the magnetic field analysis applied for the design of electromagnetic devices, the magnetic properties have been modelled by simplified Preisach models. The Preisach model was included in 2D finite element analysis, as published in e.g. [102], [103], [104], [105], [106], [107]. However, the material models are scalar models, even though for many applications the electromagnetic field analysis with ferromagnetic materials needs a 2D or even a 3D vector Preisach model. In [108] a 2D vector Preisach model using the Everett table is presented. In [109] finite element computations taking into account the material properties by the Mayergoyz vector Preisach model have been verified experimentally by comparing the numerical results with measurements on a transformer type device. Also the Jiles-Atherton model and its inverse model have been included in finite element analysis, see e.g. [110], [111]. In this work, the hysteresis models are used and studied in the numerical simulation of electromagnetic field problems in combination with the FIT.

The hysteretic ferromagnetic material behavior can be expressed in two different ways. One modelling approach is based on the relation $\vec{B} = \mu_0(\vec{H} + \vec{M})$, where the magnetization \vec{M} includes the information of the hysteretic material. The other modelling approach exploits the relation $\vec{B} = \mu\vec{H}$, where the permeability μ contains the information of the hysteretic material.

For the first modelling approach, combined with a discrete formulation on the basis of the FIT, the vector $\widehat{\mathbf{m}} = \{\widehat{\mathbf{m}}_i\} = \{\int_{\tilde{L}_i \in \tilde{G}} \vec{M} \cdot d\vec{s}\}$ along the dual grid edges corresponding to a magnetization \vec{M} , and the vector of magnetic facet fluxes $\widehat{\mathbf{p}} = \{\widehat{\mathbf{p}}_j\} = \{\int_{A_j \in \tilde{G}} \vec{P}_m \cdot d\vec{A}\}$ corresponding to a magnetic polarization \vec{P} with $\widehat{\mathbf{p}} = \mathbf{M}_{\mu_0} \widehat{\mathbf{m}}$ yields the relation

$$\widehat{\mathbf{b}} = \mathbf{M}_{\mu_0} \widehat{\mathbf{h}} + \widehat{\mathbf{p}}, \quad (4.1)$$

which is the discrete form of the magnetic polarization. The vector $\widehat{\mathbf{p}}$ depends on the ferromagnetic material behavior as given by the $M(H)$ curve.

For the second modelling approach, a constitutive material relation between the vectors $\widehat{\mathbf{h}}$ related to the magnetic field strength and the vectors $\widehat{\mathbf{b}}$ related to the magnetic flux density is used. The modelling approach can be expressed for fields discretized by FIT by

$$\widehat{\mathbf{h}} = \mathbf{M}_\nu(\widehat{\mathbf{b}})\widehat{\mathbf{b}}, \quad (4.2)$$

where the reluctivity matrix \mathbf{M}_ν depends on the $H(B)$ curve of ferromagnetic materials.

According to the two different modelling approaches mentioned above, the hysteretic numerical algorithms are classified as *magnetic polarization update scheme* and *magnetic reluctivity nonlinear update scheme*. The different hysteresis models are embedded in the hysteretic numerical algorithms. The overview of the different numerical algorithms combined with the hysteresis models is shown in Table (4.1).

Table 4.1: Overview of the numerical algorithms combined with the hysteresis models

	scalar hysteresis model	vector hysteresis model
magnetic polarization update scheme	- classical Preisach model + (4.1) + FIT	
magnetic reluctivity nonlinear update scheme	- inverse Preisach model + (4.2) + FIT - inverse Jiles-Atherton model + (4.2) + FIT	- simplified vector Preisach model + (4.2) + FIT

4.1 Magnetic Polarization Update Scheme

4.1.1 Implementation of the Scalar Preisach Model

The Preisach model can be implemented by using the formulas (2.44) and (2.45) related to experimentally measured first-order transition curves. Although the approach is straightforward, there are two main problems to combine these formulae into a numerical computation scheme in time domain with FIT. First, it is required to define the average input and output values of the Preisach model in each cell along a certain direction in order to reduce the numerical inaccuracy. Secondly, an interpolation is required to determine the output value of the Preisach model from the limited first-order transition measured curves, the material memory and the input value.

Determination of the field strength in a grid cell

The average field strength \overline{H} is selected as input value of the Preisach model used in the magnetic polarization update scheme. As was introduced in the basic theory of FIT, each magnetic field strength is allocated at the dual grid edge, which causes the field strength in a cell being dependent on different components. The field strength within a grid cell is calculated from its components in the three coordinate directions as follows:

$$\overline{H} = \sqrt{\overline{H}_x^2 + \overline{H}_y^2 + \overline{H}_z^2}. \quad (4.3)$$

In order to improve the numerical accuracy of the material equations provide by the discrete material matrices, the calculation of the components of field strength are dependent on the geometry of the grid cell, and is for example different for a full cubic grid cell and a trigonal prism grid cell. For hysteretic materials the calculation of the different components of the field strength is presented in Fig. 4.1.

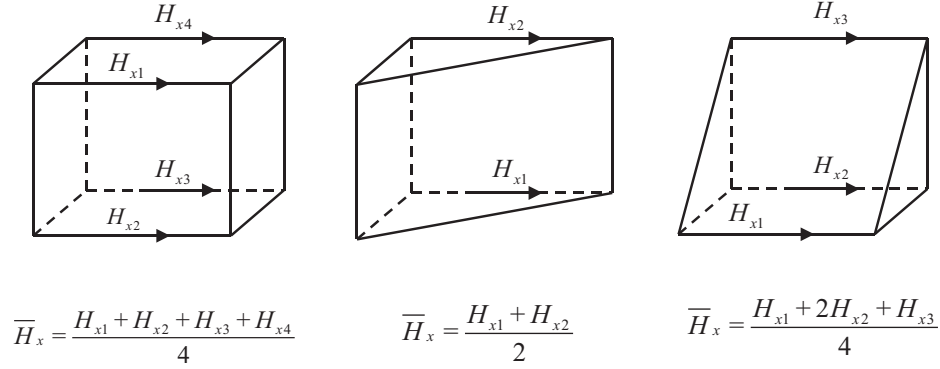


Figure 4.1: Components which are used for the calculation of the averaged field strength in one coordinate direction (here: x -direction).

Interpolation between the measured curves

After the determination of the average field strength \bar{H} in all cells, the flux densities are determined, from which the output values of the Preisach model must be calculated using the first-order transition measured curves according to the numerical implementation formula (2.44) for the monotonically decreasing input and (2.45) for the monotonically increasing input. Each measured first-order transition curve is generally defined by a number of $B - H$ value pairs. The measured $B - H$ values are limited by the interval of input values H . A difference with the common nonlinear case is that the hysteretic material response does not only depend on the local measured curve but also on some turning points in the hysteresis history. The turning point is the point where the hysteretic curve changes from a monotonically decreasing curve into a monotonically increasing curve or from a monotonically increasing curve into a monotonically decreasing curve. It represents the maximum or minimum value of the field strength at each monotonically decreasing or increasing curve. The special characteristics of hysteresis require a series of measured first-order transition curves with different turning points. In principle the more experimentally measured first-order transition curves are selected, the more accurate results will be obtained from the Preisach model. This, however, requires a huge $B - H$ table to store the given information of the measured curves. Considering the computational accuracy and the memory requirement for the $B - H$ table, a suitable number is selected to range between four and six measured curves. If the input value or the input turning point is between two measured discrete points, interpolation is required.

We can construct a Lagrange polynomial interpolation with the form

$$P(x) \equiv \sum y_i L_i(x), \quad (4.4)$$

where the L_i are themselves polynomials with coefficients which depend only upon the x_i . These polynomials are

$$L_i(x) = \prod_{j \neq i} [(x - x_j)/(x_i - x_j)]. \quad (4.5)$$

An alternative to the computation of the Lagrange polynomials $L_i(x)$ is the use of divided differences in the construction of Newton's interpolation formula. The polynomial

$$P(x) = a_0 + (x - x_0)a_1 + (x - x_0)(x - x_1)a_2 + \dots + (x - x_0)(x - x_1)\dots(x - x_{n-1})a_n, \quad (4.6)$$

is of degree n and the values $f(x_i)$ at x_i are given by

$$\begin{aligned} f(x_0) &= a_0, \\ f(x_1) &= a_0 + (x_1 - x_0)a_1, \\ f(x_2) &= a_0 + (x_2 - x_0)a_1 + (x_2 - x_0)(x_2 - x_1)a_2, \dots \end{aligned} \quad (4.7)$$

The coefficients a_i can be determined recursively from these relations. If the two-point polynomial interpolation is selected, the polynomial (4.6) becomes

$$P(x) = f(x_0) + \frac{f(x_1) - f(x_0)}{x_1 - x_0}(x - x_0). \quad (4.8)$$

From formula (4.8), the same two-point polynomial interpolation can be rewritten as

$$P(x) = \frac{x - x_0}{x_1 - x_0}f(x_1) + \frac{x_1 - x}{x_1 - x_0}f(x_0). \quad (4.9)$$

The two expressions (4.8) and (4.9) are used for interpolation in the hysteresis case.

The interpolated results depend on some turning points and the applied field. It is interpolated between two measured first-order transition curves. The numerical implementation is different in case of monotonically decreasing input (2.44) and in case of monotonically increasing input (2.45), the two formulae are constructed by a series of interpolated results. The output value of the Preisach model is obtained from the series of interpolated results according to the formula (2.44) or (2.45). More detail are given in the following.

Case I: In case of decreasing input field strength H , take a simple example with only one turning point α in the hysteresis history. The field strength H is between two measured values H_i and H_{i+1} , and the turning point α is between the two experimentally determined turning points α_j and α_{j+1} . Each interpolated result does not only depend on the applied field but also on the turning points. For this reason, it requires a two-step interpolation. The two-step interpolation process to obtain value $B(H)$ is described in Fig. 4.2. In the first step the value $B_j(H)$ is interpolated using expression (4.8) from the measured values $B_j(H_i)$, $B_j(H_{i+1})$, and the value $B_{j+1}(H)$ is interpolated using expression (4.8) from the measured values $B_{j+1}(H_i)$, and $B_{j+1}(H_{i+1})$. In the second step the value $B(H)$ is interpolated using formula (4.9) from the calculated values $B_j(H)$ and $B_{j+1}(H)$.

In case of decreasing input field strength H , (2.44) is used as the formula of the numerical implementation, the output value of the Preisach model $B(t)$ is given as

$$B(t) = -f^+ + f_{\alpha, H(t)} - f_{\alpha, \beta_0}, \quad (4.10)$$

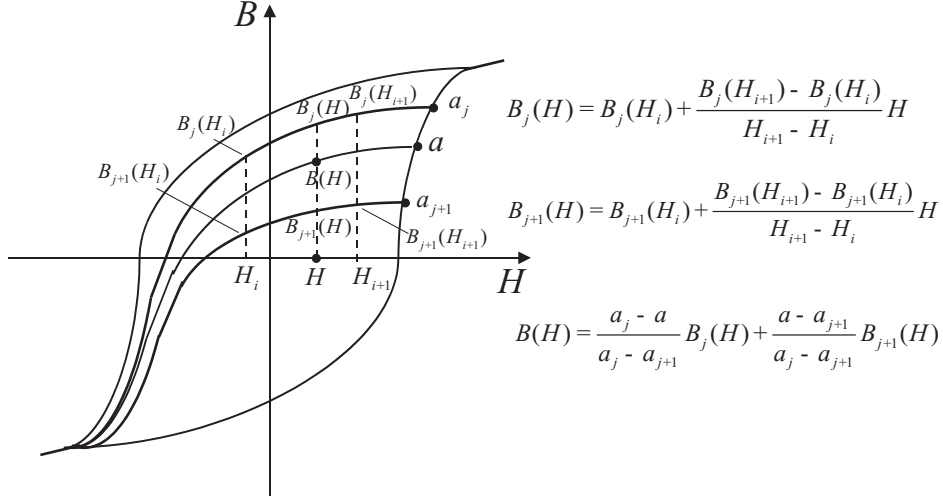


Figure 4.2: The two-step interpolation of the experimentally measured first-order transition curves for the Preisach model.

where $B(H)$ is inserted for $f_{\alpha,H(t)}$, and $f_{\alpha,\beta_0} = f^-$, therefore $f^+ + f_{\alpha,\beta_0} = f^+ + f^- = 0$. Expression (4.10) becomes

$$B(t) = B(H). \quad (4.11)$$

Case II: In case of increasing input field strength H , take a simple example with a pair of turning points (α, β) , where β is obtained at a point following α in the hysteresis history, assuming $\alpha > 0$ and $\beta < 0$. From (2.29) and the symmetry property of the Preisach model, we have the mathematical term $f_{\beta,H(t)} = -f_{-\beta,-H(t)}$. As a consequence, all the mathematical term $f_{\beta,\gamma}$ with negative turning point β can be transformed into the mathematical term $-f_{-\beta,-\gamma}$ with positive turning point $-\beta$. The field strength H is between two measured values H_i and H_{i+1} , and the absolute value of the turning point $|\beta|$ is between the two experimentally determined turning points α_j and α_{j+1} . Each interpolated result requires a two-step interpolation, too. The same two-step interpolation process as in case I is used.

For case of increasing field strength H input, formula (2.45) is used as the formula of the numerical implementation, the output value of the Preisach model $B(t)$ is given as

$$B(t) = -f^+ + f_{\alpha,\beta} - f_{\alpha,\beta_0} + f_{-\beta} - f_{\beta,-H(t)}, \quad (4.12)$$

where $f_{\alpha,\beta_0} = f^-$, therefore $f^+ + f_{\alpha,\beta_0} = f^+ + f^- = 0$.

The value $f_{\alpha,\beta}$ depends on the turning point α and the applied field β . It is interpolated by the same two-step interpolation process as in case I.

The value $f_{-\beta}$ depends on the turning point $-\beta$ and the applied field $-\beta$, it's two-step interpolation process is same as in case I.

The quantity $f_{\beta,-H(t)}$ is equal to $-f_{-\beta,H(t)}$ according to the symmetry property of the Preisach model. If the turning point is given at $-\beta$ and the applied field is taken as $H(t)$, the value $f_{-\beta,H(t)}$ is interpolated by the same process as in case I.

If there are more than two turning points in the hysteresis history, the two-step interpolation process is always used as basic process in the both cases. The output value of the Preisach model is obtained from the series of interpolated results according to the formulae (2.44) and (2.45), respectively.

4.1.2 Hysteresis Losses

In general, the hysteresis loss density in each cell of the doublet grid $\{G, \tilde{G}\}$ is computed from

$$w = \int H \cdot dB, \quad (4.13)$$

where for the 2D case, $H = \sqrt{H_x^2 + H_y^2}$ and $B = \sqrt{B_x^2 + B_y^2}$, and for the 3D case, $H = \sqrt{H_x^2 + H_y^2 + H_z^2}$ and $B = \sqrt{B_x^2 + B_y^2 + B_z^2}$.

The H_x , H_y and H_z are the average field strengths along the x , y , and z coordinate direction. The flux density B_x , B_y and B_z correspond to these average field strengths along the x , y , and z direction, respectively. The flux densities in x , y , and z direction are calculated by the Preisach model using the interpolation between the measured first-order transition curves.

A formula which relates the hysteretic losses occurring for arbitrary input variations to the losses occurring for certain periodic input variations was introduced in subsection (2.3.4). If the hysteresis loop is a closed loop, the hysteretic loss density is expressed by (2.51). If the hysteresis loop is not a closed loop, the hysteretic loss density is calculated by (2.50). Assuming the input value of the Preisach model is a sinusoidal excitation, the calculation of the hysteretic loss density has to be considered for the case of increasing envelope input and for the case of decreasing envelope input.

Case I: For the case of decreasing envelope input, the excitation starts from the maximum value of the amplitude (Fig. 4.3). The hysteresis loops are assumed as close loops, the hysteresis loss density is computed with (2.51).

For the starting hysteretic curve, which begins from the negative maximum value and stops at the positive maximum value, we define the starting hysteretic curve as the no-turning-point case. The loss density is given as the shaded area A in Fig. 4.3 (A). Because the starting hysteretic curve is not a closed loop, a corresponding decreasing curve is added in order to obtain a closed loop.

If the hysteretic curve starts from the first turning point and stops at the second turning point, we define it as the one-turning-point case. The losses density is given as the sum of the shaded area B in Fig. 4.3 (B) and the shaded area A in Fig. 4.3 (A).

If the hysteretic curve starts from the second turning point and stops at the third turning point, we define it as the two-turning-point case. The loss density is given as the sum of the shaded area C in Fig. 4.3 (C), the shaded area B in Fig. 4.3 (B) and the shaded area A in Fig. 4.3 (A).

The calculation of the loss density in the case with more than two turning points is similar to the two-turning-point case. The hysteresis loss density is the sum of some areas in the

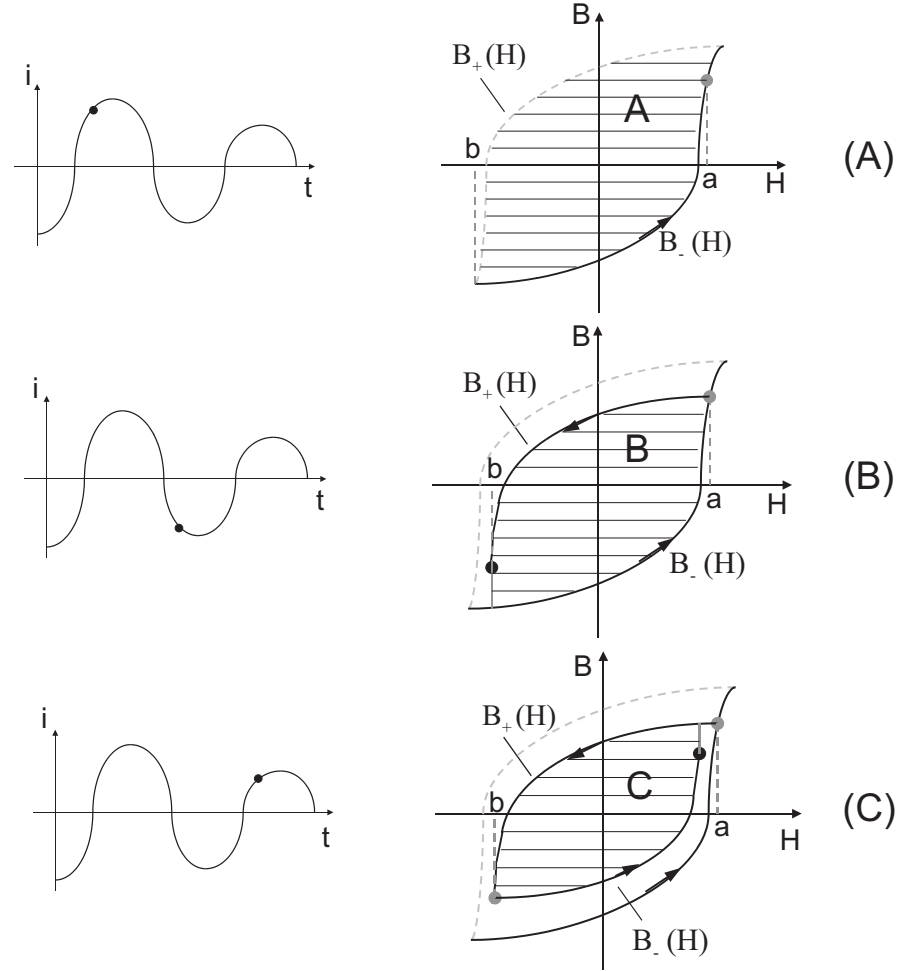


Figure 4.3: *Hysteresis loss density in case I, (A) in the no-turning-point case, (B) in the one-turning-point case, (C) in the two-turning-point case.*

$B - H$ diagram, which are drawn shaded in Fig. 4.3. A suitable integration technique is required to calculate the shaded areas in Fig. 4.3.

Case II: For the case of increasing envelope input, the excitation starts from zero (Fig. 4.4). The hysteresis loop is not a closed loop, the hysteresis loss density is calculated with (2.50) and (2.51).

If the hysteretic curve starts from zero and stops at the first turning point, we define the hysteretic curve as no-turning-point case. The loss density is given as the shaded area A in Fig. 4.4 (A). It is computed from (2.50).

The case with one turning point is the hysteretic curve from the first turning point to the second turning point. The loss density is the sum of the shaded area A in Fig. 4.4 (A), the shaded area B in Fig. 4.4 (B) and the shaded area C in Fig. 4.4 (B). The shaded area B is computed from (2.51) and the shaded area C is computed from (2.50).

We define the hysteretic curve from the second turning point to the third turning point

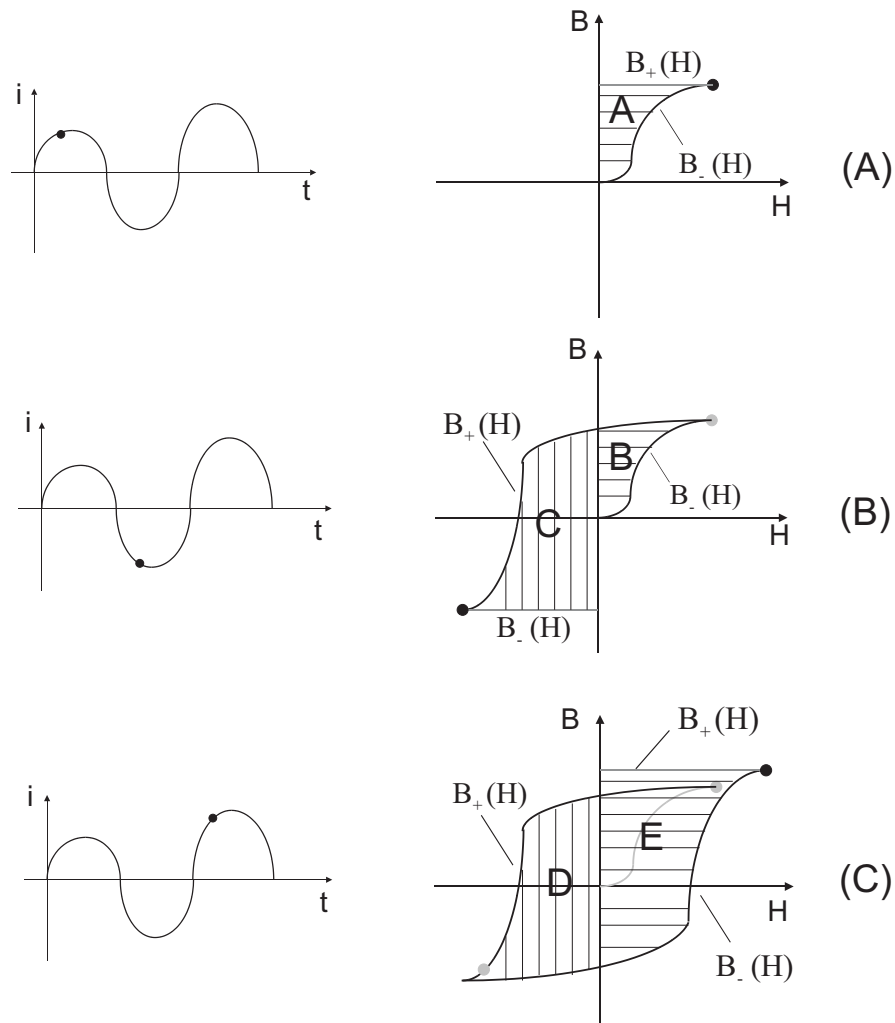


Figure 4.4: *Hysteresis loss density in case II, (A) in the no-turning-point case, (B) in the one-turning-point case, (C) in the two-turning-point case.*

as the two-turning-point case. The loss density in this case is the sum of the shaded area A in Fig. 4.4 (A), the shaded areas B and C in Fig. 4.4 (B) and the shaded areas D and E in Fig. 4.4 (C). The shaded area D is computed from (2.51) and the shaded area E is computed from (2.50).

The case with more than one turning point is similarly treated as the two turning point case. The loss density is the sum of some shaded areas. An integration technique is required to calculate these shaded areas.

The Romberg integration method is an application of the Richardson extrapolation method on the basis of multi-trapezoidal integration formulas. Compared to the trapezoidal integration method, it has a quadratic convergence. The Romberg integration method is selected to calculate the hysteresis loss density. The method is shown in Algorithm 2.

Algorithm 2: The Romberg integration method for solving the shaded areas shown in Fig. 4.3 and Fig. 4.4.

polarization update cycle. Because $\mu_0 H$ is very small, the $M(H)$ curve is approximated by the $B(H)$ curve in the numerical simulation.

The magnetic polarization update cycle for (4.15) at each time step is shown in the following flowchart (Fig. 4.5).

There are two different update cycles in the flowchart: the time step iteration and the magnetic polarization update cycle. Each time step iteration includes magnetic polarization updated cycles, and the magnetic polarization update cycles are repeated until the convergence limit of the polarization update cycle is reached.

The first step of the flowchart is the initialization at the first time step iteration. The current source is initialized by $\widehat{\mathbf{j}}_e^{(0)}$, and the magnetic polarization is given as zero.

In the second step of the flowchart, the vectors related to current, magnetic polarization and field strength are updated at the n th time step iteration. These vectors are taken as the initial values for the magnetic polarization update cycle.

In the third step of the flowchart, the magnetic polarization update cycle starts. The vector $\widehat{\mathbf{m}}_i^{(n)}$ is updated according to the last result in the $(i-1)$ -th magnetic polarization update cycle. If $i=1$, the vector $\widehat{\mathbf{m}}_i^{(n)}$ is provided by the initial values, which were defined in the second step of the flowchart.

The purpose of the fourth, fifth and sixth step of the flowchart is to obtain the vector $\widehat{\mathbf{h}}_i^{(n)}$. The three steps provide the applied field $\widehat{\mathbf{h}}_i^{(n)}$ as input value to the Preisach model. The fourth and fifth steps of the flowchart calculate the component of the magnetic vector potential $\widehat{\mathbf{a}}_{m,i}^{(n)}$ and $\widehat{\mathbf{a}}_{s,i}^{(n)}$ using formula (4.15), where the vector $\widehat{\mathbf{a}}_{s,i}^{(n)}$ only depends on the current source, the vector $\widehat{\mathbf{a}}_{m,i}^{(n)}$ only depends on the magnetic polarization source, and the total combined vector $\widehat{\mathbf{a}}_i^{(n)}$ is defined by $\widehat{\mathbf{a}}_i^{(n)} = \widehat{\mathbf{a}}_{s,i}^{(n)} + \widehat{\mathbf{a}}_{m,i}^{(n)}$. The vector $\widehat{\mathbf{h}}_i^{(n)}$ is obtained according to the component $\widehat{\mathbf{a}}_{s,i}^{(n)}$ in the sixth step of the flowchart.

In the seventh step of the flowchart, the vector $\widehat{\mathbf{m}}_{i+1}^{(n)}$ is obtained by the Preisach model according to the applied field $\widehat{\mathbf{h}}_i^{(n)}$, the turning points and the interpolation between the measured first-order transition curves.

The magnetic polarization update cycle is controlled by the convergence limit ε , it is defined as $\frac{\|\widehat{\mathbf{m}}_{i+1}^{(n)} - \widehat{\mathbf{m}}_i^{(n)}\|_2}{\|\widehat{\mathbf{m}}_{i+1}^{(n)}\|_2} \leq \varepsilon$. If the convergence limit is reached, the magnetic polarization update cycle is complete. The eighth step of the flowchart jumps to the tenth step of the flowchart. The new time step iteration starts. If the convergence limit is not reached, the magnetic polarization update cycle is repeated again.

For the rapid convergence, the vector $\widehat{\mathbf{m}}_{i+1}^{(n)}$ is modified in the ninth step of the flowchart

$$\widehat{\mathbf{m}}_{i+1}^{(n)} = \widehat{\mathbf{m}}_i^{(n)} + w(\widehat{\mathbf{m}}_{i+1}^{(n)} - \widehat{\mathbf{m}}_i^{(n)}), \quad (4.16)$$

where w is a relaxation factor which is put to $w = 0.5$.

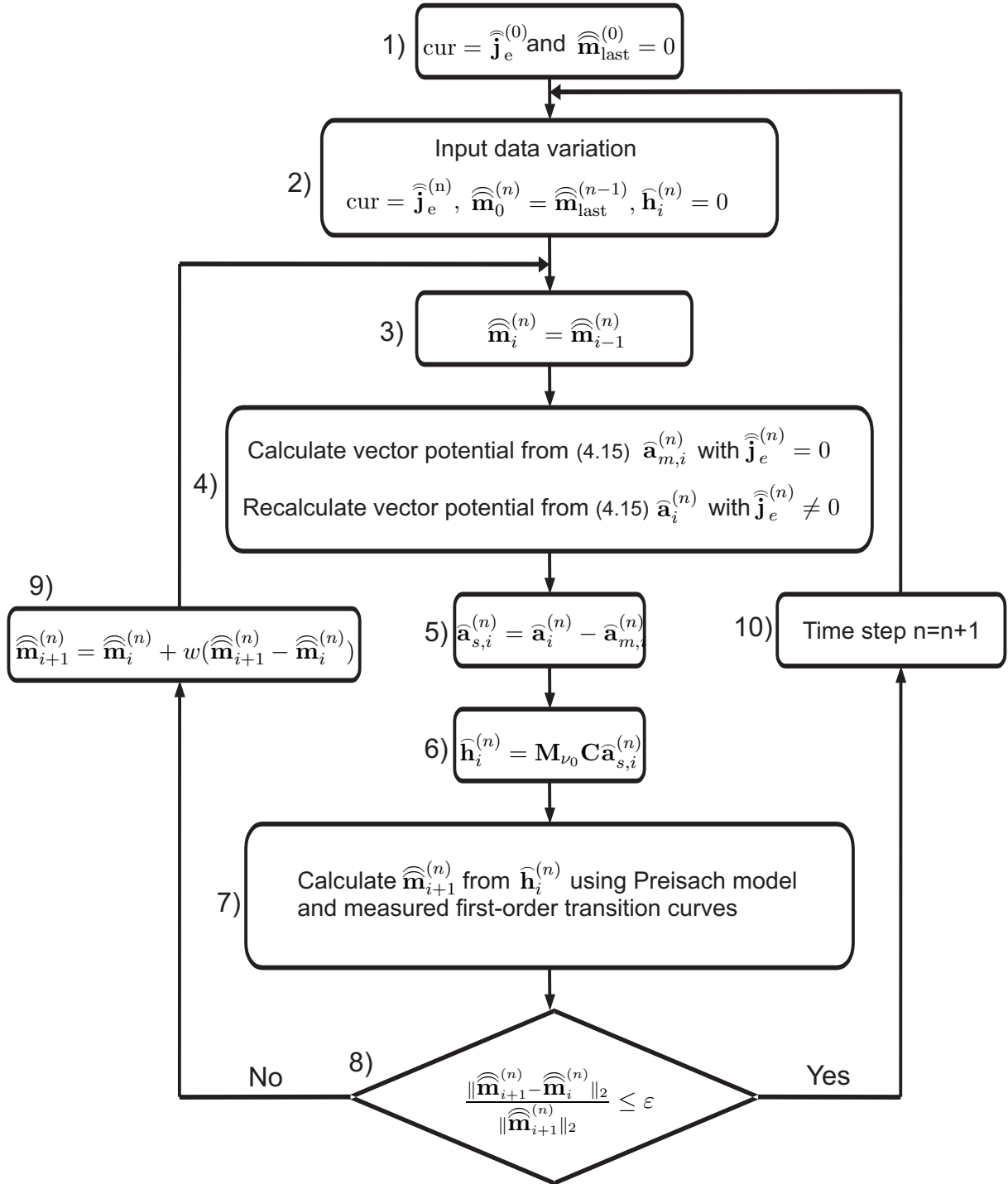


Figure 4.5: Flowchart of the magnetic polarization update cycle at each time step. (cur: current source)

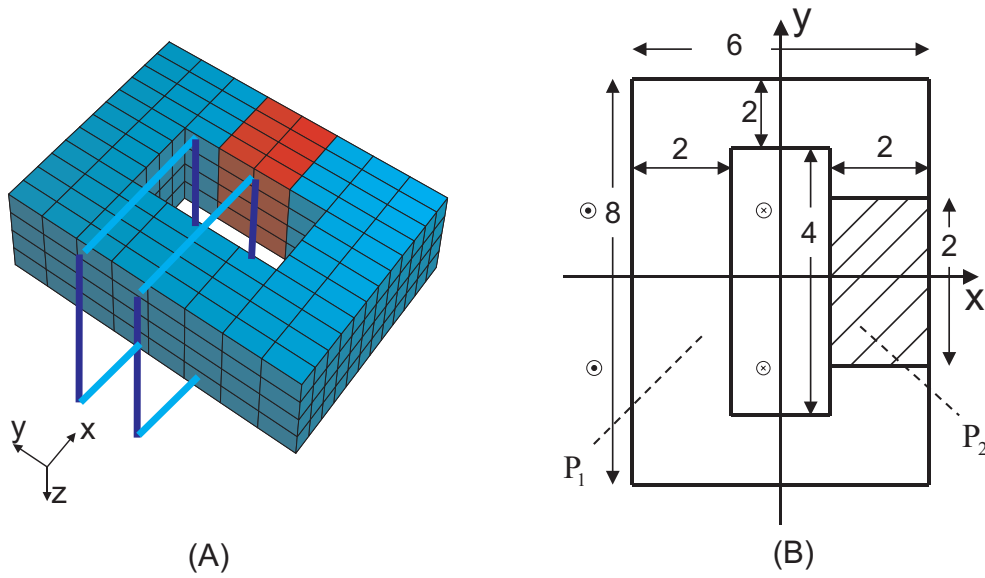


Figure 4.6: Test model: magnetic circuit with hysteretic material insert (dark) (A) 3 dimensional test model, (B) 2 dimensional cut face of the test model (dimension in m, $z = 2\text{m}$) with P1 point (non-hysteretic ferromagnetic material) and P2 point (hysteretic ferromagnetic material).

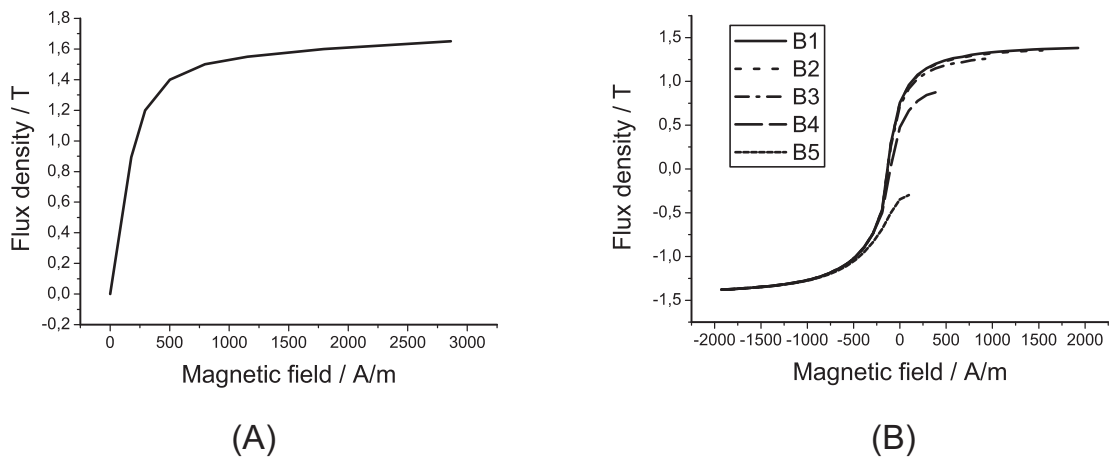


Figure 4.7: (A) Measured non-hysteretic ferromagnetic curve, (B) Measured first-order transition curves.

4.1.4 Test Example A and Discussion

A transient hysteretic test model (example A) is used for assessing the properties of the magnetic polarization update scheme with the scalar Preisach model: a C-shaped electromagnet consisting of a non-hysteretic ferromagnetic core (Appendix A: Table A.2 and Fig. 4.7 (A)) with a hysteretic ferromagnetic material insert is driven by the current in two rectangular coils. The driving current in the coil for the test problem is a sinusoid with an amplitude monotonically increasing from 0.1 kA to 5 kA. The 3D test model is shown in Fig. 4.6 (A). The 2D cut face of the test model is shown in Fig. 4.6 (B). The hysteretic magnetic characteristic is given by a set of measured first-order transition curves (Appendix A: Table A.3 and Fig. 4.7 (B)). The current excitation is shown in Fig. 4.8 (A). A set of measured symmetrical hysteresis loops of the hysteretic material is shown in Fig. 4.8 (B).

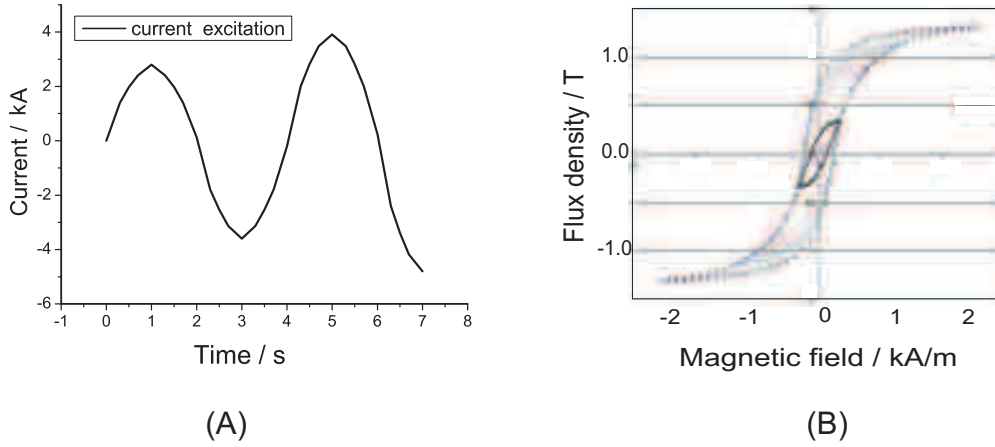


Figure 4.8: (A) Current excitation, (B) Set of measured symmetrical hysteresis loops.

The one-step backward differentiation implicit Euler scheme (BDF1) is selected to solve the hysteretic problem in time domain. The magnetic polarization update cycle is controlled by the tolerance error ε defined by $\frac{\|\widehat{\mathbf{m}}_{i+1}^{(n)} - \widehat{\mathbf{m}}_i^{(n)}\|_2}{\|\widehat{\mathbf{m}}_{i+1}^{(n)}\|_2}$ or the maximum number of magnetic polarization update cycle. The simulation is carried out for 70 time steps and 7 seconds of current excitation. In order to compare the simulated B-H curves for the hysteretic material with the simulated B-H curves for a representative anhysteretic material, a model with the same geometry and current excitation but with a non-hysteretic material is simulated. The B-H curves at points P_1 and P_2 on the 2D cut face at all for the 70 time steps are shown in Fig. 4.9. (A) and (B) are obtained for the non-hysteretic case, (C) and (D) for the hysteretic case. It is observed that the hysteresis phenomenon can significantly affect the behavior of the magnetic material. The simulated magnetic flux density at the 70th time step is shown in Fig. 4.10.

Hysteresis losses

The instantaneous hysteresis loss can be easily integrated at each time step by the Romberg integration method. The same model is taken as the above shown in Fig. 4.6. It is excited by a sinusoidal current with an decreasing amplitude (Fig. 4.11 (A)). The hysteretic curve

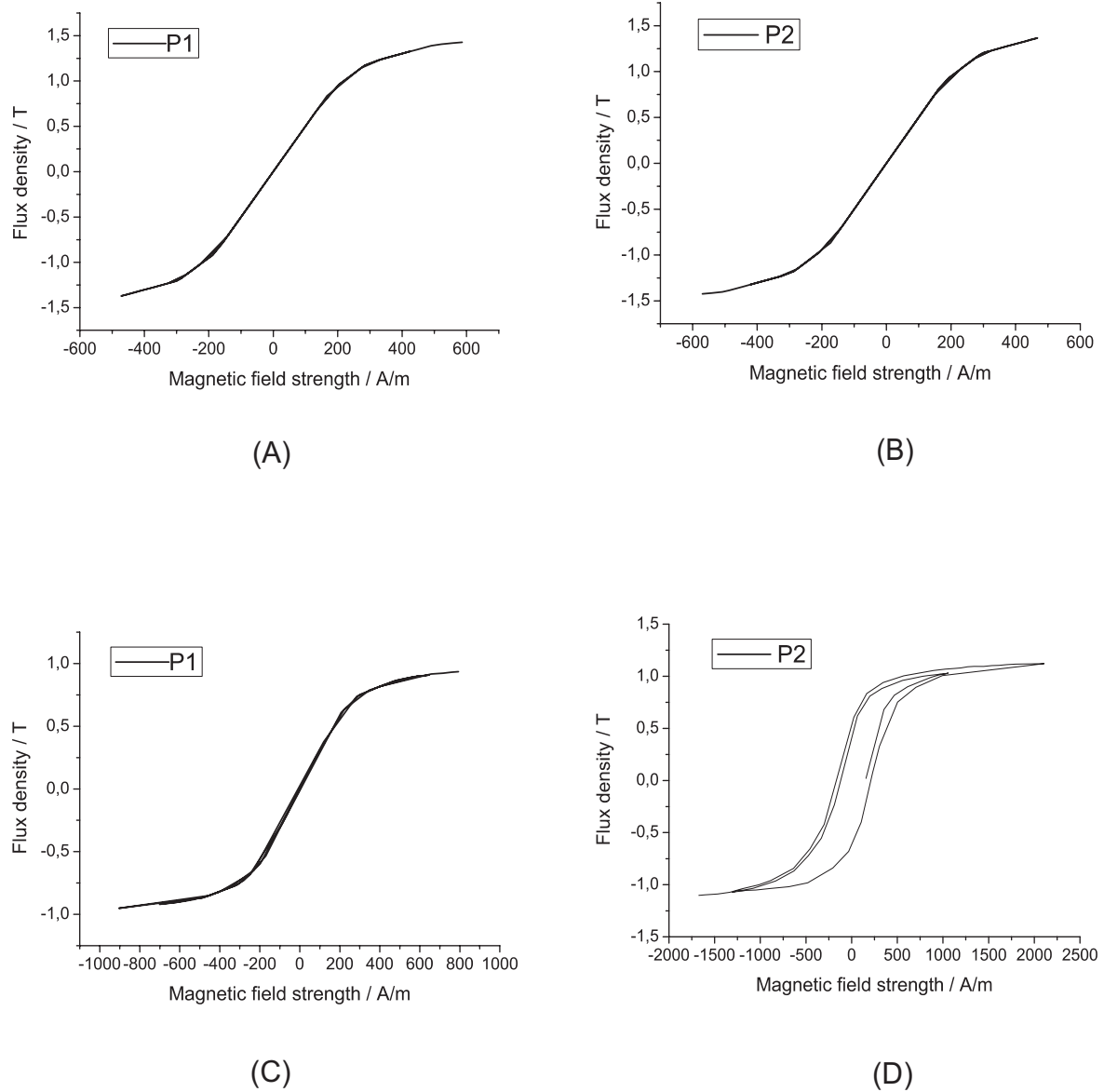


Figure 4.9: The comparison of simulated B-H curves with the same current excitation as in Fig. 4.8 (A). Simulated B-H curves with normal nonlinear material: (A) at point P_1 , (B) at point P_2 . Simulated B-H curves with hysteresis material: (C) at point P_1 , (D) at point P_2 .

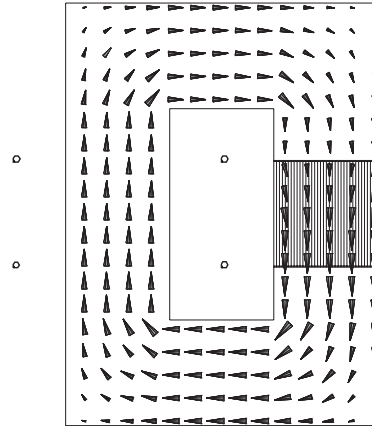


Figure 4.10: *Magnetic flux distribution on 2D cut face for the model with hysteretic material (dark).*

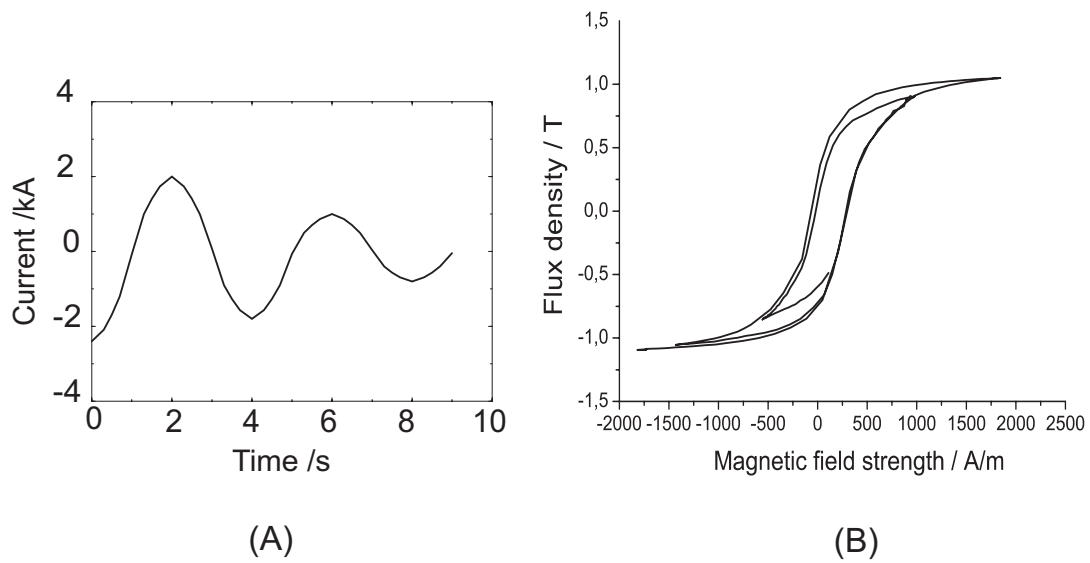


Figure 4.11: (A) *Current excitation*, (B) *Simulated B-H hysteresis loop*.

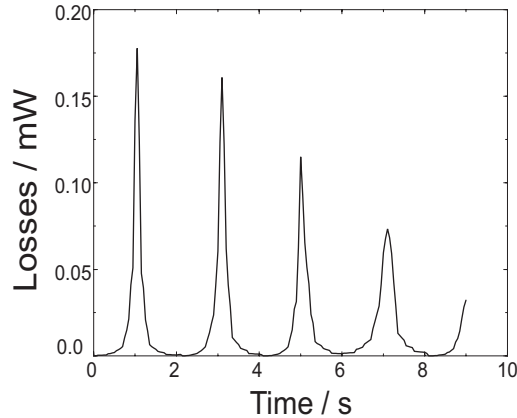


Figure 4.12: *Simulated instantaneous hysteretic loss.*

starts from the negative maximum of the amplitude. It corresponds to case I in subsection (4.1.2). The flux density and the magnetic field strength are required in the integration process. The magnetic field strength is calculated as a result of the magnetic polarization update scheme. For a soft magnetic material, the magnetic field strength is much smaller than the corresponding magnetization. Hence, the flux density is approximated as $B \approx P = \mu_0 M$ while integrating the instantaneous hysteretic loss. The magnetic polarization ($P = \mu_0 M$) is determined by means of the Preisach model according to the applied field and the sequence of turning points. The current excitation is shown in Fig. 4.11 (A). The simulated B-H hysteresis loop is shown in Fig. 4.11 (B). The simulated continuous hysteresis loop is similar to the set of measured symmetrical hysteresis loops (Fig. 4.8 (B)), so we can assume that the classical Preisach model fits well. The instantaneous hysteretic loss is shown in Fig. 4.12. The total hysteresis loss density can be integrated from instantaneous values.

4.2 Nonlinear Update Scheme

4.2.1 Implementation of the Inverse Scalar Preisach Model

The discrete material model (4.2) and the magnetoquasistatic subset of the Maxwell-Grid-Equations are combined into a nonlinear update scheme in time domain. Essential to the nonlinear update scheme is the updated magnetic reluctivity of the hysteretic material. The magnetic flux density is given as an input value. The hysteresis phenomenon is well predicted by Preisach models with respect to an input magnetic field strength in the magnetic polarization update scheme. However, when the magnetic flux density is available as an input value, an inverse hysteresis model is required. Here, the inverse Preisach model is used in the nonlinear update scheme. Several paper about the inverse Preisach model were published in the last decade. Pure mathematical inversions of the Preisach model are discussed in [114] [115]. A differential equation to compute a sequence of magnetic field strengths related to a sequence of flux densities is introduced in [116]. A simple inversion process based on the classical Preisach model [16] is described in [117]. In this subsection,

a simple inversion process is given on the basis of a numerical representation of the classical Preisach model. The formulation of the inverse Preisach model is described in the following paragraphs. Then, the interpolation between the measured first-order transition curves is described.

Inverse scalar Preisach model

The inverse Preisach model determines the averaged magnetic field strength $h(t_n + \Delta t)$ from a calculated flux density $b(t_n + \Delta t)$ at the next time instant. In the formulation of the inverse Preisach model, two distinct cases corresponding to a decrease $b(t_n + \Delta t) < b(t_n)$ and an increase $b(t_n + \Delta t) > b(t_n)$ need to be considered.

We first consider the case of a decreasing flux density: As described in the Preisach model subsection (2.3.1), the $\alpha - \beta$ diagram features an interface $L(t)$ as shown in Fig. 2.30. By adding the integral of $\mu(\alpha, \beta)$ over n trapezoids Q_k (see Fig. 2.30), the Preisach model expression with the monotonically decreasing input is written in (2.42). The magnetization output value $M(t)$ corresponds to an alternating series of dominant maxima M_k and dominant minima m_k , i.e. a series of turning points pair (α, β) , and the magnetic field strength input $h(t)$, and the measured first-order transition curves.

The basic issue in the inversion process is to isolate the values of α and β at which a flux density input $b(t)$ to the hysteresis nonlinearity results in a magnetic field strength output $h(t)$. For this reason, we denote the region under the interface $L(t)$ until reaching some vertex (M_l, m_l) as $S_l^+(t)$ and the corresponding flux density $b^{S_l^+}(t)$. The Regions $S_l^+(t)$ and $S_{l+1}^+(t)$ correspond to the vertices (M_l, m_l) and (M_{l+1}, m_{l+1}) , respectively. The first step in the Preisach model inversion is to select an index $l \in k = 1, \dots, n$ so that $b^{S_l^+}(t) < b(t + \Delta t) < b^{S_{l+1}^+}(t)$. This condition expresses the fact that the inverse corresponding to $b(t + \Delta t)$ lies upon the first-order transition curve with the turning point $\alpha = M_{l+1}$. The required value of β is defined as $\beta = h(t + \Delta t)$. The function $F_{\alpha\beta}$ in the region $m_l < \beta = h(t + \Delta t) < m_{l+1}$ at $\alpha = M_{l+1}$ is found by interpolation and is denoted by $G(M_{l+1}, \beta)$, and is a polynomial function in β . Expressing the equation in terms of the Preisach model parameters yields according to (2.42)

$$b(t + \Delta t) = -F(\alpha_0, \beta_0) + 2 \sum_{k=1}^l [F(M_k, m_{k-1}) - F(M_k, m_k)] + 2 [F(M_{l+1}, m_l) - G(M_{l+1}, \beta)]. \quad (4.17)$$

Inverting the above, the solution to the inverse problem is derived to be

$$h(t + \Delta t) = G'^{-1} \left(-F(\alpha_0, \beta_0) + 2 \sum_{k=1}^l [F(M_k, m_{k-1}) - F(M_k, m_k)] + 2F(M_{l+1}, m_l) - b(t + \Delta t) \right) \Big|_{\alpha=M_{l+1}}, \quad (4.18)$$

where G'^{-1} denotes $G'^{-1} = G^{-1}/2$.

Next we consider the case of an increasing flux density: Similar to the previous case, recasting the equation in terms of the Preisach model (2.43) with $b(t + \Delta t)$ and $G(\alpha, m_l)$, with $\alpha = h(t + \Delta t)$, leads to

$$b(t + \Delta t) = -F(\alpha_0, \beta_0) + 2 \sum_{k=1}^l [F(M_k, m_{k-1}) - F(M_k, m_k)] + 2G(\alpha, m_l). \quad (4.19)$$

Inverting the above expression, the solution to the inverse problem reads

$$h(t + \Delta t) = G'^{-1} \left(b(t + \Delta t) + F(\alpha_0, \beta_0) - 2 \sum_{k=1}^l [F(M_k, m_{k-1}) - F(M_k, m_k)] \right) \Big|_{\beta=m_l}, \quad (4.20)$$

where G'^{-1} denotes $G'^{-1} = G^{-1}/2$.

Because the polynomial functions $G^{-1}(M_{l+1}, \beta)$ in (4.18) and $G^{-1}(\alpha, m_l)$ in (4.20) are not easily interpolated from the measured curves, an approximation for (4.18) and (4.20) is constructed in the following.

In case of decreasing flux density, (4.18) can be rewritten as

$$h(t + \Delta t) = -F'(\alpha_0, \beta_0) + 2 \sum_{k=1}^l [F'(M_k, m_{k-1}) - F'(M_k, m_k)] + 2 [F'(M_{l+1}, m_l) - F'(M_{l+1}, b(t + \Delta t))]. \quad (4.21)$$

In case of increasing flux density, (4.20) can be rewritten as

$$h(t + \Delta t) = -F'(\alpha_0, \beta_0) + 2 \sum_{k=1}^l [F'(M_k, m_{k-1}) - F'(M_k, m_k)] + 2F'(b(t + \Delta t), m_l). \quad (4.22)$$

The function $F'(M_k, m_k)$ in (4.21) and (4.22) is different from the function $F(M_k, m_k)$ in (4.18) and (4.20), which describes the H(B) curves with flux densities as input values. (M_k, m_k) are the extreme magnetic flux densities.

The inverse procedure given by (4.21) and (4.22) essentially consists of two components: the update of the dominant input (M_k, m_k) in terms of the extremal magnetic flux densities at each instant of time, followed by a calculation of the input flux densities $b(t + \Delta t)$ at the each instant of time.

Interpolation between measured curves

Similar to the Preisach model, the function $F'(M_k, m_k)$ is related to measured first-order transition curves by formula (2.23). Using this formula, expressions (4.21) and (4.22) can be written in terms of the experimental data as follows:

$$h(t) = -f'^+ + \sum_{k=1}^{n-1} (f'_{M_k, m_k} - f'_{M_k, m_{k-1}}) + f'_{M_n, b(t)} - f'_{M_n, m_{n-1}}, \quad (4.23)$$

$$h(t) = -f'^+ + \sum_{k=1}^{n-1} (f'_{M_k, m_k} - f'_{M_k, m_{k-1}}) + f'_{-m_{n-1}} - f'_{m_{n-1}, -b(t)}. \quad (4.24)$$

The averaged flux density \overline{B} in each cell is taken as input value of the inverse Preisach model. As was introduced in the basic theory of FIT, each magnetic flux density is allocated through the normal grid facet, which causes the flux density within a grid cell is calculated from its different components in the three coordinate directions as follows:

$$\overline{B} = \sqrt{\overline{B}_x^2 + \overline{B}_y^2 + \overline{B}_z^2}. \quad (4.25)$$

In order to improve the numerical accuracy of the material equations provide by the discrete material matrices, the calculation of the components of flux density are dependent on the geometry of the grid cell, and is for example different for a full cubic grid cell and a trigonal prism grid cell. For hysteretic materials the calculation of the different components of the flux density is presented in Fig. 4.13.

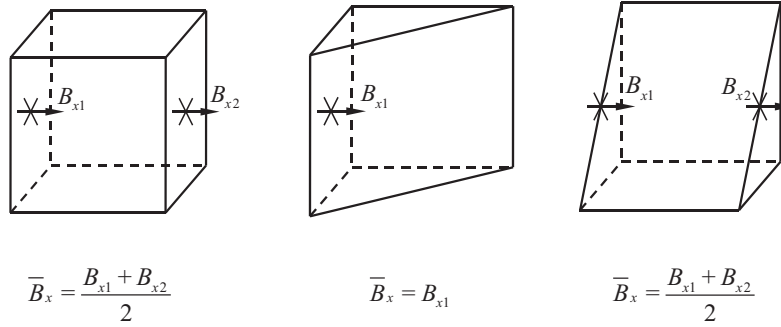


Figure 4.13: Components which are used for the calculation of the averaged flux density in one coordinate direction (here: x -direction).

The output value of the magnetic field strength H can be interpolated from the measured first-order transition curves. Similar to the interpolation needed for the Preisach model, each measured first-order transition curve is generally defined by 20 to 40 pairs of B-H values. Considering the computational accuracy and the memory requirement for the B-H curves, the optimal number of used first-order transition curves is selected to lie between 4 and 6. The selection of measured values is limited to the interval of the input flux density B . Because of the special features of hysteresis, an update of the dominant input (M_k, m_k) depending on the extreme magnetic flux density at each instant of time is necessary. If the input value or the pair of dominant input value (M_k, m_k) is between two measured data points, interpolation is required.

The numerical implementation formulae (4.23) and (4.24) represent the relation between input and output, and the output magnetic field strength is interpolated according to the input flux density and the series of dominant input values (M_k, m_k) . The two point polynomial interpolations (4.8) and (4.9) are used for the inverse procedure. The interpolation is classified as the case of monotonically decreasing input flux density (4.23) and the case of monotonically increasing flux density (4.24).

Case I: The case of a decreasing flux density is explained by the simplest example with only one turning point α in the hysteresis history. The provided flux density B is between the two measured value B_i and B_{i+1} , and the turning point α is between the two experimental input extremes α_j and α_{j+1} . The two-step interpolation process to obtain output value $H(B)$ is described in Fig. 4.14. In the first step, the value $H_j(B)$ is interpolated from the measured values $H_j(B_i)$, and $H_j(B_{i+1})$ using expression (4.8). The value $H_{j+1}(B)$ is interpolated from the measured values $H_{j+1}(B_i)$, $H_{j+1}(B_{i+1})$ using expression (4.8). In the second step, the value $H(B)$ is interpolated using formula (4.9) from the calculated values $H_j(B)$ and $H_{j+1}(B)$.

Formula (4.23) is applied to the interpolated value $H(B)$. The output value of the inverse

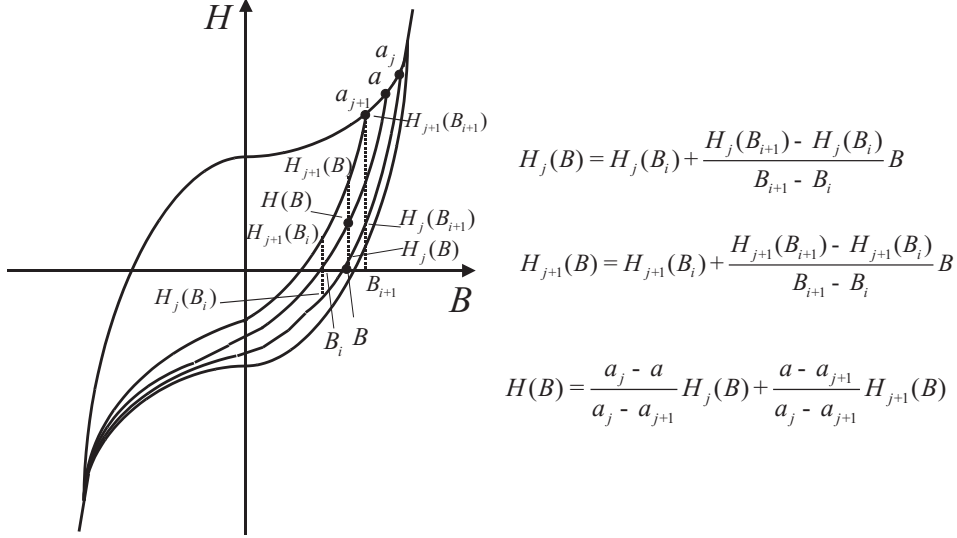


Figure 4.14: Two-step interpolation of the measured first-order transition curves for the inverse Preisach model.

Preisach model $H(t)$ is given as

$$H(t) = -f'^+ + f'_{\alpha, B(t)} - f'_{\alpha, \beta_0}, \quad (4.26)$$

where $f'_{\alpha, B(t)}$ is represented by $H(B)$, and the $f'_{\alpha, \beta_0} = f'^-$. Because we have $f^+ + f_{\alpha, \beta_0} = f^+ + f^- = 0$, expression (4.26) becomes

$$H(t) = H(B). \quad (4.27)$$

Case II: The case of increasing flux density is explained by the simplest example with a pair of turning points (α, β) in the previous hysteresis history. β is obtained at a later point than α in the hysteresis history, assuming $\alpha > 0$ and $\beta < 0$. From (2.29) and the symmetry property of the Preisach model, we have $f_{\beta, B(t)} = -f_{-\beta, -B(t)}$. The flux density B is between two measured values H_i and H_{i+1} , and the absolute value of the turning point $|\beta|$ is between the two experimentally determined turning points α_j and α_{j+1} . Each interpolated result requires two steps of interpolation. The same two-step interpolation process is used as in case I.

Formula (4.24) is used as the formula of the numerical implementation. The output value of the inverse Preisach model $H(t)$ is given as

$$H(t) = -f'^+ + f'_{\alpha, \beta} - f'_{\alpha, \beta_0} + f'_{-\beta} - f'_{\beta, -B(t)}, \quad (4.28)$$

where $f'_{\alpha, \beta_0} = f'^-$, therefore we have $f'^+ + f'_{\alpha, \beta_0} = f'^+ + f'^- = 0$.

The value $f'_{\alpha, \beta}$ depends on the turning point α and the applied field β . It is interpolated by two-step interpolation process same as in case I.

The value $f'_{-\beta}$ depends on the turning point $-\beta$ and the applied field $-\beta$. Its two-step interpolation process is same as in case I.

The quantity $f'_{\beta, -B(t)}$ is equal to $-f'_{-\beta, B(t)}$ according to the symmetry property of the Preisach model. If the turning point is given at $-\beta$ and the provided flux density is taken as $B(t)$, the value $f_{-\beta, B(t)}$ is interpolated by the same process as in case I.

For case I and case II, if there are more than two turning points in the hysteresis history, the two-step interpolation process is always used as the basic process. The output value of the Preisach model is obtained from the series of interpolated results according to the formulae (4.23) and (4.24), respectively.

4.2.2 Implementation of the Inverse Scalar Jiles-Atherton Model

The Jiles-Atherton model [25] is based on the assumption of an anhysteretic magnetization which can be represented by the Langevin function. The magnetization M is decomposed into an irreversible component M_{irr} , whose variations are due to the pinning encountered by the domain walls, and a reversible component M_{rev} , whose variations are tied to the bulging of the domain walls. The original Jiles-Atherton model commonly uses the magnetic field strength as independent input variable. However, when working with the magnetic vector potential formulation, the magnetic flux density is directly obtained. To perform such simulations, an inverse Jiles-Atherton model is required. The magnetization M is calculated from the magnetic flux density B by integrating a differential equation depending on dM/dB . To obtain this relationship, substitute (2.84) into (2.79) and differentiate the resulting term with respect to the effective flux density $B_e = \mu_0 H_e$, i.e.

$$M = M_{\text{irr}} + c(M_{\text{an}} - M_{\text{irr}}) = (1 - c)M_{\text{irr}} + cM_{\text{an}}, \quad (4.29)$$

and

$$\frac{dM}{dB_e} = (1 - c)\frac{dM_{\text{irr}}}{dB_e} + c\frac{dM_{\text{an}}}{dB_e}. \quad (4.30)$$

We re-write each of the differential terms of (4.30) as follows:

The $\frac{dM}{dB_e}$ term: One can write this term as

$$\frac{dM}{dB_e} = \frac{dM}{dB} \frac{dB}{dB_e}. \quad (4.31)$$

Using the effective flux density expression and $H_e = H + \alpha M$ and $B = \mu_0(H + M)$ gives

$$B = B_e - \mu_0 \alpha M + \mu_0 M. \quad (4.32)$$

Differentiating (4.32) with respect to B_e and substituting the results in (4.31) yields

$$\frac{dM}{dB_e} = \frac{\frac{dM}{dB}}{1 - \mu_0(1 - \alpha)\frac{dM}{dB}}. \quad (4.33)$$

The $\frac{dM_{\text{an}}}{dB_e}$ term: This expression can be rewritten as follows:

$$\frac{dM_{\text{an}}}{dB_e} = \frac{dM_{\text{an}}}{dH_e} \frac{dH_e}{dB_e}. \quad (4.34)$$

From the effective flux density equation we have $H_e = B_e/\mu_0$ and substituting $\frac{dH_e}{dB_e} = \frac{1}{\mu_0}$ in (4.34) results in

$$\frac{dM_{\text{an}}}{dB_e} = \frac{1}{\mu_0} \frac{dM_{\text{an}}}{dH_e}. \quad (4.35)$$

The value dM_{an}/dH_e in (4.35) is given by differentiating $M_{\text{an}} = M_s \left[\coth \frac{H_e}{a} - \frac{a}{H_e} \right]$ with respect to H_e , i.e., $\frac{dM_{\text{an}}}{dH_e} = \frac{M_s}{a} \left[1 - \coth^2 \frac{H_e}{a} + \left(\frac{a}{H_e} \right)^2 \right]$.

The $\frac{dM_{\text{irr}}}{dB_e}$ term: Analogously to this, one can write $\frac{dM_{\text{irr}}}{dB_e} = \frac{dM_{\text{irr}}}{dH_e} \frac{dH_e}{dB_e}$ and this gives

$$\frac{dM_{\text{irr}}}{dB_e} = \frac{1}{\mu_0} \frac{dM_{\text{irr}}}{dH_e}. \quad (4.36)$$

Substituting $\frac{dM_{\text{irr}}}{dH_e} = \frac{M_{\text{an}} - M_{\text{irr}}}{k\delta}$ in (4.36) results in

$$\frac{dM_{\text{irr}}}{dB_e} = \frac{M_{\text{an}} - M_{\text{irr}}}{\mu_0 k \delta}, \quad (4.37)$$

in which $\delta = +1$ or $(\delta = -1)$ for $dB/dt > 0$ or $(dB/dt < 0)$. The term M_{irr} in (4.37) is obtained applying (2.79) and (2.84), and $M_{\text{irr}} = \frac{M - cM_{\text{an}}}{1 - c}$.

Finally, re-writing (4.30) using (4.33) and (4.35), and isolating dM/dB gives the main equation of the inverse Jiles-Atherton model

$$\frac{dM}{dB} = \frac{(1 - c) \frac{dM_{\text{irr}}}{dB_e} + \frac{c}{\mu_0} \frac{dM_{\text{an}}}{dH_e}}{1 + \mu_0(1 - c)(1 - \alpha) \frac{dM_{\text{irr}}}{dB_e} + c(1 - \alpha) \frac{dM_{\text{an}}}{dH_e}}. \quad (4.38)$$

The numerical algorithm to obtain the magnetization M and the magnetic field H from the flux density B in a time procedure is shown in the following. For $B(t)$ and $H(t)$ known from the previous time step, for an actual time step flux density $B(t + \Delta t)$ obtained from the field calculation, calculate $H(t + \Delta t)$ by:

$$\begin{aligned} \Delta B &= B(t + \Delta t) - B(t); \\ M(t) &= \frac{B(t)}{\mu_0} - H(t); \\ H_e(t) &= H(t) + \alpha M(t); \\ M_{\text{an}}(t) &= M_s \left[\coth \frac{H_e(t)}{a} - \frac{a}{H_e(t)} \right]; \\ M_{\text{irr}}(t) &= \frac{M(t) - cM_{\text{an}}(t)}{1 - c}; \\ \frac{dM_{\text{irr}}}{dB_e} &= \frac{M_{\text{an}}(t) - M_{\text{irr}}(t)}{\mu_0 k \delta}; \\ \frac{dM_{\text{an}}}{dH_e} &= \frac{M_s}{a} \left[1 - \coth^2 \frac{H_e(t)}{a} + \left(\frac{a}{H_e(t)} \right)^2 \right]; \\ \frac{dM}{dB} &= \frac{(1 - c) \frac{dM_{\text{irr}}}{dB_e} + \frac{c}{\mu_0} \frac{dM_{\text{an}}}{dH_e}}{1 + \mu_0(1 - c)(1 - \alpha) \frac{dM_{\text{irr}}}{dB_e} + c(1 - \alpha) \frac{dM_{\text{an}}}{dH_e}}; \\ M(t + \Delta t) &= M(t) + \frac{dM}{dB} \Delta B; \\ H(t + \Delta t) &= \frac{B(t + \Delta t)}{\mu_0} - M(t + \Delta t). \end{aligned} \quad (4.39)$$

As the parameters of the inverse method are the same as of the original Jiles-Atherton method, the procedure proposed in subsection (2.4.2) can be employed to determine them.

4.2.3 Linearization Techniques for Nonlinear Problems

For magnetoquasistatic problems with nonlinear material, the reluctivity matrix \mathbf{M}_ν depends on the unknown vector potential $\widehat{\mathbf{a}}$ resulting in a nonlinear system of equations as in (3.39). The relation between material values and flux density is commonly given by discrete characteristics, which are not representable by simple operators and cannot be incorporated into the system. To solve such a nonlinear system, the equation is linearized into a sequence of linear problems.

Successive approximation technique

The successive approximation technique solves the nonlinear system by splitting it up into a sequence of linear problems [71] [86]. The reluctivity ν for determining the reluctivity matrix \mathbf{M}_ν is recalculated at each nonlinear update cycle. In order to get the necessary accuracy for the nonlinear calculation in each time step, n nonlinear iterations are needed. The iteration is repeated until the variation of the reluctivity between two steps becomes smaller than a given tolerance. The successive approximation technique is a robust but slow method.

A magnetoquasistatic formulation for the nonlinear problem is introduced with the no-gauged, nonlinear differential algebraic system of equations of index 1

$$\mathbf{M}_\kappa \frac{d}{dt} \widehat{\mathbf{a}}(t) + \widetilde{\mathbf{C}} \mathbf{M}_\nu(\widehat{\mathbf{a}}(t)) \mathbf{C} \widehat{\mathbf{a}}(t) = \widehat{\mathbf{j}}_e(t). \quad (4.40)$$

In the common nonlinear case using the successive approximation technique, the updated reluctivity ν for the matrix \mathbf{M}_ν is given by the slope of the line through the working point on the curve (see Fig. 4.15 (A)). In the hysteretic case using the successive approximation technique, the updated reluctivity corresponding to the information of the first-order transition $H(B)$ curves is not positive in the second and fourth quadrant because of the definition of the reluctivity $\nu := H/B$. This causes inaccurate numerical results. This problem is alleviated by the following procedure, where a slightly different definition of the reluctivity for the hysteretic material is chosen.

As described in subsection (2.2.1), a more general material relation is:

$$B = \mu_0(H + M), \quad (4.41)$$

where M denotes the magnetization and is defined by $M = \chi_m H + M_0$. The magnetic susceptibility χ_m is brought into relation with the magnetic permeability by $\mu := \mu_0(1 + \chi_m)$, and B_0 is defined by $B_0 := \mu_0 M_0$. The material relation is given as:

$$B = \mu H + B_0. \quad (4.42)$$

In this way, the negative value of the hysteretic reluctivity in the second and fourth quadrant can be avoided. With the modified definition of the reluctivity $\nu := H/(B - B_0)$ and a suitable choice of B_0 , the reluctivity along the hysteretic curve is always positive. As a consequence, the positive definition of the material matrix is guaranteed.

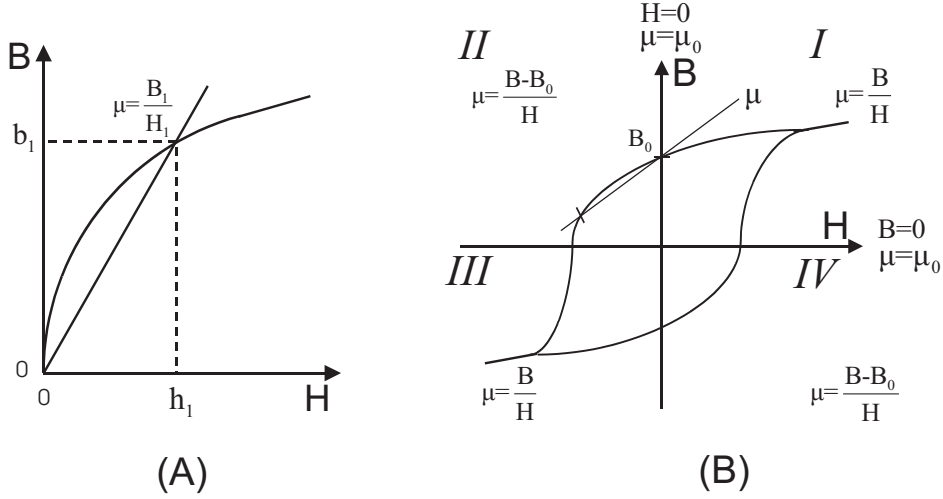


Figure 4.15: Updating the reluctivity ν on the BH -curve for the successive approximation technique (A) For non-hysteretic ferromagnetic material, (B) For hysteretic ferromagnetic material.

The updated reluctivity ν determining the entries for the matrix \mathbf{M}_ν is given by the slope of the line from the remanence point $(0, B_0)$ and the working point on the curve (see Fig. 4.15 (B)). The value B_0 is chosen to be the physical remanence. For each reluctivity definition in the second and fourth quadrant, the value B_0 is interpolated according to the measured first-order transition curves and the last extreme maximum in the hysteresis history (i.e. the last turning point).

Newton-Raphson method

In general all kinds of nonlinear equations can be written as $F(x) = 0$ [87] [88]. The $\mathbf{F}(\hat{\mathbf{a}}(t))$ from the magnetoquasistatic nonlinear formulation (3.39) at each time step t can be written as

$$\mathbf{F}(\hat{\mathbf{a}}(t)) = \mathbf{M}_\kappa \frac{d}{dt} \hat{\mathbf{a}}(t) + \tilde{\mathbf{C}} \mathbf{M}_\nu(\hat{\mathbf{a}}(t)) \mathbf{C} \hat{\mathbf{a}}(t) - \hat{\mathbf{j}}_e(t). \quad (4.43)$$

The Newton-Raphson method is an efficient linearization technique for nonlinear problems. It solves the equation $\mathbf{F}(\hat{\mathbf{a}}(t)) = 0$ starting from an initial guess vector potential $\hat{\mathbf{a}}_0$ and updates this starting vector with an update vector $\Delta \hat{\mathbf{a}}_{i+1}$ that needs to be determined in each linearized cycle

$$\hat{\mathbf{a}}_{i+1} = \hat{\mathbf{a}}_i + \Delta \hat{\mathbf{a}}_{i+1}, \quad (4.44)$$

where i is the index of the nonlinear iteration cycle, $\hat{\mathbf{a}}_0$ is the starting vector which corresponds to the magnetic vector potential at time t_0 , $\hat{\mathbf{a}}_i$ is the vector at the i -th cycle, $\hat{\mathbf{a}}_{i+1}$ is the vector at the $(i+1)$ -th cycle, and $\Delta \hat{\mathbf{a}}_{i+1}$ is the difference between the solution vectors $\hat{\mathbf{a}}_i$ and $\hat{\mathbf{a}}_{i+1}$.

Using a Taylor-Series expansion, the update vector potential $\Delta \hat{\mathbf{a}}_{i+1}$ can be determined by:

$$0 = \mathbf{F}(\hat{\mathbf{a}}_i + \Delta \hat{\mathbf{a}}_{i+1}) = \mathbf{F}(\hat{\mathbf{a}}_i) + \left[\frac{\partial \mathbf{F}}{\partial \hat{\mathbf{a}}} \right] \Delta \hat{\mathbf{a}}_{i+1} + \dots \quad (4.45)$$

By considering only the linear part of the series expansion from equation (4.45) the update vector $\Delta\widehat{\mathbf{a}}_{i+1}$ can be obtained from:

$$\Delta\widehat{\mathbf{a}}_{i+1} = -\mathbf{J}_F^{-1}(\widehat{\mathbf{a}}_i)F(\widehat{\mathbf{a}}_i), \quad (4.46)$$

with the Jacobian matrix \mathbf{J}_F :

$$\mathbf{J}_F = \begin{bmatrix} \frac{\partial \mathbf{F}_1}{\partial \mathbf{a}_1} & \frac{\partial \mathbf{F}_1}{\partial \mathbf{a}_2} & \frac{\partial \mathbf{F}_1}{\partial \mathbf{a}_3} & \cdots \\ \frac{\partial \mathbf{F}_2}{\partial \mathbf{a}_1} & \frac{\partial \mathbf{F}_2}{\partial \mathbf{a}_2} & \cdots & \cdots \\ \vdots & \vdots & \vdots & \vdots \end{bmatrix}.$$

From (4.46) it follows directly that the Jacobian matrix needs to be evaluated and inverted for each step of the iteration. To save computation time the inversion of the Jacobian is avoided by iteratively solving the linear system of equation:

$$\mathbf{J}_F(\widehat{\mathbf{a}}_i)\Delta\widehat{\mathbf{a}}_{i+1} = -\mathbf{F}(\widehat{\mathbf{a}}_i). \quad (4.47)$$

When using the FIT the update of the Jacobian matrix reduces to the problem of updating a diagonal material matrix $\mathbf{M}_{\nu_d}(\widehat{\mathbf{a}})$ only. Because only the differential reluctivity matrix $\mathbf{M}_{\nu_d}(\widehat{\mathbf{a}})$ is changing in the Jacobian matrix, the update for the Jacobian matrix needs the differential reluctivity ν_d . The differential reluctivity is the inverse of the differential permeability which is the slope of the tangent to the active hysteretic curve at the actual working point (Fig. 4.16).

The differential reluctivity ν_d is approximated by $\nu_d = \frac{d\mathbf{H}}{d\mathbf{B}} \cong \frac{\Delta\mathbf{H}}{\Delta\mathbf{B}}$. The Newton-Raphson method features a quadratic convergence, but only in the vicinity of the solution. For this reason, the difference of the flux density $\Delta\mathbf{B}$ is required to be as small as possible. The matrix \mathbf{M}_{ν_d} is calculated by

$$\{\mathbf{D}_{\nu_d}\}_{jj} := \frac{\{\widehat{\mathbf{h}}_{i+1}\}_j - \{\widehat{\mathbf{h}}_{d,i+1}\}_j}{\{\widehat{\mathbf{b}}_{i+1}\}_j - \{\widehat{\mathbf{b}}_{d,i+1}\}_j}, \quad (4.48)$$

and

$$\mathbf{M}_{\nu_d} := \mathbf{D}_{\widetilde{\mathcal{L}}}\mathbf{D}_{\nu_d}\mathbf{D}_A^{-1} \quad (4.49)$$

where $\{\mathbf{D}_{\nu_d}\}_{jj}$ is the value of the differential reluctivity where the dual grid edge \widetilde{L}_j penetrates the normal face A_j , $\mathbf{D}_{\widetilde{\mathcal{L}}}$ is the diagonal matrix of dual grid edge lengths, and \mathbf{D}_A is the diagonal matrix of primary grid face areas. The vector $\{\widehat{\mathbf{b}}_{d,i+1}\}_j$ through the normal grid facet A_j is given by

$$\{\widehat{\mathbf{b}}_{d,i+1}\}_j = \{\widehat{\mathbf{b}}_{i+1}\}_j + \varepsilon_b \left(\{\widehat{\mathbf{b}}_{i+1}\}_j - \{\widehat{\mathbf{b}}_p\}_j \right) \operatorname{sgn} \left(\{\widehat{\mathbf{b}}_{i+1}\}_j - \{\widehat{\mathbf{b}}_p\}_j \right), \quad (4.50)$$

where $\widehat{\mathbf{b}}_p$ denotes the calculated flux vector at the last time step, and the parameter ε_b denotes a step length, which is selected in the interval $(0, 1)$. The function $\operatorname{sgn}(\{\widehat{\mathbf{b}}_{i+1}\}_j - \{\widehat{\mathbf{b}}_p\}_j)$ takes the value $+1(-1)$ if $\{\widehat{\mathbf{b}}_{i+1}\}_j$ is bigger (smaller) than $\{\widehat{\mathbf{b}}_p\}_j$. The vector $\widehat{\mathbf{b}}_{i+1}$ is obtained from the nonlinear iteration. After the vectors $\widehat{\mathbf{b}}_{i+1}$ and $\widehat{\mathbf{b}}_{d,i+1}$ are obtained, the vectors $\widehat{\mathbf{h}}_{i+1}$ and $\widehat{\mathbf{h}}_{d,i+1}$ are interpolated using the inverse Preisach model or the inverse Jiles-Atherton model according to the values $\widehat{\mathbf{b}}_{i+1}$ and $\widehat{\mathbf{b}}_{d,i+1}$.

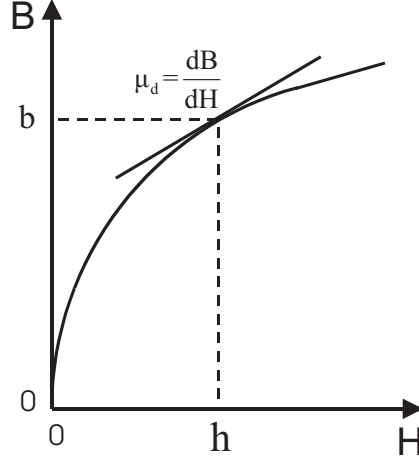


Figure 4.16: Obtaining the slope of the BH-characteristic for the Newton-Raphson method.

4.2.4 Relaxation Methods

The Newton-Raphson method features a quadratic convergence, but only in the vicinity of the solution. The successive approximation method is more robust but has a poor convergence rate. Several relaxation methods have been implemented in order to achieve global convergence and to improve the speed of convergence for both the Newton-Raphson method and the successive approximation method. For the linearization of the nonlinear problems, the vector $\bar{\mathbf{a}}$ related to the magnetic vector potential is taken as the main unknown. A relaxation factor ω is introduced to obtain $\bar{\mathbf{a}}_{i+1}$ in the next calculation cycle:

$$\bar{\mathbf{a}}_{i+1} = \bar{\mathbf{a}}_i + \omega \Delta \bar{\mathbf{a}}_{i+1}. \quad (4.51)$$

Several techniques exist to select an appropriate relaxation factor ω at each iteration step.

Heuristic relaxation method

The heuristic relaxation method directly adapts the relaxation parameter in the relaxation process. The relaxation parameter is determined by the track of the norm of the matrix of the permeability differences. The heuristic scheme is often used for the nonlinear material relaxation parameter calculation. The advantage of such an approach is that it does not need computation time for an optimization process. For the global heuristic scheme, the norm of the matrix of the permeability differences is given by

$$\| \Delta \mathbf{M}_{\mu, i+1} \|_{\infty} := \| \mathbf{M}_{\mu, i+1} - \mathbf{M}_{\mu, i} \|_{\infty}. \quad (4.52)$$

A monotonic decrease of $\| \Delta \mathbf{M}_{\mu, i+1} \|_{\infty}$ over a number of iteration steps indicates that the relaxation parameter can be increased. On the other hand, when $\| \Delta \mathbf{M}_{\mu, i+1} \|_{\infty}$ is increasing over a number of iteration steps, this indicates that the relaxation parameter can be decreased. The global heuristic scheme is summarized as:

- 1) Define a region of acceptable value for ω , i.e. $[\omega_{min} \leq \omega \leq \omega_{max}]$.
- 2) Chose a starting value for the relaxation parameter ω in the prescribed range.

3) A value for $\Delta\omega$ needs to be set. By this value the relaxation parameter will be changed according to the heuristic rule.

4) Define variables that store information on the change of \mathbf{M}_μ :

$$\begin{aligned}\beta_{i-1} &= \|\Delta\mathbf{M}_{\mu,i-1}\|_\infty - \|\Delta\mathbf{M}_{\mu,i-2}\|_\infty; \\ \beta_i &= \|\Delta\mathbf{M}_{\mu,i}\|_\infty - \|\Delta\mathbf{M}_{\mu,i-1}\|_\infty.\end{aligned}$$

5) Adapt the relaxation parameter ω for each iteration according to the following tests:

- (a) if ($\beta_{i-1} < 0$ and $\beta_i < 0$) then increase ω by $\Delta\omega$.
- (b) if ($\beta_{i-1} > 0$ or $\beta_i > 0$) then decrease ω by $\Delta\omega$.
- (c) else do not change ω .

6) Update ω according to the above rules in each iteration step until the desired accuracy for the solution is achieved.

The choice of $\Delta\omega$ is crucial because this value needs to be balanced between two opposing demands: A high value is desirable to be able to react fast and to increase the relaxation coefficient as fast as possible. On the other hand a high value for $\Delta\omega$ may cause the solution to oscillate or diverge. Therefore, to be on the safe side, it is recommended to keep the step size $\Delta\omega$ small, even if this is slowing down the convergence. A value of $\Delta\omega = 0.1$ seemed to be a good compromise [70] [71].

Brent's method

Brent's method is based on a parabolic interpolation [94] approximately alternating between parabolic steps and golden sections [94]. Brent's method consists of the following steps (see Fig. 4.17):

- 1) Evaluate the function to be minimized in three points 1, 2, and 3.
- 2) Interpolate by parabola, that fits through the three points 1, 2, and 3.
- 3) Evaluate function to be minimized at the minimum of the parabola (point 4) using (4.53).
- 4) A new parabola is fitted through the points 1, 4, and 2.
- 5) The minimum of this new parabola (point 5) approximates the minimum of the function.

The formula for the abscissa x that is the minimum of a parabola through three points $f(a)$, $f(b)$, and $f(c)$ is

$$x = b - \frac{1}{2} \frac{(b-a)^2[f(b)-f(c)] - (b-c)^2[f(b)-f(a)]}{(b-a)[f(b)-f(c)] - (b-c)[f(b)-f(a)]}. \quad (4.53)$$

This formula (4.53) fails only if the three points are collinear, in which case the denominator is zero. The formula (4.53) does not distinguish between a minimum and a maximum. Therefore, the golden section search is applied when such a failure occurs.

At any particular stage, Brent's method keeps track of six function points, a , b , u , v , w , and x , defined as follows: the minimum is bracketed between a and b ; x is the point with

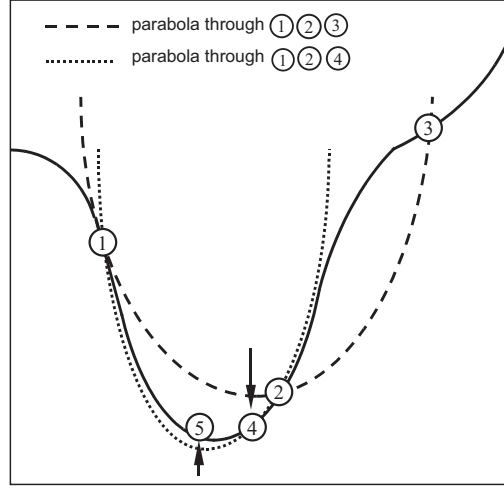


Figure 4.17: *Basic idea of Brent's method. A parabola (dashed line) is drawn through the three original points 1,2,3 on the given function (solid line). The function is evaluated at the parabola's minimum 4, which replaces point 3. A new parabola (dotted line) is drawn through points 1,2,4. The minimum of this parabola is at 5, which is close to the minimum of the function.*

the very last function value found so far; w is the point with the second last function value; v is the previous value of w ; u is the point at which the function was evaluated most recently. As one of general principles: parabolic interpolation is attempted, fitting through the points x , v , and w . To be acceptable, the parabolic step must (i) fall within the bounding interval (a, b) , and (ii) imply a change from the best current value x that is less than half the change of the last step. This second criterion ensures that the parabolic steps are actually converging to some nonconvergent limit cycle. When the parabolic steps are acceptable but useless, the method alternates between parabolic steps and golden sections, where the latter ensures convergence.

4.2.5 Nonlinear Iterative Scheme

The discrete material model (4.2) and the magnetoquasistatic FIT formulation are combined into a nonlinear formulation in time domain taking hysteresis into account. On the basis of (3.45), a linear one step θ -method [74] is given by

$$\frac{1}{\Delta t} \mathbf{M}_\kappa (\hat{\mathbf{a}}^{(n+1)} - \hat{\mathbf{a}}^{(n)}) + \tilde{\mathbf{C}} \mathbf{M}_\nu \mathbf{C} (\theta \hat{\mathbf{a}}^{(n+1)} + (1 - \theta) \hat{\mathbf{a}}^{(n)}) = \theta \hat{\mathbf{j}}_e^{(n+1)} + (1 - \theta) \hat{\mathbf{j}}_e^{(n)}. \quad (4.54)$$

If the successive approximation method is applied within each step of the backward differentiation implicit Euler scheme, a hysteretic nonlinear update scheme derived from (4.54) and (4.40) is given by

$$\left[\frac{1}{\Delta t} \mathbf{M}_\kappa + \tilde{\mathbf{C}} \mathbf{M}_\nu (\hat{\mathbf{a}}_i^{(n+1)}) \mathbf{C} \right] \hat{\mathbf{a}}_{i+1}^{(n+1)} = \frac{1}{\Delta t} \mathbf{M}_\kappa \hat{\mathbf{a}}^{(n)} + \hat{\mathbf{j}}_e^{(n+1)}, \quad (4.55)$$

where i denotes the index of nonlinear iteration cycle, and n is the index of the time step. The inverse Preisach model is selected to update the reluctivities ν for determining the material matrix $\mathbf{M}_\nu(\widehat{\mathbf{a}}_i^{(n+1)})$. The material matrix corresponds to the information given in the first-order transition measured H(B) curves. It is interpolated by the inverse Preisach model, and updated in each nonlinear iteration. In order to ensure global convergence of the nonlinear iteration loop for arbitrary start values and to improve its speed of convergence, the global heuristic relaxation method is used as the relaxation method. The nonlinear iteration cycle invoked at each time step is shown in Table (4.2):

Table 4.2: Algorithm of the successive approximation method at each time step

1.	Initialize $\widehat{\mathbf{a}}_0^{(n+1)}$, \mathbf{M}_ν , \mathbf{M}_{ν_d} , $i = 0$
2.	Repeat
(2.1)	Solve $\widehat{\mathbf{a}}_{i+1}^{(n+1)}$ from equation (4.55)
(2.2)	Update $\widehat{\mathbf{a}}_{(i+1)}^{(n+1)} = \widehat{\mathbf{a}}_i^{(n+1)} + \omega(\widehat{\mathbf{a}}_{i+1}^{(n+1)} - \widehat{\mathbf{a}}_i^{(n+1)})$ with the global heuristic relaxation parameter ω
(2.3)	Update $\mathbf{M}_\nu(\widehat{\mathbf{a}}_{(i+1)}^{(n+1)})$ from the inverse Preisach model
(2.4)	$i = i + 1$
	until the norm of the correction is smaller than the tolerance ε or until a predefined maximum of cycles is reached

If the Newton-Raphson method is applied as a nonlinear iterative scheme in each step of the backward differentiation implicit Euler scheme, the hysteretic nonlinear update scheme derived from (4.54), (4.43) and (4.47) is given by

$$\begin{aligned} & \left[\frac{1}{\Delta t} \mathbf{M}_\kappa + \widetilde{\mathbf{C}} \mathbf{M}_{\nu_d}(\widehat{\mathbf{a}}_i^{(n+1)}) \mathbf{C} \right] \Delta \widehat{\mathbf{a}}_{i+1}^{(n+1)} = \\ & \widehat{\mathbf{j}}_e^{(n+1)} + \frac{1}{\Delta t} \mathbf{M}_\kappa \widehat{\mathbf{a}}^{(n)} - \left[\frac{1}{\Delta t} \mathbf{M}_\kappa + \widetilde{\mathbf{C}} \mathbf{M}_\nu(\widehat{\mathbf{a}}_i^{(n+1)}) \mathbf{C} \right] \widehat{\mathbf{a}}_i^{(n+1)}, \end{aligned} \quad (4.56)$$

where i denotes the index of the nonlinear iteration cycle, and n is the index of the time step.

The substitution $\widehat{\mathbf{h}}_i^{(n+1)} \approx \mathbf{M}_\nu(\widehat{\mathbf{a}}_i^{(n+1)}) \mathbf{C} \widehat{\mathbf{a}}_i^{(n+1)}$ can be used instead of $\mathbf{M}_\nu(\widehat{\mathbf{a}}_i^{(n+1)}) \mathbf{C} \widehat{\mathbf{a}}_i^{(n+1)}$ in (4.56) in order to avoid the calculation of \mathbf{M}_ν . The expression is then rewritten as

$$\begin{aligned} & \left[\frac{1}{\Delta t} \mathbf{M}_\kappa + \widetilde{\mathbf{C}} \mathbf{M}_{\nu_d}(\widehat{\mathbf{a}}_i^{(n+1)}) \mathbf{C} \right] \Delta \widehat{\mathbf{a}}_{i+1}^{(n+1)} = \\ & \widehat{\mathbf{j}}_e^{(n+1)} + \frac{1}{\Delta t} \mathbf{M}_\kappa (\widehat{\mathbf{a}}^{(n)} - \widehat{\mathbf{a}}_i^{(n+1)}) - \widetilde{\mathbf{C}} \widehat{\mathbf{h}}_i^{(n+1)}. \end{aligned} \quad (4.57)$$

The updated vector $\widehat{\mathbf{h}}_i^{(n+1)}$ related to the magnetic field strength in (4.57) is given by

$$\widehat{\mathbf{h}}_i^{(n+1)} = \widehat{\mathbf{h}}_p + \mathbf{M}_{\nu_d}(\widehat{\mathbf{b}}_i^{(n+1)} - \widehat{\mathbf{b}}_p), \quad (4.58)$$

where \mathbf{M}_{ν_d} is the matrix of differential reluctivity updated at each nonlinear iterative cycle, and $\widehat{\mathbf{b}}_p$ and $\widehat{\mathbf{h}}_p$ are the last updated results at the last time step.

If the inverse Preisach model is selected as the hysteresis model, the material matrix of the differential reluctivity $\mathbf{M}_{\nu_d}(\widehat{\mathbf{a}}_i^{(n+1)})$ corresponds to the information given in the first-order

transition measured H(B) curves. It is interpolated and updated in each nonlinear iteration. The vector $\widehat{\mathbf{h}}_i^{(n+1)}$ related to the magnetic field strength is updated using (4.58) in each nonlinear iteration. The one-dimensional Brent's method is selected for determining the relaxation parameter which minimizes a cost function at each nonlinear iteration, e.g. the residual of the material property relation, the residual of the nonlinear equation, or the energy functional. Here, the norm of the residual of the nonlinear equation (4.57) $\|\frac{1}{\Delta t}\mathbf{M}_\kappa(\widehat{\mathbf{a}}_{i+1}^{(n+1)} - \widehat{\mathbf{a}}^{(n)}) + \widetilde{\mathbf{C}}\widehat{\mathbf{h}}_{i+1}^{(n+1)} - \widehat{\mathbf{j}}_e^{(n+1)}\|_2$ is selected as cost function.

If the inverse Jiles-Atherton method is selected as the hysteresis model, the material matrix of differential reluctivities $\mathbf{M}_{\nu_d}[\widehat{\mathbf{a}}_i^{(n+1)}]$ corresponds to the five material parameters (a, α, k, c, M_s) of the Jiles-Atherton model and they are updated by the inverse Jiles-Atherton model in each iteration. The vector $\widehat{\mathbf{h}}_i^{(n+1)}$ related to the magnetic field strength is updated by (4.58) in each iteration. The interpolation process is introduced in the subsection about the modelling of the inverse Jiles-Atherton model. The one-dimensional Brent's method is selected to determine the relaxation factor which minimizes the norm of the residual of the nonlinear equation (4.57) $\|\frac{1}{\Delta t}\mathbf{M}_\kappa(\widehat{\mathbf{a}}_{i+1}^{(n+1)} - \widehat{\mathbf{a}}^{(n)}) + \widetilde{\mathbf{C}}\widehat{\mathbf{h}}_{i+1}^{(n+1)} - \widehat{\mathbf{j}}_e^{(n+1)}\|_2$ at each nonlinear iteration. The nonlinear iteration procedure is controlled by the error ε , which is defined as $\|\Delta\widehat{\mathbf{b}}_i\|_2 / \|\widehat{\mathbf{b}}_i\|_2$. The iterative process is repeated until the error ε becomes sufficiently small or until a predefined maximum of cycles n_{\max} is reached.

The Newton-Raphson iteration cycle invoked at each time step is written in Table (4.3):

Table 4.3: Algorithm of the Newton-Raphson method at each time step

1. Initialize $\widehat{\mathbf{a}}_0^{(n+1)}, \mathbf{M}_\nu, \mathbf{M}_{\nu_d}, i = 0$
2. Repeat
(2.1) Solve $\widehat{\mathbf{a}}_{i+1}^{(n+1)}$ from equation (4.57)
(2.2) Update $\widehat{\mathbf{a}}_{(i+1)}^{(n+1)} = \widehat{\mathbf{a}}_i^{(n+1)} + \omega(\widehat{\mathbf{a}}_{i+1}^{(n+1)} - \widehat{\mathbf{a}}_i^{(n+1)})$ with relaxation parameter ω determined by the one-dimensional Brent method
(2.3) Update $\mathbf{M}_{\nu_d}(\widehat{\mathbf{a}}_{(i+1)}^{(n+1)})$ using the inverse Preisach model or the inverse Jiles-Atherton model
(2.4) Update $\widehat{\mathbf{h}}_i^{(n+1)}$ from equation (4.58)
(2.5) $i = i + 1$
until the correction is smaller than the tolerance ε or until a predefined maximum of cycles is reached

4.2.6 Test Example A and Discussion

In order to compare the nonlinear update scheme with the magnetic polarization update scheme, the same test example A is used for validating the scalar Preisach and Jiles-Atherton models in combination with the nonlinear update scheme linearized by either the Newton-Raphson method or the successive approximation method. The 3D model and 2D cut face of the model are shown in Fig. 4.6. The non-hysteretic ferromagnetic material is introduced in Appendix A Table A.2. The characteristics of the hysteretic material is given by a set of first-order transition measured curves (Fig. 4.8 (B)) introduced in Appendix A Table A.3.

Comparison of the Newton-Raphson method and the successive approximation method

The backward differentiation implicit Euler time integration is used for time stepping. The Newton-Raphson method and the successive approximation method are both implemented as nonlinear iterative schemes within each time step. For the same test model provided by the same current excitation, the simulated B-H hysteresis loop with the constant time step 0.1s is shown in Fig. 4.18 (A), and the simulated B-H hysteresis loop with the constant time step 0.05s is shown in Fig. 4.18 (B). The simulated results are compared with the measured first-order transition curves in Fig. 4.19 and Fig. 4.20.

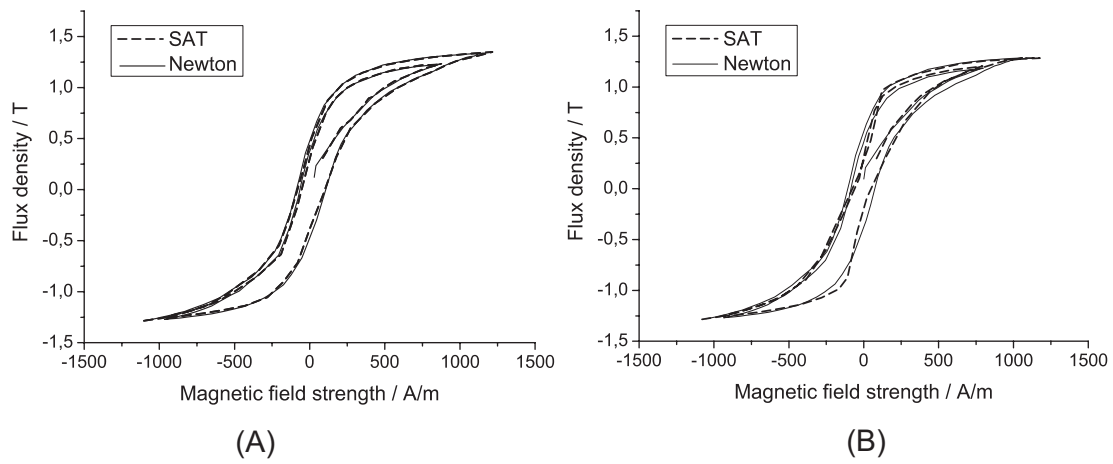


Figure 4.18: Comparison of the B-H hysteresis loop simulated by the Newton-Raphson method and the successive approximation technique (SAT). (A) Simulated with fixed time step 0.1s, (B) Simulated with fixed time step 0.05s.

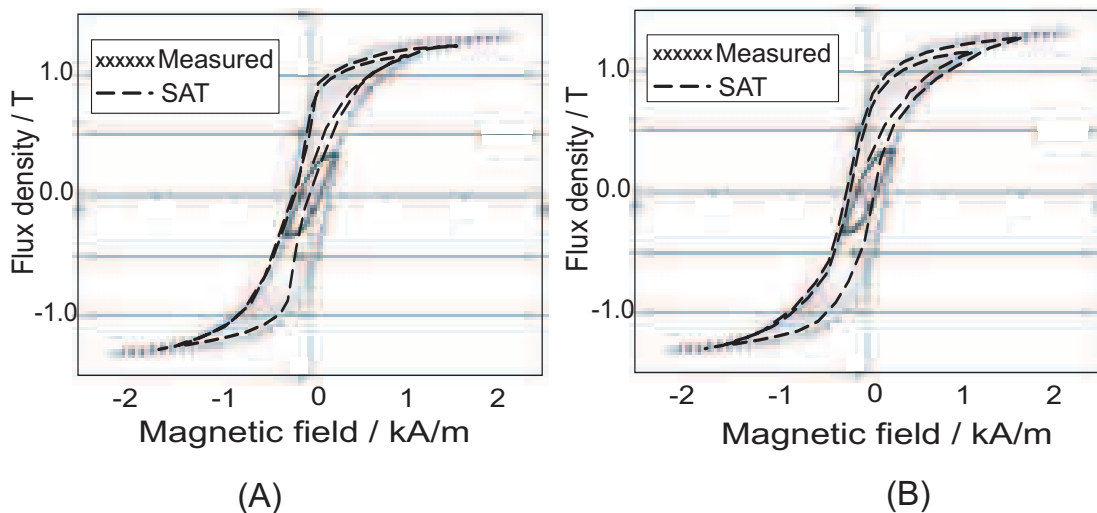


Figure 4.19: Comparison of the B-H hysteresis loops simulated by the successive approximation method with the measured curves. (A) With time step 0.05s, (B) With time step 0.1s.

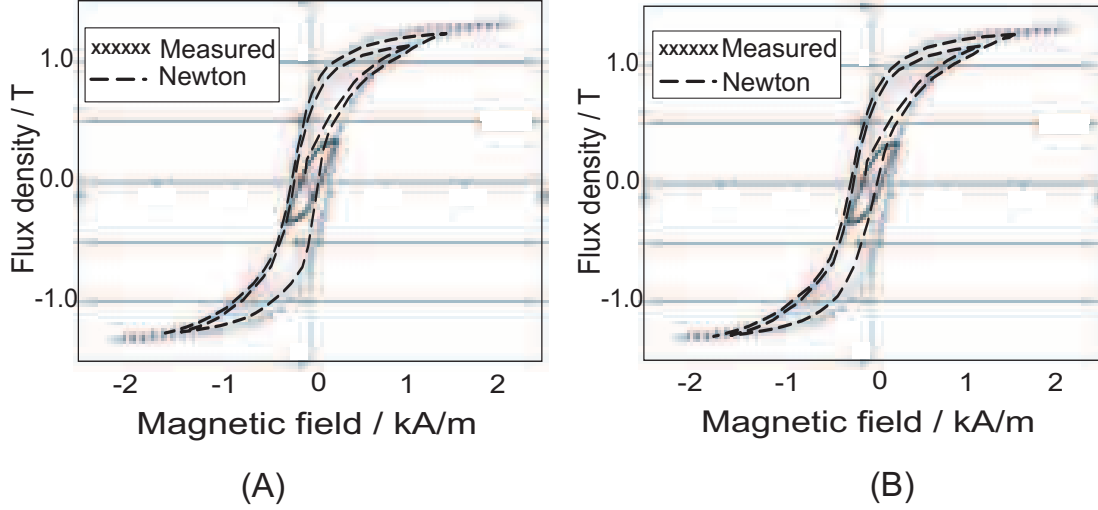


Figure 4.20: Comparison of the B - H hysteresis loops simulated by the Newton-Raphson method with the measured curves. (A) With time step $0.05s$, (B) With time step $0.1s$.

The successive approximation update scheme for the reluctivity ν has a non-smooth change in the neighborhood of the zones near the values of coercive field strength $H_c(B = 0)$ or remanent induction $B_r(H = 0)$. This requires more successive approximation update cycles at each time step in order to avoid the non-smooth change of the reluctivity, and causes a very small global heuristic relaxation parameter ω . The relaxation parameter ω always stays at minimum value in the second and fourth quadrant. With the small time step, it causes a worse agreement between measured and calculated results in the region. For this reason, the agreement between measured and simulated results to be worse for the case with time step 0.05 s (Fig. 4.19 (A)), and results to be better for the case with time step 0.1 s (Fig. 4.19 (B)).

In the Newton-Raphson iterative scheme (4.57), the updated differential reluctivity ν_d is always positive, and has a smooth change at the coercive points $B = 0$ and the remanent points $H = 0$. Because the vector $\widehat{\mathbf{h}}_i^{(n+1)}$ is used instead of the vector $\mathbf{M}_\nu(\widehat{\mathbf{a}}_i^{(n+1)})\mathbf{C}\widehat{\mathbf{a}}_i^{(n+1)}$, i.e. $\widehat{\mathbf{h}}_i^{(n+1)} \approx \mathbf{M}_\nu(\widehat{\mathbf{a}}_i^{(n+1)})\mathbf{C}\widehat{\mathbf{a}}_i^{(n+1)}$, the inaccuracy caused by the non-smooth change of the reluctivity ν is avoided in the Newton-Raphson iterative scheme. Fig. 4.20 compares the results simulated by the Newton-Raphson method with the time steps $0.05s$ and $0.1s$, respectively. The simulated results agree very well with the measured first-order transition curves, no matter if the time step is selected small or big.

The CPU time consumption is compared for both nonlinear iterative schemes. The nonlinear iteration procedure is controlled by the relative error $\varepsilon = \|\Delta\widehat{\mathbf{b}}_i\|_2 / \|\widehat{\mathbf{b}}_i\|_2$. The iteration process is repeated until the error tolerance ε is reached or if iteration number is bigger than a predefined maximum number of cycles n_{max} . For both nonlinear iterative schemes an error tolerance is selected as $1e-4$ and a maximum iteration number is defined as $n_{max} = 8$. For the same number of degrees of freedom with the current excitation for the 70 time steps of the 7 seconds, the successive approximation method consumes 798 seconds of CPU time, and the Newton-Raphson method requires 1444 seconds of CPU time. Different relaxation methods and parameters are selected for both methods. The successive approximation method uses a global heuristic relaxation method, whereas the Newton-Raphson method uses a one-dimensional Brent method which needs more time

due to the application of parabolic interpolations and golden sections in each cycle.

It is concluded that the Newton-Raphson method with relaxation 1D Brent method provides an efficient nonlinear iterative scheme for hysteretic simulation, and the Newton-Raphson iterative scheme combined with the inverse Preisach model accurately reflects hysteresis effects.

Comparison of the inverse scalar Jiles-Atherton model and the inverse scalar Preisach model

The inverse Jiles-Atherton model is compared with the inverse Preisach model. The same test model is simulated for two different current excitations by both nonlinear iterative schemes. The Preisach model depends on the measured first-order transition curves. The Jiles-Atherton model only depends on its five material parameters. The identification of the five material parameters of the inverse Jiles-Atherton model is straightforward. Using the numerical determination of hysteresis parameters [27], the test problem is simulated with the parameters: $a = 969.93A/m$, $\alpha = 1.864 \times 10^{-3}$, $c = 0.154$, $k = 2012.43A/m$ and $M_s = 1.154MA/m$.

For a low excitation current (Fig. 4.21 (A)), the B-H hysteresis loops simulated by the inverse Jiles-Atherton model and by the inverse Preisach model are shown in Fig. 4.21 (B). The loops simulated by the inverse Jiles-Atherton model are compared with the measured curves in Fig. 4.22 (A). The comparison of the loops simulated by the inverse Preisach model and the measured curves is shown in Fig. 4.22 (B). The results simulated by the inverse Jiles-Atherton model differ strongly from the results simulated by the inverse Preisach model.

For a higher excitation current (Fig. 4.23 (A)), the hysteretic ferromagnetic material gets saturated. The B-H hysteresis loops simulated by the inverse Jiles-Atherton model and by the inverse Preisach model are shown (Fig. 4.23 (B)). The measured and simulated curves are compared in Fig. 4.24. The loop simulated by the inverse Jiles-Atherton model has a good agreement to the measured curves. The two simulated results of both methods also agree well.

The identification of the parameters of the inverse Preisach model requires relatively extensive measurements, whereas the inverse Jiles-Atherton model holds the opposite. On the other hand, the correspondence with the measurements is better for the inverse Preisach model than for the inverse Jiles-Atherton model. In order to decrease the difference between the loops simulated by the inverse Jiles-Atherton model and measured curves, the identification of the five material parameters of the inverse Jiles-Atherton model can be further improved by a better identification. The applicable identification techniques are classified as scaling methods [118], optimization methods [119] and annealing technique [111]. For the test problem, both hysteresis models combined with the Newton-Raphson iterative scheme under the same numerical simulation conditions consume a comparable amount of CPU time.

Comparison of the hysteretic nonlinear iteration and the magnetic polarization iteration

Because of the two different models of nonlinear ferromagnetic material behavior (4.1) and (4.2), hysteresis effects can be implemented either by the magnetic polarization update scheme or by the hysteretic nonlinear update scheme. The simulated hysteresis loop and

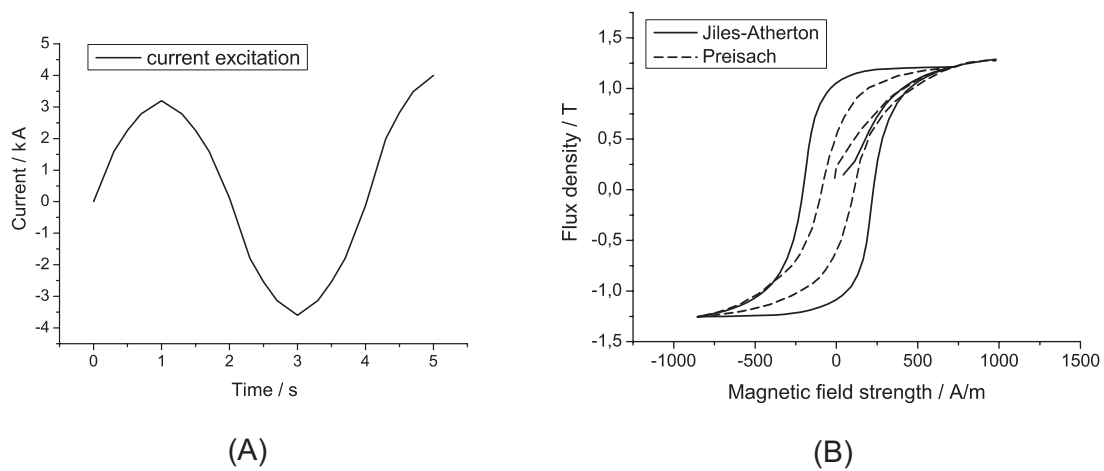


Figure 4.21: (A) Low excitation current, (B) Comparison of the hysteresis loops simulated by inverse Preisach model and by the inverse Jiles-Atherton model for low excitation current.

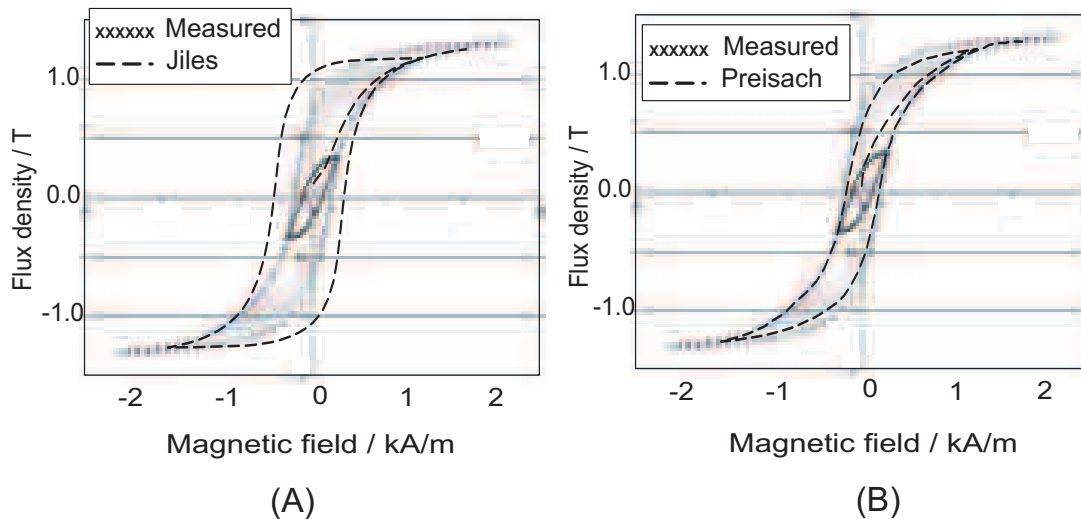


Figure 4.22: Low excitation current: (A) Comparison of the loop simulated by the inverse Jiles-Atherton model and the measured curves, (B) Comparison of the loop simulated by the inverse Preisach model and the measured curves.

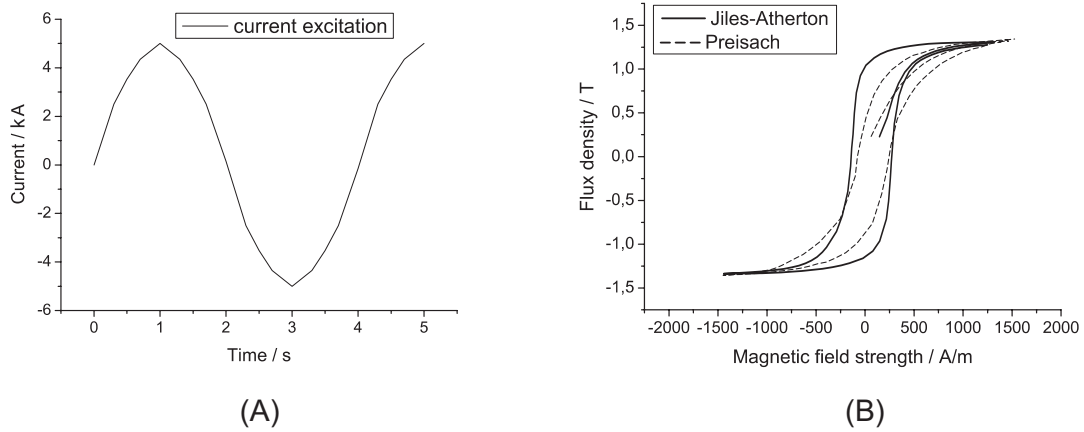


Figure 4.23: (A) High excitation current, (B) Comparison of the hysteresis loop simulated by the inverse Preisach model and by the inverse Jiles-Atherton model for higher excitation current.

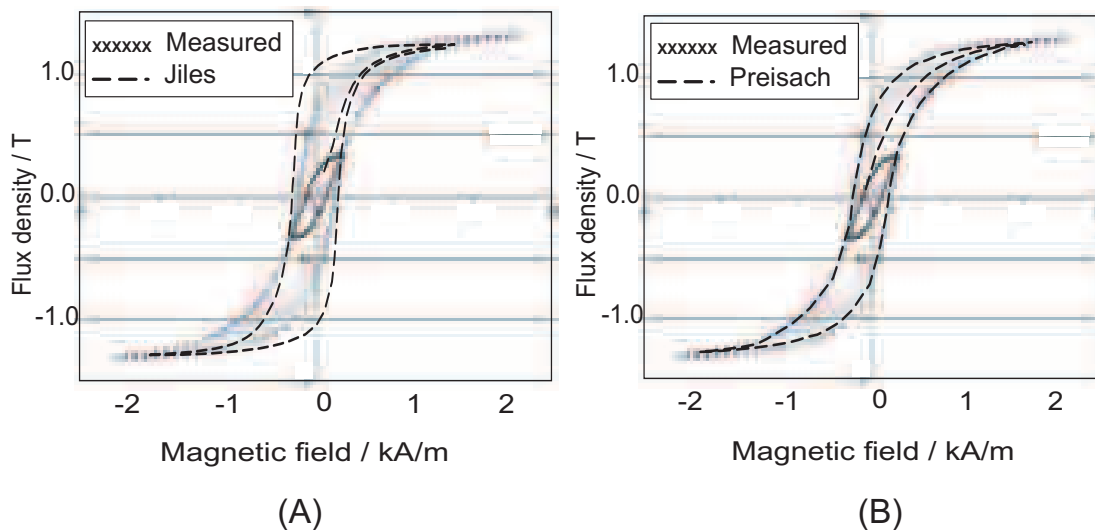


Figure 4.24: High excitation current: (A) Comparison of the loop simulated by the inverse Jiles-Atherton model and the measured curves, (B) Comparison of the loop simulated by the inverse Preisach model and the measured curves.

the CPU time consumption are compared in order to assess the properties of both update schemes. The hysteresis loops simulated by the magnetic polarization update scheme and the Newton-Raphson nonlinear update scheme with the same excitation current are compared in Fig. 4.25 (B). Both simulated hysteresis loops are also compared with the measured first-order transition curves in Fig. 4.26 (A) and (B).

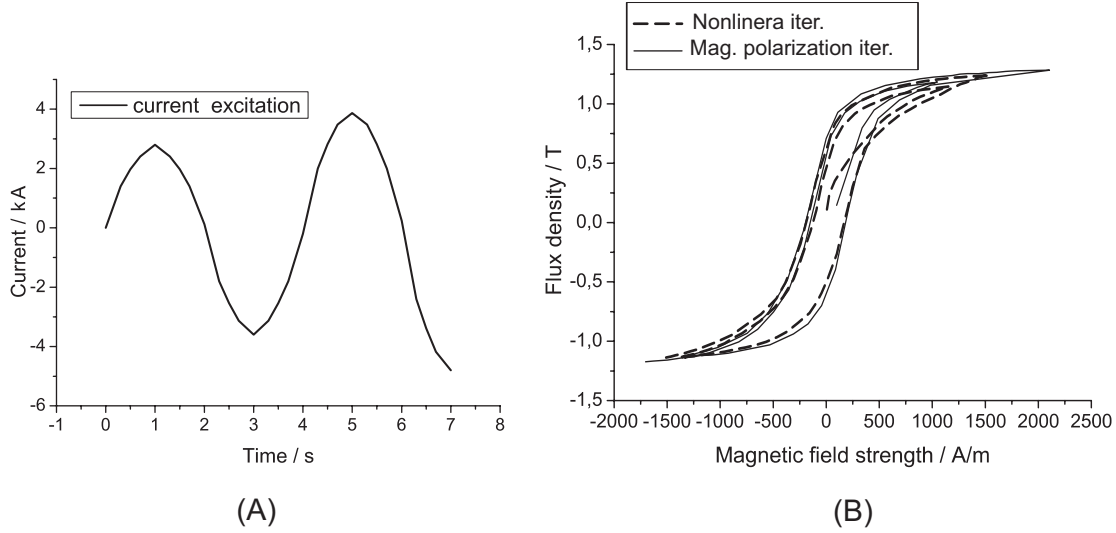


Figure 4.25: (A) Current excitation, (B) Comparison of the hysteresis loop simulated by the magnetic polarization update scheme and the hysteretic nonlinear update scheme with the same current excitation.

Fig. 4.25 (B) indicates that the hysteresis loops simulated by the magnetic polarization update scheme agrees well with the results simulated by the hysteretic nonlinear update scheme, although the two update schemes use different updated parameters. Fig. 4.26 (A) and (B) illustrate that both simulated hysteresis loops are in good agreement with the first-order transition measured curves.

Fig. 4.27 presents the CPU time consumption of the described methods for the test model with different numbers of degrees of freedom and 210 time steps. In the magnetic polarization update scheme, the error tolerance ε defined by $\|\Delta \widehat{\mathbf{m}}_i\|_2 / \|\widehat{\mathbf{m}}_i\|_2$ is set to $1e-3$. The maximum number of magnetic polarization iterations is defined by $n_{max} = 5$. In the nonlinear update scheme, the error tolerance ε defined by $\|\Delta \widehat{\mathbf{b}}_i\|_2 / \|\widehat{\mathbf{b}}_i\|_2$ is set to $1e-4$. The maximum number of Newton-Raphson nonlinear iterations is given by $n_{max} = 12$.

The advantage of the magnetic polarization update scheme is that only the right-hand side of the equation system changes during the iteration. The huge CPU time consumption and the slow convergence is a disadvantage of this update scheme. Unlike the magnetic polarization update scheme, the nonlinear update scheme changes the reluctivity material matrix \mathbf{M}_ν or the differential reluctivity matrix $\mathbf{M}_{\nu,d}$ in each nonlinear iteration. Also an inverse hysteresis model is required. However, according to the CPU time consumption, the nonlinear update scheme are computationally more efficient.

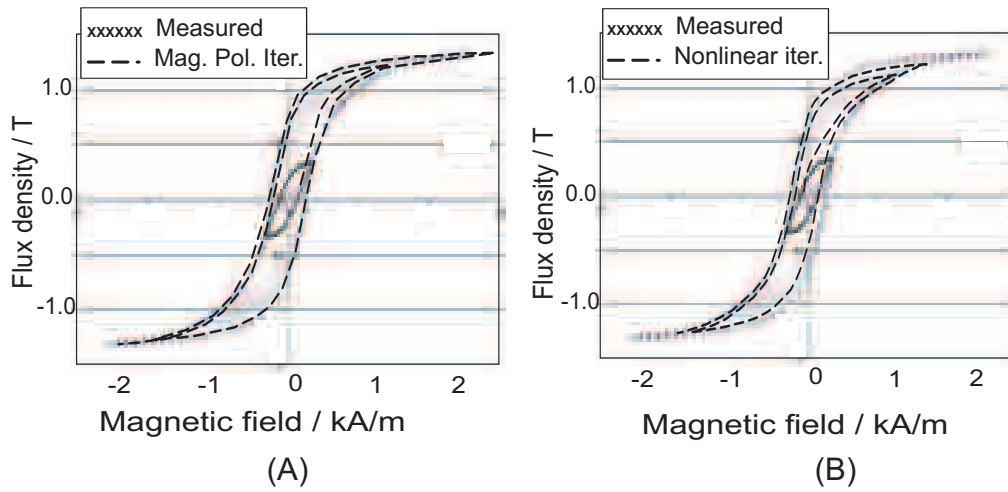


Figure 4.26: (A) Comparison of loop simulated by the magnetic polarization update scheme and the measured curves, (A) Comparison of loop simulated by the hysteretic nonlinear update scheme and the measured curves.

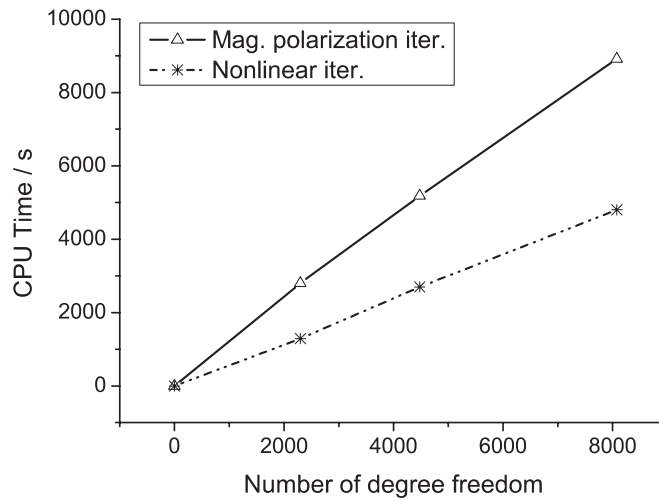


Figure 4.27: CPU time consumption of the magnetic polarization update scheme and the hysteretic nonlinear update scheme (Newton-Raphson iterative scheme) for different number of degrees of freedom.

4.3 Hybrid Newton-Polarization Method

Two schemes were presented for updating the hysteretic material properties: the magnetic polarization update scheme and the nonlinear update scheme. The polarization method is based on the magnetic polarization \vec{P} , which is updated using the scalar Preisach model [16] in the magnetic characteristic $\vec{B} = \mu_0 \vec{H} + \vec{P}$ in each iteration. The polarization approach is known to have a slow convergence. On the other hand, the Newton method applies the differential reluctivity computed by the inverse scalar Preisach model in the magnetic characteristic $\vec{H} = \nu(B) \vec{B}$ throughout the nonlinear iterations. This method can in principle lead to a faster computation, but the biggest difficulty with the method is that convergence cannot be guaranteed, and thus the algorithm generally lacks robustness. That is way the relaxed Newton methods were introduced [92], which used underrelaxation to avoid stagnation of the Newton algorithm. For some difficult strongly nonlinear problems even underrelaxation may not be able to ensure convergence due to the finite precision of the whole calculation process.

Because the polarization method guarantees convergence and the Newton method has quadratic speed of convergence, a hybrid Newton-Polarization method is studied in order to increase the robustness of the nonlinear iteration without losing the quadratic speed of convergence in the vicinity of the solution. The magnetic potential $\hat{\mathbf{a}}$ is used as the main unknown. The idea behind the hybrid method is to combine the underrelaxed Newton method and the overrelaxed polarization method at each iteration. This hybrid algorithm has already been proposed for magnetostatic nonlinear field simulation [89], [90]. This thesis extends the implementation of the hybrid method to the hysteresis case, in conjunction with Finite Integration Implicit Time Domain formulations. Underrelaxation is used to ensure the convergence of the Newton method [92], [93] whereas overrelaxation improves the convergence of the polarization method [91].

4.3.1 Newton Method and Polarization Method

When solved with the polarization method, the nonlinear equation (4.15) in the i -th nonlinear cycle is written by

$$\left[\frac{1}{\Delta t} \mathbf{M}_\kappa + \tilde{\mathbf{C}} \mathbf{M}_{\nu_0} \mathbf{C} \right] \hat{\mathbf{a}}_{i+1}^{(n+1)} = \frac{1}{\Delta t} \mathbf{M}_\kappa \hat{\mathbf{a}}^{(n)} + \hat{\mathbf{j}}_e^{(n+1)} + \tilde{\mathbf{C}} \mathbf{M}_{\nu_0} \hat{\mathbf{p}}_i^{(n+1)}. \quad (4.59)$$

Let the matrices \mathbf{M}_0 and \mathbf{N}_0 be defined as $\mathbf{M}_0 = \frac{1}{\Delta t} \mathbf{M}_\kappa + \tilde{\mathbf{C}} \mathbf{M}_{\nu_0} \mathbf{C}$, $\mathbf{N}_0 = \tilde{\mathbf{C}} \mathbf{M}_{\nu_0}$.

By writing (4.59) at two nonlinear cycles i and $i+1$

$$\begin{aligned} \mathbf{M}_0 \hat{\mathbf{a}}_{i+1}^{(n+1)} &= \hat{\mathbf{j}}_e^{(n+1)} + \frac{1}{\Delta t} \mathbf{M}_\kappa \hat{\mathbf{a}}^{(n)} + \mathbf{N}_0 \hat{\mathbf{p}}_i^{(n+1)}, \\ \mathbf{M}_0 \hat{\mathbf{a}}_i^{(n+1)} &= \hat{\mathbf{j}}_e^{(n+1)} + \frac{1}{\Delta t} \mathbf{M}_\kappa \hat{\mathbf{a}}^{(n)} + \mathbf{N}_0 \hat{\mathbf{p}}_{i-1}^{(n+1)}, \end{aligned} \quad (4.60)$$

and subtracting the two relations we get

$$\mathbf{M}_0 \Delta \hat{\mathbf{a}}_{i+1}^{(n+1)} = \mathbf{N}_0 \Delta \hat{\mathbf{p}}_i^{(n+1)}, \quad (4.61)$$

where $\Delta \hat{\mathbf{a}}_{i+1}^{(n+1)} = \hat{\mathbf{a}}_{i+1}^{(n+1)} - \hat{\mathbf{a}}_i^{(n+1)}$ and $\Delta \hat{\mathbf{p}}_i^{(n+1)} = \hat{\mathbf{p}}_i^{(n+1)} - \hat{\mathbf{p}}_{i-1}^{(n+1)}$.

For the right hand side of expression (4.61) we have

$$\begin{aligned}
\mathbf{N}_0 \Delta \widehat{\mathbf{p}}_i^{(n+1)} &= \widetilde{\mathbf{C}} \mathbf{M}_{\nu_0} [\widehat{\mathbf{p}}_i^{(n+1)} - \widehat{\mathbf{p}}_{i-1}^{(n+1)}] = \\
&= \widetilde{\mathbf{C}} \mathbf{M}_{\nu_0} \widehat{\mathbf{p}}_i^{(n+1)} + \widehat{\mathbf{j}}_e^{(n+1)} + \frac{1}{\Delta t} \mathbf{M}_\kappa \widehat{\mathbf{a}}^{(n)} - \left[\frac{1}{\Delta t} \mathbf{M}_\kappa + \widetilde{\mathbf{C}} \mathbf{M}_{\nu_0} \mathbf{C} \right] \widehat{\mathbf{a}}_i^{(n+1)} \\
&= -\frac{1}{\Delta t} \mathbf{M}_\kappa (\widehat{\mathbf{a}}_i^{(n+1)} - \widehat{\mathbf{a}}^{(n)}) - \widetilde{\mathbf{C}} [\mathbf{M}_{\nu_0} \mathbf{C} \widehat{\mathbf{a}}_i^{(n+1)} - \mathbf{M}_{\nu_0} \widehat{\mathbf{p}}_i^{(n+1)}] + \widehat{\mathbf{j}}_e^{(n+1)} \\
&= -\frac{1}{\Delta t} \mathbf{M}_\kappa (\widehat{\mathbf{a}}_i^{(n+1)} - \widehat{\mathbf{a}}^{(n)}) - \widetilde{\mathbf{C}} \mathbf{M}_{\nu_0} [\widehat{\mathbf{b}}_i^{(n+1)} - \widehat{\mathbf{p}}_i^{(n+1)}] + \widehat{\mathbf{j}}_e^{(n+1)}. \quad (4.62)
\end{aligned}$$

According to the equation (4.1)

$$\mathbf{M}_{\nu_0} \widehat{\mathbf{b}}_i^{(n+1)} - \mathbf{M}_{\nu_0} \widehat{\mathbf{p}}_i^{(n+1)} = \widehat{\mathbf{h}}_i^{(n+1)} = \mathbf{M}_\nu (\widehat{\mathbf{b}}_i^{(n+1)}) \widehat{\mathbf{b}}_i^{(n+1)}, \quad (4.63)$$

so that

$$\mathbf{N}_0 \Delta \widehat{\mathbf{p}}_i^{(n+1)} = \frac{1}{\Delta t} \mathbf{M}_\kappa \widehat{\mathbf{a}}^{(n)} - \left[\frac{1}{\Delta t} \mathbf{M}_\kappa + \widetilde{\mathbf{C}} \mathbf{M}_\nu \mathbf{C} \right] \widehat{\mathbf{a}}_i^{(n+1)} + \widehat{\mathbf{j}}_e^{(n+1)}. \quad (4.64)$$

Thus the following relation is obtained:

$$\widetilde{\mathbf{C}} \mathbf{M}_{\nu_0} \Delta \widehat{\mathbf{p}}_i^{(n+1)} = \frac{1}{\Delta t} \mathbf{M}_\kappa \widehat{\mathbf{a}}^{(n)} - \left[\frac{1}{\Delta t} \mathbf{M}_\kappa + \widetilde{\mathbf{C}} \mathbf{M}_\nu \mathbf{C} \right] \widehat{\mathbf{a}}_i^{(n+1)} + \widehat{\mathbf{j}}_e^{(n+1)}. \quad (4.65)$$

From (4.61) and (4.65), the relation is obtained for the polarization method:

$$\left[\frac{1}{\Delta t} \mathbf{M}_\kappa + \widetilde{\mathbf{C}} \mathbf{M}_{\nu_0} \mathbf{C} \right] \Delta \widehat{\mathbf{a}}_{i+1}^{(n+1)} = \frac{1}{\Delta t} \mathbf{M}_\kappa \widehat{\mathbf{a}}^{(n)} - \left[\frac{1}{\Delta t} \mathbf{M}_\kappa + \widetilde{\mathbf{C}} \mathbf{M}_\nu \mathbf{C} \right] \widehat{\mathbf{a}}_i^{(n+1)} + \widehat{\mathbf{j}}_e^{(n+1)}. \quad (4.66)$$

Comparing (4.66) with (4.56) shows that the polarization method can be understood as a Newton method with the dynamic reluctivity replaced by that of vacuum. Therefore the same code line of the Newton algorithm can be used for implementing both methods. Based on this observation, an efficient implementation of a hybrid algorithm can be achieved for transient hysteretic magnetic field problems.

4.3.2 Hybrid Newton-Polarization Method

The purpose of the hybrid Newton-Polarization method is to increase the robustness of the nonlinear iteration, without losing the quadratic speed of convergence in the vicinity of the solution. A hybrid method combining the advantages of the two methods was proposed in [90], which is a polarization $\widehat{\mathbf{p}}$ -oriented integral method for solving the nonlinear problem using the Finite Element Method. A similar hybrid method using the magnetic vector potential as the main unknown of the field problem was introduced in [89], in conjunction with the FIT. This hybrid method is extended to transient hysteretic magnetic field problems in the following. A robust polarization algorithm must, however, deal with possible non-convergence of the Newton method, by eventually switching between the truly-hybrid method and just Newton method when the iteration starts to stagnate, or appears to converge, respectively.

At each iteration, a Newton iteration and a polarization iteration are performed. The vector $\widehat{\mathbf{a}}$ related to the magnetic potential is taken as the main unknown. A hybrid solution is obtained at each nonlinear iteration cycle by writing

$$\begin{aligned}\Delta\widehat{\mathbf{a}}_{i+1}^{(n+1)} &= \gamma\Delta\widehat{\mathbf{a}}_{P,i+1}^{(n+1)} + \delta\Delta\widehat{\mathbf{a}}_{N,i+1}^{(n+1)}, \\ \widehat{\mathbf{a}}_{i+1}^{(n+1)} &= \widehat{\mathbf{a}}_i^{(n+1)} + \Delta\widehat{\mathbf{a}}_{i+1}^{(n+1)},\end{aligned}\quad (4.67)$$

where i denotes the index of the nonlinear iteration cycle, and n is the index of the time step. The vector $\Delta\widehat{\mathbf{a}}_{P,i+1}^{(n+1)} = \widehat{\mathbf{a}}_{P,i+1}^{(n+1)} - \widehat{\mathbf{a}}_{P,i}^{(n+1)}$ is computed with the polarization method, where the vectors $\widehat{\mathbf{a}}_{P,i+1}^{(n+1)}$ and $\widehat{\mathbf{a}}_{P,i}^{(n+1)}$ are computed according to formula (4.15). The vector $\Delta\widehat{\mathbf{a}}_{N,i+1}^{(n+1)} = \widehat{\mathbf{a}}_{N,i+1}^{(n+1)} - \widehat{\mathbf{a}}_{N,i}^{(n+1)}$ is computed with the Newton method, where the vectors $\widehat{\mathbf{a}}_{N,i+1}^{(n+1)}$ and $\widehat{\mathbf{a}}_{N,i}^{(n+1)}$ are computed according to equation (4.57). The values γ and δ are obtained by a two-dimensional minimization of a cost function, e.g. the residual of the nonlinear or the energy functional.

The two-dimensional Powell method [94] is used for performing this minimization with the residual norm of the nonlinear equation as a cost function. The two-dimensional Powell method is a special case of Powell's quadratically convergent method. In the hybrid method, the two-dimensional Powell method selects the best direction, i.e. the best choice of the values γ and δ in (4.67) minimizing the residual norm of the nonlinear equation $\|\frac{1}{\Delta t}\mathbf{M}_\kappa(\widehat{\mathbf{a}}_{i+1}^{(n+1)} - \widehat{\mathbf{a}}_i^{(n)}) + \widetilde{\mathbf{C}}\widehat{\mathbf{h}}_{i+1}^{(n+1)} - \widehat{\mathbf{j}}_e^{(n+1)}\|_2$, where the vector $\widehat{\mathbf{h}}_{i+1}^{(n+1)} = \mathbf{M}_\nu\mathbf{C}\widehat{\mathbf{a}}_{i+1}^{(n+1)}$ is obtained in each nonlinear iteration cycle according to equation (4.58).

4.3.3 Test Example A and Discussion

A 3D hysteretic transient test problem is used for assessing the properties of the hybrid method. In order to compare the hybrid method with the standard polarization method or the standard Newton method, the same test model (Fig. 4.6) as for the magnetic polarization update scheme or for the hysteretic nonlinear update scheme is taken. The same current excitation (see Fig. 4.25 (A)) is selected, too. The 3D model and 2D cut face of the model are shown in Fig. 4.6. The non-hysteretic ferromagnetic material is introduced in Appendix A Table A.2. The characteristic of the hysteretic ferromagnetic material is given by a set of measured first-order transient curves (4.28 (A)) and introduced in Appendix A Table A.3. The comparison of the measured and the simulated hysteresis loop is shown in Fig. 4.28. The simulated hysteresis loop is shown in Fig. 4.28 (B).

The nonlinear iterative procedure is controlled by the error $\varepsilon = \|\Delta\widehat{\mathbf{b}}_i\|_2 / \|\widehat{\mathbf{b}}_i\|_2$. Fig. 4.29 shows the convergence curves for the polarization method, the Newton method and the hybrid method in terms of the relative nonlinear error ε vs. the numbers of nonlinear iterations for one implicit Euler time step.

It can be seen that the polarization method converges very slowly. The Newton method features a quadratic speed of convergence when the nonlinear accuracy is smaller than 10^{-6} . The hybrid method needs only a few nonlinear iterations per time step, but each nonlinear iteration consumes more solving time than those of the other methods.

Fig. 4.30 presents the CPU time consumption for different numbers of degrees of freedom required for the described methods for all 140 time steps in seven seconds current excitation time.

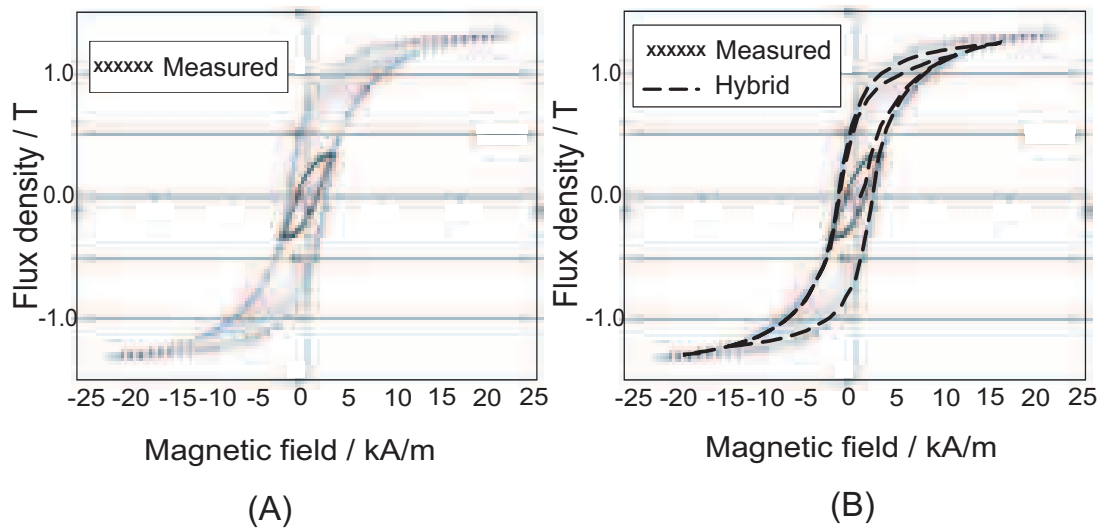


Figure 4.28: (A) Set of hysteretic loops. (B) Comparison of measured and simulated hysteresis loops.

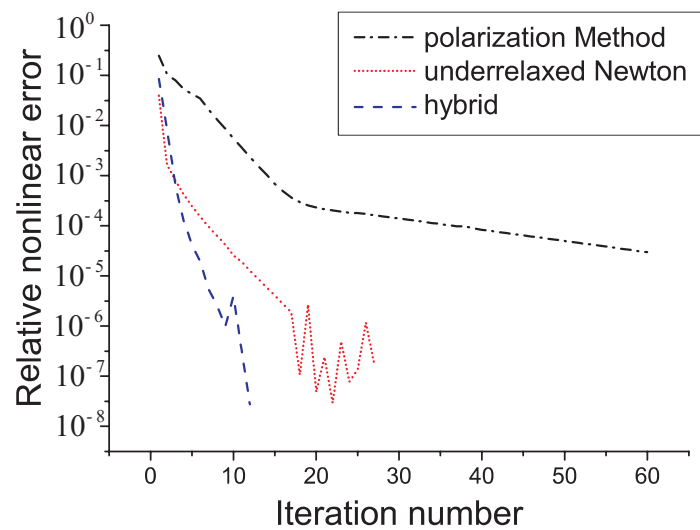


Figure 4.29: Relative nonlinear error of the iteration schemes as a function of the number of iterations.

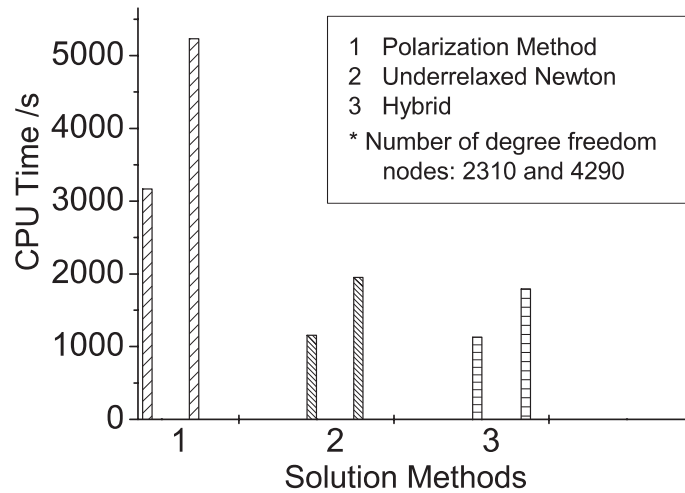


Figure 4.30: CPU time consumption of the polarization, Newton and the hybrid Newton-polarization method for 140 time steps in 7 seconds current excitation time for different number of degrees of freedom.

The various parameters used in the test problem are: linear solver precision, nonlinear iteration precision, tolerance of the 2D Powell's minimization method, and limits of the optimal values for γ and δ . By varying these parameters, the following conclusions were found:

Linear solver precision: Linear systems are solved using the Conjugate Gradient method with SSOR (Symmetric Successive Over Relaxation) preconditioning. A higher linear solver precision causes a higher CPU time consumption but also brings robustness into the nonlinear iteration [95] [97]. For this test problem, a linear solver precision of 10^{-5} is a good choice, whereas a linear solver precision of 10^{-9} takes longer for solving a system and does not improve the convergence of the nonlinear iteration.

Nonlinear iteration precision: The nonlinear iteration process is controlled by the nonlinear error ε . A too high precision leads to an increase of the computation time, a too low precision causes inaccuracies in the time stepping process [95] [97]. For this test problem, according to the comparison of the convergence rates in Fig. 4.29, it is found that the nonlinear iteration precision taken as 10^{-4} is the better choice for the hybrid methods.

Tolerance of the 2D Powell minimization method: The Powell quadratically convergent method is a direction set method that does produce N mutually conjugate directions. The tolerance of the 2D Powell minimization method does not need to be made too precise, since the self-correcting properties of the hybrid method being able to compensate for inaccuracies during the computation. For this reason, the tolerance is taken as high as 0.01 and the maximum number of iterations in the Powell method is limited to 10, which was shown to be sufficient for the test problem.

Limits for the optimal values γ and δ : Too tight or too relaxed limits for γ and δ both lead to an unacceptable increase of the computation time. To keep the idea of "relaxation", γ is selected in the interval $[0, 1]$. As the value δ , the selected interval is $[0, 1]$ as well.

The hybrid method is compared to the standard Newton method and the polarization method regarding the CPU time consumption and the convergence of the nonlinear residual. For the test problem, it can be concluded that the hybrid method requires a comparable amount of computation time as the Newton nonlinear iterative scheme. Additionally, the robustness is increased because of the combination with the polarization method.

4.4 Vector Hysteresis Model

Although scalar Preisach models have become increasingly accurate and efficient for describing hysteretic material behavior, in many cases the magnetizing processes is vectorial in nature.

The magnetization processes under rotational fields undergo several changes at different magnetization levels: at low fields 180° domain wall motion prevails, while at intermediate fields the 90° walls become important. Finally, at high induction levels the local magnetization inside a grain can deviate from the easy direction for coherent rotation. The coherent rotation process is in fact responsible for the decrease of rotational losses at high fields, when the magnetizing vector saturates and becomes parallel to the field. Aiming at the development of a physically based vector hysteresis model includes the construction of a model able to describe domain wall motion and coherent rotation and able to depict the transition from domain wall motion to coherent rotation. This makes the design of a proper vector hysteresis model a difficult task.

A vector Preisach model was introduced by Mayergoyz in [16] and [12], which is constructed from a continuum of scalar Preisach transducers, each incrementally rotated from its neighbor. The input to each transducer is the component of the applied field in the transducer's direction and the output of each transducer is a magnetization in that direction. The output of the complete model is the vector sum of the output of all transducers. It is well known that classical scalar Preisach model is limited by the congruency property and the deletion property. The limitations are modified by the moving model to relax the congruency property and by the generalized model to relax the deletion property. The vector models must feature two additional properties. The first of these properties is the saturation property, which corresponds to the requirement that all magnetization calculated by the model do not exceed saturation and that a large enough field can actually achieve saturation. The second is the loss property, which corresponds to the fact that as the size of a rotational field increases, the losses first increase and then decrease. Details on this process were introduced in subsection (2.3.5).

Another approach to vector hysteresis approximates the medium by using a small number of basic particles combined into what is called a pseudo particle. Two such models have been proposed by Oti. One uses the Stoner-Wohlfarth model for the basic particles [32], and the other uses the results of a micromagnetic calculation [33]. The vector model was treated by considering the material consisting of an assembly of identical in [34], non-interacting, single-domain uniaxial particles. This model was extended in [35] and the switching criterium was modified to that derived from the Stoner-Wohlfarth model [22]. Although the models assume that the hysterons are particles, their results can easily be extended to granular media.

In [36] a vector model was introduced in which the scalar Preisach models respond to perpendicular field components: the fundamental assumption of the proposed model is that field components perpendicular to the axis associated with a scalar Preisach model have the effect of a partial AC demagnetization on that model. This model was based on a series of measurements showing that when a material is magnetized in one direction, it eventually becomes demagnetized in the perpendicular direction. The degree of demagnetization depends on the magnitude of the field, and is complete for large magnetic fields. The vector Preisach model was proposed by Wiesen and Charap in [36] and [37]. It involves a modification of the scalar Preisach model by including a response to field components normal to the axes of the model. The simplified vector Preisach model proposed by E. Della Torre in [18] belongs to this category. A new algorithm for the simplified vector Preisach model was introduced in [20] to extend the model from 2D to 3D and to provide an efficient implementation of the model.

A composite of the scalar Preisach model and particle assembly modelling of vector hysteresis was introduced in [32], [38]. Two different straightforward identification procedures for combined Preisach and Stoner-Wohlfarth vector hysteresis models have been presented in [38] and [39], respectively. Several other vector hysteresis models have been proposed in literature [40], [41], [42], [43], [44], [45] [120].

4.4.1 Simplified Vector Preisach Model

Many vector models have been proposed which have the correct rotational properties and reduce to scalar Preisach models under the appropriate conditions. The simplified vector model is one of the most computationally efficient vector models, since the magnetization is computed without iterating between two or three independent scalar Preisach models. This is permitted by concentrating all the coupling in some selection rules. Compared with other vector hysteresis models it overcomes many limitations and implementation difficulties in the numerical computation. For this reason, the simplified vector Preisach model is implemented.

The simplified vector model consists of defining scalar Preisach models only for the principal axes of the system, two in the 2D case and three in the 3D case. The total magnetization is the vector sum of the irreversible \vec{M}_I and the reversible \vec{M}_R components

$$\vec{M} = \vec{M}_I + \vec{M}_R. \quad (4.68)$$

The simplified vector model computes the normalized irreversible magnetization vector \vec{M}_I as the product of a rotational correction factor R and three independent scalar Preisach models oriented along the x, y , and z axes. The outputs I_j from these scalar Preisach models are computed by the integral

$$I_j = \iint_{v_j < u_j} Q_j(\Omega) p(\Omega) d\Omega, \quad (4.69)$$

where $j = x, y$, or z , p is the normalized Preisach function, Ω is the collection of the up and down switching fields u and v along the three axes, and Q_j is the j component of the state function Q .

The simplified vector model computes the magnetization in several steps. First, selection rules determine the magnetic state of the system. The magnetic state value Q_j depends on the applied field h in all three directions and u and v in all three directions. The second step involves computing three independent scalar Preisach integrals and from them a rotational correction. The basic integrals are computed independently using the Preisach function, which is a function of the applied field. The rotational correction is introduced to repair the distortions introduced by the selection rules. Finally, the product of the basic integrals and the rotational correction are added vectorially to obtain the vector magnetization.

The magnetic state vector Q is first defined by selection rules delineated in two dimensions only. More information on how to determine Q for 2D models was introduced in [46], [5] and [18]. A generalization of the selection rules to three dimensions was introduced in [20]. A table determines the state $Q_j(h, u, v)$, where $j = x, y$ or z . This is illustrated in Table (4.4). If the inequality $v_j \leq h_j \leq u_j$ holds for all three directions, then there is no change in the state value for that hysteron. However, if there are any violations of the inequality, there will be a change in state. Table (4.4) shows these states as a function of the number of violations: one, two, or three. The values for Q are then used to compute the components of the irreversible magnetization \vec{m}_{Ij} values.

Table 4.4: State function values Q in 3D

Number of violations	Violations	States
0	$v_j \leq h_j \leq u_j$ holds for $j = x, y$ and z	no change
1	$h_j > u_j$ or $h_j < v_j$	$Q_j = 1$ or $Q_j = -1$ and $Q_i = 0, i \neq j$
2	Any two combinations of violations in u or v where the violated thresholds are obtained by t_j and t_k .	$Q_j = \frac{h_j - t_j}{ h_j - t_j + h_k - t_k }$ and $Q_k = \frac{h_k - t_k}{ h_j - t_j + h_k - t_k }$ $Q_i = 0, i \neq j, k$
3	Any three combinations of violations in u or v where the violated thresholds are obtained by t_i, t_j and t_k .	$Q_i = \frac{h_i - t_i}{ h_i - t_i + h_j - t_j + h_k - t_k }$ and $Q_j = \frac{h_j - t_j}{ h_i - t_i + h_j - t_j + h_k - t_k }$ $Q_k = \frac{h_k - t_k}{ h_i - t_i + h_j - t_j + h_k - t_k }$

The rotational correction factor $R(I_x, I_y, I_z)$ is used to compute the components of the irreversible magnetization \vec{m}_{Ij}

$$\begin{aligned} m_{Ix} &= R(I_x, I_y, I_z)I_x, \\ m_{Iy} &= R(I_x, I_y, I_z)I_y, \\ m_{Iz} &= R(I_x, I_y, I_z)I_z, \end{aligned} \quad (4.70)$$

or,

$$\vec{m}_I = R\vec{I}, \quad (4.71)$$

where the I 's are computed using formula (4.69), and the rotation correction factor

$R(I_x, I_y, I_z)$ is computed from the three components of I

$$R(I_x, I_y, I_z) = \frac{|I_x| + |I_y| + |I_z|}{\sqrt{I_x^2 + I_y^2 + I_z^2}}. \quad (4.72)$$

The factor $R(I_x, I_y, I_z)$ takes into account the distortion introduced the selection rules for $Q = [Q_x \ Q_y \ Q_z]$ and ensures that the magnitude of the magnetization will never exceed saturation, regardless of the direction of the applied field.

It is noted that when the applied field is not along a principal axis, none of the vector hysteresis models reduces to a simple vector model because the magnetization is not in the same direction as the applied field. Since the model involves only the computation of hysteresis models along the principal axes the efficiency of the model is guaranteed.

So far only the irreversible component of the magnetization is computed by the simplified vector model. The total magnetization is composed of an irreversible component M_I and a reversible component M_R . In order to describe realistic media, the reversible component must be added to the irreversible component. The reversible magnetic magnetization can be computed from the irreversible results according to the magnetization-dependent reversible model [5] [47] or the state-dependent reversible model [5] [48].

4.4.2 Test Example B and Discussion

The test example B is used to validate the simplified vector Preisach model combined with the nonlinear update scheme linearized by the Newton-Raphson method. In the update process for the differential reluctivity material matrix \mathbf{M}_{ν_d} in isotropic media, the differential reluctivity ν_d is calculated from the flux density components $b_{1,d}$, and $b_{2,d}$, and the field strength components $h_{1,d}$, $h_{2,d}$, where the d is along x , y , or z direction,

$$\nu_d = \frac{\sqrt{h_{1,x}^2 + h_{1,y}^2 + h_{1,z}^2} - \sqrt{h_{2,x}^2 + h_{2,y}^2 + h_{2,z}^2}}{R(b_{1,x}, b_{1,y}, b_{1,z})\sqrt{b_{1,x}^2 + b_{1,y}^2 + b_{1,z}^2} - R(b_{2,x}, b_{2,y}, b_{2,z})\sqrt{b_{2,x}^2 + b_{2,y}^2 + b_{2,z}^2}}, \quad (4.73)$$

where the flux densities components $b_{1,d}$ are calculated from expression (4.57) at each nonlinear iteration, the components $b_{2,d}$ are calculated from expression (4.50) according to the components $b_{1,d}$. The field strength components $h_{1,d}$ and $h_{2,d}$ are evaluated by the scalar inverse Preisach model according to the flux density components $b_{1,d}$ and $b_{2,d}$, respectively. The rotational correction factor $R(b_x, b_y, b_z)$ is given by

$$R(b_x, b_y, b_z) = \frac{|b_x| + |b_y| + |b_z|}{\sqrt{b_x^2 + b_y^2 + b_z^2}}. \quad (4.74)$$

A test problem is used for assessing the properties of the simplified vector model: the hysteretic material (Appendix A: Table A.3) is surrounded by a double ferromagnetic nonlinear yoke (Appendix A: Table A.2). Two systems of idealized coils with perpendicular magnetic axes are driven to realize different magnetization and demagnetization tests. The sequence of current step analyzed are: first, magnetization along the vertical axis; then,

evaluation of the remanence reducing the current to zero on the vertical coils; last, partial magnetization along the horizontal axis with a current set to half of the maximum value reached by the vertical coils. The 3D test model is shown in Fig. 4.31 (B), the 2D cut face of the test model is shown in Fig. 4.31 (A). Fig. 4.32 shows the time dependence of the current excitation, and the behavior of the flux density in case of magnetization along the vertical axis ($t = 3s$).

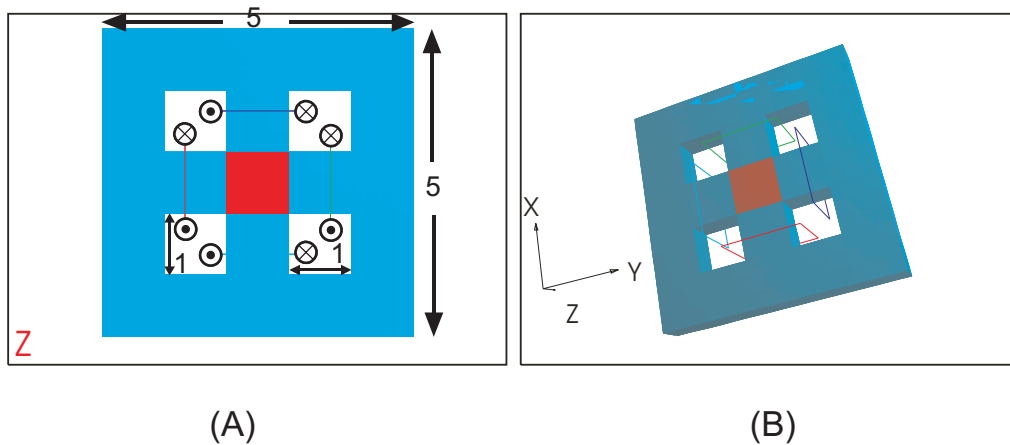


Figure 4.31: (A) 2D cut face of the test model (dimension in m, $z = 3m$), (B) 3D view of the test model: the hysteretic material (dark) is surrounded by a double ferromagnetic nonlinear yoke.

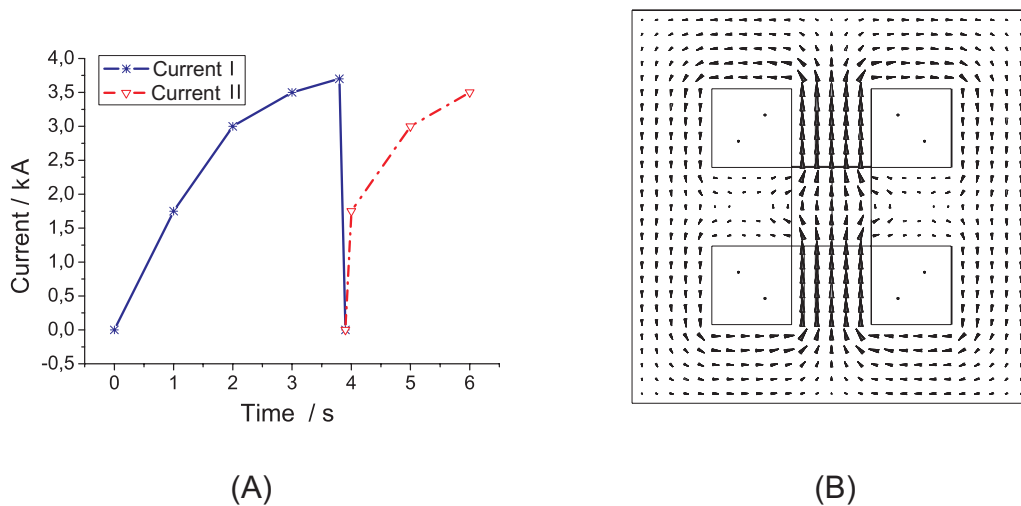


Figure 4.32: (A) The current excitation along the vertical and horizontal axis: Current I along the vertical axis, Current II along the horizontal axis. (B) Simulated flux density in case of magnetization along the vertical axis ($t=3s$).

In Fig. 4.33 (A) the behavior of the flux density in case of partial magnetization along the horizontal axis ($t > 4s$) is shown. As illustrated by the flux densities computed by a standard non-hysteretic nonlinear solution and by a hysteretic nonlinear solution, the

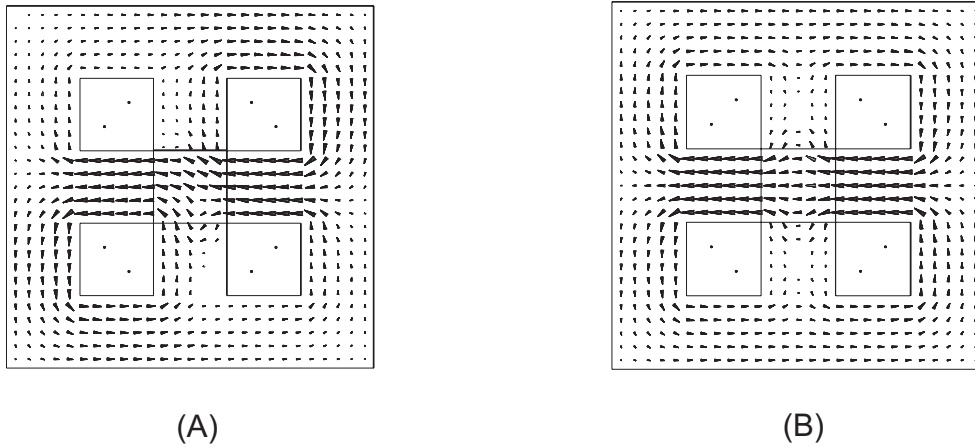


Figure 4.33: (A) Flux density in case of partial magnetization along the horizontal axis ($t > 4s$) simulated by the simplified vector Preisach model with hysteretic material, (B) Flux density in case of partial magnetization along the horizontal axis ($t > 4s$) simulated without hysteretic material.

qualitative behavior of the flux density computed by a hysteretic nonlinear solution is modified by the presence of the memory of the previous magnetization along the vertical axis.

Chapter 5

Technical Application

The previous chapters concentrated on particular aspects of hysteresis modelling, magnetoquasistatic field simulation using FIT, and implementation of hysteresis effects. The magnetic polarization update scheme and the nonlinear update scheme were discussed according to two different models of ferromagnetic material behavior. The Preisach model and the Jiles-Atherton model were considered as hysteresis models in the numerical computation. Both scalar and vector hysteresis models were used for hysteresis simulation. In this chapter, all these aspects are reconsidered, by means of the technically relevant example, known as TEAM benchmark problem 32. Basically, the example is studied with the focus on the following aspects:

- 1) magnetoquasistatic analysis,
- 2) (inverse) Preisach model,
- 3) nonlinear iterative scheme,
- 4) scalar hysteresis model and vector hysteresis model.

According to the tests in Chapter 4, the results simulated with the Jiles-Atherton model have a good agreement with the measured curves only if the excitation keeps the hysteretic material saturated. Therefore, the Jiles-Atherton model is not considered for the technical application in this chapter. The magnetic polarization iterative scheme requires much more computation time than the nonlinear updated scheme. For efficiency reasons, the magnetic polarization iterative scheme is not discussed for the example.

5.1 TEAM Benchmark Problem 32

The TEAM benchmark problem 32 [121], [122] is a typical benchmark problem for the validation of magnetic field analysis with hysteresis. The test model is a three-limbed ferromagnetic core, as presented in Fig. 5.1. The core is constructed of five Fe-Si 3.2% wt, 0.48 mm thick laminations, having a conductivity $\kappa = 1.78$ Ms/m and mass density $\delta = 7650$ kg/m³. Two windings with 90 turns are placed on the external limbs; the DC resistance of each winding is 0.32 Ω . These windings can be both connected together or supplied by two independent controlled voltage sources driven by a power amplifier. Pick-up coils (C1-C3) of 5 turns (Fig. 5.1) are placed in different parts of the core in order to

measure local magnetic flux densities. Low-noise preamplifiers, having a gain of 1 to 50000 and a noise of 1,265nV at 10 Hz, enable a satisfactory accuracy for flux density values greater than 10 mT at 10 Hz. The material experimental data are provided by a set of measured unidirectional symmetrical loops. Experimental data are available at [122]. The analysis is performed at a frequency of 10 Hz. At this frequency the signal amplitudes guarantee a good accuracy of the experimental data, while the influence of skin effect is negligible.

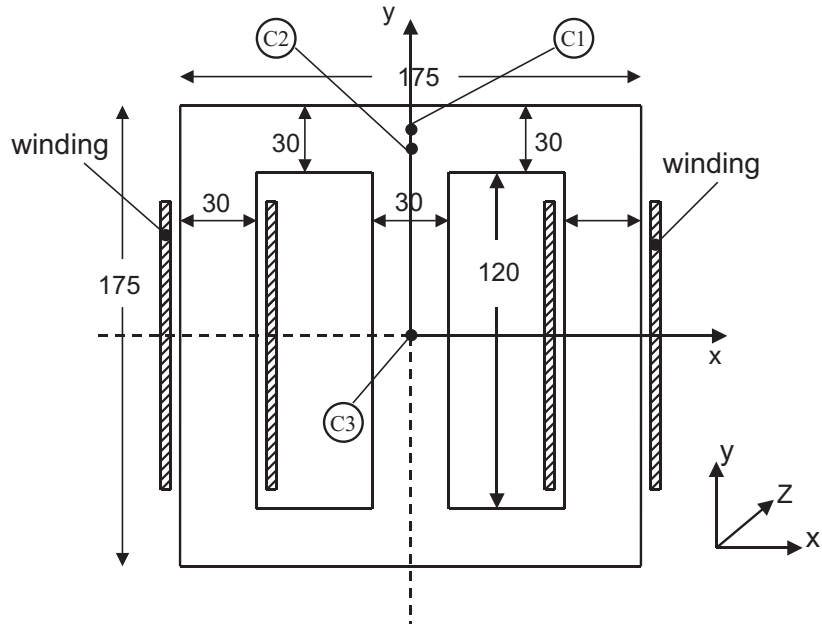


Figure 5.1: 2D structure of the three-limbed ferromagnetic core for the TEAM Benchmark Problem 32, with pick-up coils C1, C2, C3 (dimension in mm, $z = 2.5\text{mm}$).

In this thesis, the TEAM benchmark problem 32 was considered for two different supply conditions:

- **CASE I:** the windings are connected in series with an additional resistance $R_s = 11.1 \Omega$; the series is supplied by a controlled sinusoidal voltage of 13.5 V (peak value);
- **CASE II:** each winding is connected in series with a 11.1Ω resistance, one is supplied by a sinusoidal voltage (14.5 V peak value), the other is supplied by a co-sinusoidal voltage (14.5 V peak value).

Table 5.1: Overview of the different excitations

	left winding	right winding	connection condition	resistance	voltage (peak value)
Case I	sinusoidal excitation	sinusoidal excitation	in series	11.1Ω	13.5 V
Case II	sinusoidal excitation	co-sinusoidal excitation	separate	left: 11.1Ω right: 11.1Ω	left: 14.5 V right: 14.5 V

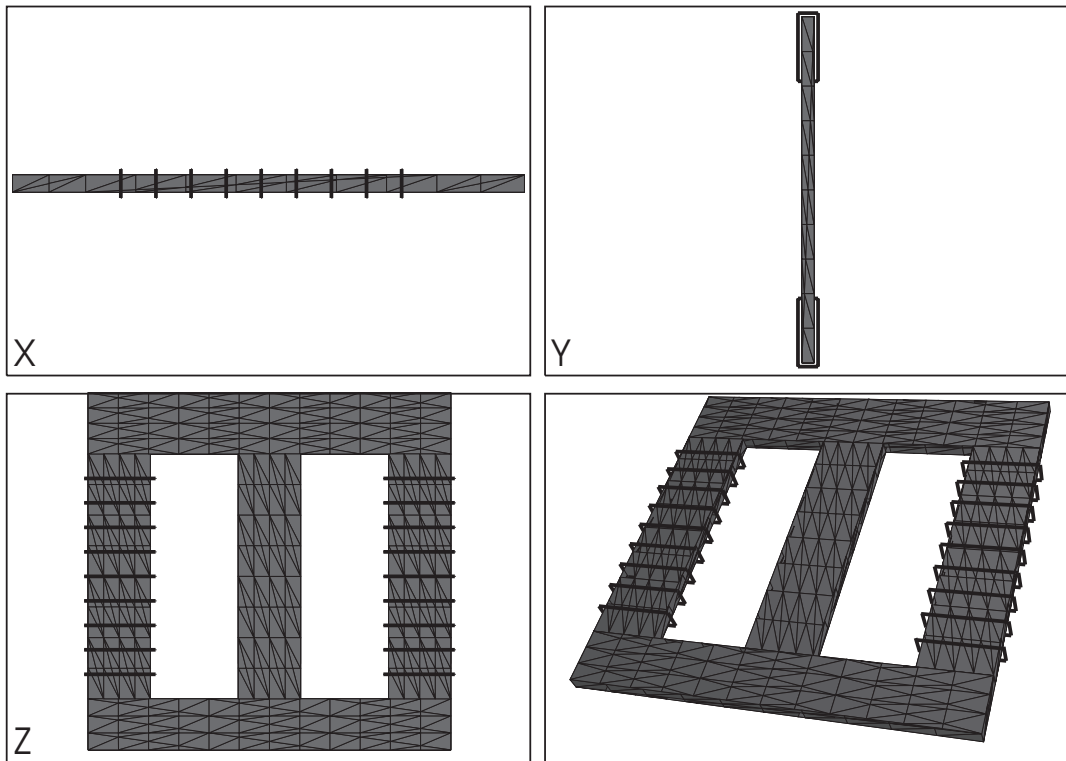


Figure 5.2: 3D model of the simplified model and 2D cut plane of the simplified model in x -, y -, z -directions, (with 9 turns of the windings around the external limbs).

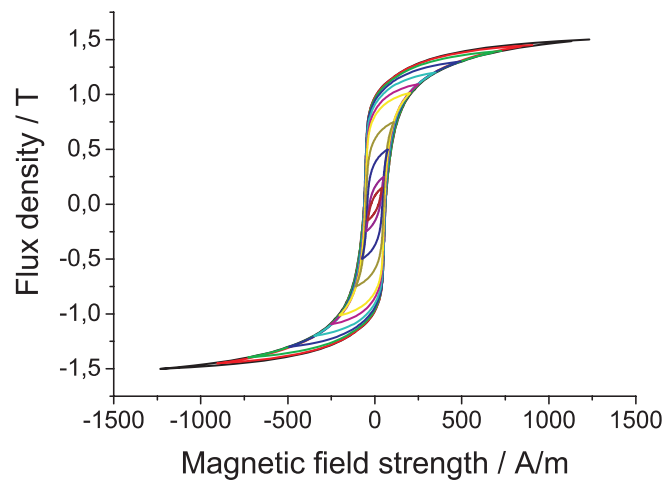


Figure 5.3: A set of measured unidirectional symmetrical hysteresis loops in rolling direction.

5.1.1 Simplified Model for the TEAM Benchmark Problem 32

The TEAM Benchmark Problem 32 was simplified in order to realize the numerical simulation in this thesis. Because the structure of the TEAM Benchmark Problem 32 is only 2.5 mm thick versus a cross section dimension of 175 mm, the big difference in the space ratio between the two directions will cause a difficulty in mesh distribution for 3D simulation. The structure of the simplified model in x-, y-, and z-directions are selected as 175 mm, 175 mm, and 6 mm, respectively. The 3D simplified model and 2D cut plane in x-, y-, and z-directions of the simplified model are shown in Fig. 5.2. The laminated structure of the three-limbed ferromagnetic core is represented by the definition of the conductivity $\kappa_z = 0$ in z-direction. The two windings on the external limbs are reduced from 90 turns to 9 turns, and the current excitations are increased to 10 times of the original excitations in order to remain the NI value (N is the coil number of the winding and I is the current excitation). For simulations which do not incorporate external circuit connections, the current waveform can be directly used as the input. For this reason, the two windings are supplied by current sources instead of the original voltage sources of the TEAM Benchmark Problem 32.

The TEAM Benchmark Problem 32 is made of rolled sheets with different magnetic direction. The measured data of the TEAM Benchmark Problem 32 are given for 0° (in rolling direction), 30° , 60° , 90° (in transverse direction). Because this thesis considers only isotropic hysteretic material, a set of measured unidirectional symmetrical hysteresis loops at rolling direction is used as experimental material data. The anisotropic behavior is neglected. The set of measured unidirectional symmetrical hysteresis loops is shown in Fig. 5.3 [122]. A series of first-order transition curves (Table A.4) are obtained from the set of measured symmetrical hysteresis loops by interpolation.

The structure of discretization is defined by $39 \times 36 \times 8 = 11232$ grid points. Because the implicit magnetoquasistatic formulation in the time domain takes the magnetic vector potential as unknown parameter, the number of degrees of freedom in the simulation is 33696.

The simplified model for the TEAM Benchmark problem 32 was simulated and compared with measured results, with the focus on the following two cases.

5.1.2 Simulated Results and Discussion for Case I

Simulated results

The simulations of case I are performed with the same current excitation in the two windings on the external limbs. Fig. 5.4 shows the time dependent waveform of the current. The hysteretic constitutive relation between magnetic flux density and magnetic field is taken into account by using both the scalar inverse Preisach model and the simplified vector model. The two hysteresis models are applied to the nonlinear systems of equations arising from Finite Integration Implicit Time Domain formulations. The nonlinear problem is linearized by means of the Newton-Raphson method with one-dimensional Brent's minimization relaxation method, giving rise to an iterative procedure. The Newton-Raphson method is applied as nonlinear iterative scheme within each step of the backward differentiation implicit Euler scheme. The linear system is solved using the Conjugate Gradient method with SSOR preconditioning.

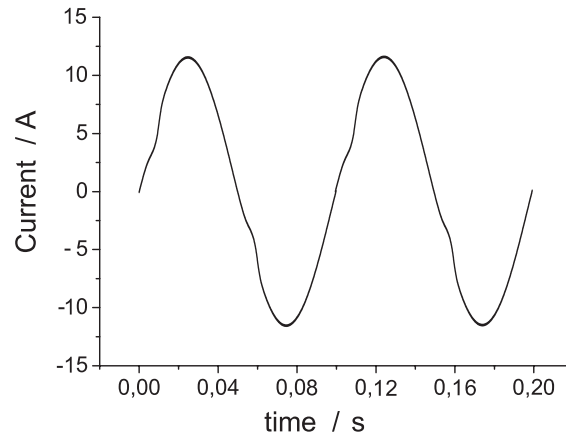


Figure 5.4: *CASE I: waveform of the current excitation.*

In case I only the flux density (along the y axis) in the middle limb is discussed. Fig. 5.5 compares the measured and computed flux densities in the pick-up coil C3 in the central limb. The two flux densities computed by the scalar inverse Preisach model and the simplified vector model are in good agreements to the measured result except for the time just after the start of the transient simulation. The agreement of simulated results for the scalar model and the vector model is satisfactory as well. The flux distribution in the 2D cut plane of the three-limbed core with maximum current excitation is shown in Fig. 5.6. The flux density in the center limb is approximately 1.35T, which is a little higher than the measured result (approximately 1.288T).

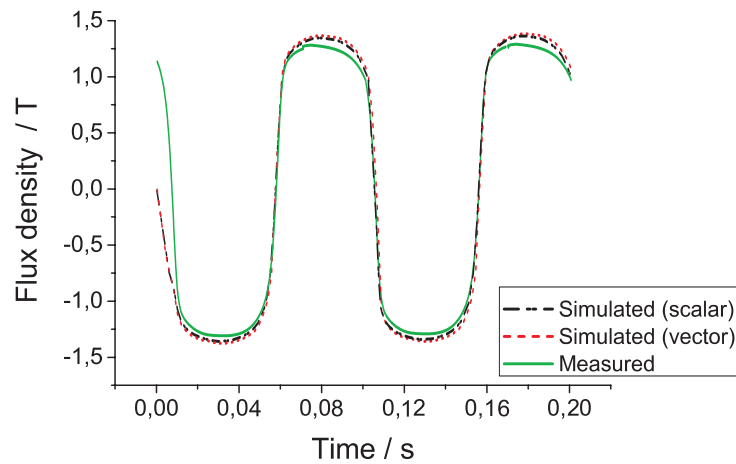


Figure 5.5: *Comparison of the simulated and measured waveforms of the magnetic flux density in the central limb (coil C3).*

Discussion

In the time just after the start of the transient simulation, the constitutive relation between magnetic flux density and magnetic field corresponds to the first magnetization curve. For this reason, the simulated flux density begins from zero value if the time dependent

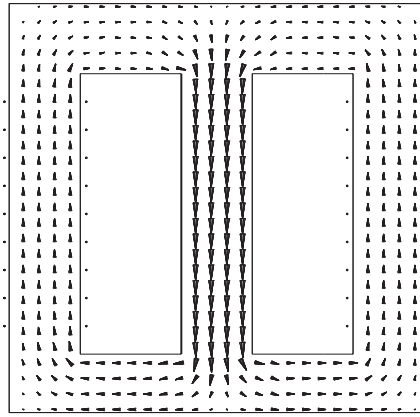


Figure 5.6: *Flux distribution in 2D cut plane at the maximum current excitation, the flux density in the middle limb is approximately 1.35T.*

waveform of the current starts with zero excitation. This causes the differences between the simulated results and measurement. If the hysteric curve changes from the decreasing curve to the increasing curve or changes from the increasing curve to the decreasing curve, the first turning point is obtained in the hysteresis history. From there, the constitutive relaxation between the magnetic flux density and the magnetic field corresponds to a measured first-order transition curve. From then on, the simulated flux densities have good agreements to the measured result.

The whole simulation is carried out for 100 time steps in 0.2 s. The fixed time step is defined as 0.002 s. The calculated discretized flux densities through each facet of the primal grid in the 3D mesh varies from approximately 1.3 T down to approximately 0.001 T. The Newton-Raphson method appears to behave better characteristics than the successive approximation method for the relatively short time step 0.002 s. The results simulated with the Jiles-Atherton model have a good agreement with the measured curves if the excitation keeps the hysteric material saturated. The simulated results show however a big differences to the measured curves for low excitations. For this reason, the Jiles-Atherton model is not selected for Case I. The magnetic polarization update scheme requires much more computation time than the nonlinear update scheme for a small test problem. For case I with the structure discretized by $38 \times 35 \times 7 = 9310$ grid cells, the nonlinear update scheme is much more efficient than the magnetic polarization update scheme. The Newton-Raphson nonlinear iterative scheme is a good choice for hysteric simulation as indicated by this example. The Newton-Raphson nonlinear iterative scheme is combined with the backward differentiation implicit Euler scheme.

5.1.3 Simulated Results and Discussion for Case II

Simulated results

The simulations of case II are performed with two different current excitations, one winding on the external limbs is supplied by a sinusoidal current, another one is supplied by a co-sinusoidal current. Fig. 5.7 shows the time dependent waveforms of both currents. The

hysteretic constitutive relation between magnetic flux density and magnetic field is also taken into account by using both the scalar inverse Preisach model and the simplified vector model. The two inverse hysteresis models are applied to the nonlinear systems of equations arising from the Finite Integration Implicit Time Domain formulations. The nonlinear problem is linearized by means of the Newton-Raphson method with the relaxation method based on a one-dimensional Brent's minimization. The Newton-Raphson method is applied as nonlinear iterative scheme within each step of the backward differentiation implicit Euler scheme. The linear system is solved using the Conjugate Gradient method with SSOR preconditioning. The whole simulation is carried out at 50 time steps in 0.1 second, the fixed time step is defined as 0.002 s.

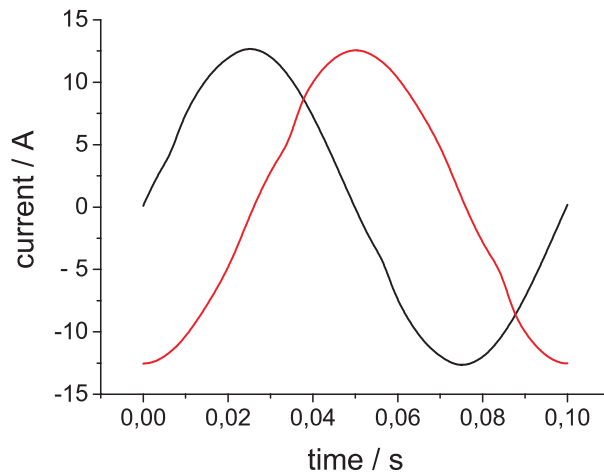


Figure 5.7: CASE II: waveforms of the two current excitations.

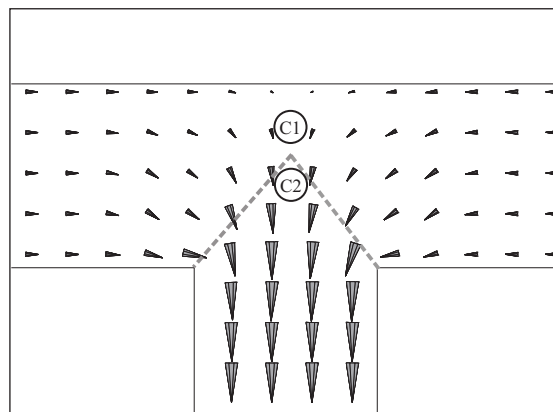


Figure 5.8: The regions of pick-up coils C1 and C2, the flux density loci in the region close to the joint between the middle limb and the yoke of the three-limbs core.

In case II, rotational effects are produced, in particular in the regions of pick-up coils C1 and C2. Fig. 5.8 shows the regions of pick-up coils C1 and C2, the flux density loci in the region close to the joint between the middle limb and yoke of the core. Rotational magnetization is predominant close to the joints of the core, in contrast to the rest of

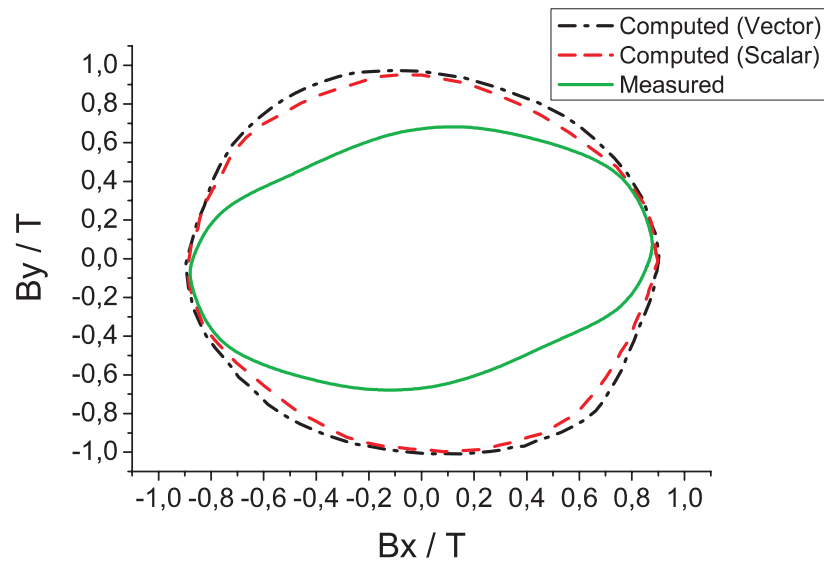


Figure 5.9: Comparison of the computed and measured flux density loci in point C1.

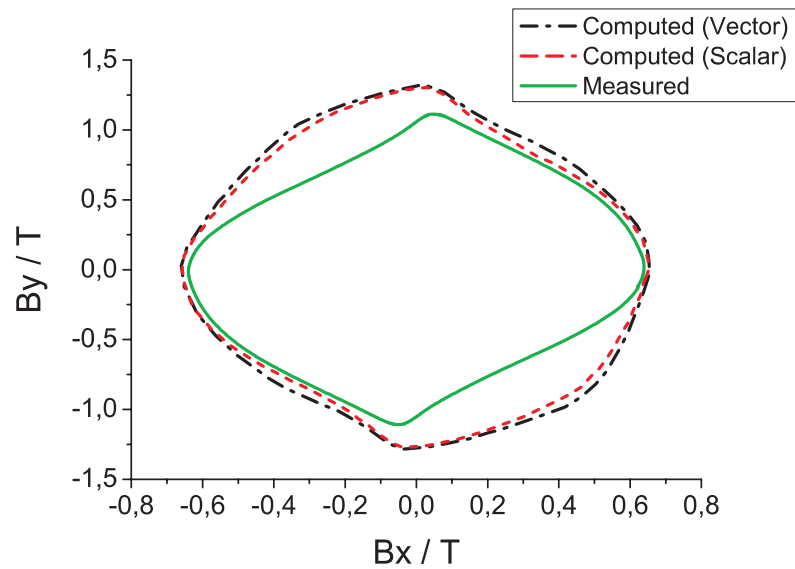


Figure 5.10: Comparison of the computed and measured flux density loci in point C2.

the core, where alternating magnetization prevails. The applied two current sources are shifted in time and generate flux components which are in quadrature at the joints such that a rotational flux pattern shows up there. In [121], [122], flux density loci in the regions of pick-up coils C1 and C2 have been measured. The simulated flux density loci by the scalar inverse Preisach model and by the vector inverse Preisach model are compared with the measurement in the region of pick-up coils C1 and C2.

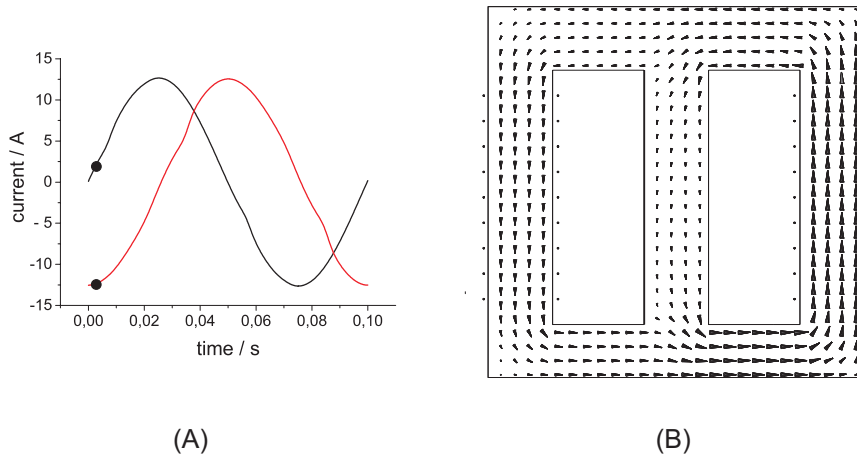


Figure 5.11: Flux distribution in the 2D cut plane at the second time step ($t=0.004s$).

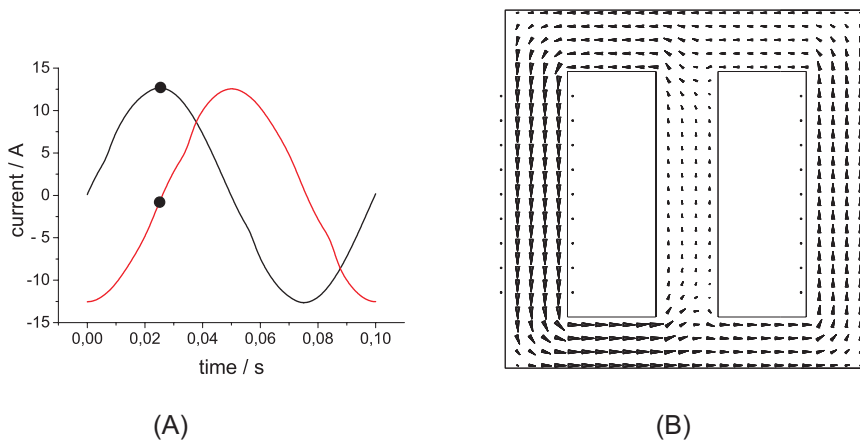


Figure 5.12: Flux distribution in the 2D cut plane at the 12th time step ($t=0.024s$).

The comparison of the computed and the measured flux density loci in position C1 is shown in Fig. 5.9, and the same comparison for position C2 is shown in Fig. 5.10. It can be seen that flux density stays close to a certain direction for a while, although its amplitude may continuously change, before it rotates towards a new direction. The steel is here assumed to be isotropic. So the difference in Fig. 5.9 and Fig. 5.10 may be explained by the fact, that the anisotropic behavior of the material is neglected. The shape of the flux

density loci simulated by the scalar and the vector inverse Preisach model better match with each other, except for the regions with similar absolute values of flux density in x- and y- directions. The flux density loci simulated by the scalar inverse Preisach model and the vector inverse Preisach model have larger magnitudes in all directions, since the increased reluctivity in the transverse direction is not considered in the isotropic case.

The flux distribution in the 2D cut plane at the second time step ($t=0.004s$) is shown in Fig. 5.11. It is supplied by a sinusoidal current excitation with approximately 0.28 A and a co-sinusoidal current excitation with a negative extreme amplitude.

The flux distribution in the 2D cut plane at the 12th time step ($t=0.024s$) is shown in Fig. 5.12. It is supplied by a sinusoidal current excitation with an extreme amplitude and a co-sinusoidal current excitation with approximately -0.16 A.

Discussion

The shape of the flux density loci simulated by the scalar and the vector inverse Preisach model better match with each other, except for the regions with similar absolute values of flux density in x- and y-directions. The permeability μ for determining the permeability matrix is defined in a different way by the scalar model and by the vector model. For the scalar model, the permeability μ is defined as $\mu = \frac{\sqrt{b_x^2 + b_y^2 + b_z^2}}{\sqrt{h_x^2 + h_y^2 + h_z^2}}$, where b_x , b_y and b_z are flux densities along x-, y-, or z-direction respectively and h_x , h_y and h_z are field strengths along x-, y-, or z-direction respectively. For the vector model, the permeability μ is defined as $\mu = \frac{R(b_x, b_y, b_z) \sqrt{b_x^2 + b_y^2 + b_z^2}}{\sqrt{h_x^2 + h_y^2 + h_z^2}}$. The rotational correction factor $R(b_x, b_y, b_z)$ is written as $R(b_x, b_y, b_z) = \frac{|b_x| + |b_y| + |b_z|}{\sqrt{b_x^2 + b_y^2 + b_z^2}}$. If the absolute values of the flux density in x- and y-directions are similar, the rotational correction factor $R(b_x, b_y, b_z)$ obtains a value in the interval $[\sqrt{2}, \sqrt{3}]$. Because of the rotational correction factor $R(b_x, b_y, b_z)$ in the vector model, we have the difference of the two simulated flux density loci in the regions with similar absolute values of flux density in x- and y-directions.

Chapter 6

Summary

In the scope of the presented thesis, the numerical simulation of hysteresis effects in ferromagnetic material is carried out by several hysteresis models in combination with different update scheme, implicit time stepping and the finite integration technique for space discretization. This presented section gives a brief summary of the essential points of all previous chapters.

Ferromagnetic hysteresis

The physics of magnetism, especially the theory of hysteresis effects in ferromagnetic material, is introduced in the first chapter, ranging from the microscopic theory of the domain structure in magnetic substances to the macroscopic description of hysteresis loops during the magnetization process.

On the basis of scientific publications, the Preisach model and the Jiles-Atherton model for the description and simulation of hysteretic magnetic materials are developed. The Preisach model is one of the most popular hysteresis models. Several researchers are working on the development of an appropriate model and on the parameter identification. The classical Preisach model is described concerning its geometric interpretation, the determination of the distribution function and the numerical implementation. In order to avoid the intrinsic limitations of the classical Preisach model from the congruency property, the generalized Preisach model considering the accommodation process is presented. Although scalar Preisach models became increasingly accurate and efficient in describing hysteretic material behavior, in many cases the magnetization process is vectorial in nature. Two vector models are introduced and compared, one of them is built from a continuum of scalar Preisach transducers, each incrementally rotated from its neighbor. The output of the complete model is the vector sum of the output of all transducers. Another vector model is introduced referred to the simplified vector Preisach model. The complete vector model is computed by two or three independent scalar Preisach models. Each scalar Preisach model is placed along the principal axis of the system, two for the 2D model and three for the 3D model. Because it overcomes many limitations and implementation difficulties in numerical computation, it is used as vector hysteresis model in this thesis. The inverse Jiles-Atherton model is implemented according to the physical principles in the determination of the five material parameters computed by experimental data. The overview of hysteresis models is show in Table (6.1).

Table 6.1: Overview of the hysteresis models

hysteresis model	Preisach model	Jiles-Atherton model	other models
scalar hysteresis model	classical Preisach model inverse Preisach model moving Preisach model nonlinear Preisach model dynamic Preisach model	Jiles-Atherton model inverse Jiles model	analytic model dynamic model Chua-Type model ...
vector hysteresis model	vector Preisach model simplified vector-Preisach model		Stoner-Wohlfarth model

The Preisach model and the Jiles-Atherton model both increase the memory requirements, since the previous state of the material has to be preserved for each material cell in the model. In this thesis, the hysteresis model is combined with magnetoquasistatic field simulation using models discretized by the FIT.

Electromagnetic field simulation

An introduction to the Finite Integration Technique is given as the basic theory for field simulation. This technique is employed, in particular, for calculating transient hysteretic magnetic field problems in time domain.

An implicit magnetoquasistatic formulation in time domain is developed based on the FIT. Because the CFL criterion restricts the length of possible stable time steps, the explicit Leapfrog FDTD schemes is no more suitable for slowly-varying magnetic field problems. For this reason, an implicit time integration scheme is used to avoid the problem of a maximum possible time step. Time integration schemes for differential algebraic formulations with index 1 for magnetoquasistatic field problems are discussed. The implicit Euler backward differentiation time integration scheme (BDF) with L-stability in one or two stages is introduced. Because of its stability properties, BDF is selected for all simulations in this thesis. The preconditioned conjugate gradient method is used as iterative method to solve the real-valued, symmetrical, linear system of equations arising in each nonlinear cycle and in each time step. SSOR (Symmetric Successive Over-Relaxation)-preconditioning is applied in this work.

Modelling and implementation of hysteresis

The magnetic polarization update scheme takes the magnetic polarization as the parameter which is updated during the iteration. The magnetic polarization is calculated by the Preisach model according to the averaged applied magnetic field strength in each grid cell. The trigonal prism filling is considered in field averaging procedure. The output value of the Preisach model is interpolated between the measured first-order transition curves using a two-point polynomial interpolation. Because the hysteretic ferromagnetic material behavior depends not only on the local applied field but also on the hysteresis history, the provided field and the maximum or minimum extremal values in the hysteresis history are

required as input values. The interpolation process between the measured first-order transition curves is divided into the case with monotonically decreasing excitation and the case with monotonically increasing excitation. The simplest case with monotonically decreasing excitation (with only one turning point α) and the simplest case with monotonically increasing excitation (with a pair of turning points (α, β)) are described as interpolation examples.

The hysteresis losses are an important fraction of the core losses occurring in almost all electromagnetic power devices. The computation of hysteresis losses is described according to the Preisach model in the case of monotonically decreasing or increasing excitation. The material model described by the magnetic polarization and the discrete magnetoquasistatic Maxwell-Grid-Equations are combined into a magnetic polarization formulation in time domain considering hysteresis phenomena. The algorithm based on the magnetic polarization is introduced at each time step.

A 3D transient hysteretic test model is presented in a numerical simulation for studying the properties of the magnetic polarization update scheme. The simulated hysteresis loop has a good agreement to the measured first-order transition curves. The computational results for hysteresis losses are given.

The nonlinear update scheme updates the magnetic reluctivity in the iteration. Because the magnetic flux density is defined as the input value in the nonlinear update scheme, an inverse hysteresis model is needed in the computation. A simple inverse Preisach model is formulated based on the formulation of the classical Preisach model. The interpolation between the measured first-order transition curves is described similar to the case of the Preisach model. An inverse Jiles-Atherton model is based on the assumption of an anhysteretic magnetization following the Langevin function.

To solve the nonlinear system, the equation has to be linearized by a sequence of linear problems for each time step. Both the successive approximation technique and the Newton-Raphson method are implemented. For the successive approximation technique, the definition of the updated reluctivity is modified in the second and fourth quadrant of the B-H curve in order to avoid a negative and un-physical reluctivity. The Newton-Raphson method features a quadratic convergence, but only in the vicinity of the solution. The successive approximation technique commonly can be considered to be the more robust, but does not achieve a quadratic convergence rate. Several relaxation methods are implemented in order to achieve global convergence and to improve the speed of convergence for both the Newton-Raphson method and the successive approximation technique. The heuristic relaxation method and the 1D minimization method of Brent are selected and implemented. The heuristic scheme is a popular relaxation method. It directly adapts the relaxation parameter in the relaxation process and does not need additional computation time for the optimization process. The heuristic scheme is used in combination with the successive approximation technique. The 1D minimization method of Brent is implemented for the Newton-Raphson method.

The material model described by the reluctivity and the discrete magnetoquasistatic Maxwell-Grid-Equations are combined into a hysteretic nonlinear formulation in time domain. The combined algorithms for the nonlinear update scheme are classified as the successive approximation nonlinear iterative scheme with inverse Preisach model, the Newton-Raphson nonlinear iterative scheme with the inverse Preisach model, and the Newton-Raphson nonlinear iterative scheme with the inverse Jiles-Atherton model.

In order to compare the nonlinear update scheme with the magnetic polarization scheme, the same 3D hysteretic transient test model is simulated. Several comparisons and discussions of the simulated results are given, such as the Newton-Raphson method compared with the successive approximation technique, the inverse Jiles-Atherton model compared with the inverse Preisach model, the hysteretic nonlinear iteration compared with the magnetic polarization iteration.

The hybrid polarization-Newton method is studied and implemented because the polarization method can be formulated as Newton method, where the dynamic reluctivity used in the Jacobian matrix of the Newton method is replaced by the vacuum reluctivity. As it is well known, the polarization method has guaranteed but slow convergence, whereas the Newton method has quadratic speed of convergence but only in the vicinity of solution. The hybrid polarization-Newton method combines both advantages in order to increase the robustness of the nonlinear scheme without losing the quadratic speed of convergence in the vicinity of solution. A 3D test problem is used to study the properties of the hybrid method. The value of the various parameters used in the test problem, such as linear solver precision, nonlinear iteration precision, tolerance of the 2D Powell's minimization method, and limits of the optimal values for the hybridization, are discussed according to the simulation example.

The simplified vector Preisach model is selected and implemented as a vector hysteresis model in this thesis, because it overcomes many limitations and implementation difficulties in the numerical computation compared with other vector hysteresis models. It is implemented into the Newton-Raphson nonlinear iterative scheme. A test problem is used for assessing the properties of the simplified vector model.

Selected example

The TEAM benchmark problem 32 is a typical benchmark problem for magnetoquasistatic field analysis taking hysteresis effects into account. Two different supply conditions for the TEAM benchmark problem 32 are selected and demonstrated. In order to realize the numerical simulation, a simplified model of the TEAM benchmark problem 32 is considered including the lamination structure and isotropic material. Cases I and II are simulated using the Newton-Raphson nonlinear iterative scheme with the inverse Preisach model. The model is discretized in time by the backward differential implicit Euler scheme. Both the scalar model and the vector model are applied to the selected example. The two hysteresis models have a different definition of the permeability. For case I, the results simulated by the scalar model have a good agreement to the simulated results by the vector model, and the two simulated waveforms of flux densities match with the measured results. For case II, the shape of the two simulated flux density loci by the scalar model and the vector model matched with each other at places in the model where only alternating fluxes occurs.

Appendix A

Magnetic Curves of Various Ferromagnetic Materials

Table A.1: Measured magnetic curve of pure iron [70]

H/[A/m]	B/[T]	μ_r	M/[A/m]
0.0	0.0	-	0.0
1.592E+01	0.045	2251	3.581E+04
3.183E+01	0.490	12251	3.899E+05
4.775E+01	0.780	13001	6.207E+05
6.366E+01	0.990	12376	7.878E+05
7.958E+01	1.130	11301	8.992E+05
1.592E+02	1.420	7101	1.130E+06
3.183E+02	1.570	3926	1.249E+06
4.775E+02	1.621	2701	1.289E+06
6.366E+02	1.641	2051	1.305E+06
7.958E+02	1.656	1656	1.317E+06
1.592E+03	1.697	849	1.349E+06
3.183E+03	1.764	441	1.401E+06
4.775E+03	1.801	300	1.428E+06
6.366E+03	1.838	230	1.456E+06
7.958E+03	1.870	187	1.480E+06
1.529E+04	2.000	100	1.576E+06
3.183E+04	2.136	53.4	1.668E+06
4.775E+04	2.185	36.4	1.691E+06
6.366E+04	2.220	27.8	1.703E+06
7.958E+04	2.250	22.5	1.711E+06
1.592E+05	2.355	11.8	1.715E+06
3.183E+04	2.556	6.4	1.716E+06

Table A.2: Measured virgin curve of Steel-1010 [70]

H/[A/m]	B/[T]	μ_r	M/[A/m]
0.0	0.0	-	0.0
1.783E+02	0.894	3993	7.116E+05
2.944E+02	1.200	3243	9.546E+05
5.013E+02	1.400	2222	1.114E+06
7.966E+02	1.500	1499	1.193E+06
1.153E+03	1.550	1070	1.232E+06
1.795E+03	1.600	709	1.271E+06
2.862E+03	1.650	459	1.310E+06
4.383E+03	1.700	309	1.348E+06
6.044E+03	1.750	230	1.387E+06
8.122E+03	1.800	176	1.424E+06
1.058E+04	1.850	139	1.462E+06
1.361E+04	1.900	111	1.498E+06
1.722E+04	1.950	90.1	1.535E+06
2.117E+04	2.000	75.2	1.570E+06
2.675E+04	2.050	61.0	1.605E+06
3.376E+04	2.100	49.5	1.637E+06
3.822E+04	2.125	44.2	1.653E+06
4.380E+04	2.150	39.1	1.667E+06
5.244E+04	2.175	33.0	1.678E+06
6.600E+04	2.200	26.5	1.685E+06
9.947E+04	2.250	18.0	1.691E+06
1.209E+05	2.280	15.0	1.693E+06
1.412E+05	2.307	13.0	1.695E+06
1.696E+05	2.344	11.0	1.696E+06
2.122E+05	2.400	9.0	1.697E+06
2.831E+05	2.490	7.0	1.699E+06
3.399E+05	2.563	6.0	1.699E+06
4.250E+05	2.671	5.0	1.700E+06
5.670E+05	2.850	4.0	1.701E+06
8.508E+05	3.207	3.0	1.702E+06
1.135E+06	3.564	2.5	1.702E+06
1.702E+06	4.278	2.0	1.702E+06
2.128E+06	4.813	1.8	1.702E+06
2.838E+06	5.705	1.6	1.703E+06
3.405E+06	6.419	1.5	1.703E+06
4.257E+06	7.489	1.4	1.703E+06

Table A.3: Measured first-order transition curves of a hysteretic material (*source of measured data from Siemens VDO AG)

H/[A/m]	B1/[T]	B2/[T]	B3/[T]	B4/[T]	B5/[T]
-1.924E+03	-1.3776	-1.3779	-1.3777	-1.3782	-1.3786
-1.828E+03	-1.3772	-1.3722	-1.3724	-1.3727	-1.3733
-1.732E+03	-1.3659	-1.3660	-1.3661	-1.3664	-1.3673
-1.636E+03	-1.3588	-1.3590	-1.3591	-1.3594	-1.3604
-1.539E+03	-1.3508	-1.3510	-1.3510	-1.3514	-1.3526
-1.443E+03	-1.3415	-1.3418	-1.3417	-1.3422	-1.3435
-1.347E+03	-1.3306	-1.3307	-1.3305	-1.3312	-1.3333
-1.251E+03	-1.3176	-1.3179	-1.3175	-1.3183	-1.3205
-1.155E+03	-1.3020	-1.3026	-1.3020	-1.3029	-1.3058
-1.058E+03	-1.2833	-1.2837	-1.2831	-1.2841	-1.2878
-9.621E+02	-1.2603	-1.2605	-1.2599	-1.2608	-1.2659
-8.659E+02	-1.2316	-1.2320	-1.2309	-1.2316	-1.2387
-7.697E+02	-1.1951	-1.1958	-1.1951	-1.1947	-1.2050
-6.735E+02	-1.1489	-1.1420	-1.1486	-1.1475	-1.1627
-5.773E+02	-1.0885	-1.0889	-1.0884	-1.0848	-1.1086
-4.811E+02	-1.0073	-1.0086	-1.0077	-1.0020	-1.0395
-3.849E+02	-0.8962	-0.8974	-0.8980	-0.8896	-0.9497
-2.886E+02	-0.7335	-0.7346	-0.7381	-0.7340	-0.8347
-1.924E+02	-0.4668	-0.4685	-0.4789	-0.5006	-0.6862
-0.962E+02	0.2938	0.2921	0.2560	0.0318	-0.5009
0	0.7559	0.7537	0.7205	0.4757	-0.3477
0.962E+02	0.9602	0.9530	0.9178	0.6672	-0.2986
1.924E+02	1.0758	1.0668	1.0317	0.7771	-
2.886E+02	1.1498	1.1417	1.1014	0.8441	-
3.849E+02	1.2006	1.1920	1.1481	0.8765	-
4.811E+02	1.2372	1.2282	1.1812	-	-
5.773E+02	1.2649	1.2554	1.2057	-	-
6.735E+02	1.2819	1.2715	1.2190	-	-
7.697E+02	1.3041	1.2934	1.2403	-	-
8.659E+02	1.3179	1.3066	1.2528	-	-
9.621E+02	1.3292	1.3174	1.2621	-	-
1.058E+03	1.3387	1.3262	-	-	-
1.155E+03	1.3466	1.3336	-	-	-
1.251E+03	1.3533	1.3400	-	-	-
1.347E+03	1.3590	1.3456	-	-	-
1.443E+03	1.3640	1.3506	-	-	-
1.539E+03	1.3684	1.3548	-	-	-
1.636E+03	1.3724	-	-	-	-
1.732E+03	1.3759	-	-	-	-
1.828E+03	1.3792	-	-	-	-
1.924E+03	1.3821	-	-	-	-

Table A.4: Interpolated first-order transition curves, according to the measured closed minor hysteresis loops of the TEAM benchmark problem 32, in the rolling direction [122]

H/[A/m]	B1/[T]	B2/[T]	B3/[T]	B4/[T]	B5/[T]
-1.232E+03	-1.5014	-1.5014	-1.5014	-1.5014	-1.5014
-1.171E+03	-1.4924	-1.4924	-1.4925	-1.4925	-1.4924
-1.109E+03	-1.4828	-1.4829	-1.4830	-1.4830	-1.4830
-1.047E+03	-1.4718	-1.4719	-1.4719	-1.4720	-1.4720
-9.862E+02	-1.4609	-1.4609	-1.4610	-1.4610	-1.4611
-9.246E+02	-1.4481	-1.4481	-1.4482	-1.4482	-1.4483
-8.629E+02	-1.4340	-1.4341	-1.4341	-1.4342	-1.4345
-8.012E+02	-1.4185	-1.4186	-1.4187	-1.4188	-1.4192
-7.396E+02	-1.4008	-1.4009	-1.4010	-1.4011	-1.4017
-6.780E+02	-1.3803	-1.3818	-1.3820	-1.3825	-1.3830
-6.164E+02	-1.3575	-1.3594	-1.3595	-1.3598	-1.3601
-5.547E+02	-1.3303	-1.3473	-1.3475	-1.3477	-1.3483
-4.931E+02	-1.3001	-1.3013	-1.3015	-1.3018	-1.3026
-4.314E+02	-1.2595	-1.2687	-1.2689	-1.2691	-1.2701
-3.698E+02	-1.2137	-1.2195	-1.2201	-1.2206	-1.2218
-3.082E+02	-1.1580	-1.1665	-1.1677	-1.1683	-1.1697
-2.465E+02	-1.0768	-1.0862	-1.0946	-1.0952	-1.0970
-1.849E+02	-0.9555	-0.9666	-0.9865	-0.9877	-0.9897
-1.232E+02	-0.7271	-0.7338	-0.7913	-0.7998	-0.8080
-0.616E+02	-0.0758	0.0085	0.0606	-0.3867	-0.6264
-0.308E+02	0.8340	0.8325	0.7864	0.4474	-0.3903
0	0.9743	0.9602	0.9052	0.5934	-0.3066
0.308E+02	1.0496	1.0341	0.9738	0.6604	-0.2301
0.616E+02	1.0989	1.0863	1.0248	0.7061	-0.2006
1.232E+02	1.1767	1.1604	1.0954	0.7671	-
1.849E+02	1.2364	1.2178	1.1371	-	-
2.465E+02	1.2815	1.2587	1.1684	-	-
3.082E+02	1.3167	1.2925	1.1905	-	-
3.698E+02	1.3449	1.3167	1.2057	-	-
4.314E+02	1.3687	1.3395	-	-	-
4.931E+02	1.3884	1.3551	-	-	-
5.547E+02	1.4060	1.3698	-	-	-
6.164E+02	1.4208	1.3809	-	-	-
6.780E+02	1.4335	1.3900	-	-	-
7.396E+02	1.4448	1.4001	-	-	-
8.012E+02	1.4551	-	-	-	-
8.629E+02	1.4635	-	-	-	-
9.246E+02	1.4719	-	-	-	-
9.862E+02	1.4786	-	-	-	-
1.047E+03	1.4853	-	-	-	-
1.109E+03	1.4908	-	-	-	-
1.171E+03	1.4961	-	-	-	-
1.232E+03	1.5014	-	-	-	-

Appendix B

Applied Notations and Symbols

General Mathematical Symbols

\mathcal{R}, \mathcal{C}	set of real, complex numbers	
\vec{r}, \mathbf{r}	spatial vector	
\vec{n}	vector normal to an area	
\mathbf{M}, \mathbf{D}	matrix, diagonal matrix	
$\mathbf{x}^T, \mathbf{M}^T$	transpose of vector \mathbf{x} and matrix \mathbf{M}	
$\mathbf{x}^H, \mathbf{M}^H$	complex conjugated transpose of vector \mathbf{x} and matrix \mathbf{M}	
\mathbf{M}^{-1}	inverse matrix of \mathbf{M}	
$\hat{u}, \hat{v}, \hat{w}$	unit vectors of the local coordinate (u, v, w)	
$(x)_u$	u - component of vector \mathbf{x}	
$m_{i,j} = (\mathbf{M}_{i,j})$	entry of matrix \mathbf{M} in row i and column j	
$\dot{x} := \partial x / \partial t$	time derivative value of x	
Δt	time step	s
f	frequency	Hz
ω	angular frequency	rad Hz
$d\vec{s}$	element of edge	m
$d\vec{A}$	element of area	m ²
$d\vec{V}$	element of volume	m ³
∂A	boundary of the area A	
∂V	boundary of the volume V	
\mathcal{O}, o	Landau symbol for the order of the truncation error	
$\ x\ _\infty$	maximum norm of vector x	
$\ x\ _2$	Euclidean norm of vector x	

Classical Continuous Field Theory

\vec{E}	electric field strength	V/m
\vec{H}	magnetic field strength	A/m
\vec{D}	electric flux density	C/m ²
\vec{B}	magnetic flux density	T
\vec{J}	total current density	A/m ²
\vec{J}_i	imposed current density	A/m ²
\vec{J}_k	current density due to finite conductivity	A/m ²
\vec{J}_q	current density due to moving charges	A/m ²
\vec{M}	magnetization	A/m
\vec{P}	electrical polarization	C/m ²
q	charge density	C/m ³
c	speed of light	m/s
A	magnetic vector potential	Wb/m
Φ	electric scalar potential	V
μ	scalar permeability	H/m
μ_0	permeability of vacuum	H/m
μ_r	relative permeability	H/m
ε	scalar permittivity	F/m
ε_0	permeability of vacuum	F/m
ε_r	relative permittivity	F/m
κ	scalar conductivity	S/m
χ	scalar susceptibility	1
χ_e, χ_m	electric and magnetic susceptibility	1

Finite Integrations Technique

G	primal grid	
\tilde{G}	dual grid	
P_n	primary grid nodes	
\tilde{P}_n	dual grid nodes	
L_n	primary grid edges	m
\tilde{L}	dual grid edges	m
A	primary grid facets	m ²
\tilde{A}	dual grid facets	m ²
V	primary grid cell	m ³
\tilde{V}	dual grid cell	m ³
$\Delta u_n, \Delta v_n, \Delta w_n$	distance of grid nodes on the primal grid	m
$\Delta \tilde{u}_n, \Delta \tilde{v}_n, \Delta \tilde{w}_n$	distance of grid nodes on the dual grid	m

$\hat{\mathbf{e}}$	electric grid voltage	V
$\hat{\mathbf{h}}$	magnetic grid voltage	A
$\hat{\mathbf{d}}$	electric facet flux	C
$\hat{\mathbf{b}}$	magnetic facet flux	Wb
$\hat{\mathbf{j}}, \hat{\mathbf{j}}_e$	vector of grid currents	A
$\hat{\mathbf{a}}$	vector of magnetic grid potential	Vs
\mathbf{q}	vector of grid charge	C
$\hat{\mathbf{m}}$	vector of grid magnetization	A/m
$\hat{\hat{\mathbf{m}}}$	vector of grid magnetic polarization	T
$\mathbf{C}, \tilde{\mathbf{C}}$	curl discrete operator on the primal/dual grid	
$\mathbf{S}, \tilde{\mathbf{S}}$	divergence discrete operator on the primal/dual grid	
$\mathbf{G}, \tilde{\mathbf{G}}$	gradient discrete operator on the primal/dual grid	
\mathbf{M}_ϵ	material matrix of permittivity	
\mathbf{M}_κ	material matrix of conductivity	
\mathbf{M}_μ	material matrix of permeability	
\mathbf{M}_ν	material matrix of reluctivity	
\mathbf{M}_{ν_d}	material matrix of differential reluctivity	
$\mathbf{D}_A, \mathbf{D}_{\tilde{A}}$	diagonal matrix of primal/dual grid facets	
$\mathbf{D}_S, \mathbf{D}_{\tilde{S}}$	diagonal matrix of primal/dual grid edges	

Hysteresis Models

α	up switching value of input
α_{stoner}	parameter of Stoner-Wohlfarth model
α_{rk}	parameter of Jiles-Atherton model
β	down switching value of input
α_0	maximum switching value of input
β_0	minimum switching value of input
(α, β)	pair of switching value of input
$u(t)$	input
$f(t)$	output
T	limited triangle
$S^+(t)$	positive area in limited triangle
$S^-(t)$	negative area in limited triangle
$L(t)$	interface between $S^+(t)$ and $S^-(t)$
$f_{\alpha, \beta}$	notation on the first-order transition curves
H_i	interaction field
H_k	interaction-free critical field
h_α	up switching magnetic field
h_β	down switching magnetic field
Q_k	trapezoid in $S^+(t)$ area
w	hysteresis loss density
Q	hysteresis loss

h_{ex}	exchange field
M_{an}	anhysteretic magnetization
M_{irr}	irreversible magnetization
M_{rev}	reversible magnetization
M_s	saturation magnetization
χ_{in}	initial susceptibility
χ_{an}	anhysteretic susceptibility
χ_r	remanence susceptibility
χ_c	coercivity susceptibility

Abbreviations

BDF	Backward Differentiation Formula
BEM	Boundary Element Method
CG	Conjugate Gradients
DAE	Differential Algebraic Equations
FDTD	Finite Difference in Time Domain
FEM	Finite Element Method
FIT	Finite Integration Technique
FI ² TD	Finite Integration Implicit Time Domain
MGE	Maxwell-Grid-Equations
ODE	Ordinary Differential Equation
PFC	Partially Filled Cells
SDIRK	Singly Diagonally Implicit Runge-Kutta Method
SGS	Symmetric Gauss-Seidel
SSOR	Symmetric Successive Over-Relaxation

Bibliography

Characteristics of magnetic and hysteretic material

- [1] R.M. Bozorth, *Ferromagnetism*, D. Van Norstrand Co. Princeton, New Jersey, 1951.
- [2] S. Chikazumi, S.H. Charap, *Physics of magnetism*, New York, London, Sydney, John Wiley and Sons, 1959.
- [3] D. Jiles, *Introduction to magnetism and magnetic materials*, Chapman and Hall, London, 1991.
- [4] G. Bertotti, *Hysteresis in magnetism*, Academic Press, San Diego, London, Boston, New York, Sydney, Tokyo, Toronto, 1998.
- [5] E. Della Torre, *Magnetic hysteresis*, IEEE Press, The Institute of Electrical and Electronics Engineers, Inc., New York, 1999.
- [6] F. Vajda, E. Della Torre, *Ferenc Preisach, In memoriam*, IEEE Trans. on Magn., Vol. 31, pp. i-ii, 1995.
- [7] J.A. Ewing, *Magnetism in iron and other materials*, Part I-IV, Electrician, Part I. Vol. 24, 1890, Part II. Vol. 26, 1891, Part III. Vol. 27, 1891, Part IV. Vol. 28, 1892.
- [8] D.H. Everett, W.I. Whitton, *A general approach to hysteresis, Part I.*, Trans. on Faraday Soc., Vol. 48, pp. 749-754, 1952.
- [9] D.H. Everett, F.W. Smith, *A general approach to hysteresis, Part II. Development of the domain theory*, Trans. on Faraday Soc., Vol. 50, pp. 187-197, 1954.
- [10] D.H. Everett, *A general approach to hysteresis, Part III. A formal treatment of the independent domain model of hysteresis*, Trans. on Faraday Soc., Vol. 50, pp. 1077-1096, 1954.
- [11] D.H. Everett, *A general approach to hysteresis, Part IV. An alternative formulation of the domain model*, Trans. on Faraday Soc., Vol. 51, pp. 1551-1557, 1955.
- [12] I.D. Mayergoyz, *Mathematical model of hysteresis*, IEEE Trans. on Magn., Vol. 22, pp. 603-608, 1986.
- [13] I.D. Mayergoyz, G. Friedman, *On the integral equation of the vector Preisach hysteresis model*, IEEE Trans. on Magn., Vol. 23, pp. 2638-2640, 1987.

- [14] I.D. Mayergoyz, G. Friedman, *Generalized Preisach model of hysteresis*, IEEE Trans. on Magn., Vol. 24, pp. 212-217, 1988.
- [15] I.D. Mayergoyz, *Vector Preisach hysteresis models*, Jour. of Appl. Phys., Vol. 63, pp. 2995-3000, 1988.
- [16] I.D. Mayergoyz, *Mathematical models of hysteresis*, Springer, 1991.
- [17] A. Iványi, *Hysteresis models in electromagnetic computation*, Akadémiai Kiadó, Budapest, 1997.
- [18] E. Della Torre, *A simplified vector Preisach model*, IEEE Trans. on Magn., Vol. 34, pp. 495-501, 1998.
- [19] E. Della Torre, *Magnetization calculation of fine particles*, IEEE Trans. on Magn, Vol. 22, pp. 484-489, 1986.
- [20] A. Reimers, E. Della Torre, *Implementation of the simplified vector model*, IEEE Trans. on Magn., Vol. 38, pp. 837-840, 2002.
- [21] M. Pardavi-Horvath, E. Della Torre, F. Vajda, G. Vertesy, *A variable variance Preisach model*, IEEE Trans. on Magn., Vol. 29, pp. 3793-3795, 1993.
- [22] E.C. Stoner, E.P. Wohlfarth, *A mechanism of magnetic hysteresis in heterogeneous alloys*, Reprinted in IEEE Trans. on Magn., Vol. 27, pp. 3475-3518, 1991.
- [23] D. Jiles, D.L. Atherton, *Ferromagnetic hysteresis*, IEEE Trans. on Magn., Vol. 19, pp. 2183-2185, 1983.
- [24] D. Jiles, D.L. Atherton, *Theory of the magnetization process in ferromagnets and its application to the magnetomechanical effect*, Jour. Phys. D.: Appl. Phys., Vol. 17, pp. 1265-1281, 1984.
- [25] D. Jiles, D.L. Atherton, *Theory of ferromagnetic hysteresis*, Jour. Appl. Phys. Vol. 55, pp. 2115-2120, 1984.
- [26] D. Jiles, J.B. Thoelke, *Theory of ferromagnetic hysteresis: Determination of model parameters from experimental hysteresis loops*, IEEE Trans. on Magn., Vol. 25, pp. 3928-3930, 1989.
- [27] D. Jiles, J.B. Thoelke, M. Devine, *Numerical determination of hysteresis parameters for the modeling of magnetic properties using the theory of ferromagnetic hysteresis*, IEEE Trans. on Magn., Vol. 28, pp. 27-35, 1992.
- [28] A. Visintin, *Differential models of hysteresis*, in Ser. Applied Mathematical Sciences, Springer, p. 407, 1994.
- [29] F. Preisach, *Über die magnetische Nachwirkung*, Zeitschrift für Physik., vol. 94, pp. 277-302, 1935.
- [30] Yin Dong Yan, E. Della Torre, *Particle interaction in numerical micromagnetic modelling*, J. of Appl. Phys., vol. 67, pp. 5370-5372, 1990.

- [31] O. Henze, W.M. Rucker, *Identification procedures of Preisach model*, IEEE Trans. on Magn., Vol. 38, pp. 833-836, 2002.
- [32] J. Oti, E. Della Torre, *A vector moving model of both reversible and irreversible magnetizing processes*, J. Appl. Phys., Vol. 67, pp. 5364-5366, 1990.
- [33] J. Oti, E. Della Torre, *A vector moving model of nonaligned particulate media*, IEEE Trans. on Magn., Vol. 26, pp. 2116-2118, 1990.
- [34] K. Suzuki, *Theoretical study of vector magnetization distribution using rotational magnetization model*, IEEE Trans. on Magn., Vol. 12, pp. 224-229, 1976.
- [35] I. Ortenburger, R. Potter, *Self-consistent calculation of the transition zone in thick particulate recording media*, J. Appl. Phys., Vol. 50, pp. 2393-2395, 1976.
- [36] K. Wiesen, H. Charap, *Vector hysteresis modelling*, J. Appl. Phys., Vol. 61, pp. 4019-4021, 1987.
- [37] K. Wiesen, H. Charap, S. Krafft, *A rotational vector Preisach model for unoriented media*, J. Appl. Phys., Vol. 67, pp. 5367-5369, 1990.
- [38] F. Ossart, R. Davidson, S. Charap, *A 3D moving vector Preisach hysteresis model*, IEEE Trans. on Magn., Vol. 32, pp. 1785-1788, 1995.
- [39] C.S. Koh, S.Y. Hahn, G.S. Park, *Vector hysteresis modeling by combining Stoner-Wohlfarth and Preisach models*, IEEE Trans. on Magn., Vol. 36, pp. 1254-1257, 2000.
- [40] S. Kurz, J. Fetzer, *Numerical implementation of the 3D vector Preisach model*, Proceedings of 10th IGTE Symposium, pp. 251-255, 2002.
- [41] C. Vernescu-Spornic, A. Kedous-Lebouc, S. Spornic, F. Ossart, *Anisotropic and vector hysteresis model for magnetic materials applications to a cubic textured NiFe sheet*, Physical B, Vol. 275 pp. 99-102, 2000.
- [42] A. Bergqvist, *A simple vector generalization of the Jiles-Atherton model of hysteresis*, IEEE Trans. on Magn., Vol. 32, pp. 4213-4215, 1996.
- [43] A. Kedous-Lebouc, C. Vernescu, B. Cornut, *A two dimensional Preisach particle for vectorial hysteresis modeling*, J. Magn. Mat., Vol. 254, pp. 321-323, 2003.
- [44] C. Appino, M. Valsania, V. Basso, *A vector hysteresis model including domain motion and coherent rotation*, Physical B, Vol. 275 pp. 103-106, 2000.
- [45] A. Stancu, L. Spinu, *Temperature and time-dependent Preisach model for a Stoner Wohlfarth particle system*, IEEE Trans. on Magn., Vol. 34, pp. 3867-3875, 1998.
- [46] A. Reimers, E. Della Torre, *Fast Preisach-based vector magnetization model*, IEEE Trans. on Magn., Vol. 37, pp. 3349-3352, 2000.
- [47] E. Della Torre, J. Oti, G. Kádár, *Preisach modeling and reversible magnetization*, IEEE Trans. on Magn., Vol. 26, pp. 3052-3058, 1990.

- [48] F. Vajda, E. Della Torre, *Characteristics of magnetic media models*, IEEE Trans. on Magn., Vol. 28, pp. 330-336, 1992.

Theory of electromagnetic field and FIT

- [49] J.D. Jackson, *Classical Electrodynamics*, New York: John Wiley and Sons, 1998.
- [50] K.S. Yee, *Numerical solution of initial boundary value problems involving Maxwell's equations in isotropic media*, IEEE Trans. on Antennas and Propagation, Vol. AP-14, pp. 302-307, 1966.
- [51] T. Weiland, *A discretization method for the solution of Maxwell's equations for six-component fields*, AEÜ Archiv für Elektrotechnik und Übertragungstechnik, Band 31, pp. 116-120, 1977.
- [52] T. Weiland, *A numerical method for the solution of the eigenwave problem of longitudinally homogeneous waveguides*, AEÜ Archiv für Elektrotechnik und Übertragungstechnik, Band 31, pp. 308-314, 1977.
- [53] T. Weiland, *Lossy waveguides with an arbitrary boundary contour and distribution of material*, AEÜ Archiv für Elektrotechnik und Übertragungstechnik, Band 33, pp. 170-174, 1979.
- [54] T. Weiland, *On the unique numerical solution of Maxwellian eigenvalue problems in three dimensions*, Particle Accelerators, Vol. 17, pp. 227-242. 1985.
- [55] T. Weiland, *Time domain electromagnetic field computation with finite difference methods*, International Journal of Numerical Modelling: Electronic Networks, Devices and Fields, Vol. 9, pp. 295-319, 1996.
- [56] M. Clemens, T. Weiland, *Transient eddy current calculation with the FI-method*, IEEE Trans. on Magn., Vol. 35, pp. 1163-1166, 1999.
- [57] M. Clemens, P. Thoma, T. Weiland, U. v. Rienen, *A survey on the computational electromagnetic-field calculation with the Finite Integration method*, Surveys on Mathematics in Industry, Vol. 8, No. 3-4, pp. 213-232, 1999.
- [58] M. Clemens, T. Weiland, *Discrete electromagnetism with the Finite Integration technique*, Progress in Electromagnetic Research (PIER) Monograph Series, PIER 32, pp. 65-87, 2001.
- [59] F. Mayer, R. Schuhmann, T. Weiland, *Flexible subgrids in FDTD calculations*, Proceedings of the International Symposium on IEEE Antennas and Propagation, San Antonio, Texas, pp. 252-255, 2002.
- [60] T. Weiland, *Elektromagnetisches CAD - Rechnergestützte Methoden zur Berechnung von Feldern*, Skriptum zur Vorlesung Feldtheorie II, TU-Darmstadt, 1998.
- [61] T. Weiland, *Zur numerischen Lösung des Eigenwellenproblems längshomogener Wellenleiter beliebiger Randkorrektur und transversal inhomogener Füllung*, Dissertation, Technische Hochschule Darmstadt, 1977.

- [62] O. Poděbrad, *Finite Integration der Maxwellschen Gleichungen auf lokal verfeinerten orthogonalen Gittern*, Dissertation, Technische Universität Darmstadt, 2001.
- [63] P. Thoma, *Zur numerischen Lösung der Maxwellschen Gleichung im Zeitbereich*, Dissertation, Technische Universität Darmstadt, 1998.
- [64] R. Schuhmann, *Die nichtorthogonale Finite-Integration-Methode zur Simulation Elektromagnetischer Felder*, Dissertation, Technische Universität Darmstadt, 1999.
- [65] K. Holm, *Zur numerischen Berechnung transienter elektromagnetischer Felder in gyrotropen Materialien*, Dissertation, Technische Universität Darmstadt, 2000.
- [66] M. Hilgner, *Zur Generierung problemangepasster Gitter zur Berechnung elektromagnetischer Felder mit der Methode der Finiten Integration*, Dissertation, Technische Universität Darmstadt, 2001.
- [67] M. Dohlus, *Ein Beitrag zur numerischen Berechnung elektromagnetischer Felder im Zeitbereich*, Dissertation, Technische Hochschule Darmstadt, 1993.
- [68] M. Clemens, *Zur numerischen Berechnung zeitlich langsam veränderlicher elektromagnetischer Felder mit der Finite-Integrations-Methode*, Dissertation, Technische Universität Darmstadt, 1998.
- [69] P. Hahne, *Zur Numerischen Berechnung zeitharmonischer elektromagnetischer Felder*, Dissertation, Technische Hochschule Darmstadt, 1992.
- [70] B. Wagner, *Numerische Simulation von elektromagnetischen Feldern in nichtlinearen Materialien*, Dissertation, Technische Hochschule Darmstadt, 1996.
- [71] S. Drobny, *Numerische Simulation transienter elektromagnetischer Felder in nichtlinearen Materialien*, Dissertation, Technische Universität Darmstadt, 2001.

General numerical mathematics

- [72] O.C. Zienkiewicz, W.L. Wood, N.H. Hine, *A unified set of single step algorithms. Part I: General formulation and applications*, Int. J. Num. Meth., Vol. 20, pp. 1529-1552, 1984.
- [73] C.R.I. Emson, J. Simkin, *An optimal method for 3-D eddy currents*, IEEE Trans. on Magn., Vol. MAG-19, pp. 2450-2452, 1983.
- [74] A. Nicolet, *Implicit Runge-Kutta method in magnetodynamic problems*, COMPEL, Vol. 16, pp. 49-55, 1997.
- [75] H.R. Schwarz, *Numerische Mathematik*, B.G. Teubner Verlag, Stuttgart, 1993.
- [76] A. Quarteroni, R. Sacco, F. Saleri, *Numerische Mathematik*, Berlin, Heidelberg, New York, Hongkong, London, Mailand, Paris, Tokio: Springer, 2002.
- [77] C.W. Cryer, *On the instability of high order backward-difference multistep methods*, BIT, Vol. 13, pp. 153-159, 1973.

- [78] R. Alexander, *Diagonally implicit Runge-Kutta methods for stiff ODE's*, SIAM J. on Num. Anal. Vol. 14, pp. 1006-1022, 1977.
- [79] K. Burrage, *A special family of Runge-Kutta methods for solving stiff differential equations*, BIT, Vol. 18, pp. 22-41, 1978.
- [80] K.E. Brenan, S.L. Campbell, L.R. Petzold, *Numerical Solution of initial-value problems in differential-algebraic equations*, SIAM Classics in App. Math., Philadelphia, Vol. 14, 1989.
- [81] M.R. Hestenes, E. Stiefel, *Methods of conjugate gradients for solving linear systems*, Journal of Reseach of the National Bureau Standards, Vol. 49, pp. 409-436, 1952.
- [82] E. Stiefel, *Relaxationsmethoden bester Strategie zur Lösung linearer Gleichungssysteme*, Comment. Math. Helv., Vol. 29, pp. 157-179, 1955.
- [83] Y. Saad, M.H. Schultz, *GMRES: A generalised minimal residual method for solving nonsymmetric linear systems*, SIAM Journal on Scientific and Statistical Computing, Vol. 7, pp. 856-869, 1986.
- [84] J.A. Meijerink, H.A. Van der Vorst, *An iterative solution method for linear systems of which the coefficient matrix is an M-matrix*, Mathematics of Computation, Vol. 31, pp. 148-162, 1977.

Numerical computation of electromagnetic fields

- [85] W. Müller, et al, *Numerical solution of 2- or 3-Dimensional nonlinear field problems by means of the computer program PROF1*, Archiv für Elektrotechnik, Vol. 65, pp. 299-307, 1982.
- [86] S. Drobny, T. Weiland, *Iterative algorithms for nonlinear transient electromagnetic field calculation*, ISEM 99, Pavia, Italien. Studies in Applied Electromagnetics and Mechanics, IOS Press, Vol. 18, pp. 385-388, 2000.
- [87] S. Drobny, T. Weiland, *Numerical calculation of nonlinear transient field problems with the Newton-Raphson method*, IEEE Trans. on Magn., Vol. 36, pp. 809-812, 2000.
- [88] S. Drobny, M. Clemens, T. Weiland, *Dual nonlinear magnetostatic formulations using the Finite Integration technique*, Proceedings of CEFC 2000, Milwaukee, USA, p. 392, 2000.
- [89] I. Munteanu, S. Drobny, T. Weiland, D. Ioan, *Nonlinear electromagnetic field computation with FIT and triangle search method*, COMPEL, Vol. 20, pp. 417-430, 2001.
- [90] D. Iona, G. Ciuprina, C. Ciobotaru, *Hybrid algorithms for nonlinear equations of the magnetic field*, IEEE Trans. on Magn., Vol. 36, pp. 1553-1556, 2000.
- [91] F. Hantila, G. Preda, M. Vasiliu, *Polarization method for static fields*, IEEE Trans. on Magn., Vol. 36, pp. 672-675, 2000.
- [92] J. O'Dwyer, T. O'Donnell, *Choosing the relaxation parameter for the solution of nonlinear magnetic field problems by the Newton-Raphson method*, IEEE Trans. on Magn., Vol. 31, pp. 1484-1487, 1995.

- [93] K. Fujiwara, T. Nakata, H. Ohashi, *Method for determining relaxation factor for modified Newton-Raphson method*, IEEE Trans. on Magn., Vol. 29, pp. 1962-1965, 1993.
- [94] W.H. Press, S.A. Teukolsky, B. Flannery, *Numerical recipes in Fortran: the art of scientific computing*, Cambridge University Press, 1994.
- [95] H. Sande, W. Deprez, J. Coster, F. Henrotte, K. Hameyer, *Reducing the computation time of nonlinear problems by an adaptive linear system tolerance*, IEEE Trans. on Magn., Vol. 40, pp. 1306-1309, 2004.
- [96] H. De Gerssem, *Simulation of field-circuit coupled motional eddy current problems by Krylov subspace methods and multilevel techniques*, Dissertation, Katholieke Universiteit Leuven, 2001.
- [97] H. Vande Sande, *Modelling and Finite Element simulation of non-linear and anisotropic quasi-static electromagnetic systems*, Dissertation, Katholieke Universiteit Leuven, 2003.

Modelling and application of hysteresis

- [98] R. Del Vecchio, *An efficient procedure for modelling complex hysteresis processes in ferromagnetic materials*, IEEE Trans. on Magn., Vol. 16, pp. 809-811, 1980.
- [99] G. Miano, C. Serpico, L. Verolino, C. Visone, *Comparison of different hysteresis models in FE analysis of magnetic field diffusion*, IEEE Trans. on Magn., Vol. 31, pp. 1789-1792, 1995.
- [100] L. Dupré, O. Bottauscio, M. Chiampì, M. Repetto, J. Melkebeek, *Modelling of electromagnetic phenomena in soft magnetic materials under unidirectional time periodic flux excitations*, IEEE Trans. on Magn., Vol. 35, pp. 4147-4184, 1999.
- [101] L. Dupré, R. Van Keer, J. Melkebeek, *Complementary 2D finite element procedures for the magnetic field analysis using vector hysteresis model*, Intern. J. for Num. Meth. in Eng., Vol. 42, pp. 1005-1023, 1998.
- [102] N. Takahashi, S. Miyabara, K. Fujiwara, *Problems in partial finite element analysis using Preisach model*, IEEE Trans. on Magn., Vol. 35, pp. 1243-1246, 1999.
- [103] G. Park, S. Hahn, S. Lee, H. Jung, *Implementation of hysteresis characteristics using the Preisach model with MB-variables*, IEEE Trans. on Magn., Vol. 29, pp. 1542-1545, 1993.
- [104] J. Gyselinck, L. Dupré, L. Vandeveld, J. Melkebeek, *Calculation of no load induction motor core losses using the rate dependent Preisach model*, IEEE Trans. on Magn., Vol. 34, pp. 3876-3881, 1998.
- [105] J.H. Lee, J.C. Kim, D.S. Hyun, *Dynamic characteristic analysis of synchronous reluctance motor considering saturation and iron loss by FEM*, IEEE Trans. on Magn., Vol. 34, pp. 2629-2632, 1998.

- [106] J.H. Lee, D.S. Hyun, *Hysteresis analysis for the permanent magnet assisted synchronous reluctance motor by coupled FEM and Preisach modeling*, IEEE Trans. on Magn., Vol. 35, pp. 1203-1206, 1999.
- [107] J.H. Lee, D.S. Hyun, *Hysteresis characteristics computation on PWM fed synchronous reluctance motor using coupled FEM and Preisach modeling*, IEEE Trans. on Magn., Vol. 36, pp. 1209-1213, 2000.
- [108] Sz. Gyimóthy, A. Iványi, *Implementation and application of the 2D vectorial Preisach model for field calculation with the finite element method*, 6th International IGTE Symposium Proceedings, September 26-28, Graz, Austria, pp. 89-94, 1994.
- [109] O. Bottauscio, M. Chiampi, C. Ragusa, L. Rege, M. Repetto, *A test case for validation of magnetic field analysis with vector hysteresis*, IEEE Trans. on Magn., Vol. 38, pp. 893-896, 2002.
- [110] N. Sadowski, N.J. Batistela, J.P.A. Bastos, M. Lajoie-Mazenc, *An inverse Jiles-Atherton model to take into account hysteresis in time stepping finite element calculations*, IEEE Trans. on Magn., Vol. 38, pp. 797-800, 2002.
- [111] H. Igarashi, D. Lederer, A. Kost, T. Honma, T. Nakata, *A numerical investigation of Preisach and Jiles models for magnetic hysteresis*, COMPEL, Vol. 17, pp. 357-363, 1998.
- [112] Y.O. Amor, M. Féliachi, H. Mohellebi, *A new convergence procedure for the finite element computing associated to Preisach hysteresis model*, IEEE Trans. on Magn., Vol. 36, pp. 1242-1245, 2000.
- [113] M. Dotterweich, G. Szymanski, M. Waszak, F. Weiland, *Calculation of 3D electromagnetic field taking hysteresis into account*, 9th International IGTE Symposium Proceedings, Graz, Austria, pp. 67-69, 2000.
- [114] E. Cardelli, E. Della Torre, B. Tellini, *Direct and inverse Preisach modeling of soft materials*, IEEE Trans. on Magn., Vol. 36, pp. 1267-1271, 2000.
- [115] R. Venkataraman, P.S. Krishnaprasad, *Approximate inversion of hysteresis: theory and numerical results*, 39th IEEE Conference on Decision and Control Proceedings, Sydney, Australia, pp. 4448-4454, 2000.
- [116] A. Reimers, E. Della Torre, *Fast Preisach-Based magnetization model and fast inverse hysteresis model*, IEEE Trans. on Magn., Vol. 34, pp. 3857-3866, 1998.
- [117] S. Mittal, C.H. Menq, *Hysteresis compensation in electromagnetic actuators through Preisach model inversion*, IEEE Trans. on Mech., Vol. 5, pp. 394-409, 2000.
- [118] K.H. Kenneth, H. Carpenter, *A differential equation approach to minor loops in the Jiles-Atherton hysteresis model*, IEEE Trans. on Magn., Vol. 27, pp. 4404-4406, 1991.
- [119] J.V. Leite, N. Sadowski, P. Kuo-Peng, N.J. Batistela, J.P.A. Bastos, *The inverse Jiles-Atherton model parameters identification*, IEEE Trans. on Magn., Vol. 39, pp. 1397-1400, 2003.

- [120] J. Gyselinck, P. Dular, N. Sadowski, J. Leite, J.P.A. Bastos, *Application of the Newton-Raphson method to FE magnetic field computations with vector hysteresis*, Proceedings of the XI International Symposium on Electromagnetic Fields in Electrical Engineering (ISEF 2003), 18.-20.09.03, pp. 485-488, 2003.
- [121] Testing Electromagnetic Analysis Methods (T.E.A.M.) Web-Page,
<http://www.compumag.co.uk/teamindex.html>.
- [122] TEAM Benchmark Problem 32 Web-Page,
<http://www2.polito.it/ricerca/cadema/Team32/home.html>.

Publications in international conference proceedings and journals

- [123] J. Yuan, K.D. Zhou, *Simulation and analysis on influence of permanent-magnet for doubly salient permanent magnet motor system*, Proceedings of the 4th International Conference on Electromagnetic Field Problem and Applications (ICEF'00), Tianjin, China, 18.-20.09.00, pp. 322-325, 2000.
- [124] J. Yuan, M. Clemens, H. De Gersem, T. Weiland, *3D Electromagnetic Simulation of a DSPM System Using the FI-Method*, Refereed article in *Electromagnetic Fields in Electrical Engineering*, eds. A. Krawczyk and S. Wiak, IOS Press, series *Studies in Applied Electromagnetics and Mechanics*, Vol. 22, pp. 153-157, 2002. (ISBN 1 58603 232 1) (Proceedings of the X International Symposium on Electromagnetic Fields in Electrical Engineering (ISEF 2001), Cracow, Poland, 20.-22.09.01)
- [125] H. De Gersem, M. Clemens, J. Yuan, M. Wilke, T. Weiland, *Simulation of the Nuclotron Magnet by a Hybrid 2D Finite-Element Spectral Element Discretization*, Gesellschaft für Schwerionenforschung (GSI) Report 2002, p. 199, May 2002.
- [126] H. De Gersem, M. Clemens, M. Wilke, J. Yuan, T. Weiland, *Finite Element Models Accounting for Eddy Current Effects in Superconductive Cables with Finite Inter-Wire Resistance*, Gesellschaft für Schwerionenforschung (GSI) Report 2003, p. 203, May 2003.
- [127] J. Yuan, M. Clemens, T. Weiland, *Simulation of Hysteresis Effects Using the Classical Preisach Model in FI^2TD Formulations*, IOS Press, *International Journal of Applied Electromagnetics and Mechanics* Vol. 19, Nos.1-4, pp. 19-24, 2004. (ISSN 1383-5416) (Proceedings of the 11th International Symposium on Applied Electromagnetics and Mechanics (ISEM'03), Versailles, France, 12.-14.05.03, pp. 88-89, 2003.)
- [128] J. Yuan, M. Clemens, T. Weiland, *Transient Magnetic Field Calculations in Hysteretic Media with FI^2TD Formulations*, Proceedings of the 5th International Conference on Electrical Machines and Systems (ICEMS'03), Beijing, China, 09.-12.08.03, pp. 769-773, 2003.
- [129] M. Clemens, G. Benderskaya, H. De Gersem, S. Feigh, M. Wilke, J. Yuan, T. Weiland, *Formulations and Efficient Numerical Solution Techniques for Transient 3D Magneto- and Electro-Quasistatic Field Problems*, Report No. 11/2004, Workshop on Computational Electromagnetism, Mathematisches Forschungsinstitut Oberwolfach, 22 - 28.02.04, pp. 21 - 22, 2004.
- [130] H. De Gersem, M. Wilke, M. Clemens, G. Moritz, C. Mülle, J. Yuan, T. Weiland, *Simulation of the Eddy Current Losses in the Nuclotron Magnet Yoke Using the Finite Integration*, Gesellschaft für Schwerionenforschung (GSI) Report 2004, p. 256, May 2004.
- [131] J. Yuan, M. Clemens, H. De Gersem, T. Weiland, *Solution of Transient Hysteretic Magnetic Field Problems with Hybrid Newton-Polarization Methods*, *IEEE Trans. on Magn.*, Vol. 41, pp. 1720-1723, 2005. (Proceedings of the 11th Biennial IEEE conference on Electromagnetic Field Computation (CEFC'04), Seoul, Korea, 06.-09.06, p. 102, 2004.)

- [132] J. Yuan, M. Clemens, H. De Gersem, T. Weiland, *The Jiles-Atherton Model Combined with the Newton-Raphson Method for the Simulation of Transient of Hysteretic Field Problems*, Proceedings of the XVIII Symposium Electromagnetic Phenomena in nonlinear circuits (EPNC'04), Poznan, Poland, 28.-30.06.04, pp. 19-20, 2004.
- [133] J. Yuan, H. De Gersem, M. Clemens, T. Weiland, *A Vector Preisach Model Combined with a Newton-Raphson Method for Transient Magnetic Field Computations*, Proceedings of the 5th International Symposium on Hysteresis and Micromagnetic Modeling (HMM'05), Budapest, Hungary, 30.05-01.06.05, pp. 59-60, 2005.

Acknowledgements

At this point of completing this dissertation, I would like to express my gratitude to all the people, who directly or indirectly helped me throughout the whole time of this Ph.D. work.

First of all, I would like to thank Prof. Dr.-Ing. Thomas Weiland for the scientific supervision and opening the excellent possibility to work in his group TEMF. Without his support in science and finance, it would have been impossible for me to successfully complete this Ph.D. work in the TU Darmstadt.

I would like to thank Prof. Dr.-Ing. habil. Andreas Binder for kindly and carefully reviewing and correcting this dissertation as co-referee.

Special thanks to Dr.-Ing. Herbert De Gersem and Dr. rer. nat. Markus Clemens for their scientific guidance and for their correcting till the last version of this dissertation. I have learned a lot from both of them, not only the careful and diligent research attitude.

During the research activities at TEMF, my present and former colleagues provided the pleasant and friendly atmosphere. It is impossible to express my thanks in so few words.

Other special thanks to two colleagues at CST. To Dr.-Ing. Min Zhang and his family, who gave me a lot of help in working and living. To Dipl.-Ing. Wigand Koch for carefully reading and commenting on this manuscript.

I want to express my deep thanks to my parents for their supporting throughout all of my life. Thanks also to my brother and his family, making me feel understood.

At last I would like to thank my former Master degree supervisor Prof. Ke Ding Zhou, who guided me into the present research region. His diligent work spirit impressed me and guides me to the future career.

Thanks to all of you!

Curriculum Vitae

Jing Yuan

born on 06. April 1975 in Wuhan (China)

- 1981-1987 Baihechun primary school in Wuhan
- 1987-1990 The No. 23 junior middle school in Wuhan
- 1990-1993 The No. 3 senior middle school in Wuhan
- 1993-1997 Bachelor degree study at Department of Electrical and Electronic Engineering of Hubei University of Technology in Wuhan
- 1997-2000 Master degree study at Department of Electrical and Electronic Engineering of Hubei University of Technology in Wuhan
- 1998-1999 Master thesis research in ABB Corporate Research Center in Heidelberg
- 2000-2005 Research assistant at Institut für Theorie Elektromagnetischer Felder of Darmstadt University of Technology in Darmstadt

